CHALLENGING MECHANISTIC PARADIGMS IN COPPER MONOOXYGENASE

By

Evan Welch

A DISSERTATION

Presented to the
Biomedical Engineering Department
within the Oregon Health and Science University
School of Medicine
in partial fulfillment of
the requirements for the degree of
Doctor of Philosophy
in
Biomedical Engineering

March 2025

CERTIFICATE OF APPROVAL

This is to certify that the PhD dissertation of

Evan Welch

Has been approved by

Advisor

Ninian Blackburn

Summer L. Gibbs

Chair

Xiaolin Nan

Committee Member

Daniel M. Zuckerman

Committee Member

Pierre Moënne-Loccoz

Committee Member

TABLE OF CONTENTS

List of Figures

List of Tables

Acknowledgements

Completing this PhD study has been one of the most difficult and rewarding experiences of my life, and I owe that accomplishment to many people.

First, I must thank my mentor, Dr. Ninian Blackburn. A night a very long time ago we were huddled around a screen collecting (bad) data and you asked me if I was happy doing preparatory work for the lab as a technician. When I told you that I was, you told me that was the wrong answer. I must thank you emphatically for proving me wrong many times.

Thank you to my dissertation advisory committee, Dr. Summer L. Gibbs, Dr. Xiaolin Nan, and Dr. Daniel M. Zuckerman, who advised me to clarify and simplify. Their comments were instrumental in this work.

I also thank the members of my lab present and previous. Special thanks to Dr. Renee Arias for being a wonderful friend, colleague and mentor. Dr. Katherine Alwan for bringing me into the lab and her continued patience thereafter. Tamar Conner for her tireless work to enable my experiments. My sincere thanks also go to Dr. Pierre Möenne-Loccoz for his expertise with instruments and his graciousness for new users.

This process would have been impossible without my family. I thank my parents, writers, musicians, artists, who taught me the beauty of things unquantifiable. I also thank Pan, an adopted member of my family, his undaunted spirit buoyed me through this process.

And a final thanks to Avery. You, foundational to my life, are foundational to this work.

Chapter One: Introduction

1.1 Terminal amidation and PAM

Bioactive peptides are among the most important signaling molecules, controlling physiological functions as disparate as blood pressure, hunger and satiation, homeostasis, and more[1,2]. Early isolation of these peptides revealed bioactive forms with a c-terminal amidation, as well as immature pro-peptides that were instead glycine-extended[3]. Further, this terminal amidation was determined to have several roles in peptide function. Amidation of the c-terminal end of peptides may increase hydrophobicity via neutralization of the ionizable carboxy group, and increase receptor binding[4]. Initially it was speculated that terminal amidation was a result of transamination with no enzymatic catalyst, but this was discounted by studies that used a radiolabeled peptide to detect reaction products such as radiolabeled glyoxylate, which are inconsistent with transamination[5]. This made the existence of an enzyme that recognized the glycine extended pro-peptide likely. Further studies involving the purification of secretory granules from rat and bovine pituitary glands revealed this enzyme, and elucidated several notable characteristics[6]. The enzyme was determined to be dependent on copper, oxygen, and ascorbate (vitamin C). These properties were remarkably like a previously identified enzyme, dopamine beta-monooxygenase (DBM), also dependent on copper, oxygen, and ascorbic acid. Based on these similarities, this mystery amidating enzyme was determined to be a monooxygenase, an enzyme that splits diatomic O_2 and incorporates one atom into its substrate, and dubbed peptidylglycine alpha-amidating monooxygenase (PAM).

The detection of a stable intermediate revealed that peptide amidation by PAM proceeds in two main steps (Figure 1-1)[5]. The first of these steps is hydroxylation, which is accomplished by the addition of a hydroxyl group on the alpha-carbon of the terminal glycine, resulting in an alpha-hydroxyglycine intermediate. These alpha-hydroxyglycine intermediates are relatively stable at physiological pH, necessitating further refinement to

reach a fully amidated form. This is accomplished by cleaving along the N-C bond (shown in red) resulting in an alpha-amidated peptide and glyoxylate. Initially this second cleavage step was believed to be accomplished by a separate enzyme or cofactor, but subsequent examination of PAM cDNA indicated that it encoded two separate enzymatic domains, each responsible for one step of the peptide amidation[7,8]. The enzyme domain for the first step, hydroxylation, was named peptidylglycine alpha-hydroxylating monooxygenase (PHM), while the enzyme domain responsible for the second step, cleavage of the glyoxylate to reach a finished product, was named peptidylglycine alpha-amidating lyase (PAL). Collectively these domains are referred to as PAM, which is often referred to as the "bifunctional" enzyme in this context.

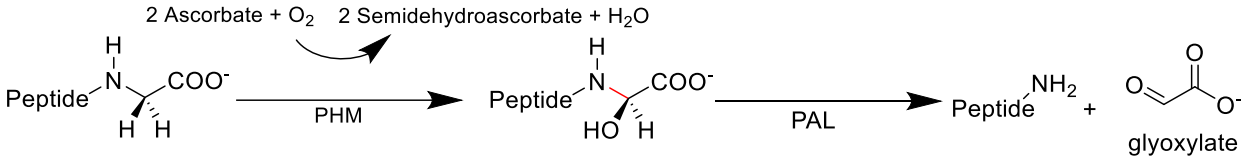

Figure 1-1 Overall PAM reaction to achieve peptide amidation. *First, the peptide substrate is hydroxylated via peptidylglycine alpha-hydroxylating monooxygenase (PHM), the resulting alpha-hydroxyglycine is then cleaved by PAL resulting in a peptide amide and glyoxylate.*

PAM is a widely distributed and ancient enzyme[9]. Versions of PAM can be found in organisms as disparate as humans, *drosophila*[10], marine mollusc *aplysia*[11], the flatworm *Schistosoma mansoni*[12], and amazingly green algae, which raises the possibility it predates the evolutionary split of plants and animals. PAM is also important physiologically and developmentally. Homozygous deletion of PAM is embryonic lethal in *drosophila*[13] and murine[14] models. Heterozygous deletion of the PAM gene in murine models leads to a wide array of symptoms including increased adiposity, glucose intolerance, modified fear response, seizure hypersensitivity, and more[14,15]. Experiments have shown high levels of PAM expression in numerous rat tissues including neural tissue, in the anterior pituitary, and the hypothalamus. Expression is particularly high in the heart where it represents more than .1% of all mRNA isolated[16]. These different tissues also show stark differences in expression, which are discussed further below.

The bifunctional enzyme PAM has a flexible expression pathway. In work done by the Eipper lab, the cDNA of PAM was determined to encode a 108 kDa precursor protein[7]. This precursor protein is comprised of a localization sequence, a transmembrane domain, and the bifunctional PAM protein. PAM cDNA also encodes for several endoprotease sensitive linker regions between the two enzymatic domains. Endoproteolytic cleavage of these linkers allows the bifunctional enzyme to be modified to two separate soluble enzymes. Beside this "original" variant of PAM cDNA (called PAM-1), two other main isoforms have been isolated (Figure 1-2). The PAM-2 isoform entirely lacks the endoprotease sensitive linker region, which largely prevents it from being cleaved into its two separate domains. The PAM-3 isoform does not include the endoprotease-sensitive region or the transmembrane domain. The additional removal of the transmembrane domain allows for the secretion of soluble, bifunctional PAM. This allows the secretion of soluble PHM and PAL separately via PAM-1, secretion of membrane localized PAM via PAM-2, and soluble PAM-3. While PAM expression is detectable in virtually all mammalian cells, different isoforms are present in different tissues. Heart and neural tissue are especially varied, with a complex and varied pattern of splicing, secretion, and endoproteolytic cleavage[16,17]. Perhaps the most illustrative of this pathway's extreme importance is the presence of soluble PHM and PAL in neural secretory granules and in cerebrospinal fluid[18]. This co-expression along with neurotransmitters and signaling peptides is indicative of its importance.

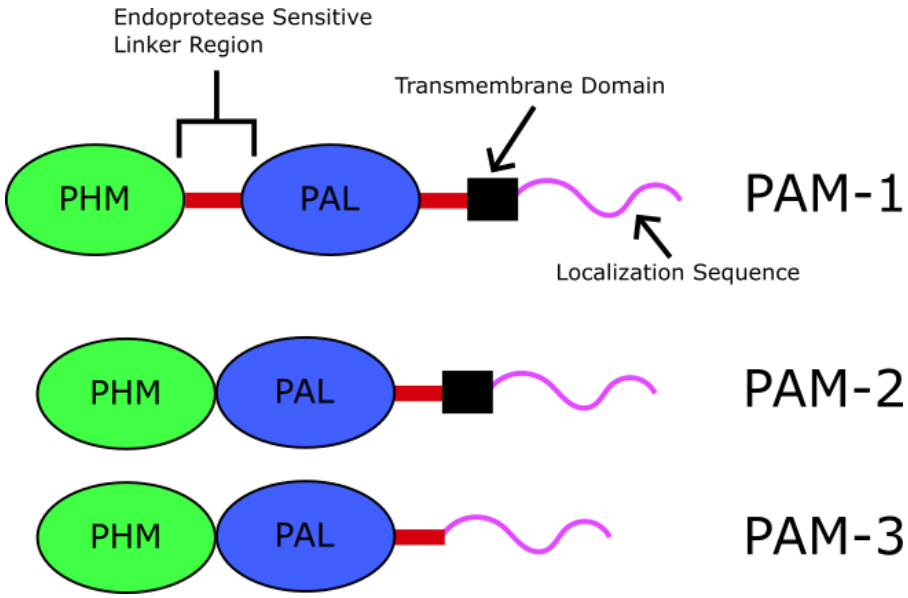

Figure 1-2 Major PAM Isoforms. *Major PAM isoforms 1-3 are shown. PAM-1 encodes for both enzyme domains, an endoprotease-sensitive linker region, a transmembrane domain, and a localization sequence, allowing expression of soluble PHM and PAL. PAM-2 lacks the endoprotease-sensitive linker region generating membrane bound bifunctional PAM. PAM-3 lacks the transmembrane domain and the linker region allowing for the expression of soluble PAM.*

Given its physiological importance there has been intense study on the structure and function of PAM, particularly the PHM domain, which has implications in other physiologically relevant monooxygenases. The next section focuses on the PHM domain's structure, function, and homologous enzyme DBM.

1.2 Structure of PHM and homologue DBM

As previously mentioned, PAM, particularly its subdomain PHM, was determined to be a monooxygenase based on its oxygen sensitivity, copper requirements, and ascorbate dependence. Studies have focused on the "catalytic core" of the PHM domain, often rendered as PHMcc (residues 42 – 356), but will hereafter be referred to simply as PHM. PHM is capable of catalyzing peptide hydroxylation when provided with all necessary materials[19] without the rest of the PAM protein. Notably, PHM has 30% sequence identity with DBM over a 286 amino acid region, including eight conserved cysteines and six conserved copper ligands. Based on their similar structure, reaction products, and

reaction reagents it is believed that these enzymes have similar, or identical, reaction mechanisms. Here we discuss the most salient aspects of PHM and DBM structure.

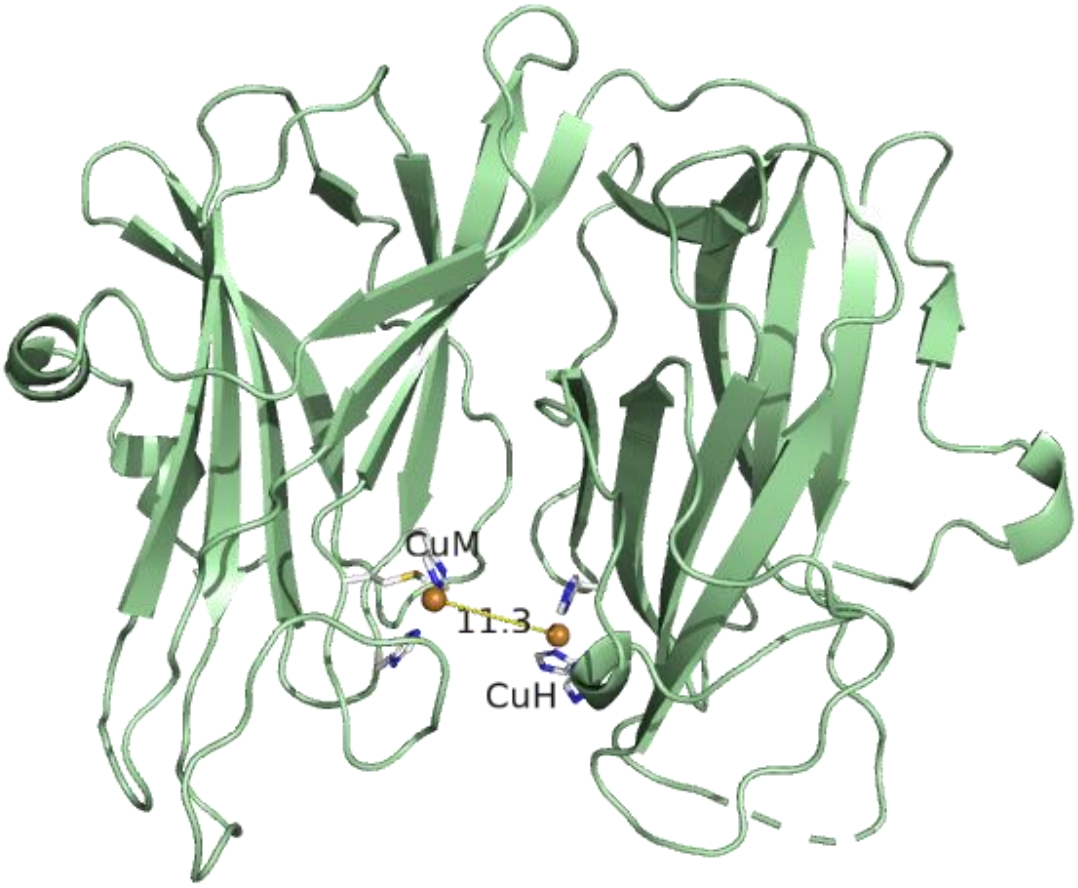

Figure 1-3 Diagram of oxidized PHM protein. *Protein backbone is shown in light green with copper atoms as orange spheres. Carbon atoms are shown in white, nitrogen in blue, sulfur in yellow. Coordinating ligands at each copper site are shown, as well as Cu-Cu distance in angstrom. PDB Identifier 1PHM.*

PHM is a 310 residue, 36 kDa, globular protein. It consists of two large "lobes", each made of a nine-stranded beta-sandwich domain[19] (Figure 1-3). Each domain is approximately 150 residues in length and binds one copper atom. These two lobes are linked together with a short linker domain where they are closely associated with a hydrophobic contact, expanding to a large solvent filled cleft averaging 8 Å in separation. The two lobes are designated by their inequivalent copper sites. The first copper site is referred to as the CuH site (in older literature CuA), referring to its coordination with three

histidine residues, H107, H108, and H172. The second copper site is referred to as the CuM site (in older literature CuB), coordinated with two histidine residues and its namesake methionine, H242, H244, and M314. This M314 ligand is of particular interest, as it has been shown spectroscopically to be quite fluxional[20]. The oxidized Cu(II)M site shows no interaction of the M314 ligand, which only coordinates in the reduced Cu(I)M state. Even then, the spectroscopic signal of the M314 is also pH dependent suggesting a complex and dynamic role[21]. The two copper sites are separated by 11 Å across the solvent filled cleft (Figure 1-4).

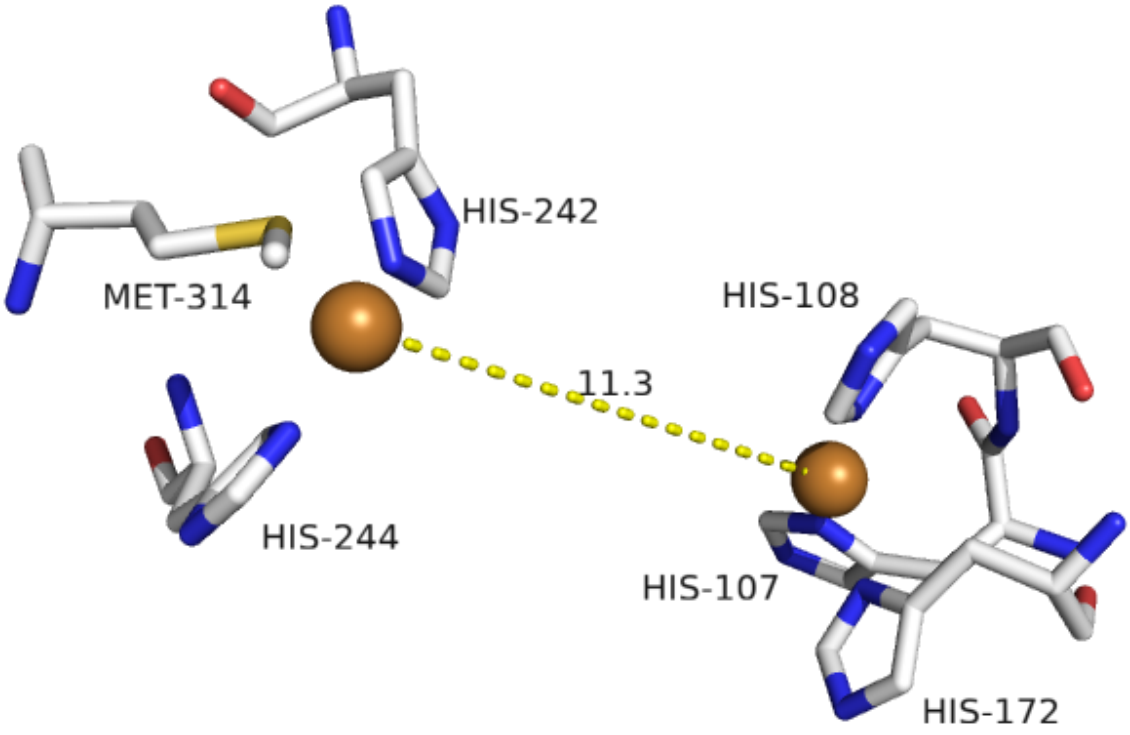

Figure 1-4 Diagram of PHM active site. *Coordinating residues are labeled, and Cu-Cu distance in angstroms is shown. While M314 ligand is shown here, in oxidized PHM it coordinates loosely.*

These six copper ligating residues are conserved among PHM and DBM, and mutagenesis of any of these residues results in almost complete loss of activity (>95% loss). The implications of mutagenesis and specific discussion of mutants are addressed later in section 1.6. This large separation between the two copper sites is an important and characteristic element of both PHM and DBM. Based on this separation, both monooxygenases are considered "noncoupled", which indicates that their catalysis and oxygen binding occur at only one metal site. This is in contrast with coupled enzymes, which use two or more metal centers in tandem to bind and perform catalysis. Based on DFT computational studies[22] and observations of synthetic and biological compounds[23,24] the Cu-Cu distance to allow for coupled interactions is approximately 4 Å. Coupled Cu monooxygenases, such as tyrosinase, are well understood[25]. In these enzymes, oxygen binds in a bridging or semi-bridging modality between the two copper sites, and electron transfer from both sites is facile, enabling catalysis. The mechanism in noncoupled monooxygenases is much murkier, which is discussed at length in section 1.3.

Substrate has been determined to bind in the solvent filled cleft close to the CuM site, shown in Figure 1-5. Substrate binding has not been shown to dramatically change PHM's structure[26]. Using crystallography, oxidized, substrate-bound PHM does not show significantly moved residues, and its copper-copper distance remains ~11 Å. The only structural change on substrate binding is the rotation of N316 to hydrogen bond with the substrate. Three other residues, R240, Y318, and N316 form hydrogen bonds with the peptide backbone to anchor it in the enzyme active site. Additionally, CuM ligand M314 has contact with the substrate in its binding pocket. Oxygen has been shown crystallographically[27] and spectroscopically[28] to bind to the CuM site exclusively.

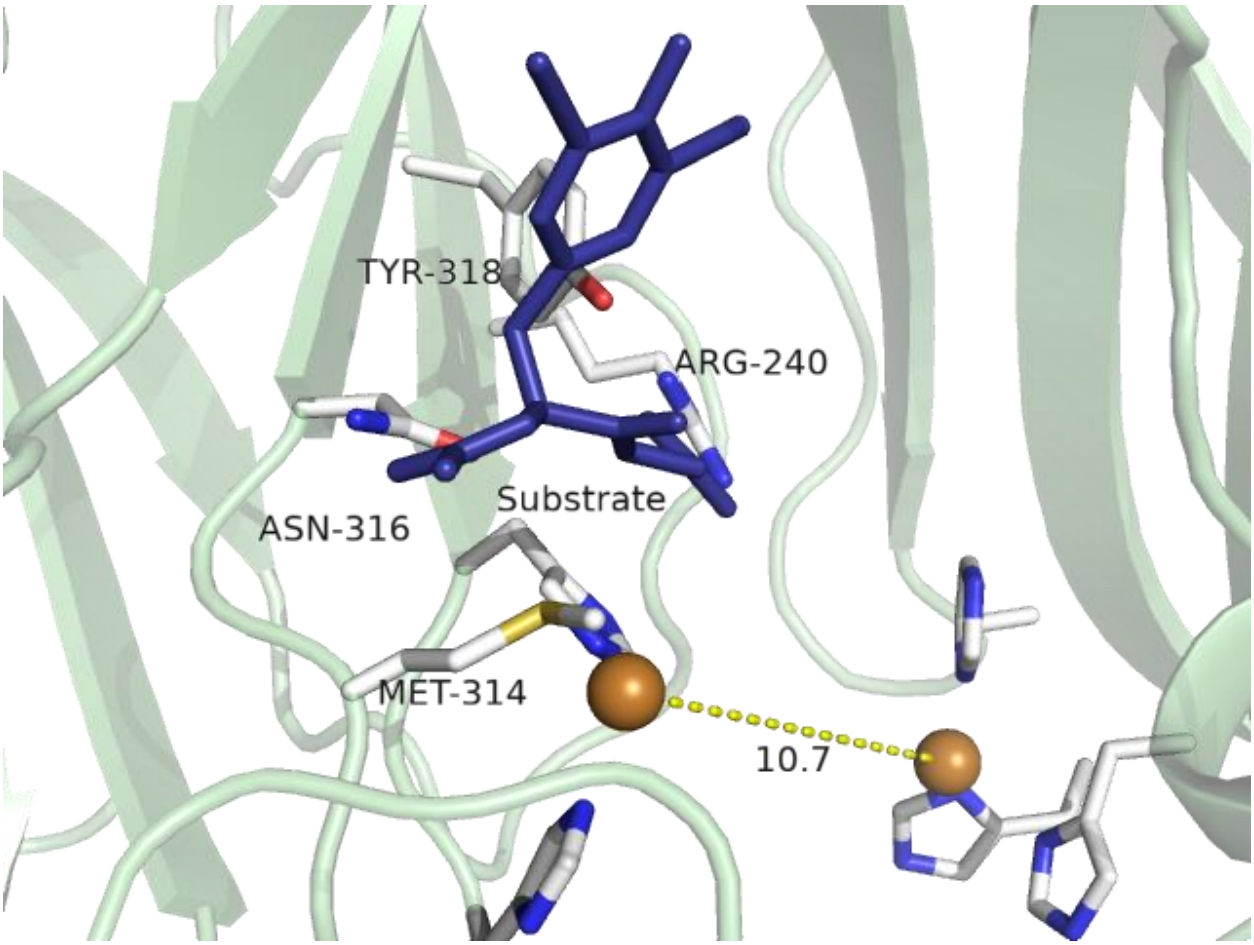

Figure 1-5 Diagram of PHM active site with bound substrate. *PDB identifier 1OPM. Substrate is small peptide is acetyl-diiodotyrsoglycine (Ac-Dil-YG), shown in purple. Residues coordinated to substrate are labeled.*

The most important crystal structure in the context of the canonical mechanism of PHM (discussed at length in section 1.3) is the so called "precatalytic" form, shown in Figure 1-5[27]. This structure was obtained by crystallizing the enzyme in the presence of oxygen, ascorbate, and a slow substrate. Since PHM is capable of slow turnover even in a crystal lattice[29], a slow substrate was employed with the goal of capturing a precatalytic form. The resulting structure shows substrate bound as in previous structures, and oxygen bound the CuM site in an end-on configuration. The oxygen of this structure was determined to be either dioxygen or superoxide ($O_2^{\bullet-}$) based on the O-O bond length. While this structure is referred to as a "precatalytic" structure, that is solely based on the presence of bound substrate and oxygen and there is no definitive proof that it is

catalytically relevant. Nonetheless, this structure is the basis for computational approaches.

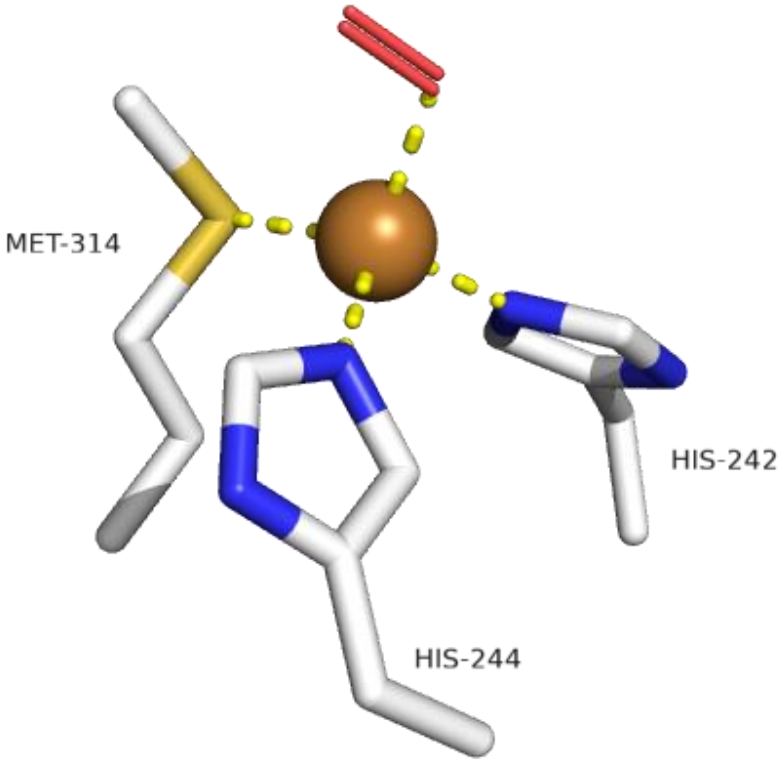

Figure 1-6 Diagram of PHM CuM site coordinated with dioxygen. *PDB identifier 1SDW. Oxygen is shown as red rod in an end-on configuration.*

Besides the 11 Å copper-copper separation observed in WT PHM there is an alternative structure with CuH and CuM sites positioned much more closely. H108A mutant PHM crystalized with citrate is radically different, shown below in Figure 1-7[26]. The H108A mutant loses copper at the CuH site, which is accompanied by a rotation of the entire domain by ~18º. This large interdomain movement reduces the distance between the two sites to 4 Å. The remaining copper is ligated by a combination of residues from the typical CuM and CuH site, coordinating with H242 (CuM site), H244 (CuM site), and H172 (CuH site). Citrate has an important role in this transformation, where it spans the gap between the CuM and the CuH site through three contacts: coordination to the remaining copper and two hydrogen bonds to R240 and H172. These two hydrogen bonds are evocative in the context of these residues' function. R240 is as previously mentioned one

of the active site anchoring residues, while H172 has been demonstrated to be especially critical for enzyme turnover[30]. Notably the molecular structure of citrate and the physiological reductant ascorbate show some similarity, raising the possibility that ascorbate could accomplish similar site-bridging, although no ascorbate binding site is known and no ascorbate bound structures have been crystallized. This 4 Å distance structure is often referred to as the "closed" conformer of PHM. There are no crystal structures of WT PHM in this closed conformer which has led to significant debate of its relevance in a catalytic cycle. This doubt comes from first, the H108A mutant was crystalized without copper in its CuH site, and second because some catalytic turnover occurs in WT crystals soaked with substrate, where it is presumed no conformational change is possible[29], however, it is notable that this turnover is extremely slow. For these reasons the H108A mutant and closed structures of PHM in general are historically believed to be artifacts of crystallization or mutagenesis.

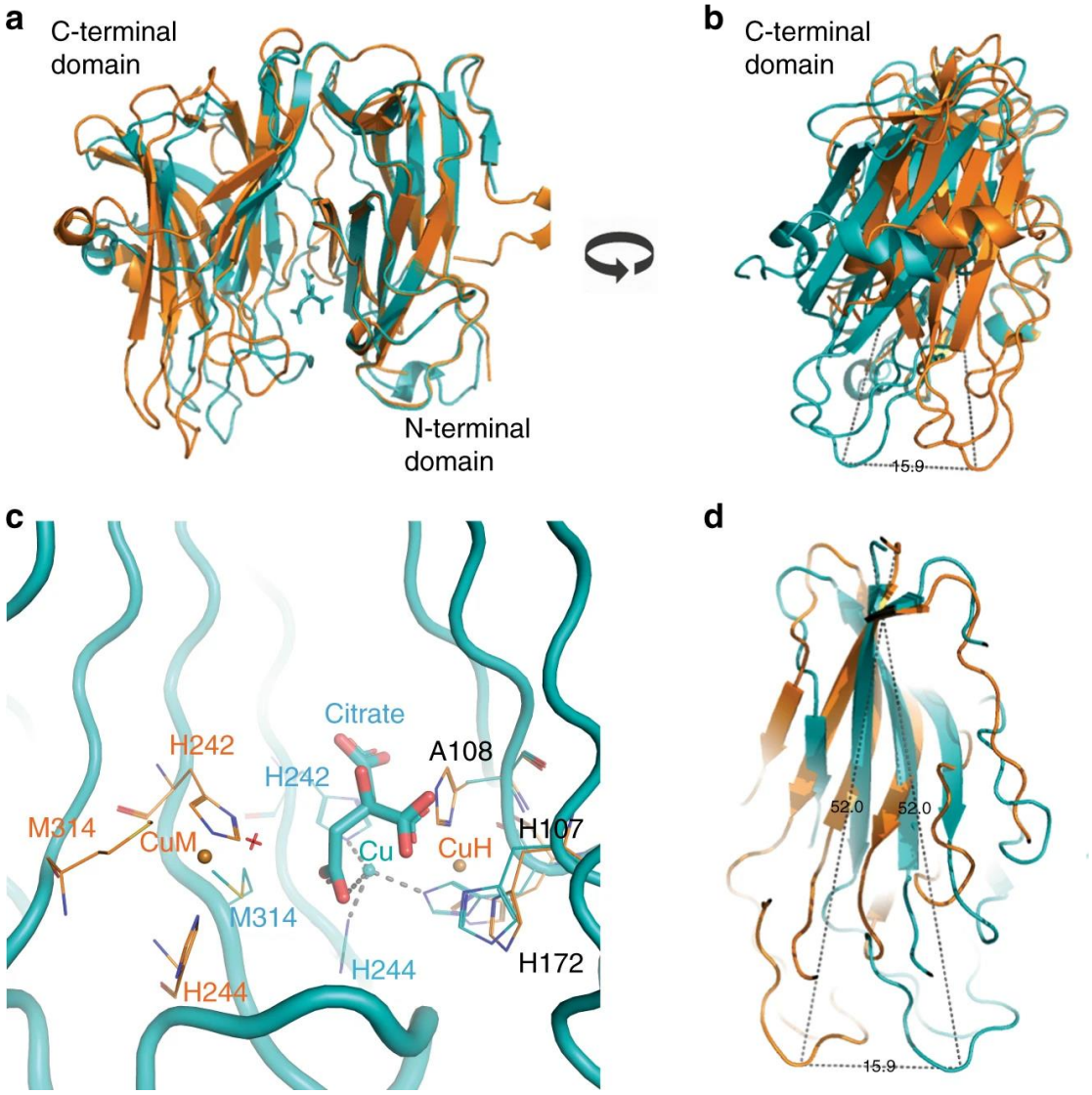

Figure 1-7 Overlaid structures of WT PHM and H108 mutant. *WT PHM (orange, PDB 1PHM) and H108A mutant in complex with citrate (blue, PDB 6ALA). Panel **a** shows complete protein structure, revealing a large-scale transformation of the C-terminal domain which has rotated towards the N-terminal domain. Panel **b** shows 90° rotation around the vertical axis, and tracks a residue (T301), distant from the axis of rotation, revealing it has moved by 15.9 Å, emphasizing the magnitude of the rotation. Panel **c** shows the interdomain cleft, where the distance between H172 and H242 has been decreased from more than 11 Å in WT PHM to 4 Å. The ligand set of the sole copper atom in H108A is a hybrid of the CuM and CuH ligand set, H242, H244, and H172. Panel **d** shows a close-up of the c-terminal domain, which shows an 18° rotation toward the N-subdomain relative to WT PHM. Figure adapted from Maheshewari et al 2018.*

A closed conformer has also been isolated in DBM[31]. In 2016 the Vendelboe lab successfully crystalized DBM in the form of a heterodimer. In this heterodimer one of the two monomers was found to be in an "open" conformation resembling the characteristic

11 Å separated PHM structure. The other monomer, however, was found to be in a closed conformation, rotating along the hinge domain to reduce the copper-copper distance to approximately 4 Å (Figure 1-8). While the authors acknowledge that this could be an artifact of crystallization, they also explore the possibility that this closed conformer could have catalytic competency or even be a requirement of the catalytic cycle. Under this hypothesis the heterodimer could engage in a “flip-flop” style mechanism, where substrate binding and reduction occur in the open unit, and product formation occurs in the closed unit, alternating to release product and rebind new substrate.

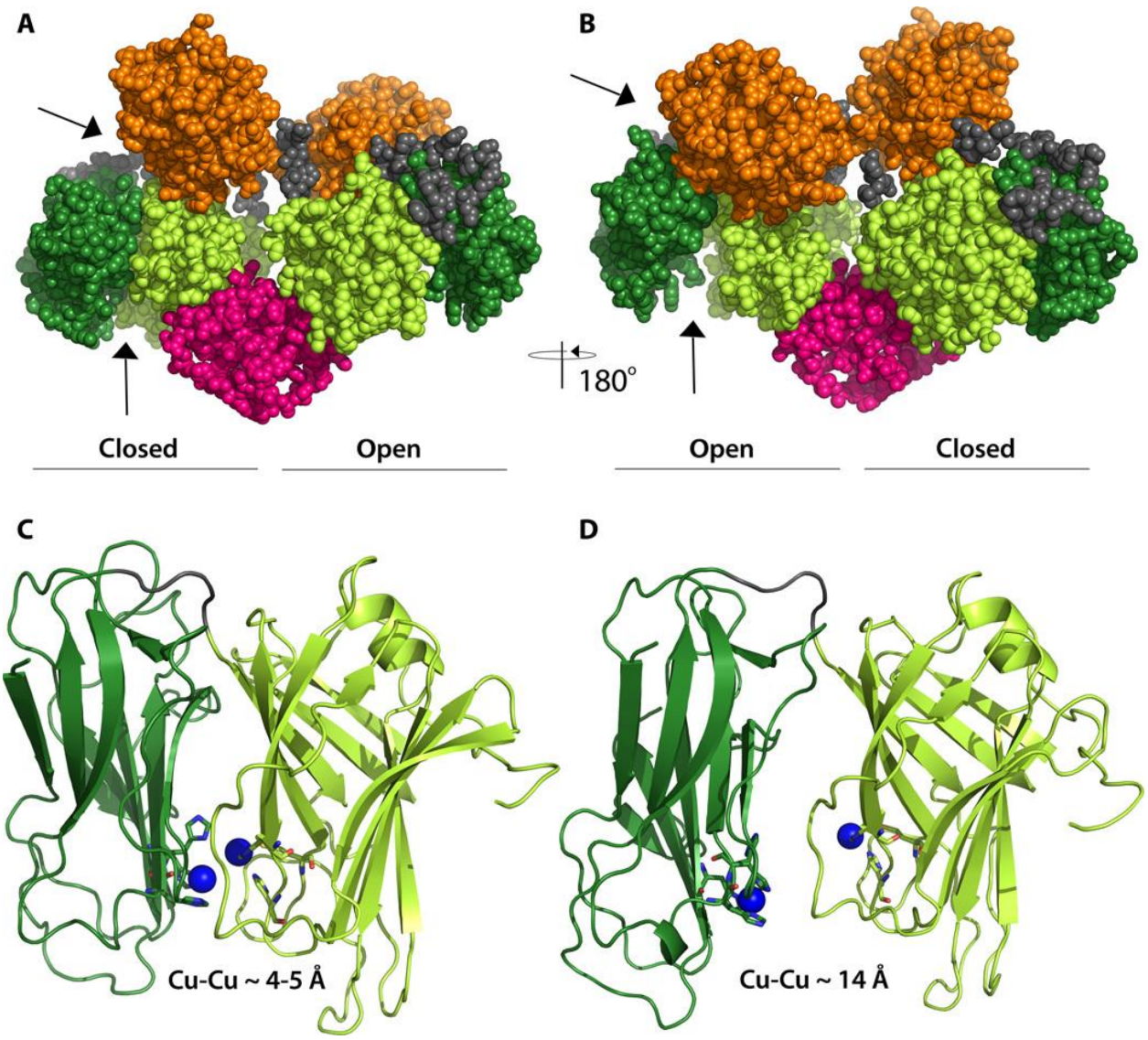

Figure 1-8 Crystal structure of DBM heterodimer with closed and open conformers. *Different domains are colored coded as follows CuM domain in light green, CuH domain in dark green, dimerization linker in purple, and dopamine beta-monooxygenase N-terminal domain (DOMON) shown in orange, the DOMON domain is not well understood but may have implications in cellular surface adhesion[32]. Panel **A** and **B** show two views of a DBM heterodimer with a 180° rotation between, black arrow indicates areas of largest change between conformers. Panel **C** shows one subunit of a DBM heterodimer with a Cu-Cu distance of 4-5 Å. Panel **D** shows the other subunit of DBM, in an open conformer with a Cu-Cu distance of 14 Å. Figure adapted from Vendelboe et al 2016[31].*

1.3 The Canonical Reaction mechanism, caveats and unknowns

Before discussing the canonical mechanism, an important question needs to be asked, why do we care? Is there really a necessity to understand the nuts and bolts of this reaction? Parallel to efforts to understand PHM, and by extension PAM, were efforts to use PHM as a druggable target[33]. This led to the production of several inhibitors of PHM, mostly substrate analogue inhibitors[34-36]. Without fully understanding the PHM reaction mechanism researchers have so far been confined to crude substrate inhibitors that are poorly understood and lacking specificity. This lack of specificity is important in the context of PHM's rising role as a biomarker for disease. PHM has been shown to be a biomarker in specific cancers and may even contribute to their pathology[37-39]. Both increased and decreased levels of PHM expression were correlated with increased disease severity in these studies, suggesting that dysregulation in general is dangerous. For these reasons a deeper understanding of the PHM reaction mechanism is pivotal. Greater understanding could lead to the development of higher affinity, tissue specific, second-generation inhibitors.

A key constraint on reaction mechanisms is the coupling of PHM catalysis. WT PHM and DBM, as well as all mutants characterized thus far, exhibit 100 percent coupling, i.e. the amount of substrate, oxygen, and ascorbate consumed is directly proportional to the amount of hydroxylated product generated[40,41]. This tight coupling remains even with substrates or mutants with greatly reduced catalytic rate. This constraint therefore requires that any reaction mechanism proposed must recapitulate this tight coupling.

Through a large number of spectroscopic[42,43], kinetic[44], and computational[45,46] studies a canonical reaction mechanism has emerged, shown below in Figure 1-9[47]. First, two molecules of ascorbate reduce the two Cu(II) centers to their Cu(I) state, with two molecules of semidehydroascorbate as byproducts[48]. This is followed by the binding of dioxygen at the CuM site and substrate binding at the nearby binding site. The binding of Cu(I) and dioxygen results in the formation of a Cu(II)-superoxo species at the CuM site. This highly reactive complex abstracts a hydrogen atom (abstraction is the transfer of a

neutral hydrogen), generally shown to be from the substrate, resulting in a Cu(II)-peroxo and a substrate radical. From here the pathway diverges, in the oxyl radical pathway, long range electron transfer occurs from the CuH site, most often shown traveling through ordered solvent, to break the O-O bond of the Cu(II)-peroxo resulting in a Cu(II)-O^{-}• oxyl radical. Next, radical rebound occurs between the oxyl radical and the substrate radical, resulting in a copper-bound substrate-oxo complex. Finally, rereduction by ascorbate releases this complex as a peptide hydroxyl. An alternate, but quite similar, reaction proceeds through proton-coupled electron transfer (PCET, a process where a proton and an electron are transferred together)[46]. In the PCET form, instead of an oxyl radical, radical rebound occurs between the substrate radical and the Cu(II)-peroxo, breaking the O-O bond to form a Cu(II)-O-substrate radical species. This unstable species provides a strong driving force for PCET from the CuH site, resulting in a Cu(II)-product complex that is then released as part of reduction, similar to the other schema. In both of these related mechanisms catalysis occurs exclusively at the CuM site, with the CuH site operating only as an electron storage and transfer site. These reactions are consistent with many, but not all, experimental observations. Several key unknowns remain: the identity of the oxygen intermediate, how electron transfer occurs, and the structure and relevance of alternate conformers. The next few sections describe several experimental approaches and their results, as well as how these experiments conflict with this canonical mechanism.

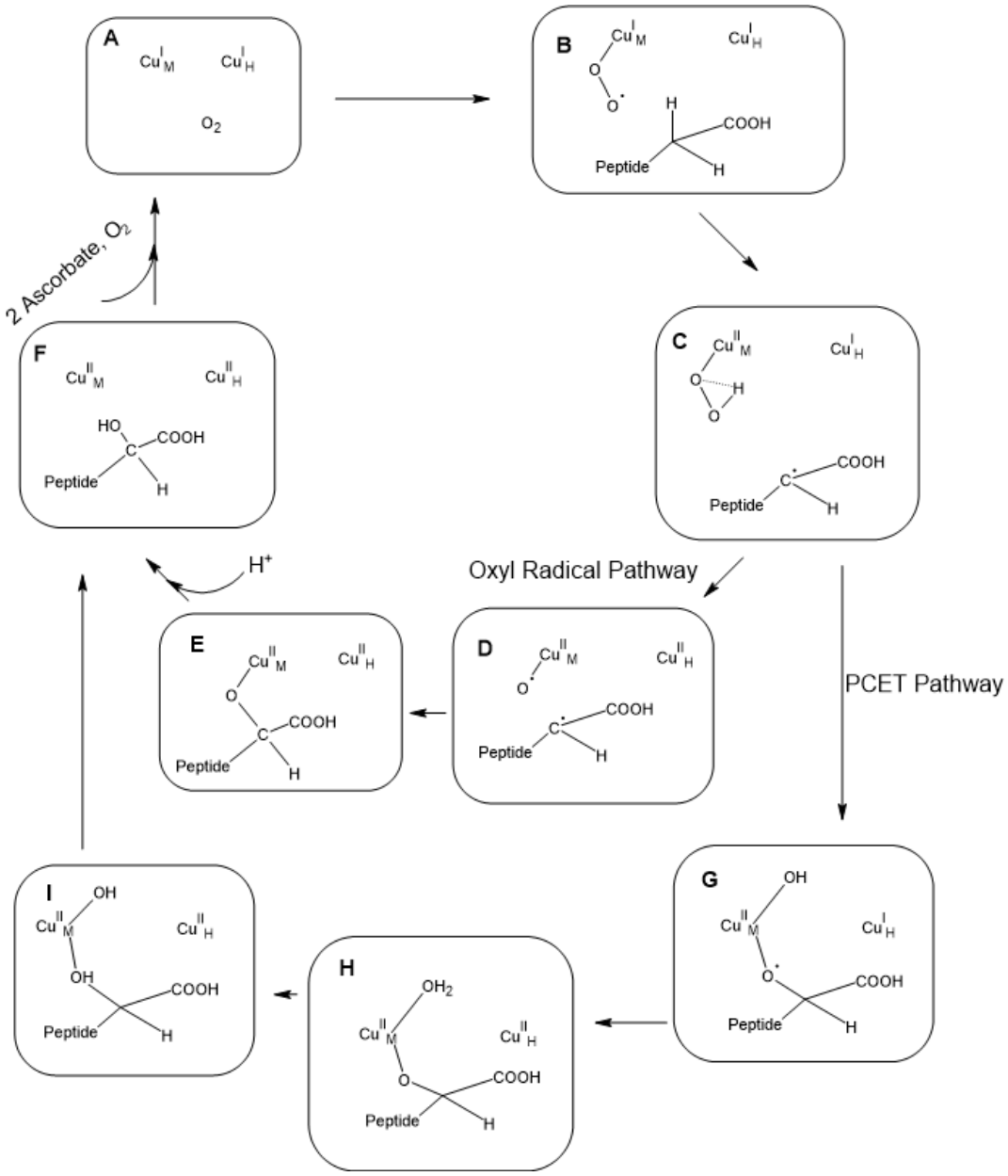

Figure 1-9 Canonical reaction mechanism. *Step **A** the reaction begins with two reduced copper centers. Step **B** oxygen binds to the CuM center, forming a Cu^{II} end on superoxo species. Step **C** the superoxo species abstracts a hydrogen atom from substrate resulting in a substrate radical and a Cu^{II} peroxo. Step **D** an electron is transferred from the CuH site to CuM site through an unknown mechanism, breaking the O-O bond and creating an oxyl radical. Step **E** radical rebound occurs between the substrate and oxyl radical resulting in a Cu^{II} bound substrate. Step **F** a free H$^+$ releases the product as a peptide hydroxyl. Step **A** ascorbate re-reduces the copper centers for another catalytic turnover. In the PCET version, beginning at step **G** radical rebound with distal, nonprotenated oxygen results in a Cu(II)-O-substrate radical. Step **H** PCET from CuH occurs, transferring a H$^+$ and an electron. Step **I** intramolecular rearrangement of the H$^+$ occurs creating a substrate hydroxyl. Step **F** product is released as a peptide hydroxyl.*

1.4 FTIR experiments

The first important experimental observation comes from spectroscopic studies of copper carbonyls. Fourier transform infrared spectroscopy (discussed at length in Chapter 2) is a useful technique for assessing the electronic characteristics of copper dioxygen binding centers. This technique uses carbon monoxide (CO) as an oxygen surrogate, exploiting its strong binding to Cu(I) sites, then detecting the carbon-oxygen stretching frequency. This carbon-oxygen stretching frequency is dependent on π-backbonding, where electron density on the metal ion is partially transferred to the ligand, in this case CO, reducing the C-O bond order slightly. The degree of back-bonding is dependent on the overall electron density on the Cu(I) ion, which in turn is dependent on the overall sigma donation from other ligands in the complex. Or, succinctly, the ligand set of a metal ion affects the stretch frequency of the C-O bond in a predictable way. FTIR of copper-CO complexes in copper monooxygenases is therefore a useful method of determining relative stability and activation of copper-oxygen sites.

CO binding monitored by FTIR was employed on both DBM and PHM. First, it was essential to determine if CO was bound at one or both copper centers and if the bound copper's ligand set was conserved between DBM and PHM. Half-apo variants (lacking copper at one site) of DBM[49] and PHM[28] were prepared by removing copper preferentially from the CuH site via potassium cyanide. These half-apo, CO derivatives of PHM and DBM showed a single FTIR band at 2093 cm^{-1} and 2089 cm^{-1} respectively, which was consistent with experiments in regular di-copper variants, showing unambiguously that these enzymes bind CO (and therefore oxygen) exclusively at the CuM site in each enzyme. Next the effect of substrate binding on FTIR stretching frequencies was assessed[50]. In the presence of substrate, CO-bound PHM continued to generate the characteristic 2093 cm^{-1} band, but also gave rise to a 2063 cm^{-1} band[42]. This 2063 cm^{-1} band was found to be substrate concentration dependent, reaching a maximum at approximately 2 molar equivalents of substrate (1 mM) (Figure 1-10). Additionally, these two bands were found to be somewhat interconvertible, although not precisely at a 1:1 ratio. Finally, the same study demonstrated that this 2063 cm^{-1} band actually *was* present in substrate free samples,

albeit at a low level (~10% of total signal). These results in tandem provide evidence that PHM has access to multiple conformational states, and that those conformational states are in some way substrate dependent.

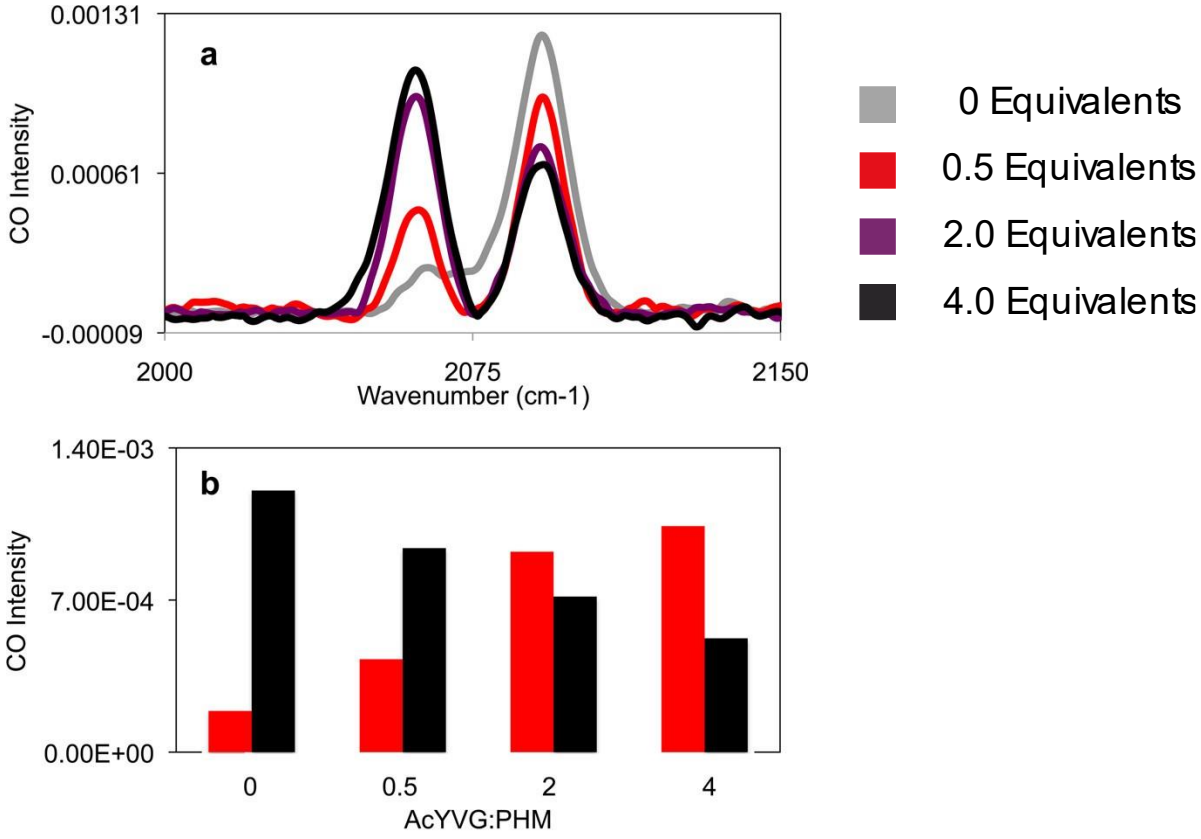

Figure 1-10 Substrate Dependance of PHM Carbonyl *(**a**) Comparison of WT PHM CO band intensity for different concentrations of substrate. 0 equivalents of substrate are shown in grey, .5 equivalents in red, 2 equivalents in purple, and 4 equivalents in black. (**b**) A graphical representation of the same comparison. Relative equivalents of substrate are compared with the intensities of the 2063 cm^{-1} band (red) and the 2093 cm^{-1} band (black). Adapted from Kline and Blackburn (2016)[50].*

It is also useful to examine the particular stretching frequencies and what they suggest about the electronic configuration of the active site. The predominant substrate-free band of 2093 cm^{-1} occurs at a similar frequency to other His_2Met and His_3 ligand sets, which generally fall in the range of 2075 to 2100 (see Table 1-1), whereas the 2063 cm^{-1} band is significantly lower, indeed one of the lowest reported frequencies for a ligand set of this type. Rather, it falls much closer to proteins like hemocyanin and cytochrome

oxidase[51]. In these proteins, the CO is ligated to two positively charged metal sites in a bridging or semi-bridging modality such that its stretching frequency is influenced by the positive charge on two metal ions. These results together suggest that a substrate inducible form of the enzyme includes a highly π-backbonded binuclear species, which the canonical reaction mechanism does not include.

Table 1-1 Carbon monoxide stretching frequencies from copper proteins and model complexes. *Table adapted from Welch 2022*[52].

Sample	Ligand Set (excluding CO)	Coord. No (including CO)	Frequency (cm^{-1})	Reference
PHM	$2N_{(His)}$ $1S_{(Met)}$	4	2093	[42]
DBM	$2N_{(His)}$ $1S_{(Met)}$	4	2089	[53]
PHM + AcYVG	$2N_{(His)}$ $1S_{(Met)}$	4	2093, 2063	[42]
PHM + Benzoylglycine	$2N_{(His)}$ $1S_{(Met)}$	4	2093, 2075	[42]
PHM M314H	$3N_{(His)}$	4	2075	[50]
PHM M314H + AcYVG	$3N_{(His)}$	4	2051	[50]
CusF W44AM49H (M-site model)	$2N_{(His)}S_{(Met)}$	4	2089	[54]
SeM CusF W44AM49H (M-site model)	$2N_{(His)}Se_{(Met)}$	4	2087	[54]
Hc (mollusk)	$3N_{(His)}$ + Cu-Cu	4	2062	[51]
Hc (limulus)	$3N_{(His)}$ + Cu-Cu	4	2053	[51]
Hc (arthropod)	$3N_{(His)}$ + Cu-Cu	4	2043	[51]
aa_3-cytochrome oxidase	$3N_{(His)}$ + Cu-Fe	4	2066, 2054, 2039	[55]
ba_3-cytochrome oxidase	$3N_{(His)}$ + Cu-Fe	4	2054	[55]
Aβ(10-14) YEVHH	$2N_{(His)}$	3	2110	[56]
Histidylhistidine (Nδ coordinated)	$2N_{(His)}$	3	2110-2105 weak	[57]
Histidylhistidine + N-methylimidazole	$2N_{(His)}N_{(imid)}$	4	2075 strong	[57]
HisXHis (X=Gly) (Nε coordinated)	$2N_{(His)}$	3	2092 strong	[58]
bis-dimethylimidazole ($[Cu\text{-}(Me_2imid)_2]^+$)	$2N_{(imid)}$		No reaction	[59]
tris-dimethylimidazole ($[Cu\text{-}(Me_2imid)_3]^+$)	$3N_{(imid)}$	4	2069	[59]
tris-(3,5-pyrazolyl)borate	$3N_{(pyrazole)}$	4	2083	[60]
tris-(3,5-dimethylpyrazolyl)borate	$3N_{(pyrazole)}$	4	2066	[60]
tris-(3,5-diisopropylpyrazolyl)borate	$3N_{(pyrazole)}$	4	2056	[60]
tris-(3-trifluoromethyl,5-H-pyrazolyl)borate	$3N_{(pyrazole)}$	4	2100	[60]
tris-(2-methylpyridyl)amine (TMPA)	$3N_{(py)}$ and $4N_{(py)}$	4 and 5	2094, 2075	[61]
1*H*-imidazol-4-yl)-*N,N*-bis((pyridin-2-yl)methyl)ethanamine	$2N_{(py)}N_{(imid)}$	Probably 4	2082	[61]
2-Ethylthio-N,N-bis(pyridin-2-yl)methylethanamine	$2N_{(py)}S_{thioether}$ or $3N_{(py)}$	4	2094	[62]

1.5 The Peroxide Shunt

One elegant and oft-ignored experiment in the field is the so-called peroxide shunt. Peroxide shunt chemistry is a class of reactions where normal biological processes are bypassed by presenting the oxidized form of a metalloenzyme with hydrogen peroxide and substrate. In the case of PHM, the Cu(II) enzyme is given peroxide, peptide substrate, and no exogenous ascorbate. In these experiments neither ascorbate nor oxygen are required for catalysis, as the reduction and oxygen binding steps have been short circuited, allowing turnover in their absence. Examples of peroxide shunt chemistry have been performed in other coupled monooxygenases[63-65] where they are used to demonstrate the existence of a peroxo intermediate that can be reached by the peroxide shunt "shortcut", as well as provide useful spectroscopic or structural information about that peroxide intermediate. Particularly useful are isotopically labeled peroxide experiments, where ^{18}O peroxide is employed. In the prototypical peroxide shunt experiment, the isotope labeled oxygen is quantitatively transferred to the products, which can be detected by high performance liquid chromatography (HPLC). These peroxide shunt mechanisms often have wildly different turnover rates compared to their biological mechanism, which elucidates features of the electron transfer and oxygen binding that have been circumnavigated.

The PHM peroxide shunt experiment was performed to determine if a Cu(II)-peroxo intermediate was present[66]. PHM was reacted with ^{18}O labeled peroxide under otherwise strictly anaerobic conditions, leading to the stoichiometric formation of ^{18}O labeled product. However, the reaction kinetics and binding constants were greatly different. The affinity for substrate in the peroxide shunt reaction was greatly reduced (K_M of substrate binding in the peroxide reaction was 800 μM versus 5.1 μM in the ascorbate/O_2 reaction) indicating that some key factors of ascorbate reduction or oxygen binding greatly increase the enzyme's affinity for substrate. The rate of the reaction was also moderately reduced (WT k_{cat} in this experiment was 9.2 s^{-1} versus 5 ± 3 s^{-1} in the peroxide shunt reaction). Despite the slower turnover and disrupted substrate binding, the reaction remained entirely coupled with no consumption of peroxide that did not ultimately get incorporated into product. The precise mechanism of the peroxide shunt is still unknown. One final

observation of the peroxide shunt mechanism is particularly difficult to reconcile with the canonical reaction mechanism. The peroxide shunt reaction using ^{18}O labeled peroxide was performed in the presence of ambient $^{16}O_2$. The hypothesis under the canonical mechanism was that the product should be 100% ^{18}O labeled, because there is no step where dioxygen and Cu(II)-peroxo are in equilibrium, therefore no exchange would be possible with ambient O_2. However, contrary to this hypothesis, the labeling of the product was scrambled, 35% of the formed product contained the ^{18}O label, but 65% had exchanged their label with the ambient $^{16}O_2$. This places a key constraint on the possible reaction mechanisms; they must include an intermediate where a Cu(II)-peroxo species is in equilibrium with a Cu(I)-dioxygen species. These are the only conditions where the labeled peroxide could exchange with the unlabeled diatomic oxygen while maintaining stoichiometry without uncoupling. This observation directly challenges the canonical reaction mechanism, which is dependent on long ranged electron transfer through substrate or solvent. These reaction mechanisms explicitly cite a strong driving force, e.g. an irreversible transformation, which cannot be reconciled with this observation[46]. At the time of these experiments, the scrambling was justified with the suggestion that perhaps peroxide reacts at the CuH site to form a Cu-superoxo species that somehow transfers over to the CuM site, but this fails to explain how the reaction remains tightly coupled, especially in the light of later slow mutant studies where uncoupling was predicted under this mechanism[50], and this explanation has been discounted.

1.6 PHM mutagenesis and implications on reactivity

Extensive mutagenesis on PHM has been performed, both at the active site and at other residues of structural importance. Some of the most interesting mutants and their effects are presented here.

H172A[41]: This CuH site mutant retains full copper binding and still catalyzes hydroxylation with full coupling of O_2 consumption and product formation, albeit at an extremely reduced rate (WT V_{max} = 55 s^{-1}, H172A V_{max} = .029 s^{-1}, or a ~2000 fold reduction). This reduction was initially hypothesized to be due to the decreased rate of electron

transfer. This is a cogent hypothesis in the context of CuH site's role as an electron storage site -- changes to its geometry and electronics could affect how efficiently it can transfer an electron, but once the electron is transferred, catalysis should proceed as normal. Experiments determined this was not the case, the affected step was determined, rather, to be hydrogen atom abstraction. Under the canonical mechanism, hydrogen atom abstraction occurs solely at the CuM site, before any long-range electron transfer. This study had no clear explanation for this unexpected result and speculated that mutations at the CuH site resulted in subtle changes to the protein backbone and hydrogen-bonding network that had somehow changed hydrogen atom abstraction, but they did not present specific evidence of that hypothesis. H172A has relatively similar CO chemistry to WT PHM, with a 2092 cm^{-1} IR band and a substrate inducible 2065 cm^{-1} IR band. The small blue shift in the substrate induced form is not understood.

M314H[67]: This CuM site mutant changes the ligand set of the CuM site from His_2Met to His_3, identical to the CuH site. This mutant also retains full copper binding and still catalyzes hydroxylation, also at a greatly reduced rate. This reduction is due to a decrease in turnover (WT K_{cat}13.8 s^{-1}, reduced in M314H to K_{cat} 2.5 s^{-1}), as well as a decrease in substrate affinity (WT K_m 8.2 uM increased to M314H K_M 37 uM). Despite this decrease in overall reaction rate, M314H maintains full coupling between O_2 consumption and product formation. The most important feature of the M314H mutant is its carbonyl chemistry. This mutant tests if the fluxional methionine is responsible for the 30 cm^{-1} change observed on substrate binding. Under that hypothesis, substrate presence or absence should have no effect on CO stretching frequency given that the M314H ligand does not have this fluxional character. This is not what is observed, instead the M314H carbonyl produces a red-shifted 2075 cm^{-1} band and a substrate inducible 2052 cm^{-1} band. This has several implications, first it demonstrates that the fluxional character of the M314 residue is not sufficient to explain the substrate inducible 2063 cm^{-1} band. Secondly, since both bands are red-shifted it definitively assigns both to the CuM center. Finally, the 2052 cm^{-1} substrate induced band is comparable to binuclear proteins such as hemocyanin, and much lower than mononuclear His_3 sites, providing further evidence of a binuclear state.

H108A[26]: This CuH site mutant has been crystalized under several conditions. When crystalized in a buffer without citrate it produces a crystal structure with no major conformational changes, save for a loss of copper at the CuH site. When crystalized in the presence of citrate, however, a largescale conformational change is revealed, as discussed earlier. The CuH site is found to be coordinated to the carboxylate of the citrate, while the CuM site is now coordinated by a previous ligand of the CuH site, H107. This large conformational change is the sole example for the closed conformer in PHM, where the site-site distance is reduced to ~4 Å. The carbonyl chemistry of the H108A mutant was performed without the addition of citrate. Without substrate or citrate it produces a single band at 2093 cm^{-1}. The addition of substrate slightly blue shifts this band to 2087 cm^{-1}, the importance of which is unclear.

1.7 Competing Computational Models

PHM chemistry has also been studied at length computationally, particularly using density functional theory (DFT), discussed at greater length Chapter 2. DFT is a quantum mechanical approach that uses complex and relatively difficult to compute theory to produce accurate simulations. These simulations are useful for predicting intermediates, transition states, and even expected spectroscopic signals. However, these computational approaches also have pitfalls and caveats[68]. Even when confined to a relatively robust approach such as DFT, there are many different combinations of parameters (basis set, functional, computer program, etc). Further, some systems are especially difficult to analyze with DFT, including metals with a partially filled d orbitals, such as copper. Notwithstanding, computational models are useful as a starting point. They create testable targets such as intermediates, spectroscopic signals, and transition states, which can then be verified by experiments. Exact agreement between computational models and experiments about energy barriers is not generally possible or even required. Rather, computational models are useful for predicting trends of reactivity, such as evaluating two possibilities for a transition state and determining which is more energetically favorable.

The canonical reaction mechanism is supported, and is in many ways defined, by a series of computational studies[45,46,69]. Shown in Figure 1-11 is a reaction coordinate diagram of one computationally determined reaction mechanism. Of key importance in this reaction mechanism is its prediction of long-range electron transfer between the CuH and CuM sites. This long-range proton coupled electron transfer (PCET) is calculated to be highly energetically favorable with a strong driving force. This mechanism, which separates the two electron transfers from copper sites to substrate is also deemed favorable on the grounds that a coupled reaction would result in a peroxide, calculated to have relatively poor H-atom abstraction compared to a superoxo species. In addition to the previously enumerated contradictions with experiments, there are several other concerns. The first is the calculated energy for hydrogen atom abstraction. Their diagram shows an energy barrier of 14.4 kcal/mol, which is extraordinarily close to the experimental value of 14 kcal/mol. However, the energy barrier produced by their model was actually 22.2 kcal/mol. They adjust this value by subtracting 7.8 kcal/mol on the basis that the same DFT approach overestimated the energy barrier of superoxo hydrogen atom abstraction in a model complex by 7.8 kcal/mol compared to experiments[70], therefore this error could be subtracted as it represented a systematic overestimation of this energy barrier by their chosen functional. While exact numeric agreement with experimentation is not required or possible, a miss of approximately 8 kcal/mol is worth noting. Secondly, the k_{ET} is stated to be on the order of 10 s^{-1}, while the k_{cat} of the PHM is 39 s^{-1}, and the rate limiting step is believed to be product release, not electron transfer. Further, the PCET mechanism was found to be unfavorable in competing studies of a similar copper site[71].

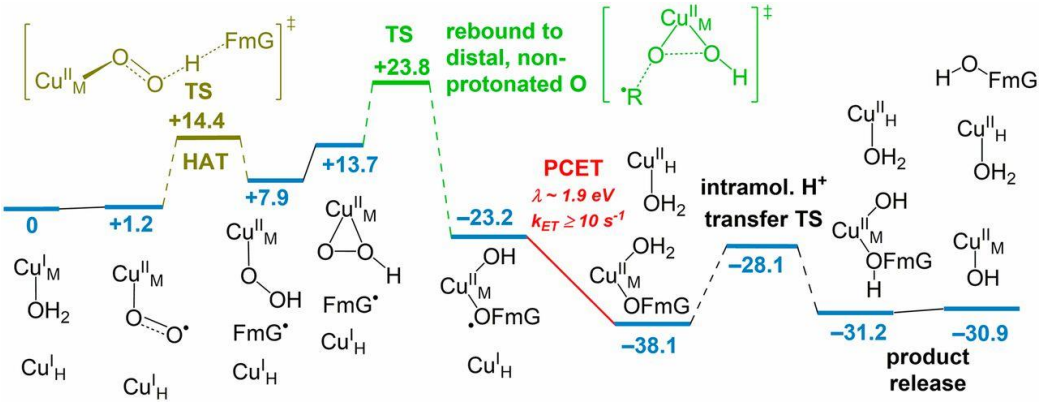

Figure 1-11 Reaction coordinate diagram for the PCET reaction. *Energies of each species are shown in kcal/mol. Hydrogen atom abstraction transition state (HAT) shown in tan, radical rebound transition state shown in green, PCET step shown in red. Adapted from Cowley et al 2016.*

An alternate computational model was published in 2019[72], which is reproduced in Figure 1-12. Based on the closed crystal structure of DBM the Wang lab explored the possibility that a closed conformer could provide a more favorable pathway for oxygen reactivity. The reaction mechanism is at first similar to the canonical mechanism, beginning with reduction and oxygen binding to form a superoxo. At this point they examined the hydrogen atom abstraction of substrate by Cu(II)-superoxo and found quite a different energy barrier, falling between 26.1 – 37.5 kcal/mol depending on the functional employed, deemed energetically unfavorable. Instead, they found a much more energetically favorable hydrogen atom abstraction target: ascorbate. The energy barrier for this reaction was determined to be 7.1 – 12.5 kcal/mol, much closer to the experimentally determined value of 14 kcal/mol. This reaction produces a Cu-peroxide which triggers a conformational change from open to closed, resulting in a semi-bridged Cu-peroxo species. This unusual Cu(I)Cu(II)-OOH mixed valence species is found to be surprisingly energetically favorable, and provides an experimental target. Electron transfer from the CuH site results in a bridged radical species that can abstract a hydrogen from substrate, resulting in a substrate radical and two bridged hydroxyls. Radical rebound by the substrate results in a hydroxylated product, accompanied by a conformational change that releases the product and sets the enzyme up for its next catalytic cycle.

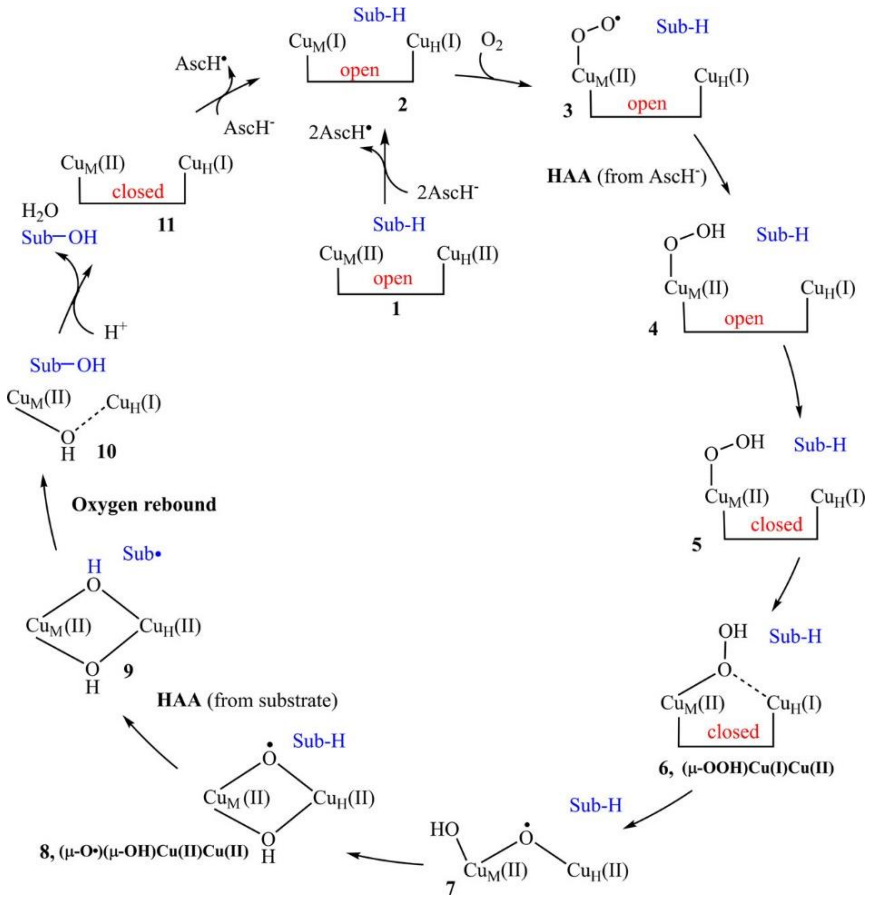

Figure 1-12 Calculated reaction mechanism with an open to closed conformational change. *Step **1** reduces both copper centers. Step **2** substrate enters the binding pocket. Step **3** oxygen binds and forms a Cu(II) superoxo. Step 4 the superoxo abstracts hydrogen from ascorbate, forming a Cu(II) peroxide. Step **5** hydrogen atom abstraction triggers an open to closed conformational change. Step **6** copper centers are in proximity and may couple electronically, forming an unusual mixed valence Cu(I)Cu(II)-OOH species. Step **7** electron transfer from the CuH site results in the formation of bridged oxygen radical species. Step **8** the OH group migrates to form a di-bridged Cu(II)Cu(II)(O•)(OH), which is found to be a relatively stable intermediate. Step **9** hydrogen atom abstraction from substrate results in a substrate radical. Step **10** radical rebound occurs, resulting in a substrate hydroxyl product. Step **11** acid cleavage of remaining OH group prepares for next catalytic cycle. Step **2** reduction by ascorbate opens enzyme, cycle repeats. Figure adapted from Wu et al 2019[72].*

This alternate computational model does offer several advantages and consistencies with previous experiments, which are laid out in Table 1-2. The most important observations are also rehashed here. The presence of a semi-bridged peroxo

species (diCu(II)-peroxo) entirely explains the 2063 cm^{-1} CuM carbonyl band. This same species also explains the peroxide shunt chemistry, as diCu(II)-peroxo is in equilibrium with a diCu(I)O_2 species. This model also explains why there is no decoupling even with a slow substrate, as product formation is gated by conformational changes that prevent "leakage" of radical intermediates. At the same time, this model also has several features that are apparently incongruous with experimentation. First, it indicates a catalytic cycle should require just one molecule of ascorbate once the copper centers are initially reduced, which is not supported experimentally. Second, product is shown leaving before active site opening, which is not supported structurally.

Table 1-2 Summary of numerous observations and their explanations under coupled and non-coupled hypotheses.

Observation	Coupled Hypothesis	Non-coupled Hypothesis
Closed Conformer	Closed conformer is essential to reactivity and is energetically accessible	Closed conformer is an artifact of mutation and crystallization
2063 cm^{-1} and 2093 cm^{-1} FTIR Bands	Closed conformer with a semi-bridged species provides explanation for 2063 cm^{-1} FTIR band. It is substrate inducible.	No explanation
Peroxide Shunt	diCu(II)-peroxo is in equilibrium with diCu(I)-O_2, permitting O_2 label exchange	Migration of superoxo from the H-site
Hydrogen Atom Abstraction	Hydrogen atom abstraction from ascorbate	Hydrogen atom abstraction from substrate
Electron Transfer	Electron transfer occurs across 4Å, common for coupled mechanisms	Electron transfer across 11Å solvent filled gap through a mixture of solvent and substrate

Despite its advantages, this model remains just that – a model. Without experimental underpinning this model is only hypothetical. We now ask ourselves what experiments and observations would lend credence and verify the presumed reaction mechanism? One key characteristic of this model is the importance of ascorbate, not only as a reductant but perhaps as a source of hydrogen atoms or driver of conformational change. This characteristic is investigated in chapter three. Another prerequisite is the feasibility of conformational change. The only structure of a closed PHM conformer is in a half-apo mutant, so can we find conformational changes in WT PHM enzyme? This question is investigated in chapter four. Finally, the presence of a mixed valence species (the Cu(I)Cu(II)-OOH) suggests a powerful spectroscopic target. Can the enzyme be trapped in a conformer where this species can be detected? This question is explored in chapter five.

Chapter Two: Instrumentation and Techniques

Scientific questions are defined by the tools that can be used to answer them. This chapter delves into several specific techniques that are used in the following chapters and goes over their theory and application. Each section begins with a short overview which lays out, in broad strokes, the function and purpose of each technique.

2.1 Ultra-violet Visible Spectroscopy (UV-Vis)

> ***Function:*** *Detects wavelengths of light absorbed by a sample that indicates the presence of excitable electrons. Wavelength and absorption give indicators of species present and their concentrations.*
>
> ***Purpose:*** *Used for diagnostic purposes to ensure purity of enzyme employed. Used with a reporter compound to detect oxidation state of enzyme indirectly. Used to survey for an intervalence charge transfer band that would be indicative of copper site coupling.*

UV-Vis spectroscopy is the most characteristic and simple spectroscopic technique. It is useful in both quantitative and qualitative assays where it can detect small changes in chemistry. It functions via a monochromator, which sends a single wavelength of light through a sample, if that wavelength of light excites an electron in the sample, that light is absorbed. The wavelength of absorbed light is characteristic of the electron transitions induced. These transitions fall into one of several categories:

1. Electrons in the highest-occupied molecular orbital (HOMO) of a σ bond and electrons in a π bonding orbital can be transitioned to an excited state, denoted σ* and π* respectively, or a free electron pair (denoted n) can be excited to either a σ* or π* orbital. These are collectively “inner sphere transitions”.
2. “d-d” orbital transitions are transitions from an occupied to an unoccupied d orbital. They tend to have relatively weak absorption.

3. Transitions between a molecular orbital with metal character and a molecular orbital with ligand character. These are called charge transfer bands and can be extremely intense. A particular version of this charge transfer band is the intervalence charge transfer band (IVCT), which is instead between two metal centers in different oxidation states (e.g. an electron transferring between Cu(I) and Cu(II)).

A further application of UV-Vis spectroscopy is stopped-flow. Stopped flow is a methodology where precise volumes of reactants are mixed and reacted on a known, variable, timescale. The progress of the reaction is monitored by the change of a UV-Vis detectable signal at a single wavelength or across a rapidly scanned range of wavelengths. This strategy can provide useful information about the kinetics and intermediates of a reaction, with several caveats. Some component of the reaction must be spectroscopically detectable and second the reaction must proceed more slowly than the time of mixing and line filling (the so called “dead time”).

All three transitions are detected in the studies featured in chapters three and five. In chapter three, PHM reduction and oxidation kinetics are monitored using sodium azide. Cu(II)-azido complexes have an extremely intense 390 nm charge transfer band, but Cu(I) does not complex with azide, giving a simple and eminently detectable marker of reduction. In chapter five a synthetic peptide inhibitor is used to trap the enzyme in a state which produces a 925 nm band, determined to be an intervalence charge transfer band. Stopped-flow was used to study the reaction kinetics of both the reduction by ascorbate and the single-turnover reactions in chapter three. Finally, UV-Vis was also used in diagnostic steps of all procedures to determine protein concentration and purity.

2.2 Electronic Paramagnetic Resonance (EPR)

Function: *Detects the presence and relative concentrations of paramagnetic species, e.g. species with an unpaired electron.*

Purpose: *Used to directly assess the redox of the enzyme without the need of a reporter in a quantitative manner. Samples are assessed at low temperature providing "snapshots" of reactivity. Used to search for spin-coupled systems where a previously EPR-detectable species is now absent, indicative of coupling between copper centers, as well as searching for paramagnetic radicals.*

Electronic paramagnetic resonance (EPR) is a technique which allows the detection and characterization of unpaired electrons. This is useful in the study of metalloenzymes where it can be used to directly assess the redox state of a metal center. For instance in the context of copper, Cu(II) is paramagnetic and EPR detectable while Cu(I) is not. It has further usefulness in the context of PHM monooxygenase chemistry because of its ability to detect radicals.

EPR exploits the magnetic moment of an electron to produce a signal. Consider a single, free, unpaired electron. Every electron has a magnetic quantum number, m_s, of either + ½ or -½, often called spin up or spin down respectively. In the presence of an external magnetic field an electron will align itself either parallel (m_s = ½) or antiparallel (m_s = - ½). The energy of these two different states is given by the equation:

$$E = m_s g_e \mu_B B_0$$

where E is the energy of the state, m_s is the magnetic quantum number, g_e is the g-factor, a dimensionless factor which characterizes a particle's magnetic moment and for a free electron is 2.002319, μ_B is Bohr's magneton, a physical constant, and B_0 is the strength of the magnetic field. That means that the difference of energy (ΔE) between the higher energy m_s = ½ and lower energy m_s - ½ can be given by:

$$\Delta E = g_e \mu_B B_0$$

Since $\mu_{B,}$ and g_e are constants, the difference of the two energy states is directly proportional to the applied magnetic field, B_0. Therefore, ΔE increases as the relative magnetic field increases as shown in Figure 2-1.

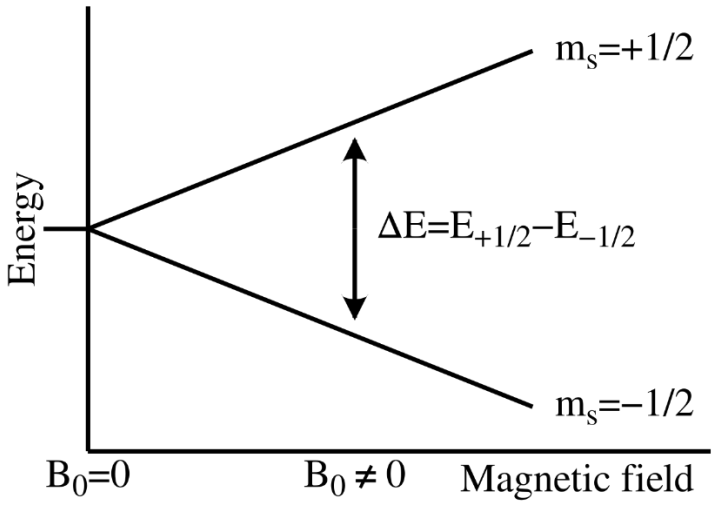

Figure 2-1 Energy separation between spin up and spin down states. *Graph showing the relative difference in energy between the two magnetic spin numbers as the outside magnetic field increases.*

From here EPR functions in many ways like other forms of absorbance spectroscopy. The paramagnetic sample is held in a magnetic field, the intensity of which varies over the experiment. The sample is simultaneously exposed to microwaves of known energy. Absorption occurs when the energy of the microwave radiation is equal to the separation between the two energy states, causing excitation from the lower to the higher state. Theoretically either the magnetic field or microwave energy could be varied, but practically the microwave is held constant and the magnetic field varied.

In practice EPR is not performed on single free electrons. Instead, it is influenced by the atomic nucleus, as well as surrounding ligands. All these factors become part of the previously mentioned g_e, the g-factor. This g-factor characterizes the response of the paramagnetic species as influenced by local atomic nuclei, ligands, etc, and therefore creates a unique chemical “fingerprint”, which is characteristic of a particular paramagnetic species. These signals are also quantitative, which means that the concentration of a species can be determined when compared to a standard.

One important part of that chemical "fingerprint" arises from a principle called hyperfine splitting. Hyperfine splitting is caused by the interaction of the unpaired electrons with their local atomic nuclei, which have their own magnetic moments sufficiently intense to affect unpaired electrons. Because this splitting arises from the atomic nuclei, it is influenced by the nuclear spin, which in the context of copper is $I = 3/2$. This nuclear spin coupled with the magnetic spin of the electron gives rise to eight different slightly different energy levels, shown in Figure 2-2. These separate energy levels give rise to four slightly different transitions, which contribute to the unique EPR signal of a given sample.

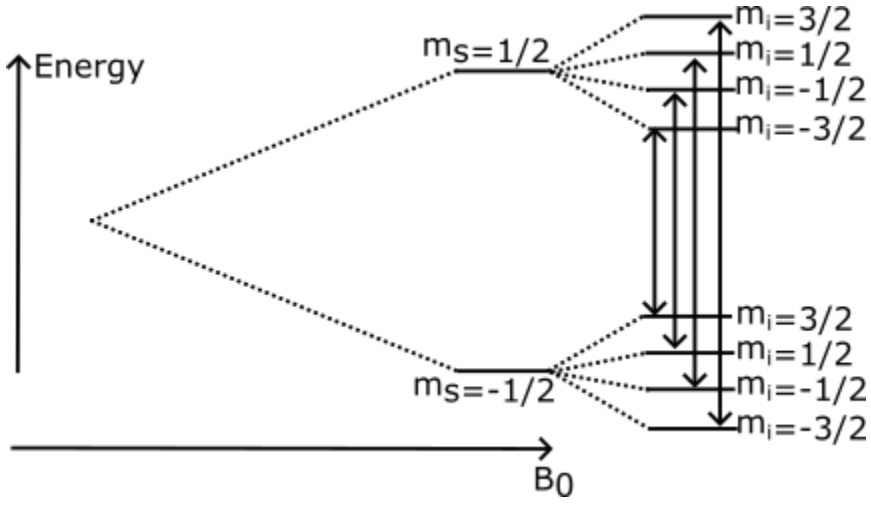

Figure 2-2 Hyperfine Splitting due to nuclear coupling. *Graph showing the relative difference between two energy states as the magnetic field increases. Additionally, the two magnetic spins are further subdivided into four smaller energy levels due to coupling with the nuclear spin, in this case I = 3/2 such as in copper. The four allowable transitions are shown, all slightly different energy.*

EPR is used in the following studies to directly assess the concentration of EPR detectable, oxidized Cu(II) versus EPR indetectable Cu(I) or spin coupled species. Specifically, EPR is employed in chapter three to assess the oxygen sensitivity of WT PHM, where oxidation can be directly measured at several time points, and to determine the redox state of WT PHM in a pre-steady state condition. EPR is employed in chapter five to characterize a mixed-valance species in the presence of peptidyl substrates.

2.3 X-ray absorption spectroscopy

> ***Function:*** *Detects the presence and relative concentration of an absorbing atom determined by the energy of x-rays chosen. Also detects the distance and occupancy of ligands near an absorbing atom. Does not directly distinguish between absorbing atoms of the same element if present.*
>
> ***Purpose:*** *Used to determine what each copper center "sees", e.g. what atoms are nearby and at what distance, which provides a wealth of structural information. The absorption edge profile directly assesses the redox of copper centers as well. Can measure samples in relatively native conditions at very low temperature.*

X-ray absorption spectroscopy (XAS) is a useful tool in studying metalloenzymes such as PHM. The basis of XAS is the excitation of a core electron via powerful x-rays. Over the course of an XAS observation the sample is exposed to varied energies of x-rays. As the energy of the x-rays increase, they eventually reach an energy where they can eject a core electron from the 1s orbital of the metal. This causes a massive increase in absorbance (called an absorption "edge") where x-rays carry sufficient energy to fully eject an electron from the metal, into the "continuum", in this state they become photoelectrons where they are scattered by nearby atoms. The characteristic structure of an XAS spectrum is shown below in Figure 2-3.

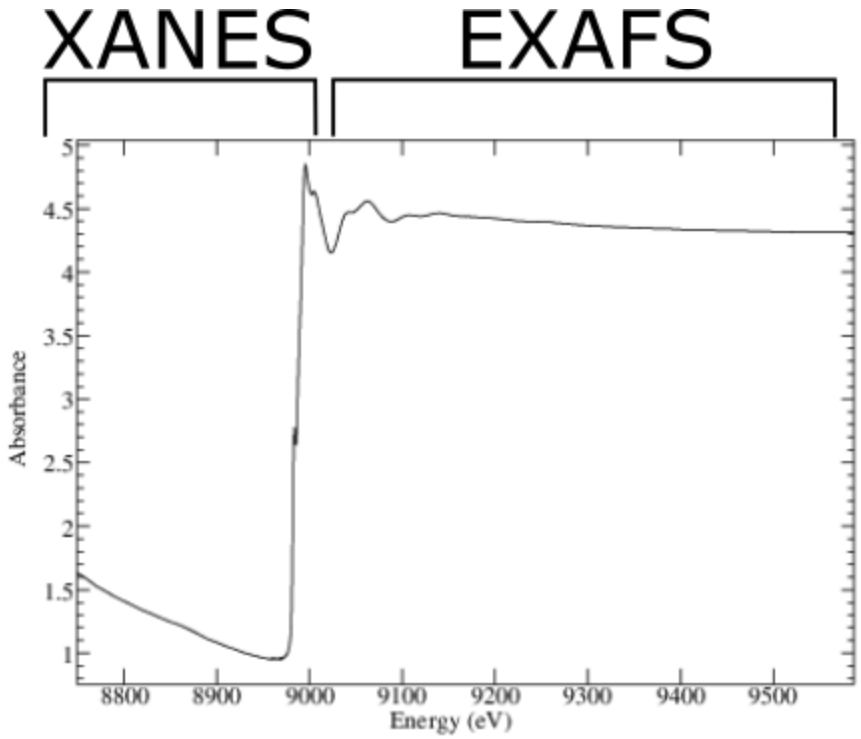

Figure 2-3 Example raw XAS Spectra. *XAS spectra of reduced, WT PHM complexed with CO. X-ray absorption near edge structure (XANES) and extended x-ray absorption fine structure (EXAFS) are labeled.*

XAS spectra can be broken into two regions, each of which provide different information about the sample. These regions are the X-ray absorption near edge structure (XANES), and the extended x-ray absorption fine structure (EXAFS) region.

The XANES region is characterized by absorption of x-rays with insufficient energy to completely eject a core electron, as well as features which appear on the edge, or just slightly beyond it. They are particularly sensitive to changes in redox chemistry, where the edge energy and pre-edge features change significantly depending on the redox state of the metal. This is simply explained; more positive overall charge will increase the energy required to eject a negatively charged electron, thus shifting the edge energy. The XANES region also includes transitions between the core electron and unoccupied valence electron levels which are sensitive to changes in geometry around the absorbing atom. The lowest energy photoelectrons, those just beyond the edge, are prone to multiple scattering events where they interact with several nearby scatterers. These multiple-scattering

events are difficult to model and predict, but provide a unique fingerprint indicative of geometry.

The EXAFS region is characterized by complete ejection of a core electron. These ejected core electrons become photoelectrons, and the ejected photoelectron's energy is based on the energy of the exciting x-ray. This photoelectron can then be thought of as a wave, where it expands out from the absorbing atom and interacts with nearby atoms which essentially function as point scatterers. The backscattered electron waves then interact with the forward propagating waves, resulting in a modulation of the absorbance spectra. This modulation causes sinusoidal oscillations in the EXAFS spectra, where each of these sinusoidal oscillations represent an atomic point scatterer at a certain distance. The EXAFS equation, which gives the modulations in the EXAFS region is:

$$\chi(k) = \sum_j \frac{N_j e^{-2k^2\sigma_j^2} e^{-2R_j/\lambda_k} f_j(k)}{kR_j^2} \sin[2kR_j + \delta_j(k)]$$

While complicated, each of these terms has a relatively intuitive meaning in the context of EXAFS. $\chi(k)$ is the oscillations as a function of the wave number, k, reflecting its periodicity as you move away from the edge. It is derived from the sum of all neighbors (j), where N_j is the coordination number of the neighboring atom, and σ^2, called the Debeye-Waller factor, is the mean-square disorder of the neighboring atom, and *R* is the distance from the neighbor. The remaining terms, $f(k)$, $\lambda(k)$, and $\delta(k)$ are photoelectron scattering properties of the neighboring atom at a given *k* and are calculable for a particular atom. This means that, while mathematically complex, these oscillations contain the information of coordination number, distance, and relative disorder, and can be simulated.

Converting these sinusoidal oscillations to interpretable data is simple in theory but challenging practice. In essence the goal is to perform a complex Fourier transform that turns each of these sinusoidal oscillations into an amplitude at a frequency. Each of these frequencies will then refer to the distance and identity of the scatterer (See Figure 2-4). To do so, the EXAFS region is extracted and then simulated to reasonable chemical

situations, and the suitability of that simulation is evaluated. Some of the challenges of processing XAS data are; the collected data are over a region of frequencies and are not infinite, which therefore requires truncation of the data, resulting in peak broadening. The data has a significant background component which must be removed by fitting a polynomial spline, but overfitting of the spline removes the oscillations entirely. Oscillations further from the edge have greatly attenuated amplitude and are therefore weighted to salvage their information, referred to as *k* weighting, but overweighting increases noise.

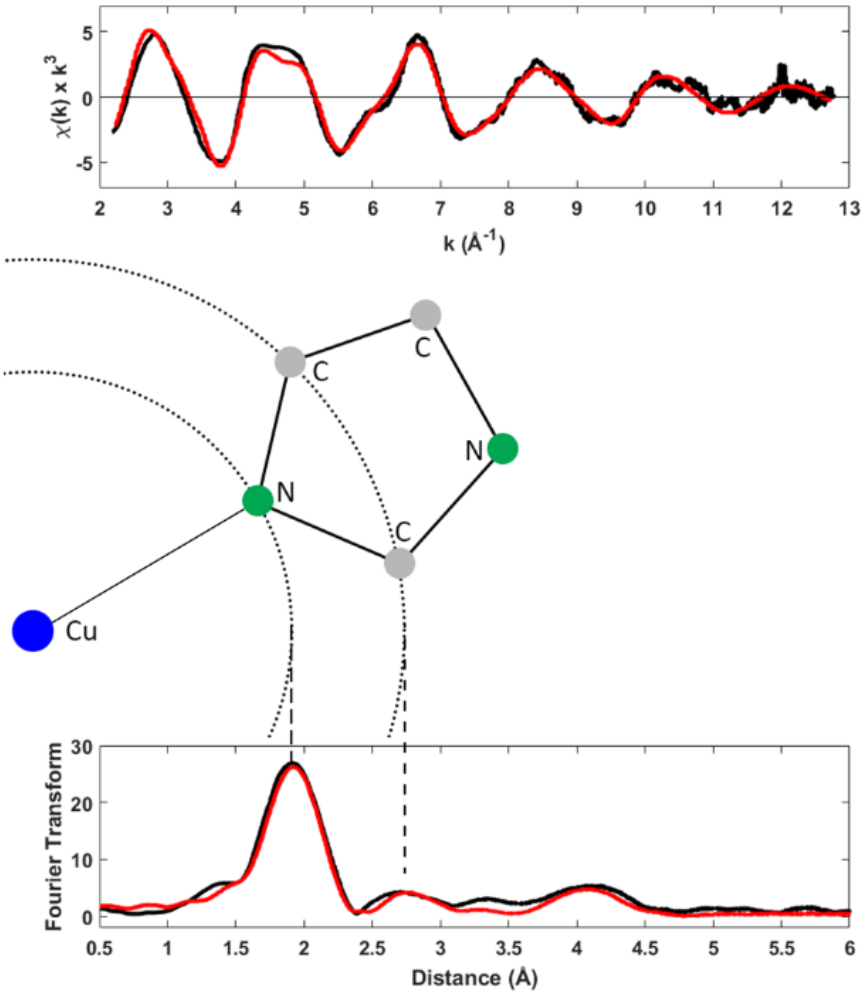

Figure 2-4 EXAFS and Fourier Transform connected to atomic distances. *Top panel: EXAFS oscillation, experimental data in black, simulated in red. Middle panel: Schematized representation of a copper scatterer near a histidine. Bottom panel: Fourier transform converts EXAFS into atoms at certain distances. Figure adapted from Chauhan 2016*[73].

XAS is a powerful tool that provides a wealth of structural information of copper active sites. It is often summarized as allowing the researcher to determine what each metal center “sees”, e.g. the identity and distance of atoms in proximity of the absorber. It is employed in chapter four to assess the copper coordination in two mutants of PHM. In chapter five it is used to detect a binuclear state of PHM, and coordination of the copper site to the peptide lure.

2.4 X-Ray crystallography

Function: *Allows determination of the complete structure of a biological molecule including bound ligands, metals, etc. Crystallization is fundamentally "non-native", so artifacts of crystallization are possible.*

Purpose: *Used to visualize and isolate new conformers of PHM. A myriad of crystallization conditions can be easily tested which may have implications on reactivity.*

X-ray crystallography is one of the most powerful and well-known tools in the molecular biologist's toolbox. Crystallography allows the determination of the structure of a protein at a high resolution (2 Å or lower is common). These crystal structures contain a wealth of structural information and remain one of the best tools for determining and presenting protein structure. Some considerations and limitations are worth noting. The technique is contingent on the crystallization of the protein, and many proteins are simply not amenable to crystallization, with membrane bound proteins being a particularly infamous example. Additionally, since crystals are lattices of identical unit cells, arranged and "frozen" in a crystal, it inherently strips away information about protein dynamics and mobility. The conditions of crystallization are another factor – since crystallization is performed in unusual combinations of buffer, salt, added metal, etc. it may generate crystal structures that are entirely unrelated to protein function. Nonetheless, x-ray crystallography is still a powerful and relatively accessible method of protein structure determination.

The fundamental principle that underpins x-ray crystallography is Bragg's law, which is displayed visually in Figure 2-5. An x-ray hits the crystalline lattice, with layers separated by distance d, with a certain angle, θ. The x-ray is then either diffracted by the electron cloud of the atoms, where it is then reflected away with the same angle θ, or continues unimpeded to deeper layer of the crystal. This process is repeated many times for the layers of the crystal. The resulting diffracted x-ray waves will then interfere

constructively or destructively. They only interfere constructively when a certain condition is filled, which gives Bragg's law of:

$$2d \sin\theta = n\lambda$$

which explains that for a given wavelength of light, only a certain subset of angles will interfere constructively.

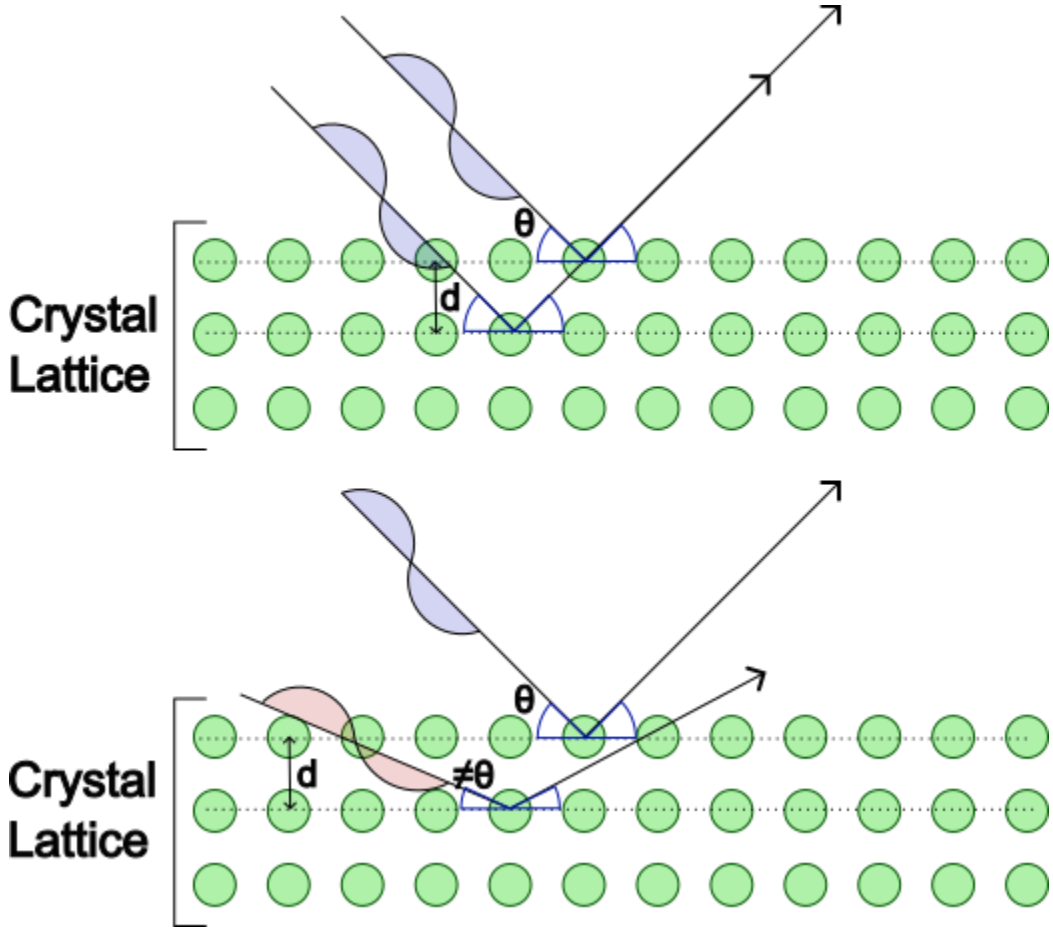

Figure 2-5 Schematic representation of Bragg's law. *Top panel: Constructive interference occurs only at critical angle, θ, as a function of the separation of the crystal lattice, d and wavelength of the light. Bottom Panel: For a given wavelength of light, waves that are not at angle θ do not interfere constructively.*

In practice, a protein crystal is placed in an intense beam of monochromatic x-rays. This creates a diffraction pattern which has regular spots caused by the constructive interference of x-rays. The crystal is then repeatedly rotated and has its diffraction pattern collected, until a large dataset of all orientations is collected. This dataset of diffraction

patterns is then computationally “solved”, to reconstruct the 3d structure of one of the unit cells that yielded it.

X-ray crystallography was used primarily in chapter four where the crystal structures of several mutants and WT PHM are collected, showing new conformations not previously described. Additionally, existing crystal structures were used at all levels of the studies to plan and guide experimentation.

2.5 Fourier-Transform Infrared Spectroscopy

> ***Function:*** *Analogous to UV-Vis, but over the infrared (IR) spectrum. IR light is passed through a sample, and the absorption and wavelengths of absorption are detected.*
>
> ***Purpose:*** *Carbon monoxide was used as an oxygen surrogate, and the resulting copper-carbonyl species have an informative IR absorption band due to the CO stretching frequency. Changes in the electronics of the copper-carbonyl are detectable by shifts of the IR band.*

Fourier-transform infrared spectroscopy (FTIR) is a spectroscopic technique in many ways analogous to UV-Vis. The sample is exposed to infrared (IR) light, which can be absorbed by the sample, and that absorption is recorded. The absorption of IR light is due to the molecular vibration of the sample. Atoms of a molecule are constantly vibrating relative to one another, and the frequency of these vibrations is based on the atoms at play, their distance, type of bonding, and the vibrational mode (stretching, rocking, etc). When the frequency of the IR light is resonant to one of these vibrations, it is absorbed. This absorption raises the ground vibrational state to an excited one, very similar to an excited electronic state in UV-Vis.

These vibrational frequencies are fundamentally based on the bond order and the masses of the concerned atoms, as given by the following equation:

$$\nu = \frac{1}{2\pi c}\sqrt{\frac{K}{\mu}} \qquad \mu = \frac{m_1 \times m_2}{m_1 + m_2}$$

where v is the wavenumber of the vibration frequency, $\frac{1}{2\pi c}$ is a unit conversion, K is the force constant of the bond and reflects the bond order, and μ is the reduced mass, itself a relationship between the masses (m_1 and m_2) of the atoms concerned.

This equation provides an approximate value for the stretching frequency, but the actual stretching frequency of a particular species is further influenced by many other factors such as the hydrogen bonding network, the local electronic microenvironment, and pi backbonding (discussed at length later). Generally FTIR provides a molecular fingerprint that can be compared to known frequencies to determine what functional groups are present. IR spectroscopy is also sensitive to subtle changes in the geometry, distance, and bond order present.

In practice, the IR spectrum is detected through interferometry, shown in Figure 2-6. In UV-Vis a monochromator is used to send through a single wavelength of light at a time, collecting absorbance spectra for each wavelength (termed scanning spectroscopy). In contrast, FTIR employs a Michaelson interferometer. In this system a light source, typically a broadband IR lamp, is shone through a beam splitter which refracts half the light to a stationary mirror, and half the light to a mirror with a variable path length. The light is then recombined and shone on the sample, and the absorbance spectra is collected. This process is repeated numerous times, adjusting the moving mirror slightly each time. Because the beam is recombined, destructive and constructive interference occurs based on the distance of the moving mirror. This gives a series of absorbances at different distances (an interferogram) which can be converted to a spectrum via the Fourier transform, which converts it into a set of absorbances at IR frequencies.

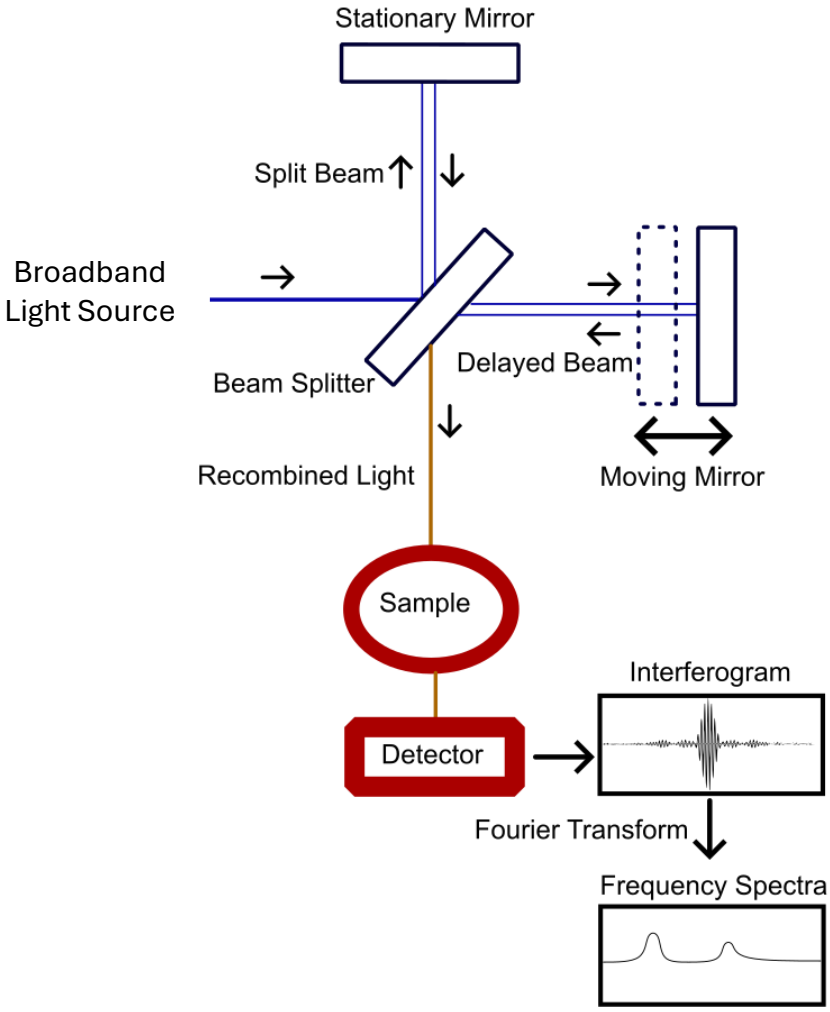

Figure 2-6 Diagram of FTIR. *Light is passed through a beam splitter which splits it 50/50 between a stationary mirror and a moving mirror giving a split beam and a delayed split beam. These beams are reflected back to the beam splitter and recombined, then passed through a sample into a detector resulting an interferogram. The interferogram is converted to a frequency spectra via the Fourier transform.*

In the context of our experiments, PHM is an oxygen dependent enzyme where the binding of oxygen is believed to be a key step in reactivity. In our studies we use carbon monoxide (CO) as a surrogate for O_2, based on their similar electronic configuration. CO is a reactive species that readily reacts with electron rich (reduced) metal centers to form a metal-carbonyl (called carbonylation). The metal-carbonyl then has an IR-absorption band that gives information about the metal binding environment. This absorption band is due to the carbon-oxygen stretching frequency, and the strength of this bond (and therefore its

vibrational frequency) is based on the electronic interaction between the metal site and the CO.

This electronic interaction is based on pi backbonding. When CO bonds to a metal center it forms a strong sigma bond that transfers electron density toward the metal center, but at the same time creates pi "backbonding", schematized in Figure 2-7. This backbonding is a transfer of electron density from the metal center's d orbital to the unoccupied antibonding orbital. This phenomenon transfers some electron density to the CO, reducing the bond order between the carbon and the oxygen. That reduced bond order between the carbon and oxygen manifests as a lower vibrational frequency. The degree of lowering is based on several factors, the identity of the metal, the charge of the metal, but also, critically, other ligands in contact with the metal. These other ligands are also donating or withdrawing electron density to the metal center. Electron donating ligands tend to make the backbond stronger (on the grounds that they make the metal a better electron donor), while withdrawing do the opposite, again reflected in a decrease in frequency for a donating ligand or an increase in a withdrawing ligand. Carbonyls are also capable of binding to multiple metals in a "bridging" mode. The frequency of these carbonyls can be dramatically lower, owing to the significantly larger amount of backbonding from multiple metal centers, all with their own ligand sets.

This allows the use of CO as a sensitive probe of the electronics of a metal center. This property is explored extensively in chapter three where it forms the basis of detecting a conformational change.

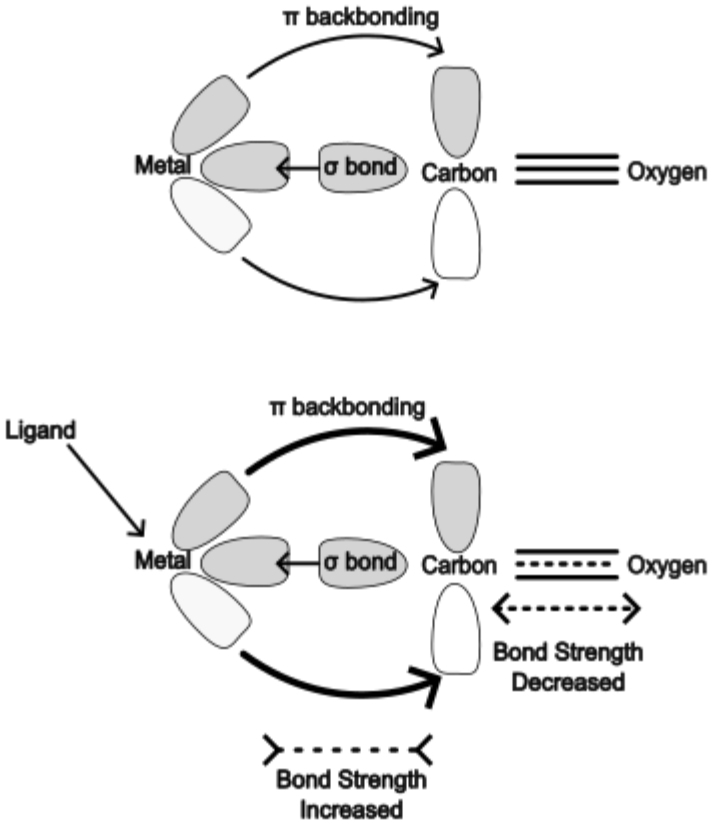

Figure 2-7 Schematized diagram of π-Backbonding. *Top panel depicts carbon monoxide interacting with a metal center. σ bond donation occurs from the carbon to the metal moving electron density to the metal center, while π-backbonding occurs from the d-orbital of the metal center to the empty antibonding orbital of the carbon. Bottom panel depicts a general electron donating ligand, which increases the relative strength of the π-backbonding, which increases the bond between the CO and the metal, while simultaneously decreasing the strength of the C-O bond.*

2.6 Hollow-Fiber Bioreactor

Function: *Mammalian cells are grown and maintained in an automated system. Waste, secreted proteins, and spent media are constantly pumped out, while fresh media and nutrients are pumped in.*

Purpose: *Large scale production of PHM, which is unsuitable for production in prokaryotic systems. Allows production of PHM mutants at a concentration required for protein intensive experiments.*

One of the defining features of our lab, despite being a preparatory step, is the hollow-fiber bioreactor. PHM is not expressed well in bacterial systems. When expressed in *e.coli*, even in specialized strains designed for human protein expression, protein disulfide bonds are scrambled resulting in protein misfolding and loss of activity. Production in mammalian Chinese hamster ovary cells (CHO) produces well-folded, highly active PHM. But typical mammalian tissue culture is extremely time consuming, prone to contamination, and produces relatively small yields compared to other expression systems.

Hollow fiber bioreactors are an extension of typical mammalian cell culture that enable protein production on a scale required for protein-intensive spectroscopy experiments. The system consists of a "cartridge", which is filled with semi-permeable, hollow, capillary membranes tubes, schematized in Figure 2-8. This creates two spaces, the intracapillary space (ICS) which is the space within the fibers, and the extracapillary space (ECS) surrounding them. The semi-permeable material of the capillaries is constructed with a molecular weight cutoff (MWCO) appropriate for the protein of interest. Cells are seeded into the ECS where they adhere to the surface of the fibers and grow and divide. The fibers provide a large amount of surface area (1-2 square meters), allowing the cells to multiply to high density.

Cells are maintained and products removed with a system of pumps. Media is continually pumped through the ICS where it can diffuse across the capillary membrane. This provides a steady stream of nutrients and oxygen, while simultaneously removing

waste products and CO_2 which diffuse into hollow fibers and are carried out. At the same time, a separate set of pumps pushes media through the ECS as well, at a low rate. The media from the ECS is heavily enriched with secreted protein, which is unable to cross through the capillary membrane due to the MWCO. This slowly pumped media is termed the “harvest” which is collected progressively over days.

While initial setup and scaleup can be time consuming, hollow fiber bioreactors have several advantages over traditional mammalian cell culture. First is the sheer amount of protein produced, as much as 10 milligrams per day of harvest collected. Second is the resistance to infection. The maintenance of the system only requires that fresh media be attached and spent media removed, providing very little opportunity for infection. Finally, the system is easily run in parallel. Once set up the bioreactors run with little maintenance, allowing multiple cartridges to be set up for different mutants.

Protein produced from hollow fiber bioreactors underpins all experiments in this work, and in many ways is the prime enabler. Large scale enzyme production of both WT and mutant forms of the enzyme are used at all levels of experimentation and permit extremely material-intensive experiments such as FTIR and chemical quench.

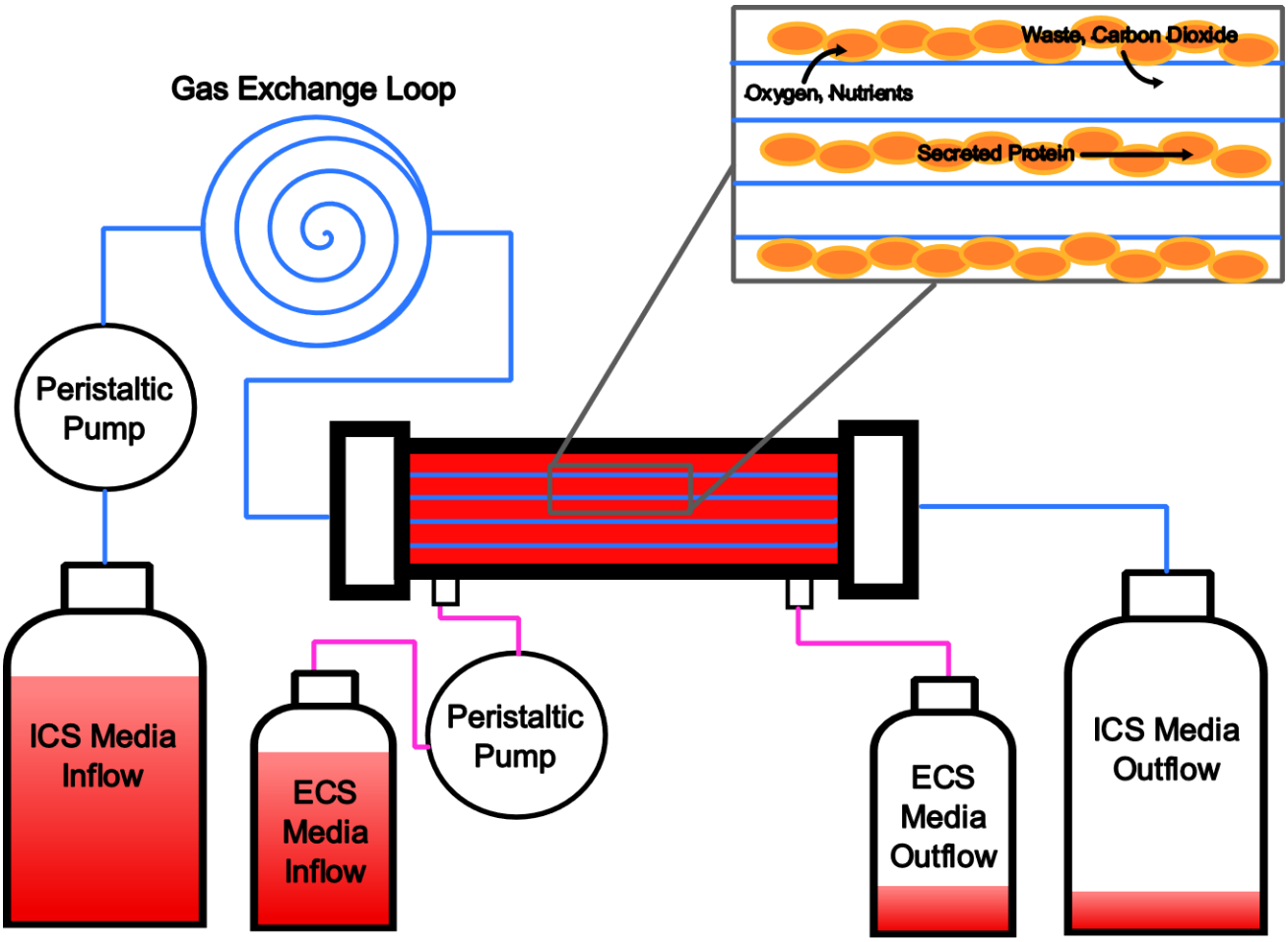

Figure 2-8 *Schematized layout of the hollow fiber bioreactor. Media is continually pushed through the ICS at a relatively high flow rate using a peristaltic pump. Gas exchange loop oxygenates media which then moves through hollow fiber where it exchanges with ECS. Exchange brings fresh nutrients and oxygen, while exporting waste and carbon dioxide to ICS outflow. ECS inflow pump slowly pushes media without dislodging adhered cells but moves secreted protein to ECS outflow. ECS outflow is collected as harvest to be concentrated and purified.*

2.7 Chemical Quench and Rapid Freeze Quench

Function: *Reaction components are mixed rapidly, then "quenched" on a known timescale. Reaction is arrested at known timepoints, then parameters of the reaction are quantified by other techniques.*

Purpose: *Kinetic experiments can be conducted under near native conditions and monitored in a time dependent manner. Used to determine the dependency of the reaction on ascorbate and assess the redox of copper sites during reactivity.*

Chemical quench and rapid freeze quench (RFQ) are two extremely similar techniques used to quantify the kinetics and characterize the enzyme during pre-steady state reactivity. Both techniques function by initiating the reaction by rapidly mixing enzyme, substrate, and other required reagents then "quenching" the reaction by arresting it through rapid freezing or the addition of an inactivating chemical. The time of quenching is determined on a millisecond timescale to allow the time dependency of a reaction parameter to be assessed.

Chemical quench was used by mixing PHM with varied concentrations of substrate and ascorbate, then quenching the reaction by adding trifluoracetic acid (TFA) to stop the reaction at known timepoints. At each of these known timepoints the concentration of product was determined by high-performance liquid chromatography (HPLC), which separates the unreacted substrate from the product.

RFQ proceeds similarly. PHM was mixed rapidly with varied concentrations of substrate or ascorbate, but rather than monitoring the formation of product, the frozen sample is then prepared for EPR (section 2.2) to allow direct assessment of the redox state of the enzyme.

Together these techniques allow monitoring the reaction indirectly (through product formation or redox state) in near native conditions. This technique is used extensively in chapter three where it demonstrates PHM's dependency on ascorbate beyond simple reduction.

2.8 Density Functional Theory (DFT)

Function: *Provides an approximate solution to the many-electron problem of chemical reactivity, allowing accurate predictions of energy barriers, transition states, etc.*

Purpose: *Allows testing the plausibility of structures or mechanisms by simulating them and evaluating their relative energy barriers. Can simulate spectroscopic signals that are empirically testable.*

One of the most important, if not most important problems in chemistry is the electronic structure problem, which is to find the ground-state energy of electrons for arbitrary positions of nuclei[74]. If this problem can be solved, the properties of a system, such as bond energies and lengths, can be determined. For very simple systems this can be accomplished by solving the Schrödinger equation, but for remotely complex systems with more than three quantum mechanical particles this turns into a many-body problem which is currently unfeasible to solve.

Density functional theory (DFT) is a powerful and widely used tool in the field of computational chemistry. It is a quantum mechanical approach, which are characterized by their relatively slow speed of computation but high chemical accuracy. This is in contrast with a molecular modeling approach which is largely based in classical physics and is relatively quickly and easily computed but is much less chemically accurate. Foundationally DFT is a framework to solve, or perhaps more accurately bypass, the many electron problems at the core of a quantum mechanical approach[74]. It rests upon the discovery that the ground-state energy of a system can be determined by the functional of the electron density of that system. Put another way, there exists a functional – a mathematical object which takes a function and gives a number – which given the electron density of a system will determine the energy. Early attempts to compute the energy of interacting systems using only electron density produced crudely accurate results. To improve upon this accuracy Kohn and Sham proposed to replace the complex, interacting system of interest with a simpler system of non-interacting electrons[75]. This fictitious non-

interacting system is constructed such that its density is the same as the interacting system of interest but is constructed from several orbitals which are more easily and accurately computed. This allows the problem to be reframed from an unsolvable many electron problem to a relatively set of molecular orbitals. This is the theoretical underpinning of modern KS-DFT, for which they won a Nobel prize, and leads to a series of practical and methodological considerations.

One important consideration is DFT's poor accuracy with certain kinds of systems. Due to DFT's relatively simple implementation, though the theory is quite complex, it often implemented as a "black box" without recognition of its limitations or drawbacks. Systems that DFT have much greater difficulty describing include those involving radicals, transition metal complexes especially 3d metals with partially filled 3d-shells, including copper in the context of PHM[76,77]. This is because these are "multi-reference" systems, the reasons for this difficulty are complex but, essentially, reflect the complex and often poorly understood electronic structure of these systems which make them difficult to model with traditional DFT methods. Molecular flexibility is another important consideration when it comes to DFT suitability. For systems with few or a single accessible conformation the molecular properties given by DFT can be quite accurate, but as the number of available conformations rises these properties described less and less effectively.

Another important consideration is the solvation of the system. In general solvent molecules are not included in calculations, except where they directly participate in chemistry, but these molecules can have a dramatic effect on the structure and properties of the system[68]. To represent this effect, an implicit solvation model is employed that apply a potential across the entire system. Solvation models vary considerably, some purely electrostatic ignoring effects such as van der Waals interactions, solvent entropy, etc. Others include these effects but greatly increase the computational cost of energy minimization.

Choice of functional is perhaps the most important decision of all. There are quite literally hundreds of functionals, with new functionals emerging every year[78]. These functionals vary wildly in terms of complexity, specificity, target application, and overall

quality. Functionals are characterized by the complexity of their theory and calculation which is inversely related to their ease of computation. “Hybrid” functionals, which hybridize high level theory and DFT, are the most recognizable and widely used functionals, and among them the most characteristic and widely used is certainly the B3LYP functional which has become virtually synonymous DFT in the chemical context. It is a hybrid functional which can perform quite well in many cases but is also becoming outdated and is also subject to several systemic errors which have been corrected by more modern functionals[79-81].

While DFT is not performed in any of the following chapters, all chapters of this thesis are in conversation with computational studies. It is notable that the system of interest is subject to many of the pitfalls and complexities that challenge DFT. It concerns a copper protein with a partially filled 3d shell, the chemistry occurs inside a solvent filled cleft where solvation effects are quite complicated and poorly understood, the role of conformational changes is not well understood, and existing studies use the B3LYP functional which has known systematic errors.

Chapter Three: Pre-steady State Reactivity of Peptidylglycine Monooxygenase Implicates Ascorbate in Substrate Triggering of the Active Conformer

Overarching Question: *What are the necessary conditions to permit PHM reactivity, and what do these conditions imply about the reaction?*

Key Findings: *PHM does not react with oxygen without substrate. Full enzyme reactivity requires exogenous ascorbate, and the addition of exogenous ascorbate biases PHM to a different conformation detected by FTIR.*

This paper has been published previously in Biochemistry[82]. Changes and clarifications will be indicated by double brackets (e.g. [[a clarification]]).

This work was in many ways an inauspicious beginning to our investigation and increasing acceptance of the binuclear, open-closed model of PHM reactivity. The goal was simple; confirm some of the basic reaction parameters of the PHM hydroxylation reaction and collect pre-steady state kinetic data. We set out to perform single-turnover reactions of the enzyme, where pre-reduced aliquots of enzyme were mixed with stoichiometric amounts of substrate and oxygen in the absence of exogenous ascorbate. The problem was: it didn't work. Single turnover reactions were greatly substoichiometric, EPR indicated that dioxygen alone was not able to oxidize PHM, and stopped flow experiments (data unpublished) gave conflicting data.

This led us to question some of the core tenants of PHM reactivity. What if ascorbate wasn't just a reductant? What if it had some other role in reactivity? The recently proposed model by the Wang lab suggested as much, but it did not have widespread acceptance in the community.

We repeated the experiments in the presence of exogenous ascorbate and observed an increase in final stoichiometry. This demonstrated that ascorbate an excitatory role, though the mechanism was unclear. We probed the role of ascorbate spectroscopically with FTIR and found evidence that ascorbate was inducing an active enzyme conformer.

Pre-steady State Reactivity of Peptidylglycine Monooxygenase Implicates Ascorbate in Substrate Triggering of the Active Conformer

Evan F. Welch†§, Katherine W. Rush†‡, Renee J. Arias†¶*, and Ninian J. Blackburn†*

† Department of Chemical Physiology and Biochemistry, Oregon Health and Science University,3181 SW Sam Jackson Park Road, Portland, OR 97239, USA

§ Department of Biomedical Engineering, Oregon Health and Science University,3181 SW Sam Jackson Park Road, Portland, OR 97239, USA

‡ Department of Chemistry, Reed College, 3203 SE Woodstock Blvd, Portland, OR 97202, USA

¶ Present address: Materials & Structural Analysis Division, Thermo Fisher Scientific, Hillsboro, OR 97124, USA

* Corresponding author: blackbni@ohsu.edu

3.1 Abstract

Peptidylglycine monooxygenase (PHM) is essential for the post translational amidation of neuroendocrine peptides. An important aspect of the PHM mechanism is complete coupling of oxygen reduction to substrate hydroxylation which implies no oxygen reactivity of the fully reduced enzyme in the absence of peptidyl substrates. As part of studies aimed at investigating this feature of the PHM mechanism we explored pre-steady state kinetics using chemical quench (CQ) and rapid freeze quench (RFQ) studies of the fully-reduced ascorbate-free PHM enzyme. First we confirmed the absence of Cu(I)-enzyme oxidation by O_2 at catalytic rates in the absence of peptidyl substrate. Next we investigated reactivity in the presence of the substrate dansyl-YVG. Surprisingly, when ascorbate-free di-Cu(I) PHM was shot against oxygenated buffer containing the dansyl-YVG substrate, <15% of the expected product was formed. Sub-stoichiometric reactivity was confirmed by stopped flow and RFQ EPR spectroscopy. Product generation reached a maximum of 70% by addition of increasing amounts of the ascorbate co-substrate in a process that was not the result of multiple turnovers. FTIR spectroscopy of the Cu(I)-CO reaction chemistry was then used to show that increasing ascorbate concentrations correlated with a substrate-induced Cu(I)M-CO species characteristic of an altered conformation. We conclude that ascorbate and peptidyl substrate work together to induce a transition from an inactive to an active conformation and suggest that the latter may represent the “closed” conformation (Cu-Cu ~ 4 Å) recently observed for both PHM and its sister enzyme DBM by crystallography.

3.2 Introduction

Mononuclear copper monooxygenases constitute a family of metalloenzymes important to both the health and energy-related sciences. A prime example is dopamine β-monooxygenase (DBM)[31,83], which catalyzes a critical step in catecholamine biosynthesis, as does its insect homologue tyramine β-monooxygenase (TBM)[84]. Similarly, peptidylglycine α-amidating monooxygenase (PAM)[85,86] is a bifunctional enzyme and the only known enzyme to convert glycine-extended neuropeptide hormones into their active C-terminally amidated forms. Lytic polysaccharide monooxygenases (LPMOs) contain functional mononuclear copper centers which catalyze the chemically challenging oxidation at hexose C1 and/or C4, making them important enzymes in biomass degradation[87]. Finally, new investigations into the structure and function of particulate methane monooxygenase (pMMO) denote the likelihood of a mononuclear copper site as the catalytic center for alkane hydroxylation[88,89].

The catalytic core (PHMcc, residues 42-356) of PHM catalyzes the first step in peptide amidation via a copper-dependent hydroxylation of the α-C atom of the glycine-extended pro-peptide C-terminus (Figure 3-1). The reaction involves the transfer of four electrons to O_2, two from the C-H bond and two from an external reductant. In order to achieve this conversion, the enzyme stores the two external electrons on two non-coupled copper atoms (CuH and CuM), denoted the H-site and the M-site, respectively, which are reduced to Cu(I) by ascorbate. Powerful insights into the structure and catalytic mechanism of this copper monooxygenase have been achieved in previous crystallographic[19,26,90-92], spectroscopic[20,43,50,67,93-95], kinetic[40,41,44,96-99] and theoretical[46,72,100] studies. Structurally, it is known that the copper centers of WT PHMcc[19,92] and its complexes with exogenous ligands[90,101] are mononuclear and separated by 11 Å across a solvent-filled cleft (Figure 3-1). The M-site (CuM) is deemed responsible for initial oxygen binding and the ensuing catalytic chemistry[91], and is coordinated by H242, H244, and a weak, yet catalytically essential interaction with the thioether of M314[20,54,102,103]. The two reducing electrons provided to the M-site are hypothesized to be supplied by the H-site

(CuH) via long range ET[42,92,98,104,105]. It has been reported that exogenous ligands (O_2, CO, peroxide, and azide) can bind to the catalytic M-site but are excluded from the H-site by electronic or steric factors which are incompletely understood[42,90,91,101,104].

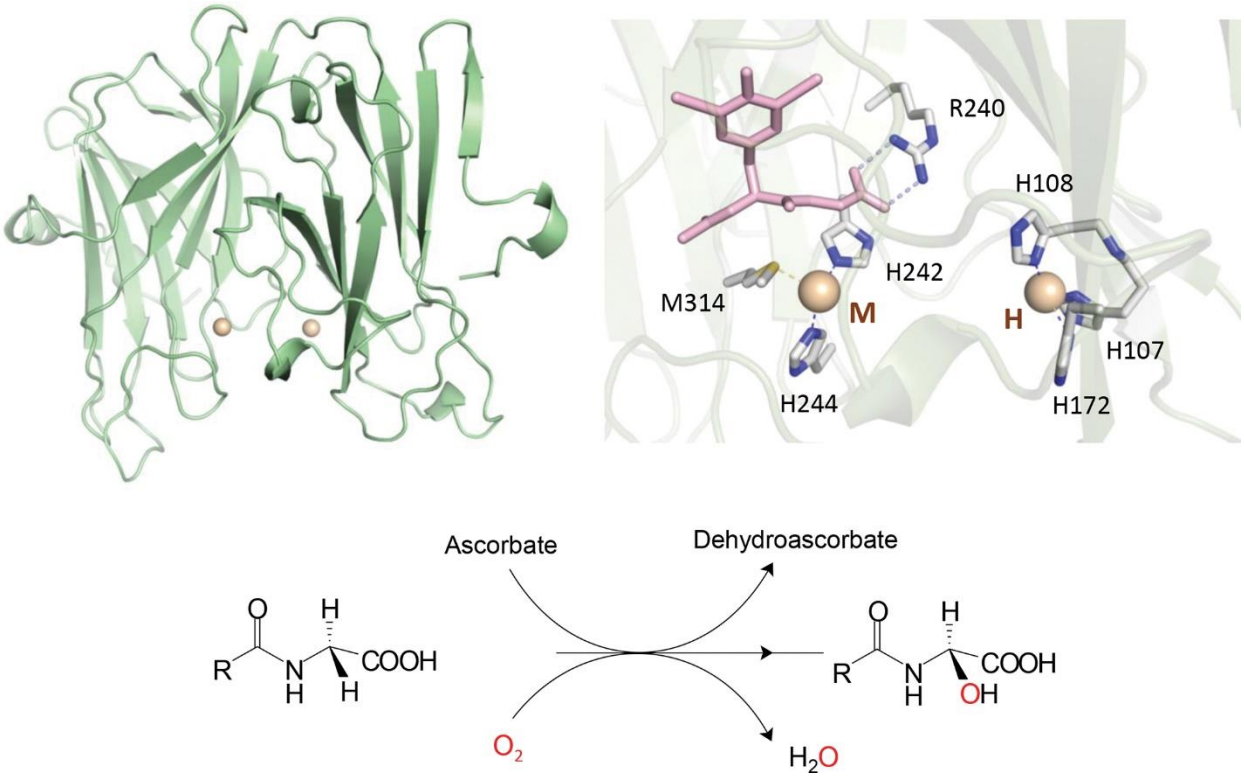

Figure 3-1 Overview of PHM Structure and Function. *Top: structure of the catalytic core of the peptidylglycine monooxygenase with bound substrate di-iodotyrosyl-glycine (pdb code 3OPM). Left panel shows the protein fold architecture and the position of the two coppercenters which are separated by 11 Å. Right panel shows an expanded view of the metal centers and their coordinated residues. Copper atoms are presumed to be in the oxidized Cu(II) state. Bottom: Reaction catalyzed by PHM.*

A number of mechanisms have been proposed to explain how the electron is transferred across the 11 Å solvent-filled cleft that separates the H- and M-subdomains. Among these, substrate-mediated ET[92] and transfer across ordered solvent[98,99] have secured the most support but another possibility proposed on the basis of crystallography[31] and computational modeling[72] is that the enzyme undergoes a conformational change to bring the copper sites closer together. Various crystallographic studies have shown examples of DBM[31] and PHM[26] in both open and closed conformations, although the biological relevance of these conformations has not yet been established. In

one study, two conformations of DBM were observed in the same asymmetric unit. In one monomer, the structure of the catalytic core aligns with the open state of PHM, where the copper ions are separated by approximately 11 Å (13-14 Å in DBM) while in the second monomer it aligns with a closed structure of PHM (mutant variant H108A in complex with citrate). In each of the closed structures the copper sites are partially occupied (DBM) or half filled (PHM, H-site absent), raising the question of whether the closed conformer is an artifact of copper loss. However, this closed conformation offers an appealing route for ET between the H- and M-sites and has been shown to be an energetically feasible active state by QMMM calculations[72].

The likelihood of multiple conformational states of the enzyme is supported by spectroscopic studies. These studies focus on CuM binding to CO, and demonstrate a substrate-induced electronic perturbation of the diatomic CO/O_2 molecule[50]. CO forms a complex with the ascorbate-reduced enzyme with a C≡O stretching frequency (ν(CO)) of 2093 cm^{-1}. The decrease in ν(CO) from that of free CO (2143 cm^{-1}) is consistent with back-bonding from the filled d-electron manifold into the empty π* CO antibonding orbitals and is assisted by electron-rich imidazole ligands. In the presence of peptidyl substrate, a red-shift in ν(CO) is observed, with acetyl-YVG substrate dropping the frequency to 2063 cm^{-1}. The ~30 cm^{-1} decrease in ν(CO) suggests a substrate-induced increase in the electron-donating power of the CuM electronic environment. Interestingly, both populations (2093 cm^{-1} and 2063 cm^{-1}) remain present at high acetyl-YVG concentration, suggesting two forms of the enzyme.

Here, we explore the pre-steady-state reaction of the fully reduced enzyme in the absence of reductant and as a function of ascorbate concentration using chemical quench, (CQ) stopped-flow, rapid freeze quench (RFQ), and Fourier transform infrared (FTIR) approaches. We show that hydroxylation of the dansyl-YVG substrate while rapid, only proceeds to <15 % of the expected product based on enzyme concentration. However, this percentage increases to about 70% in the presence of ascorbate in an ascorbate-dependent manner. Pulse-chase data suggest that this is not the result of

multiple turnovers but represents an activation of the Cu(I) enzyme by excess ascorbate. Additionally the effect appears to correlate with increase in the species responsible for the 2063 cm^{-1} infrared band. Taken together the data require a new hypothesis for substrate activation, one possibility of which includes an ascorbate-induced conformational change to bring the protein from an open to a closed conformation, facilitating electron transfer between the copper sites.

3.3 Materials and Methods

3.3.1 Chemicals

Buffer components and sodium ascorbate were purchased from Sigma-Aldrich with purities of >99%. The substrate Acetyl-Tyr-Val-Gly (Ac-YVG) was purchased from Peptide International. The substrate Dansyl-Tyr-Val-Gly (Dns-YVG) was purchased from Chi Scientific.

3.3.2 Cell production and protein purification

PHM WT was produced from transfected CHO cells in an Accusyst Minimax bioreactor, and reconstituted to 2 Cu(II) atoms per monomer. All procedures and analytical methods were as described previously[50,103,106]. Protein concentration was determined using OD_{280}(1%) = 0.980 with a Cary 50 spectrophotometer. After purification, the proteins were stored at -80°C. Unless otherwise stated reactions were carried out in 50 mM sodium phosphate buffer pH 7.5. Reactions were typically carried out at pH 7.5 since the single turnover rates were not too fast to measure at this pH.

3.3.3 Copper Reconstitution and Analysis

Protein was reconstituted by addition of 2.5 molar equivalents of copper sulfate by syringe pump over the course of an hour. Excess copper was removed by dialysis in 3 L of pH 7.5 sodium phosphate buffer overnight. Reconstitution was verified using a Perkin-Elmer Optima 2000 DV inductively coupled plasma optical emission spectrometer (ICP-OES) and was determined to be 2.0 +/- 0.2 Cu(II) per protein molecule (Table 3-S1).

3.3.4 Generation of ascorbate-free fully reduced PHM

Fully reduced PHM was generated by addition of 2.5 reducing equivalents (1.25 equivalents per copper) of buffered sodium ascorbate as a highly concentrated small volume with mixing to a solution of anaerobic oxidized enzyme in a Vacuum Atmospheres glove box. A color change was observed immediately from cerulean blue to pale straw. The solution was then desalted anaerobically using two passes in 7K MWCO Zeba spin desalting columns (Thermo Fisher). The specification of these columns quote a value of 5-10 percent of low molecular weight solute remaining after each passage implying a negligible amount of ascorbate remaining after two passages. ICP-OES measurement of copper concentration after this protocol showed little or no copper loss occurred during ascorbate reduction and removal. Representative data are listed in Table 3-S1.

3.3.5 Oxygen reactivity of fully reduced ascorbate-free PHM in the absence of peptidyl substrate

600 µL of a 500 µM solution of oxidized PHM (1 mM in Cu(II)) was split into three portions of 200 µL each. Sample 1 was transferred directly to an EPR tube for determination of the EPR detectable Cu(II) in fully oxidized PHM. Samples 2 and 3 were reduced anaerobically with ascorbate and made ascorbate-free as described above. Sample 2 was transferred anaerobically to an EPR tube for determination of the EPR detectable signal in the fully reduced anaerobic ascorbate-free enzyme. Sample 3 was exposed to air with shaking for 120 s, and then transferred to an EPR tube for Cu(II) quantitation. EPR spectra of all samples were measured and the concentration of EPR detectable Cu(II) determined via double integration versus a 300 µM Cu(II)-EDTA standard measured under identical conditions. Spectral analysis was performed using GRAMS AI spectroscopy software (Thermo). EPR spectra were measured on a Bruker Elexsys E500 spectrometer equipped with a superX microwave bridge and a dual-mode cavity with a helium flow cryostat (ESR900, Oxford Instrument, Inc). The following experimental conditions were used: frequency 9.63 GHz, temperature 100 K, microwave power 20 mW, gain 10 dB, modulation amplitude 10 G and sweep time 84 s.

3.3.6 Fully reduced ascorbate-free single turnover kinetics

The pre-steady state reaction (single turnover) of fully reduced ascorbate-free PHM was interrogated using a BioLogic microvolume quench-flow instrument (QFM-4000). 600 µM fully reduced ascorbate-free PHM was pre-incubated with 600 µM dansyl-YVG, pre-loaded into a syringe and sealed with a septum. 20 mM sodium phosphate buffer was saturated with oxygen by bubbling with pure humidified oxygen gas, then loaded into a syringe sealed with a septum. Fully reduced ascorbate-free PHM + dansyl was shot against an equal volume of oxygenated buffer at varied aging times: 5, 20, 40, 60, 80, 100, 150, 200, 250, 300, and 500 ms. The reaction mixture was quenched at each aging time with an equal volume of 8% trifluoroacetic acid (TFA), then diluted offline with 100 mM MES buffer resulting in a final concentration of 100 µM PHM + 100 µM Dns-(substrate+product). In experiments with added ascorbate the quenched, diluted reaction mixture also contained 100 µM, 500 µM, 2 mM, or 6 mM ascorbate. Samples were analyzed by via high performance liquid chromatography (HPLC) with a Varian Pro Star solvent delivery module equipped with a Varian Pro Star model 410 autosampler (250 µL syringe, 100 µL sample loop) on a 250 mm x 4.6 mm Varian Microsorb-MV 100-5 C18 column as previously reported[104]. Dansyl fluorescence was monitored with a Waters 474 scanning fluorescence detector at λ_{ex}= 365 nm, and λ_{em}= 558 nm. This fluorescence was used to monitor Dns-YVG substrate concentration and hydroxylated product (Dns-YVG-OH). Product and substrate were resolved via an isocratic method using 25% Solvent B (0.1% TFA in acetonitrile) and 75% Solvent A (0.1% TFA in water). Substrate concentrations were determined via standard curves of known concentrations of Dns-YVG in 0.1% TFA in water.

3.3.7 Ascorbate dependence of the pre-steady state reaction

Oxidized, 600 µM PHM WT was pre-incubated with 600 µM Dns-YVG. The PHM and Dns-YVG mixture was gently infused with pure oxygen in a 5 mL septum-fitted Wheaton vial for approximately 30 minutes at 23°C. When removing the vial from the oxygen infuser, a small amount of oxygen overpressure was allowed to remain in the vial. Anaerobic ascorbate was prepared from powder in a Vacuum Atmospheres anaerobic glove box

using anaerobic buffer (50 mM NaP, pH 7.5) and was prepared in 200 µM, 1 mM, 4 mM, and 12 mM concentrations. Ascorbate mixtures were pre-loaded into syringes within the anaerobic chamber, and sealed with septa when removing from the chamber. Ascorbate dependence was assessed by shooting the 600 µM PHM + Dns-YVG mixture against an equal volume of anaerobic ascorbate, with a set aging time of 300 ms. The samples were quenched with 8% TFA (4% final concentration) in water, and analyzed via HPLC as described above.

3.3.8 Pre-steady state kinetics at high ascorbate concentration

Pre-steady state kinetics were [[studied]] using the QFM-4000 system as mentioned above, but with the following adjustments. 600 µM PHM and 600 µM Dns-YVG were pre-incubated together and infused with pure oxygen at 23°C. Anaerobic ascorbate was prepared in the anaerobic chamber, pre-loaded into a syringe, and sealed with a septum. Single-turnover kinetic curves were obtained by shooting the 600 µM PHM + Dns-YVG mixture against anaerobic ascorbate resulting in a final concentration of 6 mM at varied aging times: 5, 20, 40, 60, 80, 100, 150, 200, 250, 300, and 500 ms. The samples were quenched with 8% TFA (4% final concentration) in water, and analyzed via HPLC as described above.

3.3.9 "Pulse-Chase" kinetics with acetyl-YVG and dansyl-YVG

To determine if enzyme was undergoing multiple turnovers, a pulse-chase experiment was performed using the QFM. Oxidized, 600 µM PHM WT was pre-incubated with 600 uM Dns-YVG. The PHM and Dns-YVG mixture was gently infused with pure oxygen in a 5 mL septum-fitted Wheaton vial for approximately 30 minutes at 23°C. When removing the vial from the oxygen infuser, a small amount of oxygen overpressure was allowed to remain in the vial. Anaerobic ascorbate + acetyl-YVG (Ac-YVG) was prepared from powder in a Vacuum Atmospheres anaerobic glove box using anaerobic buffer (20 mM NaP pH 7.5) at 10 mM ascorbate plus 3 mM Ac-YVG. The ascorbate mixture was pre-loaded into syringes within the anaerobic chamber, and sealed with septa when removing from the chamber. Repeated turnover was then assessed by shooting the 600 µM PHM +

Dns-YVG mixture against an equal volume of anaerobic ascorbate Ac-YVG mixture, with aging times of 0, 300 and 1000 ms performed in triplicate. The mixture was then quenched with an equal volume of 8% trifluoroacetic acid (TFA), then diluted with 20 mM NaP buffer resulting in a final concentration of 100 μM PHM + 100 μM Dns-(substrate + product) + 1.67 mM ascorbate + 500 μM Act-YVG. Samples were analyzed by HPLC with a Varian Pro Star solvent delivery module equipped with a Varian Pro Star model 410 autosampler (250 μL syringe, 100 μL sample loop) on a 250 mm x 4.6 mm Varian Microsorb-MV 100-5 C18 column as described above and previously reported[104].

3.3.10 Fully reduced ascorbate-free stopped-flow kinetics

Ascorbate-free reduced PHM WT was prepared in the anaerobic chamber as described above. The protein was prepared in a pH 7.5 buffer system containing equal volumes of 50 mM each of MES, HEPES, and sodium phosphate. 500 μM of WT PHM was shot against 5 mM Ac-YVG + 20 mM sodium azide. Data was collected for 500 ms at 395 nm with readings taken every 5 milliseconds in an Applied Photosystems SX20 stopped flow module.

3.3.11 Fully reduced ascorbate-free rapid-freeze quench EPR

Rapidly frozen EPR samples were prepared using a Quench Flow-3 (KinTek) apparatus configured for RFQ by the manufacturer. Reduced, 200 μM ascorbate-free protein samples (400 μM in Cu(I)) in anaerobic buffer and 200 μM acetyl-YVG substrate in fully oxygenated buffer ($[O_2] \approx 1.1$ mM before 1:1 dilution on mixing) were loaded onto the instrument and rapidly mixed at the desired time point. A universal buffer was used comprised of equal volumes of 50 mM MES, HEPES and CHES adjusted to pH 7.5. Mixtures were quenched in liquid ethane at -170°C. The resulting snow was then packed into 707-SQ-250M EPR tubes (Wilmad LabGlass). Oxidation was monitored in a Bruker E500 X-Band EPR spectrometer equipped with a superX microwave bridge and a dual-mode cavity with a helium flow cryostat (ESR900, Oxford Instrument, Inc). The experimental conditions were frequency 9.63 GHz, temperature 100 K, microwave power 20 mW, gain 10 dB, modulation amplitude 10 G and sweep time 84 s.

3.3.12 Fourier transform infrared spectroscopy (FTIR)

500 μM PHM in 20 mM pH 7.5 NaP buffer was deoxygenated and saturated with humidified CO by streaming across the surface of the solution with pure CO gas for 5 minutes with gentle agitation. Once carbonylated, Dns-YVG was added to a final concentration of 2.5 mM, then a small aliquot of 2 M anaerobic buffered sodium ascorbate was added to achieve final concentrations of ascorbate between 0 and 25 mM. The mixture was then carbonylated again for 5 minutes. 100 μL of solution was then added by syringe into the IR cell composed of two CaF_2 windows separated by a 50 micron Teflon spacer. FTIR data were recorded on a Bruker Tensor 27 FTIR spectrophotometer continuously purged with CO_2-free dry air as previously described.[50] One thousand scans were collected for both protein sample and buffer blank from 2250 to 1900 cm^{-1} at a resolution of 2 cm^{-1}. Spectral analysis including subtraction of the buffer-blank was performed using GRAMS AI spectroscopy software (Thermo).

Ratios of CO bands at 2063 and 2093 cm^{-1} were obtained from the peak heights rather than peak integrals. The rational for this less rigorous approach stems from several factors; the cell was taken apart and reassembled between measurements taken on several days, which introduced small changes in path-length and fill quality. Slight differences in protein and copper concentrations were introduced due to evaporation during carbonylation. Finally, different calcium fluoride windows were used across the experiment which may have very slightly different optical properties.

3.4 Results

3.4.1 PHM is unreactive to oxygen in the absence of substrate

Consensus mechanisms for PHM and DBM are predicated on the initial binding of oxygen to the reduced Cu(I)M site. To probe this chemistry, we explored the sensitivity of the Cu(I)M site to oxygen in the absence of substrate. Figure 3-2 shows EPR spectra of PHM as a function of time exposed to oxygen. A sample of fully oxidized enzyme was divided into three aliquots. One aliquot was transferred to an EPR tube and measured without further modifications. A second aliquot was reduced anaerobically with two molar equivalents of ascorbate and the excess ascorbate removed by two passages through a spin desalting column and the EPR spectrum measured. The third sample was reduced and ascorbate-depleted as described, but then exposed to oxygen for two minutes, and the EPR spectrum determined once again. The spectra were double integrated and compared to the doubly integrated EPR spectrum of the first aliquot which had not been reduced. The results are shown in Figure 3-2. Ascorbate reduction and removal resulted as expected in a low integral (3.5 % EPR detectable). However, exposure to oxygen for two minutes generated only 11.3 % of the fully oxidized Cu(II) signal, indicating oxidation on a time scale much slower than the catalytic rate. While the absence of an EPR spectrum could be attributable to a spin coupled cupric-superoxo species, such an entity should be labile leading to superoxide dissociation and disproportionation ultimately leading to an oxidized Cu(II)M center.

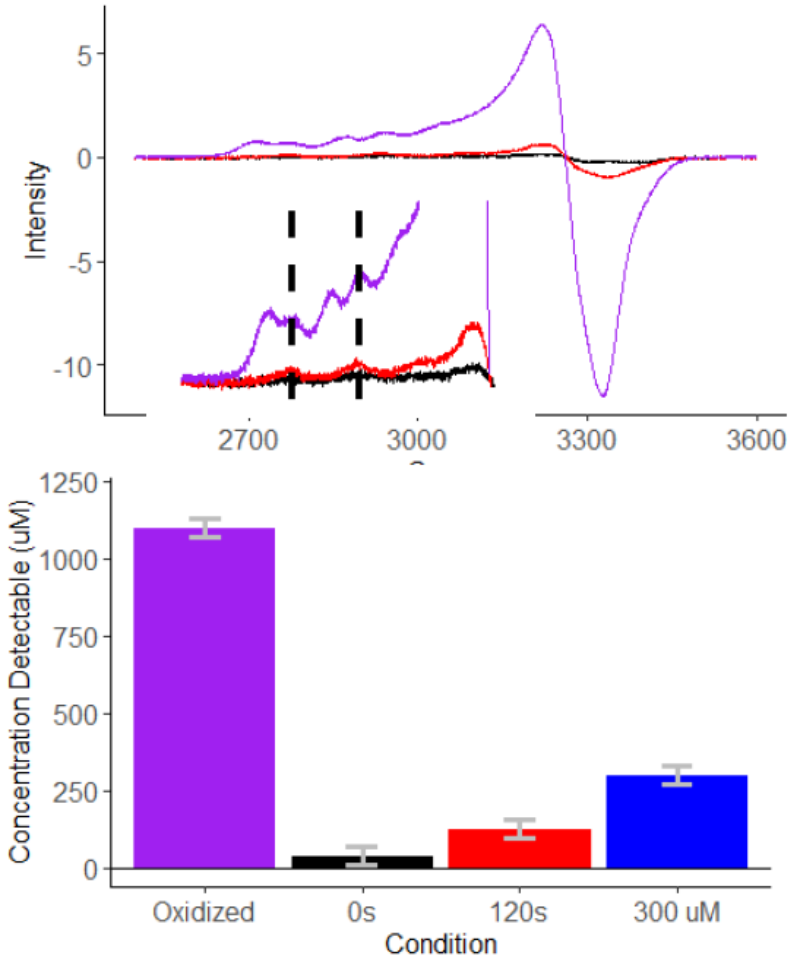

Figure 3-2 EPR spectra of WT PHM mixed with oxygenated buffer at various time points; *the purple trace shows fully oxidized, the black trace shows the ascorbate-reduced anaerobic enzyme, and the red trace shows a 120 s reoxidized enzyme. Bottom: quantitation via double integration (colors are the same as for spectra) and calibration against a standard solution of 300 μM Cu(II)–EDTA (blue). EPR conditions: frequency 9.63 GHz, T = 100 K, microwave power 20 mW, gain 10 dB, modulation amplitude 10 G, and sweep time 84 s.*

The low reactivity of the fully reduced ascorbate-free enzyme with oxygen is not unexpected, since a notable feature of these enzymes is the tight coupling of oxygen reduction to product formation[40,103,107] as well as evidence which suggests that substrate binding precedes oxygen binding[108]. These data indicate that oxygen reactivity is contingent on other factors, where the reactivity and/or redox potential of the Cu(I)M center is influenced by substrate binding. Additionally, the data demonstrates that in the absence

of peptidyl substrate, exogenous ascorbate is not required to maintain the reduced state of the enzyme, even over a relatively long duration of oxygen exposure. Interestingly while the fully oxidized enzyme clearly shows resolved components due to the two chemically inequivalent copper centers, the slow, non-catalytic re-oxidation appears to favor one of these sites as predicted by previous redox potential measurements[109].

3.4.2. Reduction stoichiometry is dependent on exogenous ascorbate

To further our understanding of PHM reaction mechanism we explored the pre-steady state reactivity of the fully reduced ascorbate-free enzyme with oxygen and peptidyl substrate. Under these conditions peptidyl substrate binding to the dicopper(I) enzyme should activate the catalysis and lead to rapid generation of the alpha-hydroxyglycyl product. Fully reduced, ascorbate-free PHM was shot against stoichiometric dansyl-YVG substrate dissolved in buffer saturated with O_2 (1.1 mM) in the absence of exogenous ascorbate using a BioLogic QFM-4000 quench-flow microvolume mixture instrument. Here substrate is the limiting reagent so the reaction should terminate when all substrate has been converted to product. Reactions were acid -quenched at successive time points with TFA and both product and substrate were quantified via HPLC using fluorescence of the associated dansyl group. Under the canonical reaction mechanism, where ascorbate is solely the physiological electron source, this pre-reduced PHM should be fully primed with reducing equivalents and should be capable of reacting stoichiometrically with substrate to reach complete product formation. Figure 3(a) shows the concentration of substrate and product over the course of the reaction, indicating that this reaction under ascorbate-free conditions while fast, is *sub-stoichiometric* achieving only approximately 10-15 % of expected product with a k_{obs} = 150 s^{-1}. Despite being fully reduced, the enzyme shows only limited reactivity with substrate and oxygen. The incomplete reactivity under these conditions is also interesting given PHM's high affinity for dansyl-YVG[104] (K_M =5 μM, $K_{D,\ reduced\ enzyme}$ = 22 μM), suggesting that while substrate must be binding to the enzyme in the presence of oxygen, turnover is not occurring.

We then explored the role of ascorbate as a possible reaction initiator by titrating the reactivity with increasing amounts of ascorbate. The addition of ascorbate resulted in an increase in the stoichiometry of product formation in a concentration dependent manner (Figures 3-3(b) and 3-3(c)) reaching a final stoichiometry of ~70% at an ascorbate concentration of 2 mM. Fig 3-3(b) shows that in the presence of excess exogenous ascorbate the reaction proceeds as expected with rapid conversion of substrate to product in a manner consistent with first-order kinetics, with a pseudo rate constant k_{obs}= 36 s^{-1} which is over 4 fold slower than for the ascorbate-free enzyme. This suggests that in the presence of ascorbate some other process is rate limiting. To address whether the inability to generate 100 percent product under saturating conditions of ascorbate was due to copper loss, we measured the Cu concentration after ascorbate reduction and removal (Table 3-S1). Results show that in some samples, copper loss equivalent to 0.3 Cu/protein was detected which could account for the 70 percent ceiling on product since loss of one of the two coppers per enzyme eliminates the activity due to *both* coppers in that molecule.

The ascorbate dependency of the pre-steady state reaction is shown in Fig 3-3(c) while Fig 3(d) plots the mole ratio of product formation as a function of ascorbate concentration. Ascorbate is seen to influence the stoichiometry of product generation via a process which involves a binding event with a K_D of 117 uM.

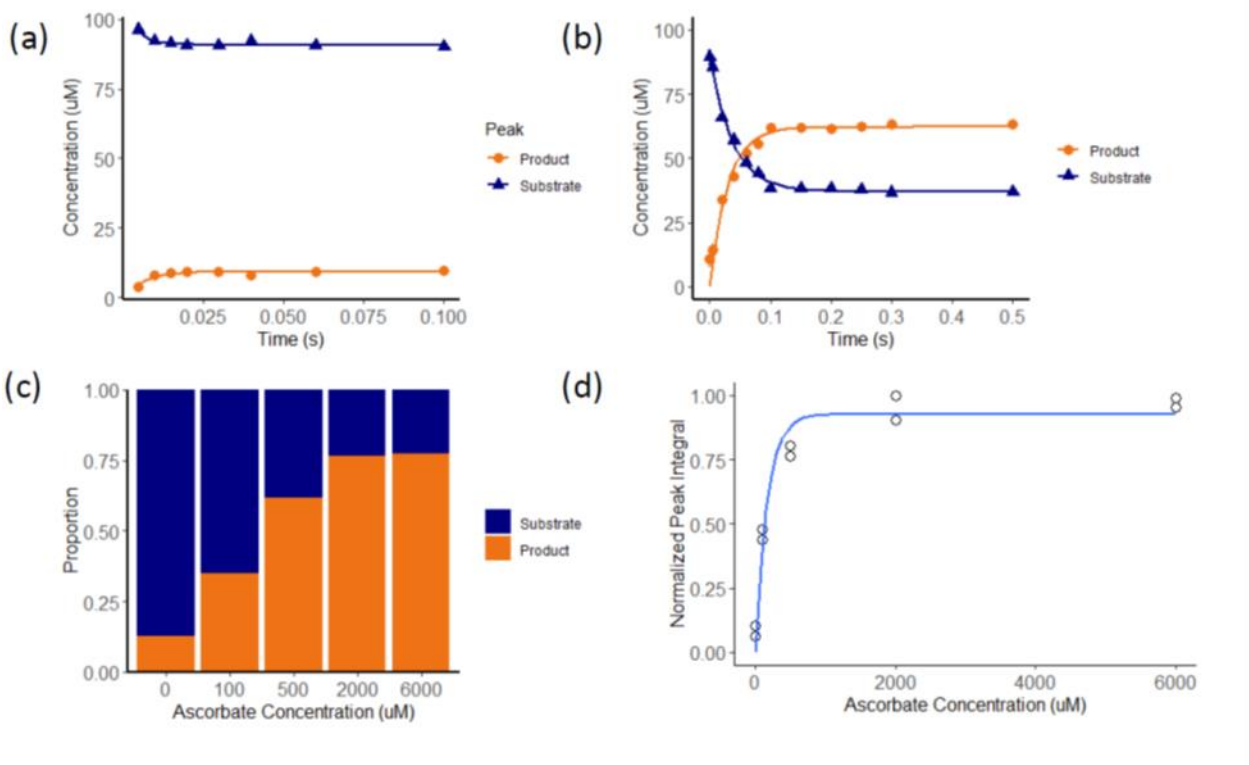

Figure 3-3 Pre-steady-state reactivity of the fully reduced ascorbate-free PHM. *(a) Time evolution of the product in the absence of excess ascorbate, k_{obs} = 150 s^{-1}: blue trace represents the consumption of dansyl-YVG substrate and orange trace is the rate of generation of the dansyl-α-hydroxyglycine-YVG product. (b) Time evolution of substrate consumption (blue) and product generation (orange) in the presence of excess ascorbate (6 mM), k_{obs} = 36 s^{-1}. (c) Bar graph showing an increase in the mole fraction of product per mole of enzyme as a function of added ascorbate. (d) Ascorbate dependence of product formation fitted to a ligand-binding event with KD = 117 μM.*

3.4.3 Ascorbate dependency is not the result of multiple turnovers

A plausible explanation for the observed behavior of ascorbate dependency of product stoichiometry is the hypothesis that a large population of the enzyme is unreactive, perhaps due to aggregation or some other feature of protein preparation. In this scenario only a small population of the enzyme is functional but can undergo multiple turnovers under the conditions of the chemical quench experiment when excess reductant is supplied. To assess this possibility a "pulse-chase" experiment was performed. Here, oxidized enzyme treated with one equivalent of dansyl-YVG in buffer saturated with O_2 was shot against excess ascorbate containing a 5-fold molar excess of the unlabeled acetyl-

YVG (Ac-YVG). Since the enzyme is pre-incubated with the fluorescent-detectable dansyl-YVG, the expectation in the case of fully reactive enzyme is rapid pre-steady state turnover to generate the dansyl-labeled product in near stoichiometric amounts. In the case of a bulk-unreactive enzyme the expectation is an approximate five-fold reduction in dansyl-labeled product as the unlabeled substrate will compete with labeled substrate for enzyme binding in the second and subsequent turnovers. Put another way, the acetyl-labeled substrate should act as a competitive inhibitor of dansylated-product production. (This experiment works because dansyl- and acetyl- labeled substrates have similar affinity for the enzyme). Figure 3-4 shows that while the rate of the reaction was marginally decreased by the unlabeled acetyl peptide, its reaction progress resembles the uninhibited reaction, consistent with full enzyme reactivity. These data together demonstrate that the enzyme requires activation to achieve full reactivity by a process that is dependent in some way on ascorbate binding. This is not due to increased reductive activity since in the absence of ascorbate the enzyme is fully reduced.

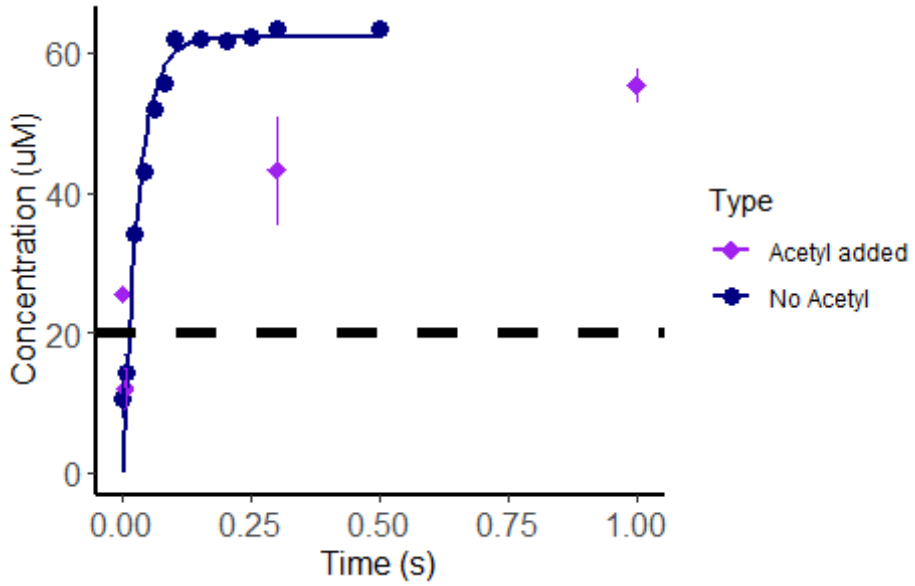

Figure 3-4 Pulse Chase Experiment. *Product generated from the reaction of dansyl-YVG with the equimolar fully reduced enzyme chased with a 5-fold excess of unlabeled Ac-YVG. Blue circles represent the product generated with equimolar dansyl-YVG and the fully reduced enzyme; purple diamonds represent the product generated when the same experiment is conducted in the presence of a 5-fold molar excess of Ac-YVG. The black dashed line represents the expected dansyl product after chasing with Ac-YVG if multiple turnovers occur.*

3.4.4 Ascorbate reduction kinetics indicate an ascorbate binding site

As a final probe on the effects of exogenous ascorbate on PHM reactivity, stopped flow was employed to determine the rate of reduction as a function of ascorbate. To accomplish this, azide was used as a reporter for the oxidized state of the enzyme. Azide is useful in these experiments as it binds only to the oxidized form of the enzyme and has a characteristic 390 nm UV-Vis signal[102] Figure 3-S1 (Supporting Information). Additionally, the formation of the PHM Cu(II)-azido complex is not rate limiting being formed within the time of mixing (Figure 3-S2 Supporting Information). Elimination of this signal by ascorbate therefore serves as a proxy for the rate of reduction. Figure 3-5 shows the rate of reduction as a function of ascorbate concentration. The reduction obeys saturation kinetics with K_D = 1120 μM, k_{obs} = 146 s^{-1} and indicates that ascorbate binds to the enzyme to accomplish reduction. This K_D is expected to reflect the affinity of ascorbate for the *oxidized* enzyme during the reduction of the di-Cu(II) to di-Cu(I) states, and should be similar to the apparent K_m determined from the dependence of product stoichiometry on ascorbate if the latter is due merely to multiple turnovers. However, as shown in Fig 3-3(d) the integrated peak signal for product plotted versus ascorbate concentration yields a K_D of 117 μM, an order of magnitude lower than that of the reduction event. This further supports a role for ascorbate in activation of the fully reduced enzyme over and above a simple role as a reducing agent.

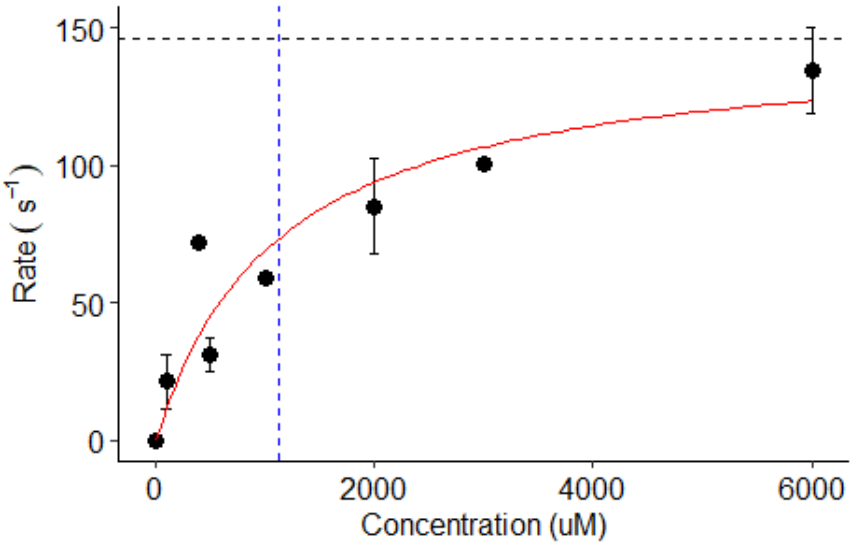

Figure 3-5 Reduction of PHM as a function of ascorbate concentration. *Ascorbate dependence of the rate of PHM reduction determined by stopped-flow using the Cu(II) PHM–azido adduct (λmax = 390 nm) as a reporter for the concentration of Cu(II)–enzyme remaining at each time point. Data are fit to a pre-equilibrium binding event with KD = 1.1 mM.*

3.4.5 Rapid freeze quench EPR of the pre-steady state reaction

The above experiments demonstrate that product formation is sub-stoichiometric without exogenous ascorbate, but do not definitively identify the redox state of the enzyme during or after the pre-steady state reaction. One possible yet unlikely explanation for the apparent ascorbate dependency is oxidation of the enzyme without product formation, initiated by substrate and oxygen binding. Here excess ascorbate would re-reduce the enzyme to allow turnover and apparent ascorbate dependency. Such reactivity does occur in other copper monooxygenase such as the LPMOs[110]. To address this possibility, rapid freeze-quench (RFQ) EPR was employed. Using this technique, the redox state of the enzyme can be assessed independent of product formation under single-turnover conditions. Figure 3-6 shows the results of shooting fully reduced ascorbate-free enzyme against oxygenated buffer containing 1 mole equivalent of substrate relative to the enzyme concentration. The results (Figure 3-6 bottom panel and Table 3-S2) show that in the absence of excess ascorbate negligible amounts of the enzyme become EPR detectable after 300 ms, a time point at which product formation has ceased. This result is remarkable as consensus mechanisms predict that in the absence of reductant, turnover

should generate two atoms of EPR detectable Cu(II) for each product molecule produced. In the present experiment if we allow for 20 percent product production we anticipate 60 μM EPR detectable Cu(II) compared with the experimentally determined amount of < 3 μM. While this result should be interpreted with caution, it may suggest that an EPR detectable entity such as a di-Cu(II) spin coupled species is formed during or after product is formed (vide infra). We note that a spin coupled Cu(II)-superoxo species is less consistent with the data as any cupric superoxide formed is expected to have been converted into hydroxylated product after 300 ms.

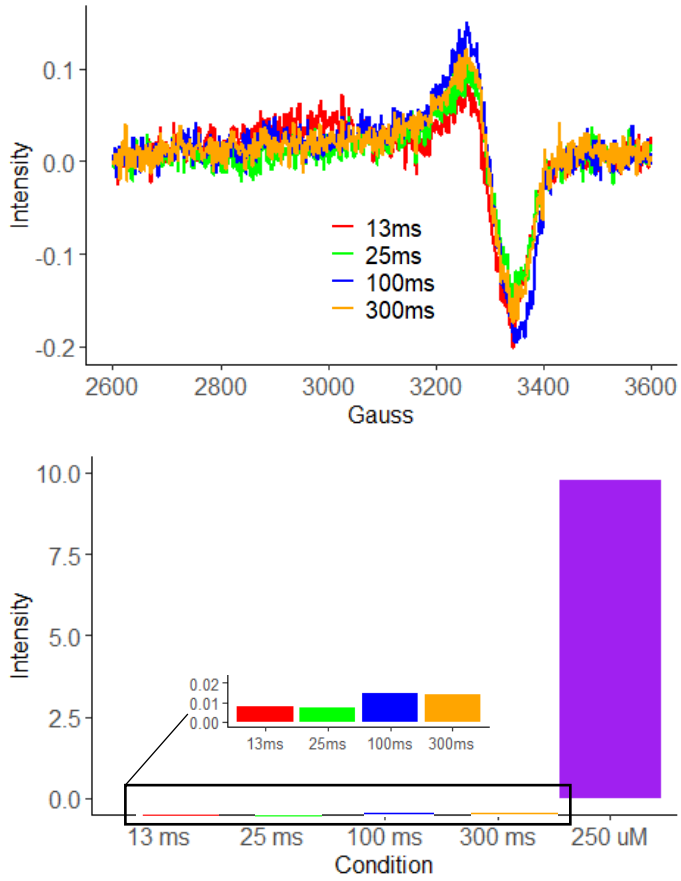

Figure 3-6 Rapid freeze-quench-derived EPR spectra of the products of the pre-steady-state PHM reaction. *EPR spectra were generated by rapidly mixing fully reduced ascorbate-free PHM (400 mM in Cu(I)) with the oxygenated buffer containing equimolar dansyl-YVG and freezing in liquid ethane (−120 °C). The top panel shows the actual spectra, and the bottom panel shows the quantitation of the Cu(II) signal by reference to a standard Cu(II)–EDTA sample: red, 13 ms; green, 25 ms; blue, 100 ms; orange, 300 ms; and purple, 250 μM Cu(II)–EDTA standard. To avoid errors from integration of noise peaks, intensities were determined from peak-to-peak heights at g⊥ relative to that of a 250 μM solution of Cu(II)–EDTA taken through an identical cycle of mixing, freezing, and packing. Errors in concentrations determined from the peak heights are estimated from triplicate measurements of a Cu(II)–EDTA standard to be ≅15% and are mainly due to differences in the packing density of the samples. EPR conditions: frequency 9.63 GHz, T = 100 K, microwave power 20 mW, gain 10 dB, modulation amplitude 10 G, and sweep time 84 s.*

3.4.6 Cu(II)-azido detected stopped flow spectrometry of the pre-steady state reaction

As discussed above, oxidized di-Cu(II) PHM reacts with azide to generate an azide-to-copper charge transfer complex with λ_{max} = 390 nm. The formation of the azido-complex

is contingent on oxidation of the enzyme and therefore serves as a reporter for pre-steady state enzyme turnover from Cu(I) to Cu(II) states. Further, its rate of formation is extremely rapid, the complex being fully formed in the time of mixing in the stopped flow (Figure 3-S2 Supporting Information). Reaction of fully reduced, ascorbate-free enzyme with Ac-YVG and oxygen was followed using stopped-flow spectrometry monitoring the rate of appearance of the 390 nm absorption. Here the fully reduced enzyme loaded with Ac-YVG was shot against buffer saturated with oxygen and containing 20 mM sodium azide. Figure 3-7 shows that in the absence of excess ascorbate less than 30% of the fully oxidized Cu(II)-azido complex is formed based on the expected absorbance for full copper oxidation (red line, Figure 3-7). Although this amount is larger than that based on product formation or RFQ EPR, it reinforces our findings that PHM has limited reactivity with substrate in the absence of excess ascorbate but may also suggest that product stoichiometry is influenced by other factors such as azide concentration.

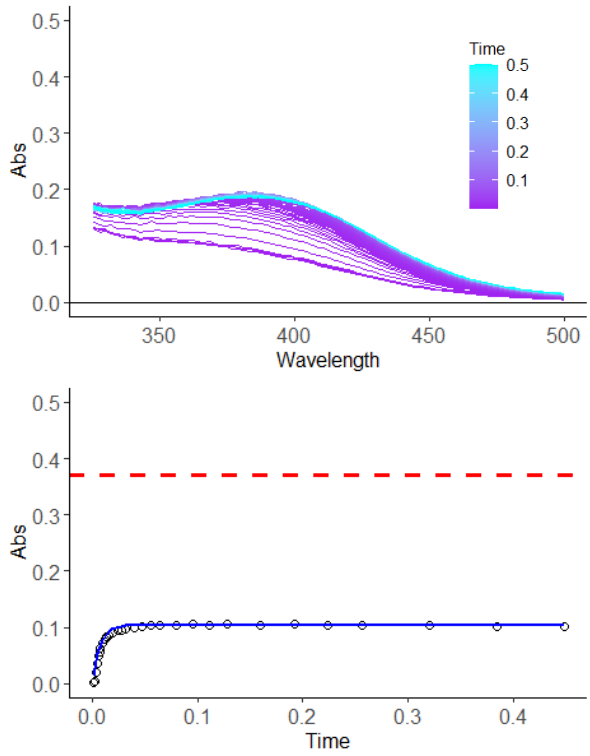

Figure 3-7 Pre-steady-state reactivity of the fully reduced ascorbate-free PHM *determined by measuring the rate of appearance of the 390 nm Cu(II)–azido adduct at 390 nm using stopped-flow spectrophotometry. 500 μM of WT PHM was shot against 5 mM Ac-YVG + 20 mM sodium azide. Data were collected for 500 ms, with readings taken every 5 ms. The top trace shows the generation of the 390 nm absorbance as a function of time in seconds. The bottom trace shows the rate curve fitted to a single exponential with* k_{obs}*= 72* s^{-1}*. The red dashed line represents the absorbance expected for complete reaction where all copper is oxidized to Cu(II) determined from a separate experiment where fully oxidized Cu(II) PHM was shot against buffer containing sodium azide under identical conditions.*

3.4.7 FTIR indicates a shift in enzyme population in response to ascorbate titration

To determine the specific effect of ascorbate on PHM reactivity, we looked to insights previously garnered from FTIR. Carbon monoxide (CO) FTIR has been used extensively to probe metal oxygen-binding active sites, where it can give remarkably detailed information about structure and oxygen binding [42,50,51,111,112]. Subtle changes to the binding site are reflected in shifts in the IR stretching frequency of the carbon monoxide.

Furthermore, carbon monoxide has been shown to bind solely to the M-site in PHM and therefore it functions as a probe of M-site configuration. It has been shown previously that varied concentrations of substrate tune two separate populations of stretching frequencies[50]. In the absence of substrate, the spectra are dominated by a large 2093 cm^{-1} stretching frequency with a minor 2063 cm^{-1} shoulder. Addition of substrate causes an increase in the 2063 cm^{-1} species with attenuation of 2093 cm^{-1}, in a concentration dependent manner. Increasing substrate concentration was, however, not sufficient to eliminate the 2093 cm^{-1} stretch, nor did a complete absence of substrate abrogate the 2063 cm^{-1} signal. These data suggested a pair of interconvertible states mediated by substrate binding, but the significance of these states to reactivity as well as their identity was unclear.

Peptidyl substrate's ability to partition the enzyme population echoes ascorbate's ability to induce a catalytically competent state, particularly since the CO binding experiments are performed in the presence of exogenous ascorbate. To probe that relationship further, we performed FTIR experiments to test if ascorbate induces an alternative enzyme configuration in a manner resembling substrate. WT PHM was exposed to carbon monoxide in the presence of substrate and varied concentrations of ascorbate. Figure 3-8 (top) shows that increasing ascorbate concentration causes the ratio of 2063 cm^{-1} to 2093 cm^{-1} to increase in a concentration dependent manner, reaching a maximum at 15 mM exogenous ascorbate while Figure 3-8 (bottom) depicts two representative spectra at 1 mM and 15 mM exogenous ascorbate respectively. Curiously, excess ascorbate beyond 15 mM resulted in decreased 2063 cm^{-1} to 2093 cm^{-1} signal but these concentrations are well above the ascorbate concentration (2 mM) required for maximum product stoichiometry. This experiment demonstrates that ascorbate, in the presence of substrate and CO, is sufficient to induce an alternate conformer of PHM.

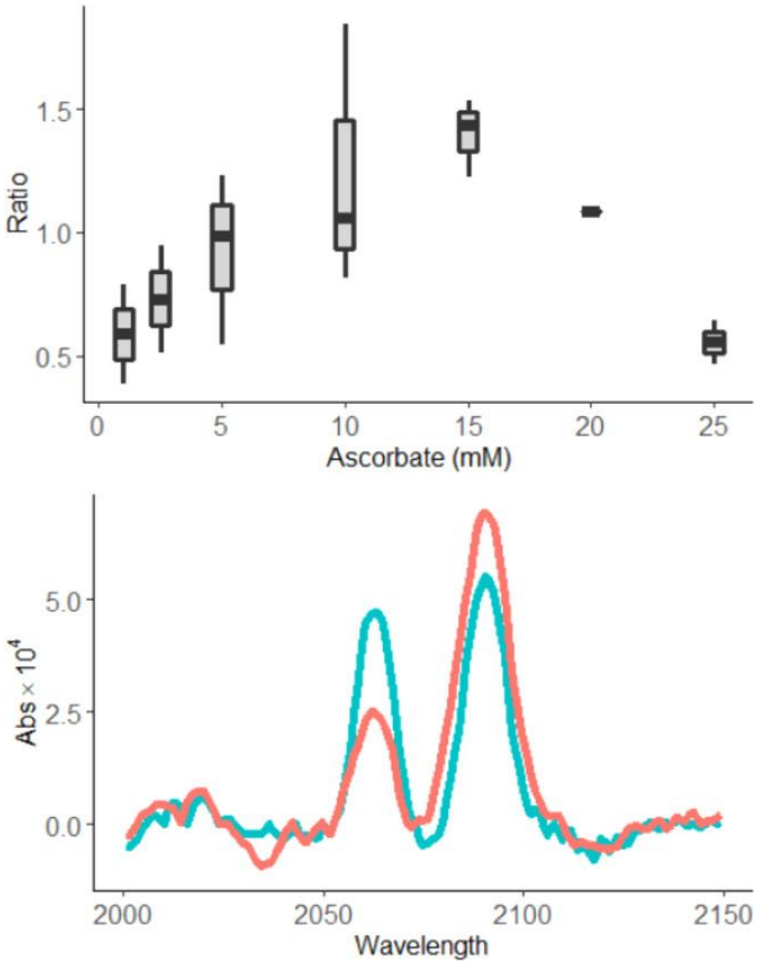

Figure 3-8 Evolution of the substrate-induced 2063 cm–1 M-site Cu(I)–CO signal as a function of the added ascorbate. *The top trace shows the ratio of 2063 to 2093 cm^{-1} peaks plotted against ascorbate concentration. The bottom trace shows the representative spectra at 1 mM (orange) and 15 mM (green).*

This explicit connection between the 2063 cm^{-1} signal and ascorbate concentration provides insights into the role of ascorbate in catalysis. Exogenous ascorbate is here shown to both bias the population of enzyme to the 2063 cm^{-1} form, as well as increase overall reactivity. This suggests that substrate and ascorbate work combinatorially to induce the 2063 cm^{-1} form of the enzyme, and presents strong evidence that this form is the active species.

The identity of this active state remains unclear. Changes to the hydrogen bonding network surrounding the CuM site have been proposed as one mechanism of substrate activation[26,50]. Another possible interpretation is a largescale conformational change. As

discussed in more detail below, ascorbate binding could potentially induce an open to closed conformational transition where the Cu site separation decreases from 11 Å to 4 - 5 Å, similar to what is observed in DBM. Once in proximity, electron transfer is facile between the two sites. There are several pieces of evidence which support this interpretation. First is the scale of the change: a 30 cm^{-1} change suggests a relatively large increase in the electron-donating power of the CuM site, larger than changes caused by mutating nearby ligands to perturb the hydrogen bonding network. Second, the red-shifted IR frequency is reminiscent of that observed in the dinuclear arthropodal hemocyanin (2043 cm^{-1}) and attributed to a semi-bridging species[51]. In the context of PHM, such a bridging species is not possible unless the copper sites were in much closer proximity, as in the case of hemocyanin, which has an intra-copper distance of 4 Å. Third is the observation of closed-conformer in crystal structures of the PHM H108A mutant in the presence of citrate[26] indicating that under certain conditions inter-domain closure is favored. Indeed, the ability for citrate to help induce a closed conformer is evocative, as citrate and ascorbate are both hydroxy acids. The binding of the citrate is interesting as well, since it binds in a manner to bridge the CuM and CuH site and may provide stability for the closed conformer, [[shown in figure 3-9]].

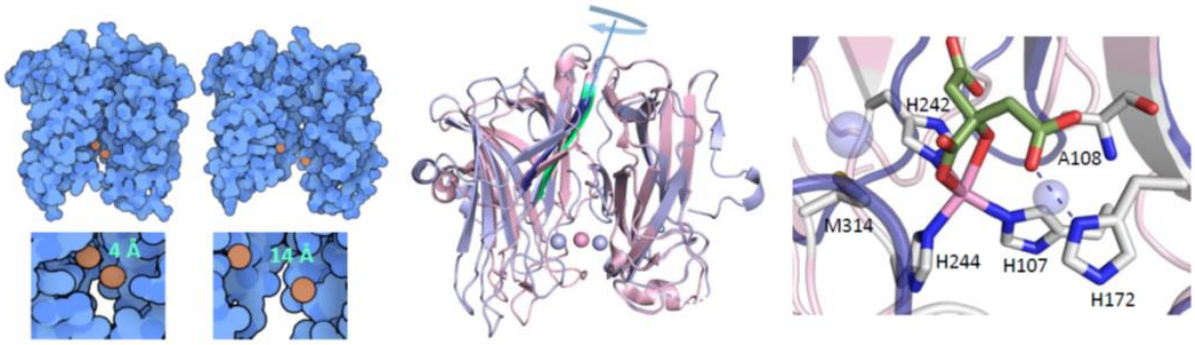

Figure 3-9 Closed and open structures of DBM and PHM. *Left, two conformers of DBM with Cu atom (bronze) locations modeled (PDB file 4EZL). Middle: alignment of the protein fold of the closed crystal structure of H108A in the presence of citrate (PDB file 6ALA), with the open structure of the oxidized PHM (PDB file 1PHM). PHM structures were aligned on the N-terminal (H) subdomain with an RMSD value of 0.41. The H108A-citrate and the oxidized native PHM main chains are depicted by pink and purple ribbons, respectively. To emphasize the hinge motion, the first β-strands of the M-domains are colored green (closed: H108A-citrate) and dark blue (open: oxidized PHM). Right: enlarged view of the metal binding site in the H108A-citrate PHM structure. The single copper atom of the closed H108A-citrate structure, which coordinates M-site residues H242 and H244 and H-site residue H107, is shown in pink, while the citrate molecule is shown as a green carbon backbone with oxygen atoms in red. The positions of the two copper sites in the open PHM structure are shown as transparent slate spheres.*

3.5 Discussion

In the present paper we explored pre-steady state kinetics of PHM as a function of ascorbate concentration using chemical quench and rapid freeze-quench studies of the fully-reduced ascorbate-free enzyme. When ascorbate-free di-Cu(I) PHM was shot against oxygenated buffer containing the dansyl-YVG substrate and the dansylated product quantified by HPLC using fluorescence detection, <15% of the expected product was formed. This result was recapitulated to varying degrees by RFQ EPR spectroscopy, and stopped flow monitoring of the oxidized Cu(II) species using the 390 nm Cu(II)-azido absorption as readout. Product generation could be increased to a maximum of 70% by addition of increasing amounts of the ascorbate co-substrate. This phenomenon could be the result of multiple turnovers of a small fraction of "active" enzyme with the remainder of the sample in a non-functional state (case 1) or activation of the fully reduced enzyme by excess ascorbate (case 2). To test which of these scenarios was most probable, we performed a pulse-chase experiment wherein the enzyme was incubated with 1 equivalent of dansyl-YVG in oxygenated buffer and then shot against a 5-fold excess of Ac-YVG. Case 1 is predicted to generate no more than 20% fluorescently-labeled product since after the first turnover unlabeled Ac-YVG would efficiently outcompete the labeled substrate, whereas case 2 is predicted to generate higher amounts of labeled product. The latter scenario was observed with 50-60% dansylated product formed. This allowed us to exclude multiple turnovers as an interpretation of the data, and to conclude that the co-substrate ascorbate not only reduces the Cu(II) centers but must also induce a conformational change to an active state. Further, the observed rate in the presence of ascorbate is 4 fold slower than that of the ascorbate-free conformer, indicating that ascorbate induces some process such as a conformational change which becomes rate limiting. In previous work we had documented that the peptidyl substrate induces a downshift in the v(CO) of the carbon monoxide complex at the M-center from 2093 to 2063 cm-1, and had suggested that this species was a substrate-triggered active conformer. Here we found that this conformer was also induced by increasing concentrations of ascorbate, confirming that ascorbate does more than act as a reducing agent. The totality

of the data led to the hypothesis that ascorbate and peptidyl substrate work together to induce a transition from the inactive to an active conformation.

The present study demonstrates a correlation between the intensity of the 2063 cm^{-1} CuM-CO band and the amount of product formed during pre-steady state turnover (since both increase with increasing ascorbate), and one may cautiously infer that the species responsible for the 2063 cm-1 band is derived from a catalytically active form, where the CO ligand is bound in the same configuration as the reactive oxygen molecule. Assigning the chemical nature of the CO-bound species is therefore important for understanding the catalytic mechanism, and the mechanism of substrate activation. The 30 cm^{-1} red-shift of the CO frequency implies a considerable degree of additional back-bonding into ligand π* orbitals which in turn weakens the CO bond via decreasing the bond order, and similar electronic perturbation applied to a Cu(I)-O_2 complex would result in significant activation of the metal-dioxygen complex.

Downshifted frequencies in Cu(I)-CO complexes can potentially arise from a number of sources such as (i) increase in N-donor (imidazole) coordination number (ii) strong H-bonding between the distal NH of the imidazole of a His ligand and a protein-derived negative charge or dipole (iii) interaction of the distal O of CO with a positive charge or dipole and (iv) a bridging or semi-bridging structure where the CO can interact with a second metal ion. In model compounds, substitution of heterocyclic rings (imidazole, pyrazole) by electron releasing groups leads to decreased frequencies while substitution by electron withdrawing groups leads to increased frequencies. Table 3-S3 of the Supporting Information lists examples which validate these trends. In a previous study[50] we showed that substitution of Met314 by His resulted in a 18 cm-1 downshift (2075 cm-1) in the absence of substrate, but addition of substrate led to a further downshift of 24 cm-1 (2051 cm-1). Therefore, simple substitution of the weakly binding Met by His does not account for the observed effect. Similarly, changes in the H-bonding networks which anchor the M-site coordinating His ligands are unlikely to generate sufficient perturbation. For example in recent unpublished work, we perturbed the H242-Q272 H-bond via a Q272E

mutation and detected a mere 4 cm-1 downshift. A substrate-induced interaction of the CO distal O with a positive dipole as documented by Spiro and coworkers[113] for heme carbonyls could lead to significant downshifted frequencies yet it is hard to see how binding of either Ac-YVG or ascorbate could increase the positive charge in the vicinity of the bound CO since both carry a negative charge at the pH of our experiments. Indeed the salt-bridge formed between the peptide carboxylate and R240 would remove a source of positive charge (protonated guanidinium) that could potentially interact with a coordinated CO. We are therefore left with the final possibility that a conformational change leads to formation of a semi-bridging CO complex where the CO can interact with a second metal ion. It is worth noting that for the M314H Cu(I)-CO the measured v(CO) of 2051 cm^{-1} is one of the lowest frequencies ever observed for a $Cu(His)_3$ ligand set (Table 3-S3), and is in the range observed for the CO complexes of hemocyanins 2063 - 2043 cm^{-1} which have the same His_3 coordination[51] and where the interaction of the O atom of the CO ligand with the positive charge of the second Cu(I) was deemed the most likely origin of the lowered frequency.

Red-shifted IR frequencies are also observed in the CuB-CO complexes of cytochrome-c-oxidase[55,114] between 2060 and 2036 cm^{-1}. Like the hemocycanin case, Cu(I)-CO frequencies at or below 2050 cm^{-1} appear to correlate with the presence of a second positively charged metal ion in the vicinity of the CO binding site. In the case of cytochrome oxidase, the Cu(I)-CO species are formed by photodissociation of the CO ligand from the ferrous heme-a_3 with subsequent rebinding to copper. Recent x-ray crystallographic studies[115] have captured an x-ray photodissociated state in the crystal where the CO binds side-on to Cu(I) with Cu-C and Cu-O distances of 2.5 and 2.3 Å respectively. While it is not known whether this state is representative of the photodissociated CuB-CO complexes detected by IR, it is indicative of a plurality of CO binding motifs that are accessible in dinuclear metal environments. In the substrate-induced PHM CuM-CO complex we may cautiously infer that interaction of the O atom with the positive charge of a second copper atom is an attractive interpretation of the red-shift

which would imply that activation is the result of an open to closed conformational transition.

Our data provides experimental context for recent computational work which has documented the energetic feasibility of the open to closed conformational transition in catalysis. The new theoretical computations that consider the closed conformer as the active species have suggested a binuclear intermediate which significantly lowers the calculated activation energy for HAA from the peptide substrate[72]. The new modeling shows that hydrogen atom abstraction by a cupric superoxo from the reductant ascorbate is always more favorable than from the peptide Cα-H implying that in the presence of excess ascorbate, any cupric superoxo that forms will always rapidly form a cupric hydroperoxo and the ascorbyl radical. The study suggests that the Cu(II)M hydroperoxo species (formed only in the presence of ascorbate) drives the conversion of open to closed conformer which are separated by only 2 kcal mol-1 and forms a μ-oxo-, μ-hydroxo- mixed-valence Cu(I)-Cu(II) entity as the active intermediate. While experimental data is yet to support such an intermediate, there is clearly sufficient evidence to warrant re-examination of the canonical mechanism. The extremely small amount of EPR detectable Cu(II) observed in our RFQ pre-steady state experiment offers the intriguing possibility that the closed conformer may persist after product formation as a starting point for subsequent catalytic cycles.

An open to closed mechanism is also more consistent with a number of experimental observations that do not fit well to the consensus mechanism. The latter posits that initial attack of O_2 on the reduced CuM center generates an electrophilic Cu(II)-superoxo intermediate capable of H atom abstraction from the peptidylglycine C_α to form a substrate radical. This mechanism fails to explain (i) how substrate binding converts the redox-inactive Cu(I)M site to an active state apparently associated with the 2063 cm^{-1} Cu(I)M-CO species; (ii) the requirement for methionine at position 314 and the inactivity of the M314H variant[50] since Cu(I)His_3 systems are known to be reactive towards O_2 in inorganic model compounds[59]; and (iii) how substrate hydroxylation can be driven by

hydrogen peroxide from the oxidized Cu(II) enzyme (peroxide shunt) in a slow catalytic reaction in which the ^{18}O of labeled peroxide is scrambled 60-70 percent with ambient $^{16}O_2$ in air[66]. However, an open to closed mechanism rationalizes all of these observations and can be discussed in the context of the H108A-citrate structure shown in Figure 3-9. We suggest that peptide and ascorbate together induce the open to closed transition in a rate-limiting step to form the active "binuclear" state. This is reactive to both oxygen in the Cu(I) state and hydrogen peroxide in the Cu(II) state. An interesting feature of the H108-citrate structure is the lengthening of the CuM to M314 Cu-S bond from 2.3 to 5.6 Å. This movement requires a labile fluxional Cu-S interaction which is provided by the Cu(I)-thioether bond as recently demonstrated in our studies of the SMet and SeMet complexes of a PHM CusF model[54,102], but conversely would be frustrated in the M314H variant due to the stronger sigma donor interaction of the Cu(I)-N(H314) bond.

The peroxide shunt chemistry is also easily interpreted within the binuclear formalism. From work published nearly two decades ago[66], we showed that the reaction was catalytic (at least 40 turnovers) and was 100% coupled to peroxide consumption. The conclusion that a mononuclear Cu(II)-peroxo species must be a reactive intermediate, was negated by the observation that 60% of the ^{18}O label was scrambled with ambient $^{16}O_2$ in air when $H_2{}^{18}O_2$ was used as the source of peroxide implying *formation of an intermediate that was in equilibrium with ambient dioxygen at some stage of the catalytic mechanism*. While difficult to rationalize within the context of the "open" PHM conformation, a binuclear intermediate formed within the closed conformer can readily explain the data due to the well-known equilibrium between di-Cu(II)-peroxo and di-Cu(I)-O_2 species.

Our studies show that ascorbate appears to play a dual role in PHM catalysis both as a reductant and as an activator but the stoichiometry and binding site(s) remain obscure. While ascorbate is technically able to supply two electrons, early work on DBM established that it functioned as a 1-electron reductant generating the semidehydroascorbate radical as the primary product which subsequently disproportionation to ascorbate and dehydroascorbate [116]. Thus we anticipate that during

the reductive cycle, ascorbate must bind and its oxidized radical must dissociate twice in order to generate the fully reduced dicopper(I) enzyme. This process appears to have a K_D of around 1.1 mM. On the other hand the activation of catalysis occurs with a lower K_D (117 μM) suggesting a different mode /site of ascorbate interaction with the enzyme. Yet another study reported *inactivation* by ascorbate with a K_D of 5 mM [117] whereas crystallography failed to identify any ascorbate binding site [85]. Interestingly, the ascorbate dependence of the 2063 cm^{-1} CO conformer shows a maximum between 10 and 15 mM ascorbate suggestive of both activation and subsequent inactivation as ascorbate concentrations rise. The data suggest complex activation/inactivation behavior for the ascorbate co-substrate over a concentration range of 0.1 – 10 mM and it is possible that this may relate to physiological regulation of hormone production in the vesicle where the ascorbate levels also span this concentration range [118].

Notwithstanding the growing evidence for the open to closed mechanism, an alternative mechanism for substrate triggering in the open-only formalism may be suggested based on the calculations of Cowley and Solomon, who concluded that the formation of the Cu(II)-superoxide at the M site was energetically favorable only if the dioxygen displaced a hydroxide ligand from the Cu(I) center[46]. While Cu(I)-OH complexes are rare, crystal structures of the reduced enzyme do show water/hydroxide density near the CuM center which appears to be a coordinated solvent species. It is therefore possible that substrate and/or ascorbate binding to the Cu(I) state deprotonates the coordinated water to a hydroxide, which destabilizes the Cu(I)M site and induces reaction with oxygen. However, the fact that the catalytic rate is inversely proportional to pH in the 4-8 pH region is inconsistent with M-site water deprotonation as the driver of substrate triggering. We continue to search for conditions where closed conformers can be formed and studied as potential intermediates.

3.6 Acknowledgements

The work was supported by a grant from the National Institutes of General Medical Sciences (R35 GM136239) to NJB.

Chapter Four: New Structures Reveal Flexible Dynamics between the Subdomains of Peptidylglycine Monooxygenase. Implications for an Open to Closed Mechanism

Overarching Question: *Are there energetically accessible alternate conformers of the enzyme? Can we crystallize a closed form of the enzyme?*

Key Findings: *The Cu-Cu distance (11 Å) is not immutable, a 14 Å Cu-Cu distance can be crystallized in WT and mutant PHM.*

This paper has been published previously in Protein Science[119]. Changes and clarifications will be indicated by double brackets (e.g. [[a clarification]]).

One of the important and testable aspects of the open-closed conformer hypothesis is an energetically accessible alternate conformer. The only alternate conformer of PHM so far crystallized was a citrate-bound, half-apo mutant with sluggish reactivity, hardly strong evidence for a physiologically relevant species.

Our goal was to find the conditions that crystallized a closed conformer of the enzyme. Our hypothesis was since substrate and ascorbate seem to bias the enzyme into a different conformation based on IR experiments, perhaps those same conditions would result in the crystallization of a new conformer.

We attempted to crystallize the enzyme under 2063 cm^{-1} inducing conditions, namely a high concentration of substrate, ascorbate, and carbon monoxide. These conditions did lead to the formation of crystals, but these crystals ultimately did not diffract usefully (data unpublished). It's speculative, but our hypothesis was that attempts to crystallize the enzyme under dynamic conditions were doomed to failure.

Fortunately, other crystallographic conditions did bear fruit. WT PHM crystallized in a microaerobic environment yielded a structure with a 14 Å Cu-Cu distance, providing evidence for the feasibility of interdomain movement and relatively accessible conformational changes.

New Structures Reveal Flexible Dynamics between the Subdomains of Peptidylglycine Monooxygenase. Implications for an Open to Closed Mechanism.

Renee J. Arias[1,3], Evan F. Welch[1,2], and Ninian J. Blackburn[1]*

[1] Department of Chemical Physiology and Biochemistry, Oregon Health and Science University, 3181 SW Sam Jackson Park Road, Portland, OR 97239, USA

[2] Department of Biomedical Engineering, Oregon Health and Science University, 3181 SW Sam Jackson Park Road, Portland, OR 97239, USA

[3] Present address: Materials & Structural Analysis Division, Thermo Fisher Scientific, Hillsboro, OR 97124, USA

* Corresponding author: phone +1 503-936-0166 email: blackbni@ohsu.edu

4.1 Abstract

Peptidylglycine monooxygenase (PHM) is essential for the biosynthesis of many neuroendocrine peptides via a copper-dependent hydroxylation of a glycine-extended pro-peptide. The “canonical” mechanism requires the transfer of two electrons from one mononuclear copper (CuH, H-site) to a second mononuclear copper (CuM, M-site) which is the site of oxygen binding and catalysis. In most crystal structures the copper centers are separated by 11 Å of disordered solvent, but recent work has established that a PHM variant H108A forms a closed conformer in the presence of citrate with a reduced Cu-Cu site separation of ~4 Å. Here we report three new PHM structures where the H and M sites are separated by a longer distance of ~14 Å. Variation in Cu-Cu distance is the result of a rotation of the M subdomain about a hinge point centered on the pro^{199}-leu^{200}-ile^{201} triad which forms the linker between subdomains. The energetic cost of domain dynamics is likely small enough to allow free rotation of the subdomains relative to each other, adding credence to recent suggestions that an open-to-closed transition to form a binuclear oxygen binding intermediate is an essential element of catalysis. This inference would explain many experimental observations that are inconsistent with the current canonical mechanism including substrate-induced oxygen activation and isotope scrambling during the peroxide shunt.

4.2 Introduction

Mononuclear copper monooxygenases constitute a family of metalloenzymes with relevance to the health and energy-related sciences. In the energy-sciences field, lytic polysaccharide monooxygenases (LPMOs) contain a functional mononuclear copper center which catalyzes the chemically challenging oxidation at hexose C1 and/or C4, making them important enzymes in biomass degradation [87]. Likewise, new investigations into the structure and function of particulate methane monooxygenase (pMMO) denote the possibility of a mononuclear copper site as the catalytic center for alkane hydroxylation [88,89]. In the biomedical arena, dopamine β-monooxygenase (DBM) catalyzes a critical step in catecholamine biosynthesis [83], as does its insect homologue tyramine β-monooxygenase (TBM) [120]. Similarly, peptidylglycine α-amidating monooxygenase (PAM) [52,85,121] is a bifunctional enzyme that is the only known enzyme to convert neuropeptide hormones into their active C-terminally amidated forms. Here we focus on new insights into the structure and mechanism of the hydroxylase domain (PHM) of the bifunctional PAM enzyme.

The catalytic core (PHMcc, residues 42-356) of PHM catalyzes the first step in peptide amidation via a copper-dependent hydroxylation of the α-C atom of the glycine-extended pro-peptide C-terminus coupled to the $4e^-$ reduction of O_2 (Figure 4-1(a)). The enzyme is first reduced by 2 electrons to form the di-Cu(I) state where the 2 external electrons are stored on two reduced copper centers denoted the CuH (H-site) and CuM (M-site) that reside in separate sub-domains. Much detail on the structure and catalytic mechanism of this copper monooxygenase has been documented by previous crystallographic [19,26,27,90,92] spectroscopic [42,43,93-95] and kinetic [40,41,44,83,97,122] studies. In the resting state the copper centers of WT PHMcc are mononuclear and separated by 11 Å across a solvent-filled inter-site cleft [19,92]. The M-site has been proposed as the site of initial oxygen binding and the ensuing catalytic chemistry, and is coordinated by H242, H244, and a weak, yet catalytically essential interaction with the thioether of M314 [20,27,67,103]. The two reducing electrons provided to the M-site are hypothesized to be supplied by the H-site (CuH) via sequential long range electron transfer (ET) events. [27,40,46,92,98] The H-

site is ligated by three coordinating His residues: H107, H108, and H172 in an unusual T-shaped geometry [19,92], and mutation of any one of these histidines eliminates >95 percent of catalytic activity [30,41,50,103]. The overall structure of the two subdomains as well as a close-up view of the metal centers and substrate binding site are shown in Figure 4-1 (b) and (c).

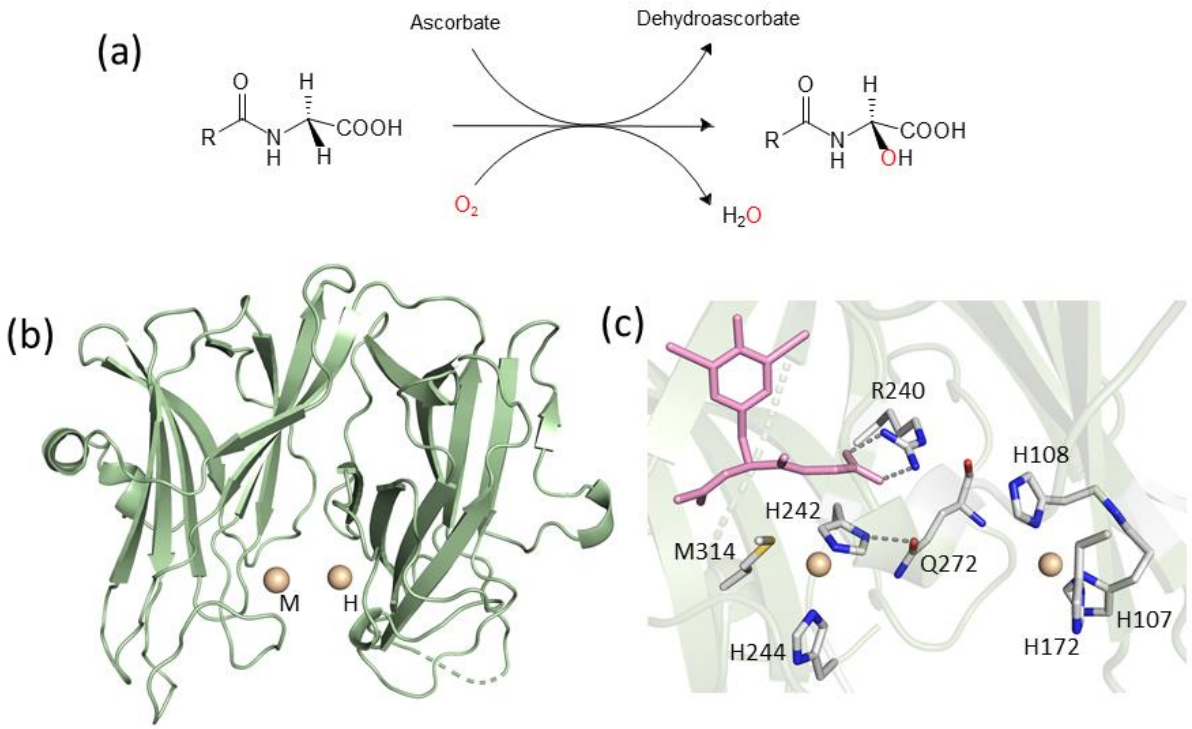

Figure 4-1 Overview of PHM Structure and Function. *(**a**) Reaction catalyzed by peptidylglycine monooxygenase. (**b**) Overall structure of the protein fold showing the two copper centers CuH and CuM. The H subdomain is on the right, the M subdomain on the left. (**c**) Close up view of the interdomain region showing the copper site ligands and the substrate di-iodo-tyrosyl-glycine (pink) bound in the active site pocket predominately via a salt bridge to Arg-240. Structures were rendered using PYMOL 2.3.3 (Schrodinger LLC) from pdb file 3PHM*

The chemical composition of the reactive oxygen intermediate remains an unresolved question of the PHM mechanism. Crystallography has visualized an end-on oxygen species coordinated at the M-site with metrical details consistent with a Cu(II)-superoxo [27]. However, this entity has been deemed a pre-catalytic oxygen complex since its conformation points away from the α-C of the peptidyl substrate. Notwithstanding,

canonical mechanisms supported by theoretical calculations have been built around the existence of a mononuclear and highly electrophilic Cu_M(II)-superoxo species capable of stereospecific hydrogen atom abstraction (HAA) from the nearby pro-S H atom of the peptidyl Cα methylene group to form a substrate radical and a CuM-bound hydroperoxide which proceeds to products via subsequent intra-protein electron transfer [46,94,100]. While elegant, this mechanism fails to incorporate a number of experimental observations [82] which include (i) the extremely low reactivity of Cu(I)M sites towards oxygen in protein-based models [54], (ii) the complete coupling of substrate hydroxylation to oxygen consumption even in the case of variants exhibiting less than 5 percent of native activity [41,50,103], establishing that no leakage of superoxide can occur and (iii) peroxide shunt chemistry initiated from ^{18}O-labeled H_2O_2 and fully oxidized di-Cu(II) enzyme where a distribution of 60 percent ^{16}O in the peptidyl-(OH)glycine product is observed [66]; this observation requires an intermediate species where a Cu(I)-dioxygen and Cu(II)-peroxo-containing species are in equilibrium to allow scrambling of the ^{18}O label with ambient $^{16}O_2$ such as occurs in the dinuclear sites of hemocyanin, catechol oxidases and dinuclear copper-dioxygen model complexes. The canonical mechanism was based primarily on the early crystal structures published by Amzel and coworkers (vide supra) that suggested an invariant Cu-Cu distance of 11 Å. More recent structures from the Amzel laboratory on His to Ala variants at the H center of PHM [26] alongside structures of its sister enzyme DBM by Christensen and coworkers [31] have established that both enzyme catalytic cores are able to undergo conformational changes that allow the two copper centers to approach to within ~4 Å of one another such that oxygen reactivity could proceed at a binuclear center. For all these reasons, we [52] and others [31,72] have suggested alternative mechanisms that posit a conformational transition that allows the H and M subdomains to open and close during the catalytic cycle, and in the process to generate a binuclear copper intermediate. Our ongoing studies are focused on obtaining additional evidence for or against this mechanism.

One of the spectroscopic markers that suggest the intermediacy of a binuclear intermediate is the substrate-induced 30 cm^{-1} downshift in the ν(C≡O) of the carbon

monoxide complex at the CuM center from 2093 to 2063 cm^{-1} [42,50,82]. CO is a surrogate for O_2 binding to CuM, and this red-shift in stretching frequency represents the activation of the bound diatomic due to the back-donation from the filled Cu(I) d-shell into the empty (CO) or partially empty (O_2) π^* orbitals of the bound ligand leading to decrease in bond order. Since catalytic activity is triggered by substrate binding, we have argued that the substrate-induced CO complex may be a structural analogue of the reactive O_2 species such that understanding the origin of the red-shift may provide insights into enzyme activation. We have noted previously [52,82] that this degree of spectral downshift could be the result of binding of CO to the binuclear center as has been documented for hemocyanins [51] and cytochrome oxidase [55,114] where the downshift is the result of either a semi-bridging mode, or the presence of an additional positive charge in the vicinity of the CO molecule. However downshifted frequencies could also be the result of other structural elements which could lead to strong electron donation from endogenous ligands. Indeed, upon inspection of the PHM crystal structure, a strong H-bond (2.8 Å) is observed between the Nδ group of the M-site ligand H242 and the amide oxygen of the sidechain of Q272 (Figure 4-1c). Further, in the presence of substrate, an additional, slightly longer interaction forms between H242 Nδ and the substrate carboxy terminus. These H-bond interactions suggest a protein-mediated deprotonation of the imidazole ring of H242 which is enhanced upon substrate binding and could lead to both O_2 activation and red-shifted CO stretching frequencies.

In the present work we have created two variants Q272E and Q272A that were designed to test the role of H-bonding in oxygen activation. The glutamate variant is expected to enhance the H-bonding while the alanine variant should eliminate it. To our surprise, these variants led to the discovery of a new fully open conformation of the enzyme with increased Cu-Cu separation and here we describe the x-ray crystal structures and metal-site EXAFS spectra of these new forms. In turn, the structures provide valuable new insights into the conformational landscape that determines the separation of the H- and M- subdomains of the enzyme. Our work suggests strongly that the separation between the two sub-domains and hence the two copper centers is continuously variable

such that the conformation adopted by any catalytic state depends on subtle energetic differences in the inter-domain region. We suggest mechanisms based on changes in the inter-domain electrostatics that could facilitate domain closure in the presence of substrate.

4.3 Results and Discussion

4.3.1 The Q272E/A mutations lead to a significant decrease in enzyme activity

The Q272 variants were expressed in hollow fiber bioreactors as the apo proteins and required reconstitution with Cu(II). The Q272E variant appeared to bind copper less tightly than the WT enzyme with average binding stoichiometry of 1.6 coppers per protein (Table 4-1). Specific activity measured under saturating conditions of peptidyl substrate and ascorbate co-substrate was significantly diminished in Q272E as compared to wild-type, giving a values of 0.49 versus 25.7 μmol O_2 / min / mg for the WT PHM, i.e. a 50-fold reduction. While some of this loss in activity could be attributed to the lower copper binding stoichiometry, loss of 0.4 coppers per protein should result in less than 40 percent decrease in activity since at least 60 percent of enzyme molecules contain their full quota of Cu. Substrate dependency of the rate resulted in kinetic parameters given in Table 4-1 with the non-linear regression analysis used to extract kinetic constants given in Figure 4-S1 (Supplementary Material). The data indicate that the reduction in activity is mostly due to the large drop in k_{cat}, with K_m for Ac-Tyr-Val-Gly only modestly higher than the wild-type enzyme.

Table 4-1 Steady state kinetic parameters for Q272E and Q262A. *Steady state kinetic parameters for the Q272E and Q272A variants of peptidylglycine monooxgenase derived from oxygen consumption measurements using an oxygen electrode. K_M and k_{cat} were calculated from fitting the Michaelis-Menton equation $V = V_{max}[S]/(K_m+[S])$ using non-linear regression with $k_{cat} = V_{max}/[E_T]$. Errors are reported as calculated from the regression analysis in Sigmaplot 14. In all cases, the total enzyme concentration E_T was 500 nM. WT values are from reference [123] Copper to protein ratios are the average of three independent measurements on separate enzyme preparations with associated standard deviations as listed.*

Variant	K_m (μM)	k_{cat} (s^{-1})[a]	Cu : PHM
WT	6.3	15	1.95 ± 0.09
Q272E	22 ± 23	0.25 ± 0.04	1.60 ± 0.16
Q272A	407 ± 87	0.53 ± 0.03	1.87 ± 0.26

The copper biding stoichiometry and kinetics of the Q272 to alanine variant were analyzed by identical methodology and gave the k_{cat} and K_m values listed in Table 4-1. The alanine variant bound copper normally with a stoichiometry of 1.9 ± 0.1. However, this variant exhibited lower specific activity (0.1 μmol O2 / min / mg) and strong perturbation in both K_m and k_{cat} (Table 4-1). Substrate binding affinity as estimated by K_m decreased by a factor of 20 although some of this effect may relate to substrate binding for subsequent catalytic cycles being frustrated by slow product release. Additionally, a large decrease in k_{cat} was observed, suggestive of perturbed reactivity of the enzyme-substrate complex similar to the Q272E variant. The almost complete abrogation of activity in the Q272 variants is notable for second sphere mutations of a metalloenzyme and will be discussed in more detail below.

4.3.2 The Q272E mutation yields a fully open PHM structure, with copper distances of 14 Å

As a prelude to structure determination of the variant proteins we explored new crystallization conditions for the wild-type enzyme. Early crystal structures of WT PHM employed crystallization buffers composed of 0.1–0.5 mM $CuSO_4$, 1.0–1.25 mM $NiCl_2$, 100 mM sodium cacodylate pH = 5.5, 3.08 mM NaN_3, and 5% glycerol, which has led to incorporation of Ni and azide ions into some structures [19,92]. In later structures [26,124], PHM was mixed with 20 % PEG 4000 in Tris/$MgCl_2$, buffer with or without citrate. We devised slightly modified conditions adding 1.5 µL of protein at 17 mg/mL in 20 mM sodium phosphate, pH 7.5 to 1.5 µL of mother liquor solution containing 16-18% PEG 20K, 20-250 mM sodium citrate, and 2 mM $CuSO_4$. A number of WT structures in the Cu(II) form were determined and compared with published structures as a control to establish equivalence with earlier work. Typical crystallized forms of PHM are in the P212121 space group with unit cell dimensions: a = 68 Å, b = 68, c = 81; α = β = γ = 90º, while the new conditions yielded crystals in the P1 space group (a = 38 Å, b = 53, c = 86; α = 84º, β = 89, γ = 78). Otherwise, excellent agreement with previously determined structures was obtained. Figure 4-S2 (Supplementary Material) shows the alignment of a WT structure using new crystallization conditions with that of oxidized PHM (1PHM) crystallized using the old conditions. It can be seen that the structures overlay well with RMSD value of 0.164. Five other WT structures under the new crystallization conditions also agree well with 1PHM, with RMSD values of 0.226, 0.191, 0.187, 0.186, 0.213 (data not shown). The new crystallization conditions do not perturb the overall structure, or the Cu-Cu distance.

The overall structure of the Q272E variant in its oxidized form as a space filling model is compared with other published PHM structures in Figure 4-2. The most striking difference between this structure and oxidized WT PHM (pdb 1PHM) is the increase in Cu-Cu distance from 11 to 14 Å. This is significant in the context of recently reported structures for the H108A variant crystallized in the presence of citrate where a “closed” conformer was observed with estimated CuH to CuM distance of ~4 Å [26]. Here a single Cu(II) ion bridged between H and M-site ligands bringing the H-and M domains into a closer juxtaposition. The structural change involved a rotation or hinge motion about residues

200 and 201 effectively allowing the complete M-domain to rotate inwards towards the H-domain. This hinge is constructed by the Pro199-Leu200-Ile201 triad which constitutes the interdomain linker and first two residues of the M-subdomain. The proline residue functions to give the linker direction, such that it forces the two subdomains to lie parallel to each other while the Leu and Ile residues permit rotation of the M subdomain relative to the H-domain allowing the observed hinge motion to occur. In the Q272E variant the increase in Cu-Cu distance to 14 Å represents a rotation about the same hinge point in the opposite direction so as to force the two domains apart. These inter domain movements are closely similar to those reported for individual molecules within the unit cell of DBM where one molecule exhibits the fully open structure (Cu-Cu $\cong$ 14 Å) while the other molecule exhibits the fully closed structure (Cu-Cu $\cong$ 4). Figure 4-3 (a - c) compares the three structures of PHM with CuH – CuM distances of 4, 11, and 14 respectively, while Figure 4-3 illustrates the rotation of the M domain about the residue 201 hinge. Key metrical details are compared in Table 4-2.

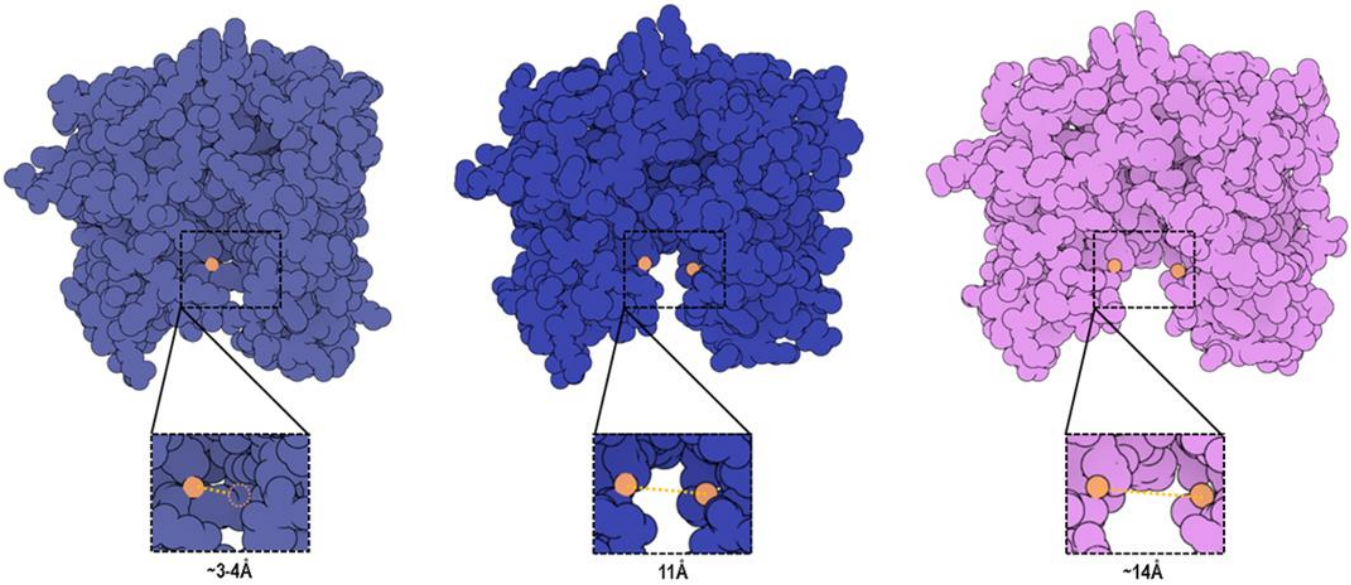

Figure 4-2 Comparison of space filling models. *Space-filling models of the Q272E PHM variant (right, pink) compared with other PHM structures: middle (dark blue) WT oxidized PHM with Cu-Cu ~11 Å from pdb file 1 PHM and left (slate), closed structure of the H108A variant crystallized in the presence of citrate where a single Cu is coordinated by ligands from both the M and H sites (see text). An estimated distance between the canonical M and H sites in this structure is ~ 4 Å.*

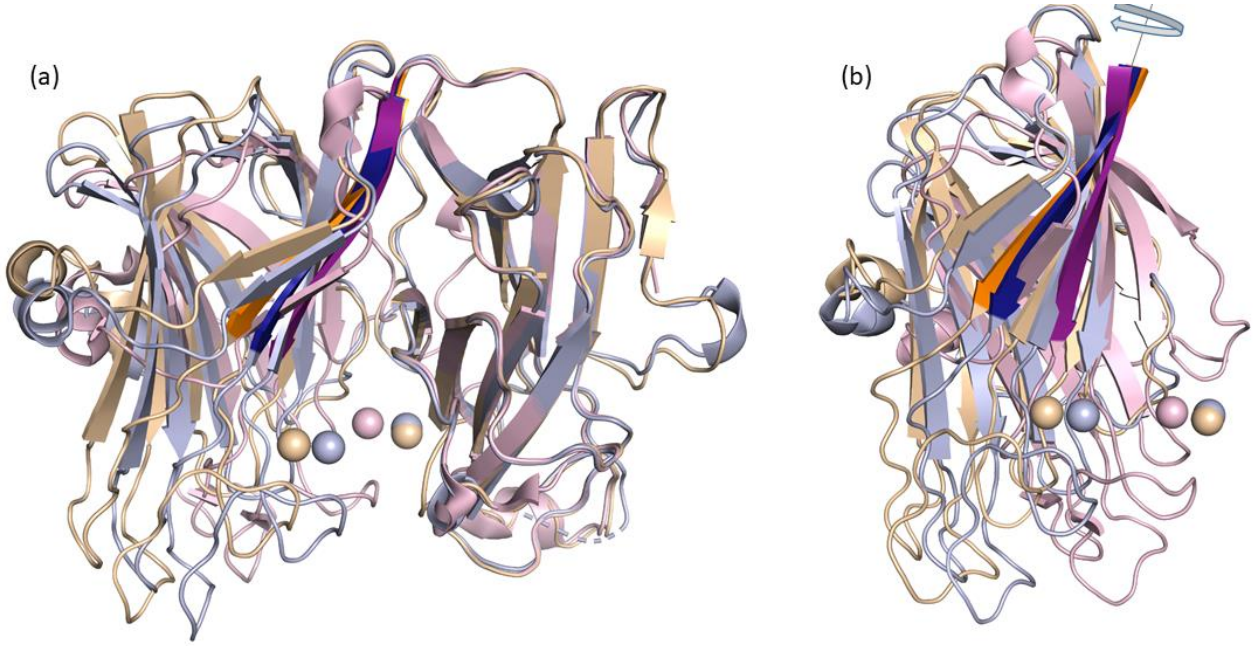

Figure 4-3 Alignment of WT PHM and two mutants. *Alignment of the fully open Q272E structure with the partially open structure of oxidized PHM (PDB file 1PHM) and closed structure of H108A in the presence of citrate (PDB file 6ALA). Structures were compared by aligning the H subdomains of all three structures with rmsd values as listed in Table 4-2. Q272A is depicted in wheat, oxidized PHM in slate-blue and H108A in pink. The positions of the copper centers are shown without their ligands for clarity, and are color-coded for their respective protein chains. (b) A rotated view of the M domain illustrating the rotation of the sub-domains about a hinge point centered on residue Ile201. The first β-strand of each structure in the M subdomain is highlighted to emphasize the rotatory motion: Q272E orange, oxidized PHM dark blue, H108A purple. Structures were aligned and rendered in PYMOL 2.3.3.*

Table 4-2. Structural parameters and metrical details of the Q272E and Q272A variants compared with PHM structures in closed, partially open and fully open conformers. *WT-11, WT-4 and WT-14 refer to structures with Cu-Cu distances of 11, 4 and 14 Å respectively*

		WT - 11	WT - 4	WT - 14	Q272E	Q272A
Cu - Cu		11.3	N/A	13.8	13.9	14.5
M Domain	RMSD	0.00	0.39	0.35	0.30	0.34
	Cu-N_{ε}(H242)	1.9	2.3	2.0	2.0	2.1
	Cu-N_{ε}(H244)	2.1	2.2	2.1	2.0	2.0
	Cu-S(M314)	2.4	5.6	2.3	2.3	2.3
	Cu-$N_{\eta 1}$(R240)	7.5	7.1	8.1	8.8	7.3
	Cu-$N_{\eta 2}$(R240)	7.8	7.8	8.8	8.8	8.5
	H242-Q272X	2.8	2.6	2.4	2.9	N/A
	Q272X-R240	3.5	3.2	4.3	4.5	N/A
H Domain	RMSD	0.00	0.32	0.48	0.42	0.49
	Cu-N_{δ}(H107)	1.9	(2.2)	2.1	2.1	2.0
	Cu-N_{δ}(H108)	1.9	N/A	2.0	2.0	2.1
	Cu-N_{ε}(H172)	2.3	5.0	2.0	2.0	2.1
PDB entry		1PHM	6ALA	8DSJ	8DSL	8DSN

4.3.3 Structure of the Q272A variant

The Q272A variant crystallized in the same space group with similar unit cell dimensions. The overall structure resembled that of Q272E with the H and M domains in the "fully open" conformation with Cu-Cu ≅ 14 Å. Some differences in the orientation of residues in the interdomain region were observed as the result of loss of the H-bond between Q272 and H242, and these are discussed in more detail below.

4.3.4 A new structure for WT PHM in the fully open (Cu-Cu = 14 Å) form

As part of efforts to determine structures for fully reduced PHM and its substrate-bound forms, we initiated crystallization trials in our Coy anaerobic chamber with oxygen levels at or below 30 ppm. The oxidized enzyme produced blue crystals which diffracted to 2.8 Å. Although of lower resolution, a structure was obtained that provided excellent definition of the position of the H and M subdomains and the positions of the two Cu(II) atoms. This structure is shown in Figure 4-S3 (Supplementary Material) and compared with that of Q272E. This new WT structure overlays well (RMSD = 0.3 $Å^2$) with Q272E with CuH to CuM distance of 13.8 Å.

4.3.5 Comparison of metal centers and important interdomain residues.

We carried out an alignment of the H- and M-subdomains of the published WT PHM structure (Cu-Cu = 11 Å) with its counterpart in each of the new structures with RMSD values listed in Table 4-2. This analysis shows that the conformation of the sub-domains does not change significantly between structures. Rather it is the rotation of the M domain with respect to the H-domain that determines the Cu-Cu separation. To assess differences in metal site structure between the variant and WT enzyme we then carried out an alignment of both the H and M sub-domains of the variant and WT PHM (Cu-Cu 11 Å) and compared the position of the copper atoms and their ligands in these individually aligned sub domains. Finally we repeated the alignment of the complete two-domain variants with WT PHM (Cu-Cu = 14 Å) since here the both H and M subdomains of the PHM 14 Å structure overlay on those of the variants. The results of this analysis are shown in

Figure 4-4 (Q272E) and Figure 4-5 (Q272A) with important metrical and alignment RMSD values listed in Table 4-2.

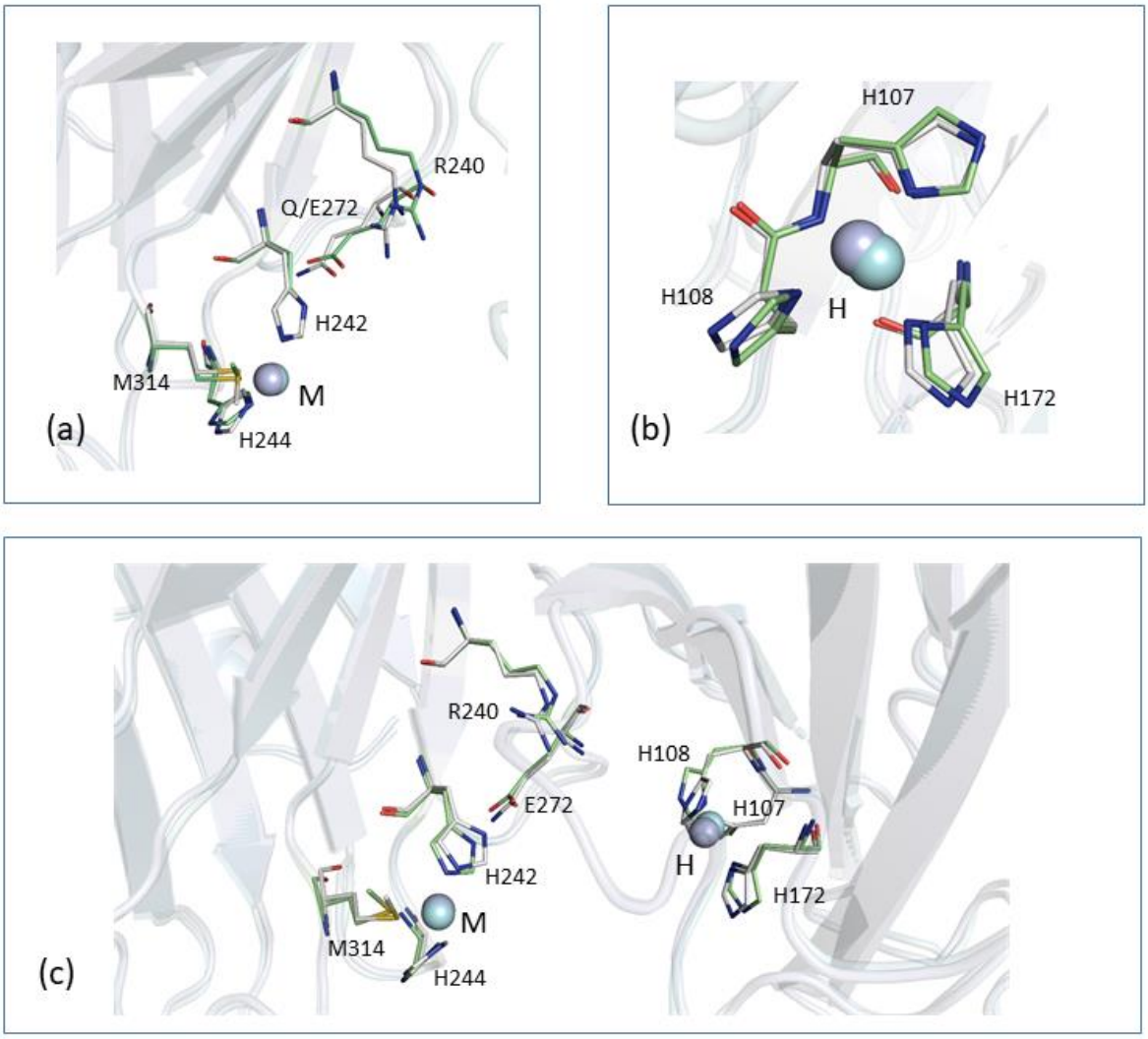

Figure 4-4 Q272E CuM site compared to WT. *(a) Comparison of the CuM centers of the Q272E variant with those of the partially open WT structure (pdb 1PHM), with Cu-Cu ~11 Å generated by aligning the H subdomains of the two structures. (b) Comparison of the CuH centers of the Q272E variant with those of the partially open WT structure (pdb 1PHM)with Cu-Cu ~11 Å generated by aligning the M subdomains of the two structures. (c) Comparison of CuH and CuM sites and the associated interactions in the intermetal cleft of Q272E and the WT anaerobic PHM structures generated by whole molecule alignment. Q272E structures are plotted with C atoms in green and Cu centers in light blue, WT structures with C atoms in white and Cu centers in grey. Structures were aligned and rendered in PYMOL 2.3.3. Metrical and other details are listed in Table 4-2.*

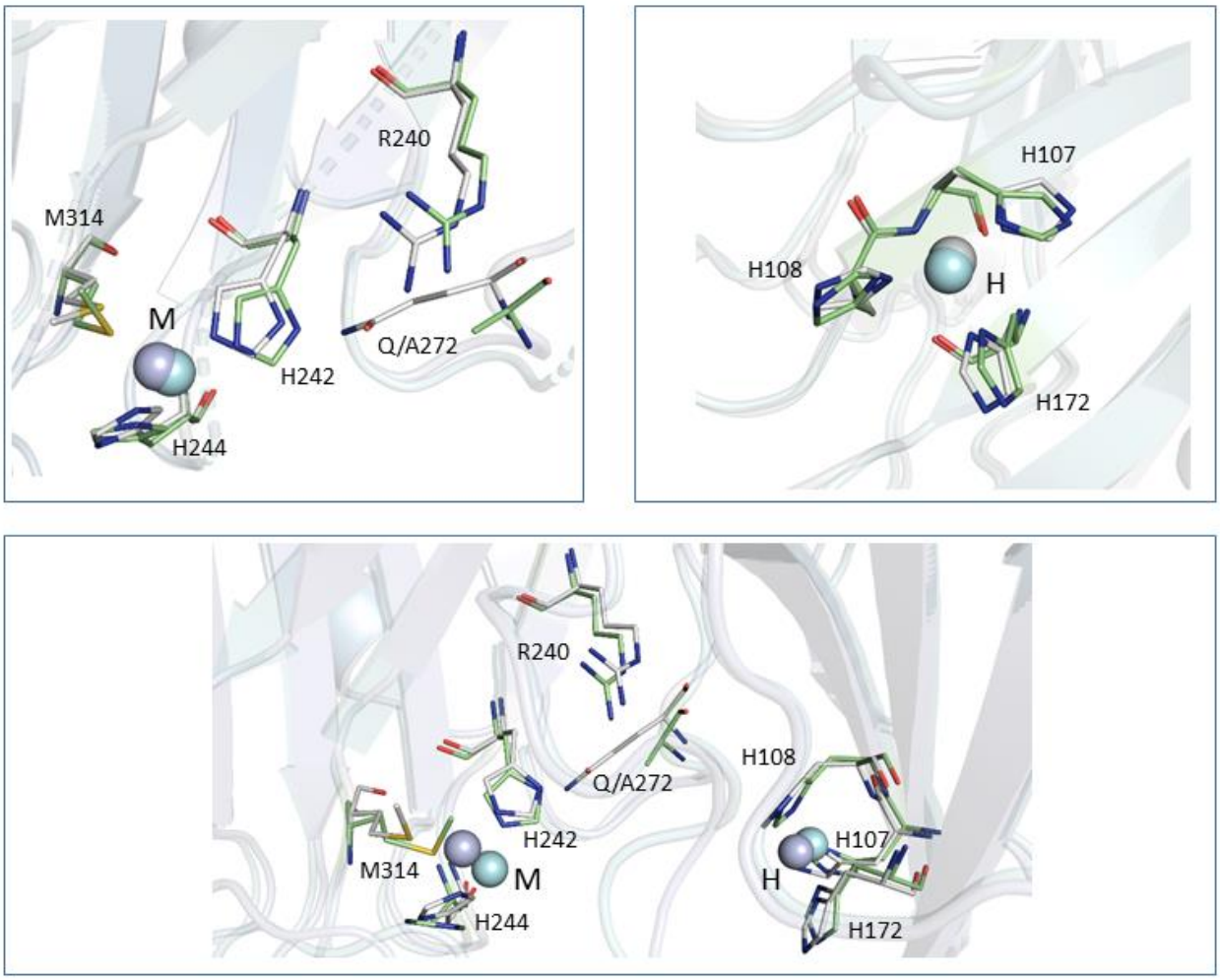

Figure 4-5 Q272A CuM site compared to WT. *(a) Comparison of the CuM centers of the Q272A variant with those of the partially open WT structure (pdb 1PHM), with Cu-Cu ~11 Å generated by aligning the H subdomains of the two structures. (b) Comparison of the CuH centers of the Q272A variant with those of the partially open WT structure (pdb 1PHM)with Cu-Cu ~11 Å generated by aligning the M subdomains of the two structures. (c) Comparison of CuH and CuM sites and the associated interactions in the intermetal cleft of Q272A and the WT anaerobic PHM structures generated by whole molecule alignment. Q272A structures are plotted with C atoms in green and Cu centers in light blue, WT structures with C atoms in white and Cu centers in grey. Structures were aligned and rendered in PYMOL 2.3.3. Metrical and other details are listed in Table 4-2.*

The overall fold of both H and M subdomains is remarkably constant and appears independent of the Cu-Cu distance. Likewise, the individual metal centers only show minor differences in conformation. For the Q272E variant the M site overlays well with the only discernable difference being a different rotameric form of the methionine methyl group. Likewise the H site appears unchanged, although the refined position of the copper center has moved by ~0.3 Å. Metal ligand distances also remain essentially unchanged (Table 4-2). Of note, the substitution of glutamate for glutamine has strengthened the H-bond between the amide O of residue 272 and the distal Nδ of CuM ligand H242 from 2.8 to 2.5 Å. Concomitant with this movement, R240 (a substrate binding residue) has moved away from the vicinity of the M site such that the Cu-N1(guanidinium) distance has increased from 7.5 to 8.8 Å. This 1.3 Å shift would distance the substrate from the M center such that H-atom tunneling during the putative H atom abstraction step would be frustrated [46,97]. We speculate that such a misalignment of the substrate with the active oxygen species due to repositioning of the peptidyl C-terminal to R240 salt bridge might be one factor in the loss of activity in the Q272E variant.

The Q272A structure, even at lower resolution, provides similar inferences. Both sub-domains align individually with their counterparts in all of the other structures as do the values of the metal ligand distances, and the orientation/conformation of the bound residues. A significant difference relative to the glutamate variant is that lack of the H-bond to H242 leaves the position of the R240 guanidinium group unchanged with respect to the WT Cu-Cu 11 Å structure.

4.3.6 X-ray absorption spectroscopy

We used x-ray absorption spectroscopy to probe the structure of the metal sites in more detail. EXAFS data provide “high-resolution” distance information on both the oxidized and reduced metal sites in solution. [[Therefore, they may be used to]] confirm the structures of the Cu(II) states in solution and extend the metallosite structure determination to the fully reduced Cu(I) forms which are not available from crystallography. Figure 4-6 compares absorption edges of the oxidized and ascorbate-reduced forms of the mutants with corresponding data for the WT enzyme. For the

oxidized proteins the absorption edges are superimposable (green and red traces) while for the reduced proteins, some differences are observed (blue and pink traces). The reduced proteins both show the expected 8983 eV peak on the rising edge assigned to a 1s → 4p transition which is diagnostic for coordination number and site symmetry. The intensity of this peak is consistent with overall average 3-coordination at CuH and CuM, but the increase observed in the variants suggests structural perturbation towards a lower average coordination number and/or a shift towards planar geometry. EXAFS data and simulations are shown in Figure 4-7. As expected from the identical edge spectra, the Cu(II) sites of Q272E simulate to an average coordination similar to that of the WT enzyme, 2.5 His residues and 1.5 O scatterers (solvent) at 1.95 Å with similar Debye-Waller and multiple scattering parameters to those published previously for WT. Reduced Q272E simulated to 2 His scatterers at 1.91 Å and 0.5 S(Met) at 2.22 Å. As previously documented for both WT and protein-based models [54,102], the Debye-Waller term for the Cu-S(Met) shell is large ($2\sigma^2$ = 0.018 $Å^2$), a feature that we have attributed (on the basis of model studies) to the weak and fluxional nature of a single Cu(I)-methionine bond. For the Ala variant, the oxidized protein exhibits very similar coordination and metrical parameters. The reduced protein however shows some significant differences that are broadly consistent with the absorption edge data. The Cu-S(Met) distance has shortened to 2.15 Å, suggestive of 2 coordination at the M center due to loss of a His ligand, and consistent with increased intensity of the 1s to 4p edge transition. The significance of these changes to the catalytic rate of the Q272A variant are presently obscure.

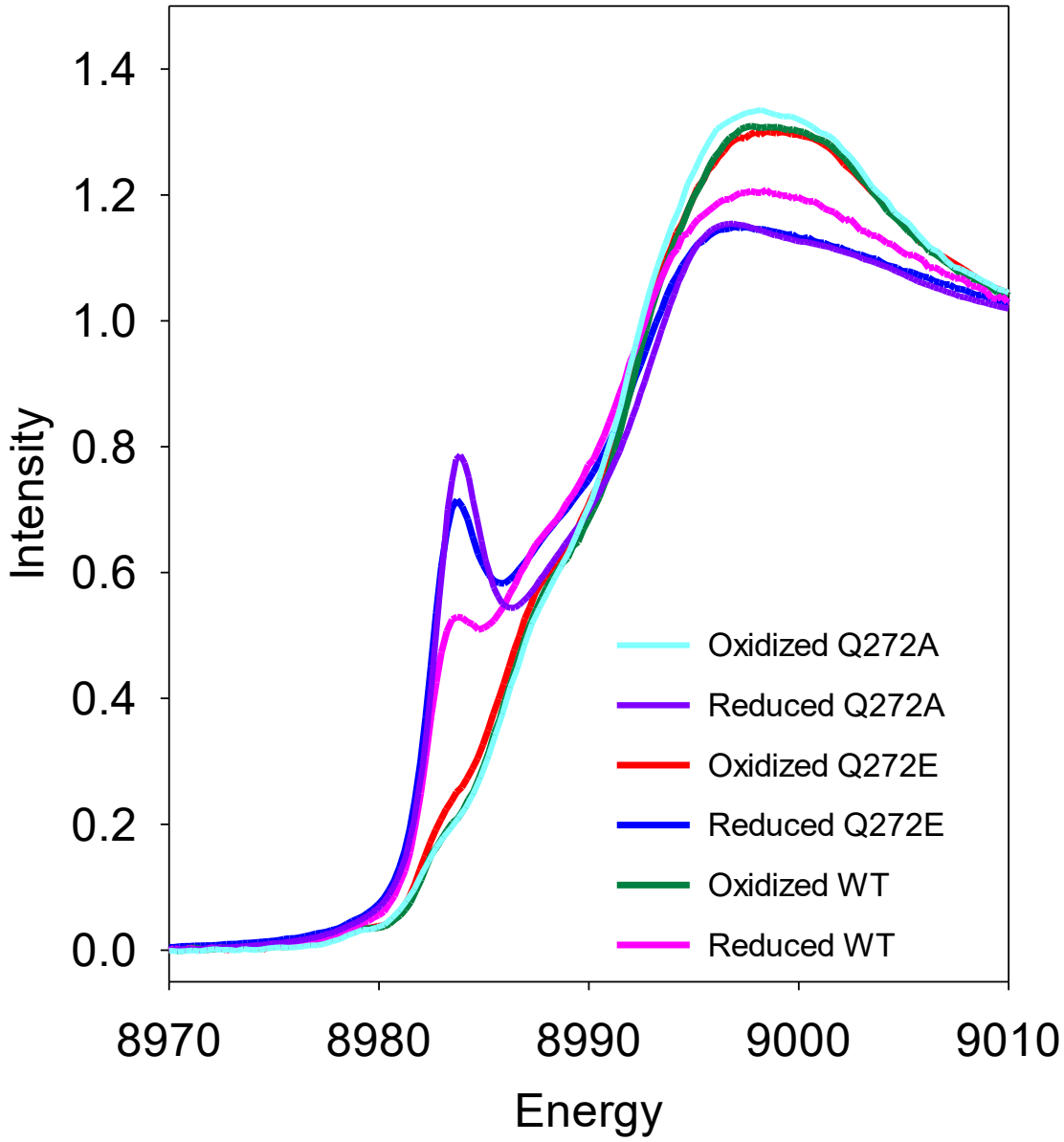

Figure 4-6 X-ray absorption edges of the Q272 variants compared with those of the WT protein. *Note that given the crystallographic evidence for multiple conformers with variable Cu-Cu distances, the conformational state in solution is not known.*

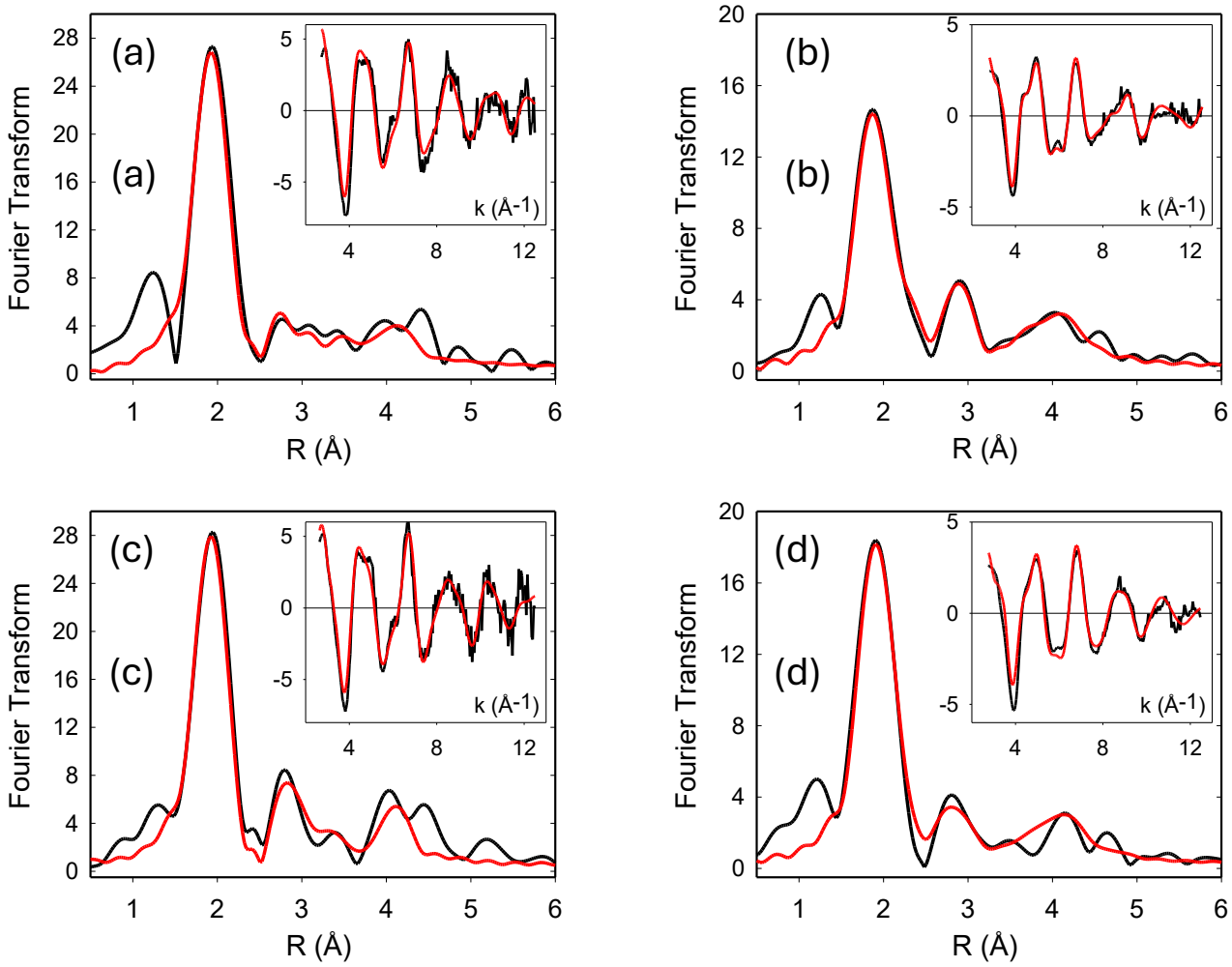

Figure 4-7 Fourier transforms and EXAFS (insets) for Q272E and Q272A variants. *Experimental spectra are in black and simulated spectra in red. Metrical details are described in the text and listed in Table 4-S2 of the Supporting Information. (a) oxidized Q272E (b) reduced Q272E (c) oxidized Q272A (d) reduced Q272A. Note that given the crystallographic evidence for multiple conformers with variable Cu-Cu distances, the conformational state in solution is not known.*

4.3.7 Implications for behavior in solution

Our new structures have documented the existence of the fully open conformer in both mutant and WT proteins. When combined with the earlier documentation of partially open and closed structures described above, a picture emerges where the two sub-domains appear free to adopt multiple conformations that differ by the extent of rotation about the residue 201 hinge (Fig 4-3). Indeed, the structural differences appear to be

restricted to variations in the extent of hinge rotation as each of the two H and M subdomains align well with one another in all of the structures and few differences in metal site coordination were detected by either crystallography or EXAFS. The discovery of the fully open structure in the anaerobic WT enzyme abrogates the premise that the fully open conformers are the result of the mutation. An interesting question then arises when we consider what conformation is likely adopted in solution. A low energy barrier to the hinge rotation would allow the enzyme to cycle between open and closed conformers which is a requisite of any mechanism that postulates a binuclear intermediate (vide supra).

Wu et al have calculated an energy difference between open and closed DBM structures of 2 kcal per mol[72] which is small enough that the conformation adopted in solution could depend on small energetic perturbations in the inter-domain region. Figure 4-8 shows a possible mechanism involving a binuclear intermediate. Central to this mechanism is the concept that the open state accommodates product release and ascorbate reduction both of which occur in the oxidized di-Cu(II) form. Substrate-binding, and oxygen binding/activation on the other hand occur in the fully reduced di-Cu(I) form. Therefore we envisage binding of substrate to a reduced form of the enzyme to be the trigger for the open to closed transition. The resting oxidized enzyme carries a net positive charge in the inter-domain region of +5, with 2 positive charges from each Cu(II) and 1 positive charge from the protonated guanidinium group of R240. We propose that the high positive charge leads to inter-domain repulsion, forcing the two sub-domains apart via the L200-I201 hinge rotation. While reduction alone is probably insufficient to cause domain closure (structures of the reduced enzyme exist in the partially open conformer), reduction coupled to substrate binding at R240 would reduce the net positive charge by 3 which may be sufficient to induce the transition. We have also recently reported that ascorbate activates the enzyme via a binding event with a K_D of 100 μM that is additional to its role as a metal-site reductant [82]. This functionality appears to coincide with the formation of the substrate-induced red-shifted CuM-CO species that we believe is a surrogate for the active oxygen species, and may represent a semi-bridging carbonyl. Mono-anionic ascorbate

binding would decrease further the inter-domain positive charge facilitating domain closure. We propose that changes in electrostatic repulsion in the inter-domain region induced by substrate binding coupled to reduction of the copper centers is sufficient to allow the enzyme to toggle between open and closed states.

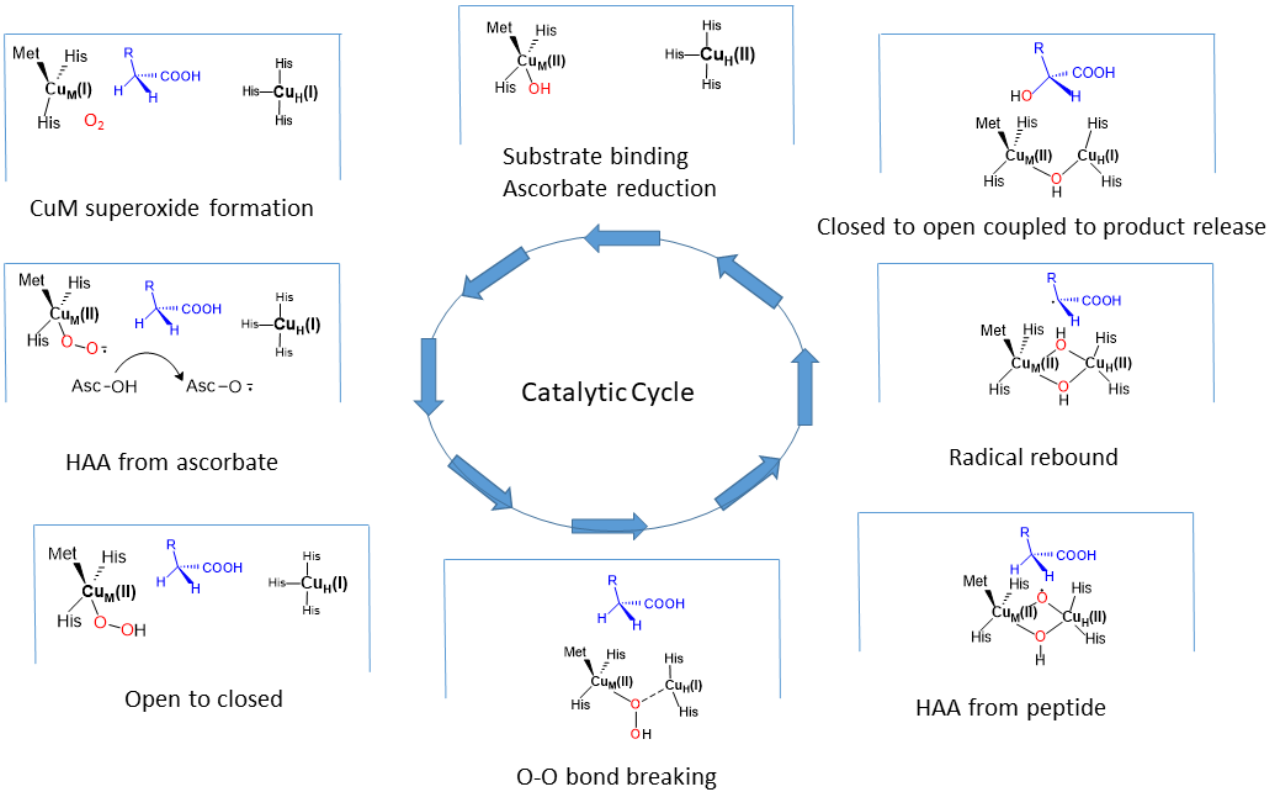

Figure 4-8 Alternate open to closed mechanism. *Open to closed mechanism adapted from that proposed from QMMM calculations Wu et al. 2019*[72].

These ideas are supported by the kinetic constants of the Q272E and Q272A variants. Both variants show a fully open structure in their Cu(II) forms which are likely the states in which product is released. We speculate that perturbation of the H242-Q272 H-bond may lead to two quite different effects. When the H-bond is strengthened as in the Q272E variant, the open conformer may be stabilized relative to its closed counterpart, and the catalytically essential open to closed transition inhibited. In this scenario, product

release which requires the open conformer would proceed essentially as normal leaving the K_m largely unperturbed, but the catalytic activity which requires accessibility of the closed conformer would be frustrated. When the H-bond is eliminated as in the Q272A variant we speculate that now it is the closed conformer that is stabilized in the reduced form. Here product release would be impaired as this process requires the transition to the open state. In this scenario we anticipate large effects on both K_m and k_{cat} as is indeed observed experimentally.

4.4 Conclusions

We have reported three new PHM structures where the H and M copper centers are separated by a longer distance of ~14 Å. The increase in Cu-Cu distance is the result of a rotation of the M subdomain away from the H subdomain about a hinge point centered on Ile201. Otherwise the fold and conformation of the individual subdomains remain unchanged and overlay on each other with small RMSD values of ~ 0.4 $Å^2$. Comparison of these new structures with published data on both PHM and DBM leads to important insights into the dynamics of the PHM and DBM molecular systems, strongly suggesting that while the individual sub domains (and their associated copper sites) are invariant, the inter-subdomain dynamics are flexible such that the M subdomain can adopt multiple positions relative to the H subdomain via simple rotation about the residue 201 hinge. The energetic cost of domain rotation appears to be small, potentially allowing a continuum of domain-domain rotamers, and Cu-Cu distances. Therefore, small perturbations in electrostatic interactions that occur as the result of catalytic cycling are likely more than sufficient to induce open-to-closed transitions. We speculate that the decrease in overall inter-domain positive charge due to Cu(II) reduction coupled to substrate binding could be the trigger that induces a transition between an open mononuclear Cu(II) environment and a closed binuclear Cu(I) environment. This inference would explain most of the experimental observations that are inconsistent with the current canonical mechanism including substrate triggering, substrate-induced diatomic (CO) activation, and isotope scrambling during the peroxide shunt (vide supra). The Q272 variants represent new

derivatives that may lead to clarity on these mechanistic issues, and our future efforts will be directed towards their further biochemical and spectroscopic characterization.

4.5 Materials and Methods:

4.5.1 Chemicals

Buffer components and ascorbate were purchased from Sigma-Aldrich with purities of >99%.

4.5.2 Cell production and protein purification (PHMcc and mutants):

Mutant proteins were prepared by standard protocols as described previously [103]. Briefly PHM variants Q272E and Q272A were introduced into the pBS.ΔProPHM382s vector (obtained from Betty A. Eipper and Richard E. Mains) using Splicing by Overlap Extension (SOEing) [20,125,126]. Sequence analysis was performed on mutant clones, and Qiagen midi prep was used to ensure 20 ug/ 20 uL of recombinant DNA for transfection. Chinese hamster ovary (CHO) DG44 cells were transfected with the recombinant DNA using Lipofectamine 2000 (Invitrogen). The transfected cells were subsequently selected for Dhfr cell lines in α-minimum Eagle's medium containing 10% dialyzed fetal bovine serum, and were utilized to create monoclonal cell lines. PHM proteins were visualized using rabbit antibody 246 [rPAM(116- 13l)] and secondary antibody-anti-rabbit IgG (Sigma). Selected cell lines were then grown using a Hollow Fiber Bioreactor, 5 MWCO (Fibercell Systems, Inc), and protein was purified as previously described [42,43,106].

Protein concentration was determined using $OD_{280}(1\%) = 0.980$ with a Cary 50 spectrophotometer. Protein was reconstituted by addition of 2.5 molar equivalents of copper sulfate by syringe pump over the course of an hour. Excess copper was removed by dialysis in 3 L of pH 7.5 sodium phosphate buffer overnight. Reconstitution was verified using a Perkin-Elmer Optima 2000 DV inductively coupled plasma optical emission spectrometer (ICP-OES) as follows. Protein samples were diluted to ~ 1 μM in 0.1% nitric acid and analyzed by ICPOES using the 325 nm emission line. Standard curves were constructed from copper standard solutions prepared and handled using identical

protocols. Each sample was measured in triplicate. Standard deviations were computed from three independent measurements on different enzyme preparations. After purification, the proteins were stored at -80°C. Copper binding stoichiometry values are listed in Table 4-1.

4.5.3 Kinetic Measurements

Enzymatic activity was measured by monitoring oxygen consumption in a Rank Brother's oxygen electrode at 37° C, as previously reported [103]. Each reaction was performed in a water-jacketed vessel in 2 mL total volume containing 100 mM MES pH 5.5, 200 µL of a 6mg/mL catalase solution (47,000 units per mg), 100 µL of 100 µM Cu(II) solution, 10 µL of 2 M stock ascorbate, and 80 µM Ac-YVG substrate. The reaction was initiated by addition of 10 to 20 µL of enzyme (concentrations varied depending on the activity of the particular variant) through the cap using a Hamilton syringe.

Steady state kinetic measurements were performed as above, varying concentrations of Ac-YVG between 2.5 and 400 µM. For the Q272A variant the range was extended to 8 mM on account of the higher K_m observed for this variant. Kinetic constants were determined by fitting raw rate data to the Michaelis-Menten equation. Specifically, rate data for a number of different substrate concentrations were collected and fitted to the Michaelis Menton equation $V = V_{max}[S]/(K_m+[S])$ using non-linear regression (SigmaPlot 14). Typically single points were collected at each substrate concentration, and the fitting error in K_m and V_{max} was computed from the regression analysis.

4.5.4 Crystallization of PHM Q272E and Q272A

PHM Q272E/A variants were crystallized using the sitting drop vapor diffusion method on Hampton Research Cryschem 24-well plates. 1.5 uL of WT PHM protein at 17 mg/mL in 20 mM sodium phosphate, pH 7.5 was added to 1.5 uL of mother liquor solution containing 16-18% PEG 20K, 20-250 mM sodium citrate, and 2 mM $CuSO_4$. Plates were sealed using transparent Duct™ tape. Crystals formed within one week, and these initial crystals were used to seed succeeding trays using the same crystal conditions. Seeding was performed using a Hampton Research seed bead and Hampton Research seeding

tool. Initial crystals (5-7 crystals) were vortexed with seed beads for 30 seconds in 30 uL mother liquor, and streaked into a new drop using the seeding tool.

4.5.5 Crystallography data collection and analysis

Diffraction data were collected at 12398 eV (1.00 Å) at the Stanford Synchrotron Radiation Lightsource (SSRL) beamline 12-2 equipped with a Dectris Pilatus 6M detector. The data were indexed, integrated, and scaled using XDS and Aimless [127-129]. Molecular replacement was used to obtain phase information, with 1PHM as the model pdb [19]. Structure refinement and modeling was performed using the CCP4-embedded programs REFMAC5 and Coot [127,129,130]. The structures were then rendered for publication in PYMOL [131]. More extensive details of crystallographic analysis together with a Table of data collection and analysis statistics (Table 4-S1) are provided in the SI.

4.5.6 Preparation of samples for X-ray absorption spectroscopy

Samples were concentrated to ~1 mM in copper. An aliquot of ethylene glycol was added to bring the final $Et(OH)_2$ concentration to 20%. Samples were transferred to 1.5 x 15 mm lucite cuvettes fitted with 6 micron capton widows, and flash frozen in liquid nitrogen for storage and transport to the synchrotron. Oxidized samples were handled in air, while reduced samples were prepared and frozen in the Coy anaerobic chamber.

4.5.7 X-ray absorption spectroscopy (XAS) and analysis

XAS data were collected on beam line 9.3 at the Stanford Synchrotron Radiation Lightsource (SSRL) configured for dilute biological XAS. The SPEAR ring operated at 3.0 GeV with a current of 500 mA in continuous top-up mode. Samples were measured as frozen aqueous glasses contained in 1.5 x 15 mm cuvettes with a focused beam size of 0.5 x 5 mm. A Si(220) double crystal monochromator was used in conjunction with an upstream Rd-coated mirror set to a 12 keV energy cutoff to provide monochromatic radiation in the 8.8 – 9.6 x-ray region free from harmonic contamination. The energy of the beam was calibrated by means of a Cu foil placed between the second and third ionization chambers. The XAS spectra were measured in fluorescence mode using a Canberra 100-

element Ge detector combined with a Ni oxide filter and Soller slit assembly to remove elastically scattered photons. Beam size and/or distance between sample and detector were adjusted to keep the total fluorescent counts below 100 kHz. For the oxidized samples, a single scan was collected to avoid photoreduction, while for reduced samples, 6 – 8 scans were averaged to ensure adequate signal-to noise. In addition of the protein samples, 4 scans of a blank containing only buffer were collected and subtracted from the protein spectra to remove residual Ni K_β fluorescence from the NiO filter, and produce a flat baseline in the pre-edge region.

Raw data was processed in EXAFSPAK [132,133]. Detector channels were summed, and resultant scans calibrated and averaged. Individual detector channels were examined and any bad channels removed from the averaged data. Processed raw data was next fitted to a cubic spline function to simulate the atomic falloff, which was subsequently subtracted from the experimental data to isolate the EXAFS and normalized to the intensity of the spine function at 9010 eV. Background-subtracted EXAFS data were converted into k-space with k=0 set to 8985 eV, and weighted by k^3. This k^3-weighted EXAFS data was simulated using the program EXCURVE version 9.2 using full multiple scattering calculations to represent the double and triple-scattering contributions from outer shell atoms of imidazole rings as previously described [43,134-136]. Parameters refined in the fits included coordination numbers, absorber-scatterer distances, Debye-Waller factors for each shell, and E_0 a small correction to the theoretical energy kept constant for all shells. Refinement used least squares minimization to arrive at the best fit combination of these parameters. In all cases alternative fits were explored to ensure that the best fit represented a global rather than a local minimum.

4.6 Acknowledgements

We thank Dr Katherine Rush for assistance in XAS data collection. The work was supported by a grant from the National Institutes of General Medical Sciences (R35 GM136239) to NJB. Use of the Stanford Synchrotron Radiation Lightsource, SLAC National Accelerator Laboratory, is supported by the U.S. Department of Energy (DOE), Office of Science, Office of Basic Energy Sciences under Contract No. DE-AC02-76SF00515. The SSRL Structural Molecular Biology Program is supported by the DOE Office of Biological and Environmental Research, and by the National Institutes of Health, National Institute of General Medical Sciences (P30GM133894).

Chapter Five: Capturing the Binuclear Copper State of Peptidylglycine Monooxygenase Using a Peptidyl-Homocysteine Lure and the Binuclear Copper State of Peptidylglycine Monooxygenase Visualized through a Selenium-Substituted Peptidyl-Homocysteine Complex

Overarching Question: *Can PHM be trapped in a closed conformer using an inhibitor?*

Key Findings: *A homocysteine inhibitor attached to a peptide substrate binds to PHM producing spectroscopic signals that are unambiguously binuclear in origin. One such spectroscopic signal is a mixed-valence, a key intermediate in the open-closed hypothesis.*

These two papers have been published previously in the Journal of American Chemical Society[137] and Dalton Transactions[138] respectively. They are presented together here due to the due to their interrelated and sequential nature.

The inhibition of PHM by peptides with homocysteine groups has been known for decades, but the mechanism of this inhibition was unknown. We reasoned that this inhibition could be due to the formation of a bridged thiol where the sulfur of the homocysteine bridges the two copper centers. Under this hypothesis the peptide-homocysteine (in this case alanine-alanine-phenylalanine-homocysteine, AAF-hCys) binds via the peptide carboxylate, just as native substrate does, and then inhibits via the formation of a thiol bridge supplanting the usual dioxygen binding.

Our experiments produced strong evidence in support of this hypothesis. WT PHM mixed with AAF-hCys inhibitor monitored by UV-Vis produces a large 925 nm^{-1} IVCT band indicative of a mixed valence. This discovery was powerful evidence of the binuclear mechanism, and the Wang open-closed mechanism explicitly includes a bridged mixed valence species.

From this initial discovery we performed a bevy of spectroscopic experiments, both with AAF-hCys peptide inhibitor and with a selenium substituted variant, AAF-hSeCys. These spectroscopic experiments provided clear and unimpeachable evidence of a binuclear, closed conformation of WT enzyme. Additionally, the formation of a mixed valence species lends great credence to the open-closed model which is contingent on a mixed valence.

These experiments therefore represent the most powerful pieces of evidence collected to date for the open-closed model and explicitly confirm several of its tenets.

Capturing the Binuclear Copper State of Peptidylglycine Monooxygenase Using a Peptidyl-Homocysteine Lure

Katherine W. Rush§, Karsten A. S. Eastman†, Evan F. Welch§‡, Vahe Bandarian† and Ninian J. Blackburn§*

§Department of Chemical Physiology and Biochemistry, Oregon Health & Science University, Portland, OR 97239, USA

†Department of Chemistry, University of Utah, Salt Lake City, UT 84112, USA

‡Department of Biomedical Engineering, Oregon Health and Science University, 3181 SW Sam Jackson Park Road, Portland, OR 97239, USA

5.1 Abstract

Peptidylglycine monooxygenase (PHM) is a copper-dependent enzyme that catalyzes C-alpha hydroxylation of glycine extended pro-peptides, a critical post-translational step in peptide hormone processing. The canonical mechanism posits that dioxygen binds at the mononuclear M-center to generate a Cu(II)-superoxo species capable of H-atom abstraction from the peptidyl substrate, followed by long range ET from the CuH center. Recent crystallographic and biochemical data has challenged this mechanism, suggesting instead that an "open-to-closed" transition brings the copper centers closer allowing reactivity within a binuclear intermediate. Here we present the first direct observation of an enzyme-bound binuclear copper species, captured by use of an Ala-Ala-Phe-hCys inhibitor complex. This molecule reacts with the fully reduced enzyme to form a thiolate-bridged binuclear species characterized by EXAFS of the WT and its M314H variant, and with the oxidized enzyme to form a novel mixed valence entity characterized by UV/Vis, and EPR. Mechanistic implications are discussed.

5.2 Introduction, Results and Discussion

Copper monooxygenases play important roles in human health and climate mitigation.[52,83,87,139,140] Peptidylglycine monooxygenase (PHM) catalyzes the post-translational amidation of neuropeptide hormones,[33,85,86] using two copper atoms, CuH and CuM, which are ligated to three histidines (H) and two histidines and a methionine (M). Early structures showed the copper atoms separated by ~ 11 Å across a solvent-filled cleft, and a substrate (di-iodo-YG) bound by its carboxy terminus to residues R240 and Y318 (Figure 5-1 top).[19,92] An oxygen adduct bound to CuM was also captured, but with the O_2 in an unproductive conformation pointing away from the substrate.[27] These structures, together with spectroscopic[42,43,93-95], kinetic[40,41,44,83,97,122] and computational[46,72,94,100,141] contributions led to the current canonical mechanism in which the substrate-bound di-Cu(I) enzyme reacts with dioxygen forming a Cu(II)M-superoxo intermediate which

subsequently abstracts a H atom at the glycyl C-alpha to form the substrate radical. Long-range electron tunneling (ET) completes the catalytic cycle with the electron being supplied either directly from CuH or via a Cu(II)M-oxyl intermediate.

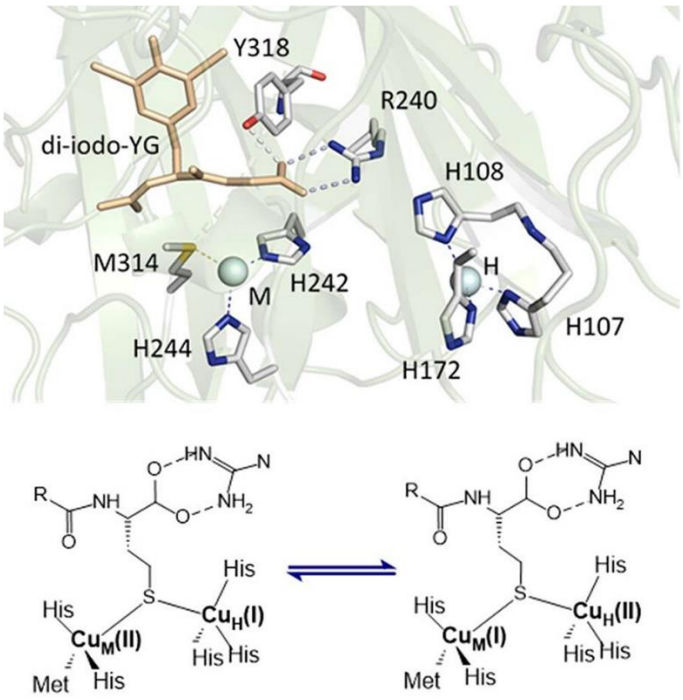

Figure 5-1 Active Site of PHM with bound substrate. *(Top) Active Site Structure of PHM (pdb 3PHM) Showing Positioning of a Dipeptide Substrate Bound via Its Carboxy Terminus to Y318 and R240; (Bottom) Mixed-Valence Formulation of the PHM-Ala-Ala-Phe-hCys Complex*

Recent insights have given cause to reconsider this mechanism.[52] In particular, new crystal structures for PHM[26,119] and its sister enzyme dopamine β-monooxygenase (DBM)[31] show the enzymes in "fully open" (Cu-Cu = 14 Å) and "closed" conformations (Cu-Cu = 4 – 5 Å). The structures suggest flexible dynamics of the two sub-domains allowing the Cu-Cu distance to vary continuously.[119] Reformulation of the mechanism to include a binuclear Cu intermediate as proposed from the DBM structure[31] and from a recent QM/MM study[72] is therefore timely. Here we describe a complex of PHM with a peptide inhibitor complex which establishes the accessibility of a binuclear state.

We reasoned that a substrate analogue bound near CuM (Figure 5-1 bottom) might capture the closed state if it carried a Cu(I)-binding functionality capable of bridging the two coppers. We chose the peptidyl inhibitor Ala-Ala-Phe-homocysteine (AAF-hCys) known to form a strong complex with the enzyme[142] where binding should occur both via the C-terminal carboxylate and via additional coordination of the thiol to copper (Scheme

1). If binding to both coppers is observed, it would show that a conformation exists with the two Cus in a closed complex, allowing a ligand such as O_2 to bridge and do chemistry. AAF-hCys was prepared by solid phase peptide synthesis. The hCys-containing peptide is largely in the thiol form, and exhibits an *m/z* of 425.19, which is within 3.29 ppm of expected (Figure 5-S1).

First, we examined the reaction of AAF-hCys with the fully reduced PHM using EXAFS spectroscopy (Figure 5-2). The intensity of the Cu-S scattering peak in the FT grew significantly relative to the unligated reduced enzyme (Figure 5-S2 and Table 5-S4 fit 1), and required simulation by 1.5 Cu-S at 2.27 Å with a Debye Waller (DW) of 0.006 $Å^2$ (Figure 5-1 (a) and Table 5-S4 fit 2). This result suggests that in addition to the CuM-S(Met314) interaction (0.5 Cu-S per Cu), both coppers now form one additional bond each to the thiolate ligand implying a mono-thiolate bridge. The correlation between coordination number and DW factor introduces uncertainty into the Cu-S shell occupancy, and a reasonable fit could be obtained with 1 Cu-S with a DW of 0.002 $Å^2$ (Table 5-S4 fit 5). However, when the S shell was split into Cu-S(thiolate) and Cu-S(met) components and the measured DW of the Cu-S(Met) shell in the reduced WT enzyme (0.012 $Å^2$, Table 5-S2, fit 1) fixed in the simulation, the Cu-S(thiolate) refined to 1.0 S per Cu with a DW of 0.004 $Å^2$ (Table 5-S4 fit 3). Furthermore, limits can be put on Cu-S(thiolate) DW factors from other studies that have established values >0.010 A^2 for Cu-S(Met) interactions[102,143,144], and values of >0.005 $Å^2$ for Cu-S(thiolate) in mixed histidine/cysteine containing systems.[145] Specifically, the DW factor ($2\sigma^2$) for the homocysteine analogue of azurin[146] (C112hCys) is 0.006 $Å^2$ while that of the bridging thiolates of CuA type sites[143] is >0.009 $Å^2$. Thus, a value of 0.006 $Å^2$ is close to the lower limit expected for mixed His/Met/Cys or hCys coordination providing validation of the bridged thiolate interpretation. Parameters used to construct these fits are listed in Table 5-S2. Additional intensity was found in the Fourier transform of the reduced WT protein in complex with the AAF-hCys inhibitor. This could be simulated by including a contribution from a weak scatterer at ~2.7 - 2.8 Å. Because the scattering is weak its origin is uncertain but it could be fit with N, O, or Cu (Table 5-S5 fits 6, 7 and 8).

While we have low confidence in this result, it is possibly the signature of a Cu-Cu interaction, or alternatively the presence of a second weakly coordinating ligand bridge.

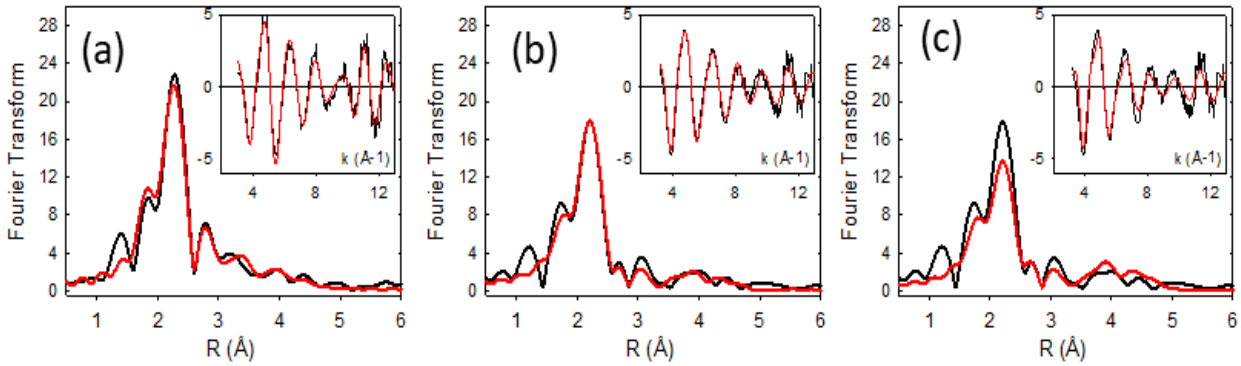

Figure 5-2 Fourier transforms and k3-weighted EXAFS (insets) for the reaction between PHM and AAF-hCys. *Experimental (black) versus simulated (red) spectra for the Cu K edge of (a) the AAF-hCys complex of ascorbate-reduced WT PHM, (b) the AAF-hCys complex of ascorbate-reduced M314H simulated with 1 S per Cu, and (c) the AAF-hCys complex of ascorbate-reduced M314H simulated with 0.5 S per Cu. Metrical details extracted from the simulations are listed in Table 5-S2.*

To remove ambiguities associated with the presence of the M314 sulfur ligand, we carried out an identical reaction with the M314H derivative which lacks the coordinating Met ligand. The ascorbate-reduced protein gave an EXAFS spectrum (Figure 5-2(b)) with the same intense S wave now simulating to 1.0 Cu-S at 2.23 Å with a DW factor (0.006 $Å^2$) similar to the WT protein (Table 5-S2 fit 9). Simulations that restricted the shell occupancy to 0.5 (expected for non-bridging thiolate coordination) were completely inadequate (Figure 5-2(c) and Table 5-S2, fit 10). This result confirms the assignments made for the WT protein and establishes that the thiol must bridge the two Cu atoms in a binuclear configuration.

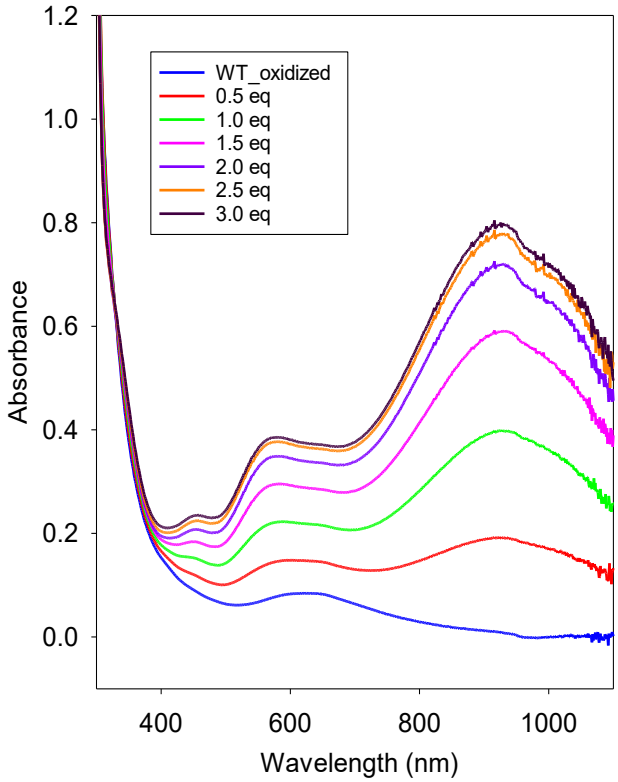

Figure 5-3. Titration of fully oxidized PHM with Ala-Ala-Phe-hCys.

Next we examined the reaction chemistry of AAF-hCys with the fully oxidized PHM. Binding of ~2.5 equivalents elicited a purple species with broad intense absorption at 925 nm (estimated ε = ~1300 M^{-1} cm^{-1}) and weaker bands at 580 and 460 nm (Figure 5-3). The 925 nm feature is characteristic of intervalence charge transfer transitions (IVCT) of a mixed-valence (MV) center such as the valence localized (class II) halide complexes of hemocyanin [147] or the valence delocalized (class III) centers of CuA of cytochrome oxidase and N_2O reductase [148-154] These two classes can be distinguished by their copper hyperfine patterns in the EPR spectra, where class II give rise to 4-line patterns and class III exhibit 7-line patterns, the latter due to additional splittings arising from strong coupling of the electron spin to both copper nuclear spins. EPR spectroscopy (Figure 5-4) of the PHM MV complex confirmed that ~30% of the copper was undetectable while reaction with ascorbate led to an immediate further reduction in intensity to 35% of the original oxidized enzyme with *no loss of color* in the first 3 minutes. These data are consistent with the initial presence of a mixture of MV and an oxidized PHM species in a ~65:35 ratio.

Serendipitously, while the residual oxidized species is rapidly reduced by ascorbate, reduction of the MV species is slow (Figure 5-S3), allowing it to be observed in the EPR of the 3-minute ascorbate-reduced sample with no interference from any residual oxidized PHM species (Figure 5-4 and Figure 5-S4). Simulation using EASYSPIN[155] suggests that the unpaired spin is localized at low temperature since the spectrum shows a 4- rather than 7-line pattern in the parallel region (Figure 5-4 top panel and Figure 5-S4 and Table 5-S4 fit 1). The species remaining after 3-min ascorbate reduction is best described by a 2-component system in a 3:1 ratio, with the major component giving g and A values consistent with a Cu(II)-thiolate species (g_3 = 2.21, A_3 = 389 MHz)[145], and the minor component (g_3 = 2.30, A_3 = 393 MHz) more characteristic of mixed O/N coordination. Inclusion of Cu-Cu nuclear interaction did not improve the simulation (Table 5-S4 fit 2, and Figure 5-S4). The data are consistent with a MV thiolate-bridged binuclear species as shown in Scheme 1 exhibiting localized class II behavior at low temperature. Whereas the UV/vis data suggest that the Cu(II) component of the MV complex is type 1-like with weak S to Cu(II) CT at 460 nm, and stronger S to Cu(II) at 580 nm, the EPR spectra are more typical of a “green” or “red” than a “blue” copper site [145]. These preliminary assignments are supported by EXAFS of the MV species which shows a long Cu-S distance of 2.28 Å (Figure 5-S2, Table 5-S5 fit 11).

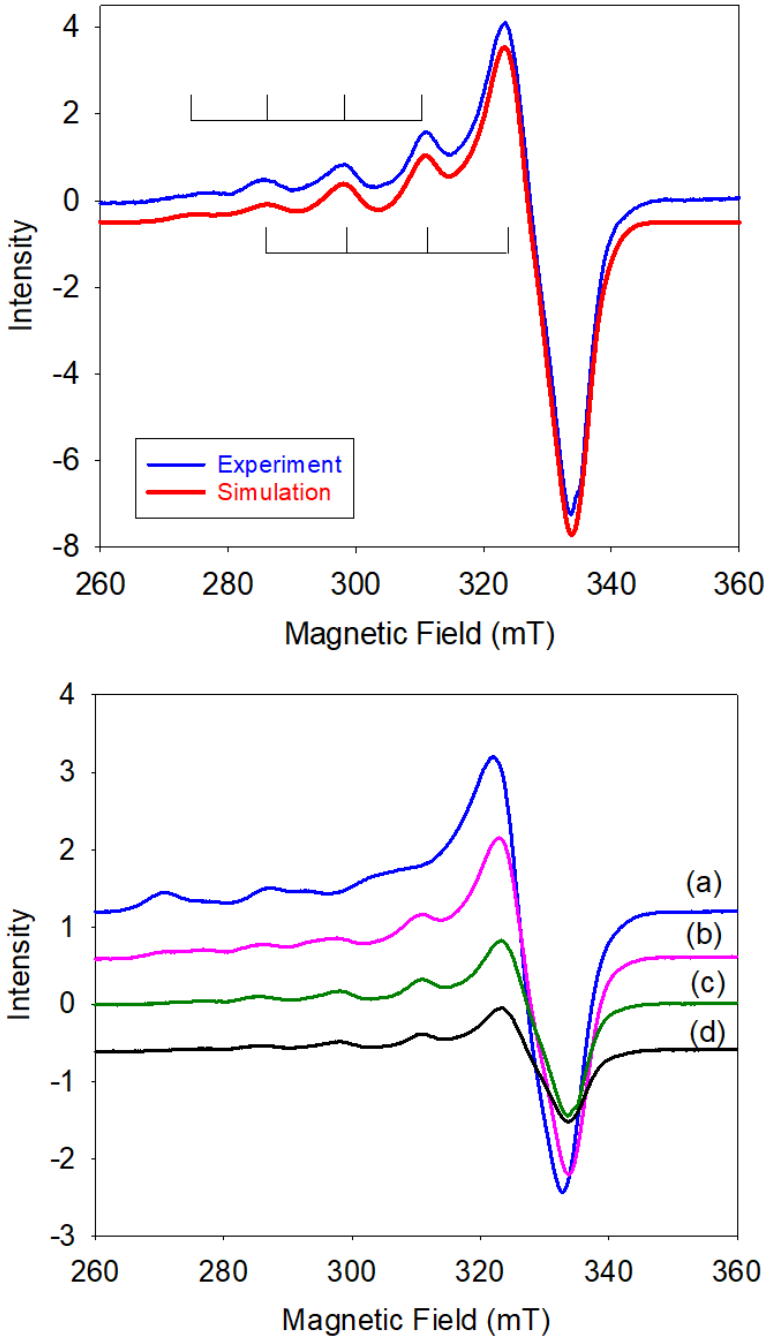

Figure 5-4 EPR spectra of WT PHM titrated with AAF-hCys. *Bottom panel: (a) WT oxidized PHM (blue); (b) WT + 3 equiv of AAF-hCys (pink); (c) 3 min reduction by 5 mM ascorbate (green); and (d) 20 min reduction by 5 mM ascorbate (black). Top panel: Simulation of the 3 min reduced sample using Easyspin. Best fit (fit 1 Table 5-S4) was a two-component system in a 1:0.35 ratio.*

The NIR band observed in the PHM-AAF-hCys complex is typical of an IVCT were one copper is in the Cu(II) state and the other in the Cu(I) state. These IVCTs arise from transitions from a doubly occupied HOMO centered on the Cu(I) center to a singly occupied LUMO centered on the Cu(II) center. Under the Robin-Day classification, class II MV complexes arise from weakly coupled binuclear sites with a thermal barrier to intersite ET, and class III from strongly coupling sites with the coupling energy H_{AB} > the reorganizational energy λ, and a low to non-existent thermal barrier for intersite ET[156]. Both class II and class III systems require a ligand bridge to couple the two metal centers. Examples of class II includes the halide-bridged complexes of half-met hemocyanin[147] while class III includes the CuA site of cytochrome oxidase [149,152,153,157], N_2O reductase[151,158], purple copper azurin[159,160], pMMOD[161] and a bis-thiolato dicopper model.[152,154] Class III complexes exhibit intersite ET rates that are fast on the timescale of electronic transitions, resulting in full delocalization of the unpaired electron over both metal centers. Class II systems on the other hand have slower rates of ET and often show a temperature dependence due to the thermal barrier. We examined the EPR of the MV complex at room temperature but the spectrum was broadened to indetectability presumably due to fast relaxation. Thus we cannot rule out the possibility that the system becomes delocalized at RT similar to the behavior of the macrocyclic MV complex described by Gagne and coworkers[162].

The class II behavior observed for PHM suggests that the bridging thiol provides weak coupling between the H and M centers, insufficient to overcome the reorganizational barrier to bringing the cupric center into a Cu(I)-favorable state, likely arising from the chemical inequivalence of the H and M centers. We note that class III to class II interconversion has been observed due to ligand set perturbation of the CuA center of purple copper azurin [163]. Notwithstanding, the IVCT provides strong confirmatory evidence that the binding of the AAF-hCys peptide induces the closed conformation and, when considered alongside the EXAFS data showing thiolate bridging in the fully reduced state, provides compelling evidence for a binuclear state.

The stability of the MV state as evidenced by its slow reduction is notable. Wang and coworkers have proposed a reaction mechanism for DBM (and by inference PHM[44]) from QM/MM calculations involving a MV binuclear intermediate with lower activation energy for H-atom abstraction than its mononuclear analogue[72] (Figure 5-5). Our current work suggests that reaction chemistry leading to such a species is accessible.

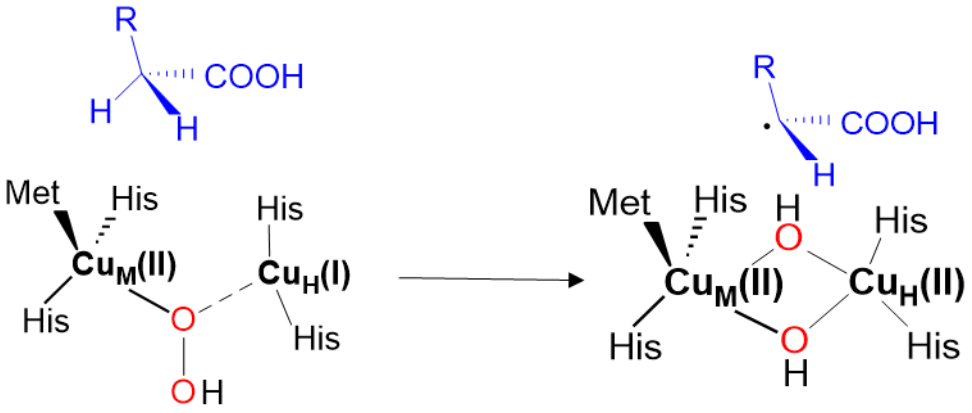

Figure 5-5 Proposed Mixed Valence Intermediate Adapted from Wang 2019[72].

A binuclear mechanism could explain many experimental findings that are inconsistent with the canonical mononuclear mechanism. In addition to structural evidence for sub-domain dynamics[26,31,52,119], the following observations can be cited. First, mononuclear *protein* models of the CuM site in aqueous solution show sluggish reactivity towards O_2[102] despite demonstrated stability of inorganic Cu(II)-superoxo complexes in organic solvents at low temperature;[70,164-174] second, ν(CO) for the CuM-CO complex is red shifted by 30 cm^{-1} in the presence of substrate reminiscent of the semi-bridged carbonyls of bi- or hetero-bimetallic sites[42,50,55,82]; third, substrate binding is always coupled to product hydroxylation establishing a requirement for substrate activation[82]; and fourth, substrate hydroxylation from oxidized enzyme and hydrogen peroxide is viable and catalytic, but leads to approximately 60 percent ambient ^{16}O exchange when $H_2{}^{18}O_2$ is used as the oxygen source[66]. This requires an intermediate where Cu(II)-peroxide can equilibrate with Cu(I)-dioxygen, also suggestive of a binuclear state. Our future efforts will

be directed towards generating binucleating substrate-analogues that bring us closer to illuminating

5.3 Materials and Methods

5.3.1 Protein expression and purification

Wild-type (wt) PHM was expressed and purified as described in previous publications from the Blackburn laboratory[42,82,106]. Briefly, the rat wtPHM gene was expressed in stably transfected CHO cells in an Accusyst bioreactor. Secreted enzyme was precipitated from harvested media using 50% ammonium sulfate and purified via size exclusion and anion exchange chromatography. Purified wtPHM was reconstituted to 2 Cu atoms per monomer by addition of $CuSO_4$ followed by dialysis to remove excess Cu(II). Cu loading of the wtPHM enzyme was determined by comparison of the protein concentration (measured using A_{280} (0.1%) = 0.98) and Cu concentration (determined by ICP-OES). The M314H variant was prepared and characterized using similar methods as described previously[20,50]. Purified M314H was reconstituted to 2 Cus per protein. All experiments in this work were conducted in 20mM Na phosphate pH 7.5 unless otherwise noted.

5.3.2 Solid-phase synthesis, purification, and mass spectrometry characterization of the AAF-hCys peptide.

Ala-Ala-Phe-hCys (AAF-hCys) peptide was synthesized on either a Prelude peptide synthesizer (Protein Technologies Inc.) or a Chorus peptide synthesizer (Protein Technologies Inc.). The synthesis used standard Fmoc procedures from the manufacturer and was carried out on a 0.050 mmol scale. All natural Fmoc-amino acids were purchased from Protein Technologies Inc. Fmoc-hCys(Trt)-OH was purchased from Millipore-Sigma (#8522660001). For the syntheses, 300 mg of 2-chlorotrityl chloride resin 100-200 mesh (ChemPep) was loaded with 0.06 mmol of hCys. The resin was washed three times with 5 mL N,N-dimethylformamide (DMF) and three times with 5 mL dichloromethane (DCM). Each respective Fmoc amino acid (AA) was dissolved in 1 mL of 1:1 DCM:DMF with 0.15 mmol diisopropylethylamine (DIPEA). This solution was added to the resin and gently shaken for 1 h. The Fmoc-AA/DIPEA solution was then drained from the resin, and the resin

was washed three times with 5 mL of DCM. The uncapped sites on the resin were capped by washing with 20 mL of 17:2:1 DCM:methanol:DIPEA. The resin was then washed three times with 5 mL of DCM and three times with 5 mL of DMF. The resin was then transferred to the reaction vessel.

All Fmoc-amino acids (0.30 mmol, 6 equivalents) were coupled by *in situ* activation with (1-[bis(dimethylamino)methylene]-1H-1,2,3-triazolo[4,5-b]pyridinium 3-oxide hexafluorophosphate (HATU) (0.30 mmol, 6 equivalents; ChemPep) in 0.6 M N-methylmorpholine. Peptides were deprotected and cleaved from the resin in a solution containing 96% (v/v) TFA, 2% (v/v) triethylsilane, and 2% (v/v) water. The solution was stirred at 40 °C for 2 h. The cleavage reaction was filtered into 30 mL of ice-cold diethyl ether to precipitate the peptide. The solution was centrifuged at 11,000xg for 3 min and the supernatant was decanted. The remaining residue was re-suspended in 30 mL of ice-cold diethyl ether and centrifuged at 11,000xg for 3 min. The supernatant was decanted again and the remaining residue was placed under a slow-flow nitrogen line for 10 min to evaporate any residual diethyl ether. The remaining peptide residue was re-suspended in 20 mL of water and flash frozen in liquid nitrogen and lyophilized.

The peptide was purified using high-performance liquid chromatography (HPLC) with a Phenomenex Jupiter C18 preparative column (21.2 mm x 250 mm, 5 µm particle size, 300Å pore size) with buffer A as 0.1% trifluoroacetic acid (TFA, HPLC grade) in nanopure water and buffer B as 0.1% TFA (HPLC Grade) in acetonitrile (ACN, HPLC grade). The separation used a flow rate of 4 mL/min with a linear gradient of buffer A from 88 to 50 percent over 60 min. The peptide eluted between 52 and 56 min using these conditions. Fractions were analyzed by LC-MS using a HPLC-MS/MS setups (Vanquish UHPLC with a diode array detector connected to a Q-Exactive) fitted with a Hypersil GOLD C18 column (2.1 mm x 150 mm, 1.9 µm particle size) for separations at 0. 2mL/min. The LC-MS program for peptide fraction identification was set up as follows: buffer A was LC-MS Optima water (Fisher)/0.1% (v/v) LC-MS Optima TFA (Fisher) and buffer B was LC-MS Optima ACN (Fisher)/0.1% (v/v) LC-MS Optima TFA (Fisher). The 12 min separation consisted of washing the column with 100% A for 3 min, followed by a linear gradient to 100% B from 3 to 6 min,

followed by washing the column with 100% B from 6 to 9 min, and finally re-equilibration in 100% A from 9 to 12 min. The MS detectors operated in positive ion mode and the FT analyzer settings are as follows: 70,000 resolution, 1 microscan, and 200 ms maximum injection time. MS data analysis used Xcalibur software (Thermo Fisher). Mass spectra of the peptide products are reported in Figure 5-S1.

5.3.3 UV-visible titration and ascorbate reduction

UV-visible data were collected on a Varian Cary 50 UV-visible spectrophotometer. Oxidized wtPHM (500 µM, 1 mM in Cu) in 20 mM sodium phosphate pH 7.5 was transferred to a 1 mL quartz cuvette. Aliquots of 0.5 molar equivalents of AAF-hCys peptide were added to the cuvette and gently inverted to mix. Spectra were collected 10 min after each addition at a scan rate of 600 nm/min. These data are reported in Figure 5-2.

The kinetics of ascorbate reduction of the wtPHM:AAF-hCys complex were also monitored by UV-vis (Figure 5-S3). 1.5 mM (3 equivalents) AAF-hCys peptide was added to 500 µM wtPHM in 20 mM sodium phosphate pH 7.5 in a 1 mL quartz cuvette. After addition and mixing of 1.25 mM sodium ascorbate by hand (~15 s), a UV-visible spectrum from 300 nm to 1000 nm was collected every minute for 1 h and every 5 min for the next 5 h. Data were fit to a single exponential + offset model and a double exponential + offset model using SigmaPlot. Kinetic parameters and residual comparisons are described in Figure 5-S3.

5.3.4 EPR sample preparation, data collection, and simulation

Oxidized wtPHM (500 µM) containing 3 molar equivalents of AAF-hCys peptide (1.5 mM) was frozen in a quartz EPR tube to generate the pink spectrum in Figure 5-3 (b). 5 mM sodium ascorbate was added to the wtPHM:peptide complex and frozen after 3 min (Figure 5-3(c), green spectrum) and 20 minutes (Figure 5-3(d) black spectrum). EPR data were collected using a Bruker E500 X-Band EPR spectrometer equipped with a liquid nitrogen cryostat. Spectra represent an average of 2 scans and were collected at a frequency of 9.398 GHz, 100 K temperature, 2 mW microwave power, 10 Gauss modulation amplitude,

and 40 s sweep time. Experimental data were simulated using EasySpin[155]; full EPR simulation parameters are listed in Table 5-S4.

5.3.5 XAS sample preparation and data collection

wtPHM (500 μM) was equilibrated in an anoxic glove box, treated with 5 mM sodium ascorbate and 1.5 mM AAF-hCys and incubated for 4 hours. Excess peptide was removed using spin desalting columns pre-equilibrated 4 times with 20 mM sodium phosphate pH 7.5. Twenty percent ethylene glycol was added to the desalted enzyme:peptide complexes as a glassing agent. Samples (~100 μL total volume) were loaded into XAS sample holders, flash frozen in liquid nitrogen, and stored under liquid nitrogen prior to synchrotron data collection.

EXAFS data were collected at the Stanford Synchrotron Radiation Laboratory (SSRL) on beamline 9-3. The accelerator ring was operating at 3 GeV with currents at 500 mA maintained by continuous injection. The Cu edge was calibrated to 8980.3 eV (Cu) using an element foil placed between the second and third ion chambers. Harmonic rejection was accomplished using a Rh-coated mirror upstream of the monochromator set to 13 keV energy cutoff. A Z-1 oxide filter (Ni) and Soller slit assembly were used to minimize the intensity of elastic scattering relative to the Cu Kα fluorescence. Data were collected in fluorescence mode using a Canberra 100-element Ge detector and sample temperature was maintained at 10 K using a liquid He cryostat.

EXAFS data were processed using EXAFSPAK[133] and simulated using EXCURV9.2[134-136,175]. A buffer-only sample was measured and subtracted during processing to remove contributions from the filter Kβ fluorescence and generate a flat pre-edge baseline. Threshold energy (k = 0) of 8985.0 eV was used for spectral simulation in EXCURV. Coordination numbers (N), interatomic distances (R, in Å), and Debye-Waller factors ($2\sigma^2$, in $Å^2$) were refined by least-squares curve fitting to the experimental spectra. Multiple scattering contributions from histidine imidazole ligands were included in the Cu EXAFS simulations and Debye-Waller factors consistent with established values were used for Cu-S

interactions as described in the main text. Full EXAFS simulation parameters can be found in Table 5-S5.

5.4 Acknowledgements

Use of the Stanford Synchrotron Radiation Lightsource, SLAC National Accelerator Laboratory, is supported by the U.S. Department of Energy (DOE), Office of Science, Office of Basic Energy Sciences under Contract No. DE-AC02-76SF00515. The SSRL Structural Molecular Biology Program is supported by the DOE Office of Biological and Environmental Research, and by the National Institutes of Health, National Institute of General Medical Sciences (P30GM133894).

The Binuclear Copper State of Peptidylglycine Monooxygenase Visualized through a Selenium-Substituted Peptidyl-Homocysteine Complex

Evan F. Welch§•, Katherine W. Rush§†, Karsten A. S. Eastman‡, Vahe Bandarian‡ and Ninian J. Blackburn§*

§Department of Chemical Physiology and Biochemistry, Oregon Health and Sciences University, Portland, OR 97239 USA

•Department of Biomedical Engineering, Oregon Health and Science University, 3181 SW Sam Jackson Park Road, Portland, OR 97239, USA

† Department of Chemistry and Biochemistry, Auburn University, Auburn, AL 36849 USA

‡Department of Chemistry, University of Utah, Salt Lake City, UT 84112, USA

* To whom correspondence should be sent

5.5 Abstract

Bioactive peptides generally require post-translational processing to convert them to their fully active forms. Peptidylglycine monooxygenase (PHM) is a copper-dependent enzyme that catalyzes C-alpha hydroxylation of a glycine-extended pro-peptide, a critical post-translational step in peptide amidation. A canonical mechanism based on experimental and theoretical considerations proposes that molecular oxygen reacts at the mononuclear CuM-center to form a reactive Cu(II)-superoxo intermediate capable of H-atom abstraction from the peptidyl substrate, followed by long range ET from the CuH center positioned 11 Å away across a solvent-filled cleft. However, recent data has challenged this mechanism, suggesting instead that an "open-to-closed" conformational transition brings the copper centers closer to facilitate reaction at a binuclear copper site. Here we present direct observations of an enzyme-bound binuclear copper species, which was enabled by the use of an Ala-Ala-Phe-homoselenocysteine (hSeCys) species. EXAFS, UV/vis, and EPR studies are used to show that this reagent reacts with the oxidized enzyme to form a novel mixed valence entity which is subtly different from that observed previously for the S-peptidyl complex (J. Am. Chem. Soc. (2024)146, 5074-5080). In the ascorbate-reduced Cu(I) state of PHM, EXAFS measurements at both the Se and Cu absorption edges provide a unique signature of a bridging mode of binding, with Se-Cu site occupancy (1.8) measured from the Se-EXAFS simulating to twice that of the Cu-Se site occupancy (0.85) measured at the Cu edge. The ability of the hSeCys entity to induce a binuclear state is further emphasized by the XAS of the selenomethionyl peptide complex, where no such bridging chemistry is observed. The properties of the binuclear PHM derivative are of interest due to their unique chemical signatures, as well as providing the basis for a completely new mechanistic paradigm for PHM and its monooxygenase congeners.

5.6 Introduction

The mechanism of action of copper monooxygenases has attracted attention due to the role of these enzymes in important biological processes such as hormone biosynthesis, climate mitigation and peptide processing. Peptidylglycine monooxygenase (PHM) [33,52] and its sister enzymes dopamine β monooxygenase (DBM) and tyramine β monooxygenase (TBM) [47,176] catalyze the biosynthesis of neuropeptide hormones and catecholamine neurotransmitters respectively and thus play central roles in the regulation of bodily functions including the endocrine and sympathetic nervous systems. X-ray crystal structures reveal that the enzymes share a common active site composed of a pair of copper atoms termed CuH and CuM which in the resting oxidized enzymes are separated by ~11-14 Å across a solvent-filled cleft (Figure 5-6(a)) [31,85]. CuH is coordinated by three His residues (H107, H108, H172 PHM numbering) while CuM is coordinated by two histidines and a methionine residue (H242, H244, M314 PHM numbering), Scheme 1(b). Very recently a related enzyme class has been described named the BURP domain which catalyzes cyclization of ribosomally synthesized and posttranslationally modified peptides (RiPPs) using a pair of mononuclear copper centers with coordination similar to the PHM M-center. [177] Understanding the detailed mechanism of these enzymes thus continues to garner significant attention.

Extensive spectroscopic[21,42,43,45,95], kinetic[40,41,44,97,122] and computational[46,69,72,94,141] studies on PHM have made it the system of choice for detailed mechanistic studies. Here, a C-terminal glycine- extended pro-peptide undergoes initial hydroxylation at the glycine α-C to form an α-hydroxyglycine intermediate (Figure 5-6 (c)), which is further processed by a second enzymatic activity (peptidylglycine α-hydroxylating lyase, PAL) to generate the amidated peptide product. Substrate-bound structures visualize the peptidylglycine substrate bound to R240 and Y318 via its C-terminal carboxylate (Figure 5-6 (b)) which brings the α-C into the proximity of the CuM center. Using the slow substrate tyrosyl-D-threonine, Amzel and coworkers obtained a structure of an oxygen adduct bound to CuM but with the O_2 in an unproductive conformation pointing away from the substrate C-alpha.[27] Based on these studies, a canonical “mononuclear” mechanism for substrate

hydroxylation was proposed[46,69,94] in which the substrate-bound Cu(I) enzyme reacts with dioxygen at the CuM site to form a Cu(II)M-superoxo intermediate capable of extracting the pro-S H atom from the glycyl C-alpha methylene group to form a substrate radical. The catalytic cycle is completed by a long-range electron tunneling (ET) event from CuH or via formation of a Cu(II)M-oxyl intermediate.

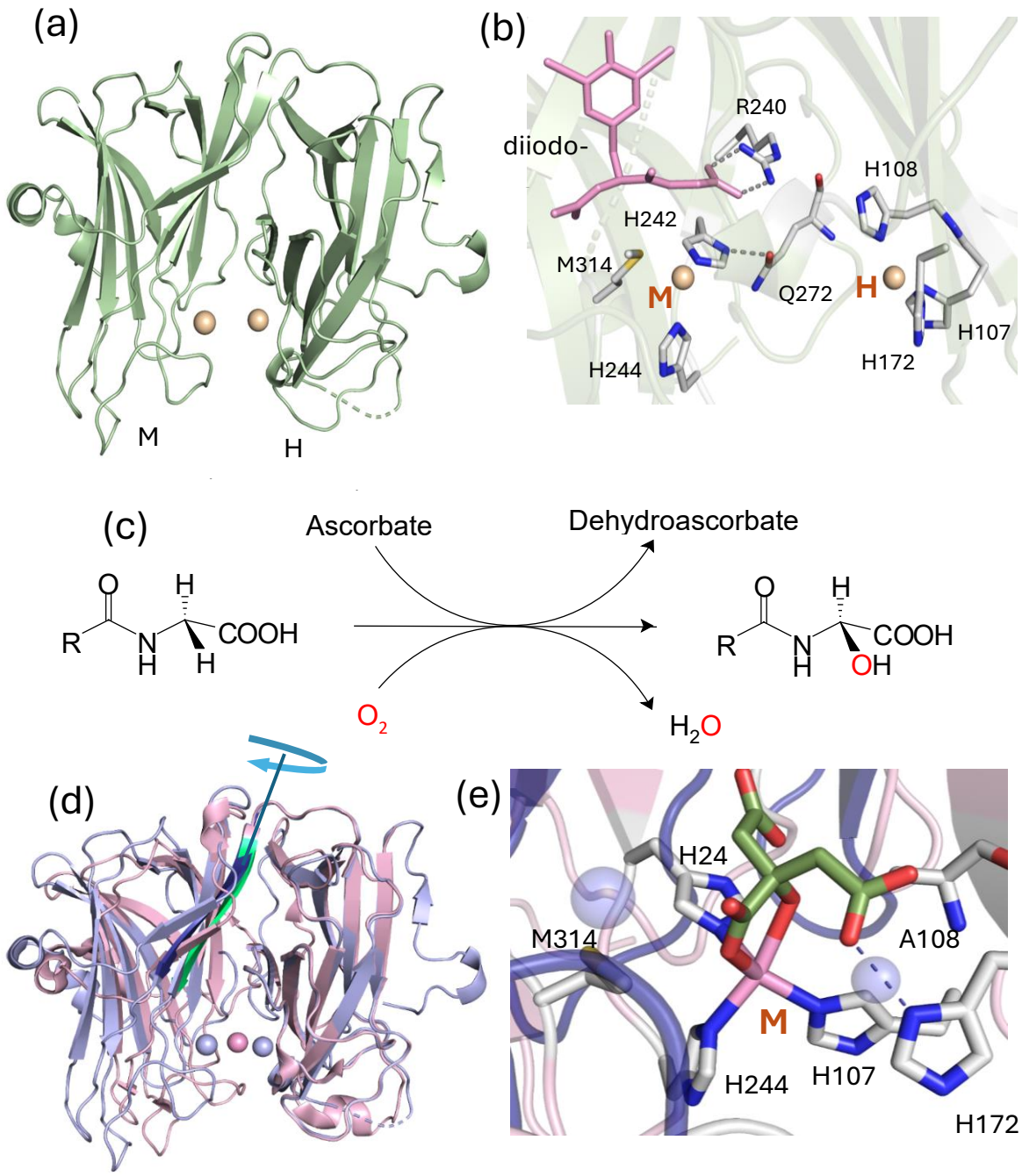

Figure 5-6 Structure and reactivity of peptidylglycine monooxygenase (PHM). *(a) 2-domain structure of showing the H- and M-domains each binding a Cu atom separated by ~11 Å (b) active site structure showing the coordination environment of the CuH and CuM and the position of the bound substrate di-iodo-tyrosylglycine (c) reaction catalyzed by PHM (d) sub-domain movement about I201generating open and closed states of PHM with either long (11-14 Å) or short (4-5 Å) Cu-Cu distances (e) closed conformer of PHM showing the singly bound CuM in pink coordinated by three M-site and 1 H-site ligands. The positions of the Cu centers in the open structure are shown as decolorized blue spheres. Reproduced using PDB files 3PHM ((a) and (b)), 3PHM, 6ALA, and 8DSJ (d) and 6ALA (e).*

The mononuclear or "canonical" mechanism is based on the assumption derived from early crystal structures that the two sub-domains that harbor the CuH and CuM centers are locked into a conformation that precludes any change in the 11 Å Cu-Cu distance. However, a number of structures challenging this premise have emerged recently both for PHM[26,119] and DBM[31] in what have been termed fully open (Cu-Cu = 14 Å) and closed conformations (Cu-Cu = 4 – 5 Å). A closed conformation for the PHM variant H108A is shown in Figure 5-6 (d,e) where the M domain has rotated relative to the H domain about a hinge residue (I201) located on the interdomain loop which brings the copper centers closer together. This structure lacks the CuH metal ion and instead, the CuM is coordinated by two M-site histidines, one H-site histidine and a citrate molecule. The occurrence of both open and closed structures suggests flexible dynamics between the two copper-containing sub-domains which may allow the Cu-Cu distance to vary continuously,[119] raising the possibility that binuclear states of the enzyme might contribute to the reaction coordinate. This idea has been explored computationally for DBM [72] and found to be energetically plausible with two specific attributes, first that the energy of conversion from open to closed conformer is a mere 2 kcal mol^{-1}, and second that the reactive species is a hydroperoxo-bridged mixed valence dinuclear complex.

For these reasons we sought a method of probing the conformational landscape of PHM with the goal of isolating binuclear states that could be characterized spectroscopically. Recently we communicated an initial report of the chemistry and spectroscopy of complexes of oxidized and reduced PHM with the peptidyl inhibitor Ala-Ala-Phe-homocysteine (AAF-hCys) [137]. This study was based on the concept that this bifunctional peptidyl substrate analogue could react at the carboxylate binding site in the vicinity of CuM but would also be capable of capturing the H-site Cu via coordination of its thiolate to both CuM and CuH forming a thiolate bridge that would induce the open to closed transition. This chemistry was indeed observed and validated by EXAFS spectroscopy. In addition, reaction of AAF-hCys with the fully oxidized enzyme generated an unusual mixed valence (MV) complex with an intervalence charge transfer band at 925

nm. The latter observation was significant given the evidence for the intermediacy of such a species from QM/MM [72].

In the present paper we explore the chemistry of formation of the binuclear state in detail using the Se analogue Ala-Ala-Phe-homoselenocysteine (AAF-hSeCys). Substitution with the heavier chalogenic congener has allowed the characterization of reduced forms using X-ray absorption (XAS) at both Cu and Se edges, where the requirement for structural mirroring in the X-ray absorption fine structure (EXAFS) data provides more accurate description of the complexes. Further, differences in redox potential between S and Se homocysteine analogues lead to perturbation of both the spectroscopy and stability of the MV species. The results expand and fully validate the chemistry and spectroscopy of the binuclear states of PHM presented in our earlier communication.

5.7 Results

We recently described the reaction of the AAF-hCys (S-thiol) peptide with oxidized PHM to generate a localized mixed valence species, and with reduced PHM to form the thiolate-bridged dinuclear complex characteristic of the closed conformer.[137] The S-containing peptide was synthesized as the reduced thiol with only small (<10 percent) contribution from the disulfide form and therefore underwent reactivity with both oxidized and reduced PHM without the need for further treatment. The monomeric form of the Se analogue (AAF-hSeCys) was synthesized by solid-phase peptide synthesis; however, during cleavage and deprotection, the highly reactive selenol rapidly oxidized, resulting in the diselenide as the primary species present after purification (Figure 5-S6), which did not react with either redox state of the enzyme unless first reduced to the selenol form.

5.7.1 HPLC-HRMS Characterization of the AAF-hSeCys Diselenide Peptide

The diselenide $(AAF\text{-}hSeCys)_2$ eluted as a single peak from 7.75 to 7.95 minutes, as shown in the HPLC chromatogram trace (Figure 5-S6(a)). Analysis of the high-resolution mass spectrometry (Figure 5-S7(b) and S7(c)) data revealed two charge states present in the mass spectrum: a doubly charged species (z = 2) and a singly charged species (z = 1).

The expected monoisotopic mass (m/z) for the z = 2 charge state is 472.1219, while the observed monoisotopic mass is 472.1207, resulting in a ppm error of -2.54. For the z = 1 charge state, the expected monoisotopic mass is 943.2366, with the observed monoisotopic mass being 943.2362, yielding a ppm error of -0.81.

5.7.2 Reduction of the AAF-hSeCys Diselenide to its Reactive Selenol Form

Reduction of the AAF-hSeCys diselenide proved to be challenging since the Se-Se bond is more stable than the homologous disulfide and requires stronger reductants. X-ray absorption spectroscopy at the Se edge provided a convenient method for studying the progress of reduction by various reagents. The Fourier transform (FT) of the starting diselenide-containing material showed a weak first shell peak due to the Se-C at ~1.95 Å, and an intense second shell feature at 2.31 Å due to the Se-Se interaction of the diselenide covalent bond (Figure 5-7 (black trace)) with intensity that is expected to decrease as the diselenide is reduced. In aqueous buffer, reduction by dithiothreitol (DTT) was about 30 percent effective in reducing the diselenide but TCEP and sodium borohydride were ineffective (Figure 5-S7). The most effective reductant in aqueous medium was sodium dithionite which led to complete reduction at 50 mM but almost no reduction at concentrations (12.5 mM) suitable for enzyme studies (Figure 5-S7). We also considered the effect of high concentrations of dithionite and borohydride on the activity of PHM, since small molecule reductants could not effectively be removed from the peptide reagent and must therefore be benign relative to the enzyme activity. Both were lethal to the enzyme (Figure 5-S8), possibly via a mechanism that reduces the 5 critical disulfide linkages and denatures the protein.

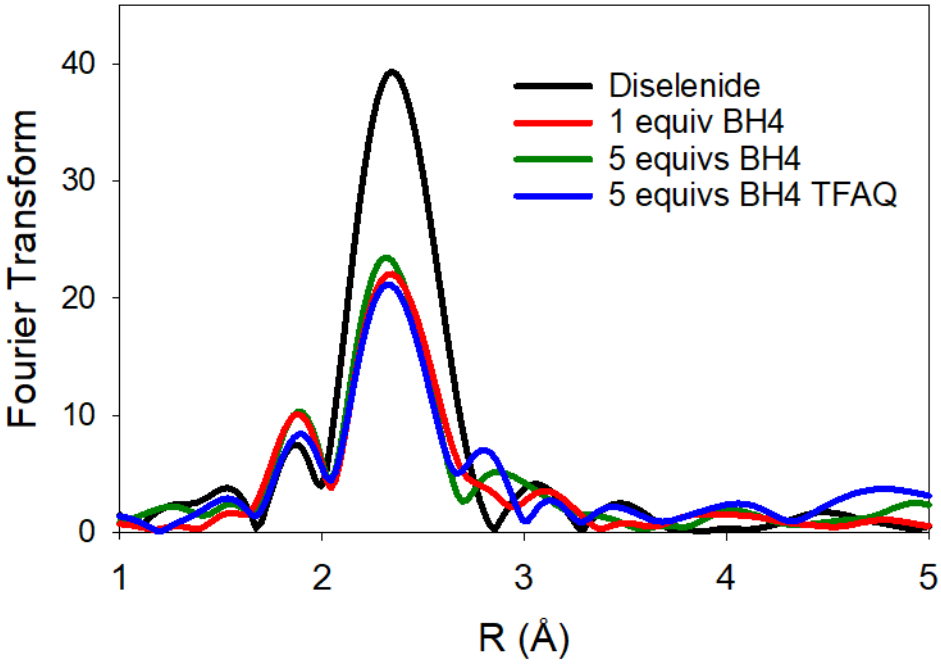

Figure 5-7 Se edge phase-corrected Fourier transforms of the AAF-hSeCys peptide treated with various reductants. *1 mM peptide in anhydrous with sodium borohydride in the same solvent. Black trace untreated diselenide; red trace + 1 molar equivalent $NaBH_4$; green trace + 5 molar equivalents $NaBH_4$; blue trace + 5 molar equivalents $NaBH_4$ after quenching with TFA*

Against this background, we explored alternative approaches. Borohydride is known to undergo degradation in aqueous media via protonation of the hydride ion, and generation of hydrogen gas, but an aprotic environment could lead to effective reduction. Reaction of one equivalent of $NaBH_4$ in anhydrous DMSO with the AAF-hSeCys in the same solvent led to ~ 30 percent reduction (Figure 5-7 red trace) to the selenol. 5-fold excess of $NaBH_4$ should in principle lead to full reduction but under the same experimental conditions did not appear to increase the percent of reduced selenol (Figure 5-7 green trace). Additionally, excess borohydride was undesirable due to its inhibitory effect on the enzyme. We tested whether it could be removed from the peptide by treatment with trifluoroacetic acid (TFA) in anhydrous DMSO. In a test reaction 50 mM AAF-hSeCys in anhydrous DMSO was reacted with a 5-fold excess of $NaBH_4$ and the reduction allowed to proceed for 30 minutes. The resulting reaction mixture was then titrated with small aliquots of TFA diluted in anhydrous DMSO. Addition of 1 equivalent of TFA led to vigorous

evolution of gas (H_2 + B_2H_6) which was allowed to subside before further TFA addition. An additional 0.2 equivalents of TFA produced a solution that no longer effervesced on further TFA addition. The FT of this solution at the Se edge showed approximately 50 percent reduction (Figure 5-7 blue trace) similar to the result without TFA quench. Currently we do not have an explanation for why excess BH_4^- does not appear to increase the extent of reduction, but (*vide infra*) it is possible that the selenol is initially fully reduced by the excess borohydride, and that the observed residual diselenide results from reoxidation due to dilution into the measurement buffer (50 mM phosphate + 20% ethylene glycol). This TFA-quenched solution was used for further studies.

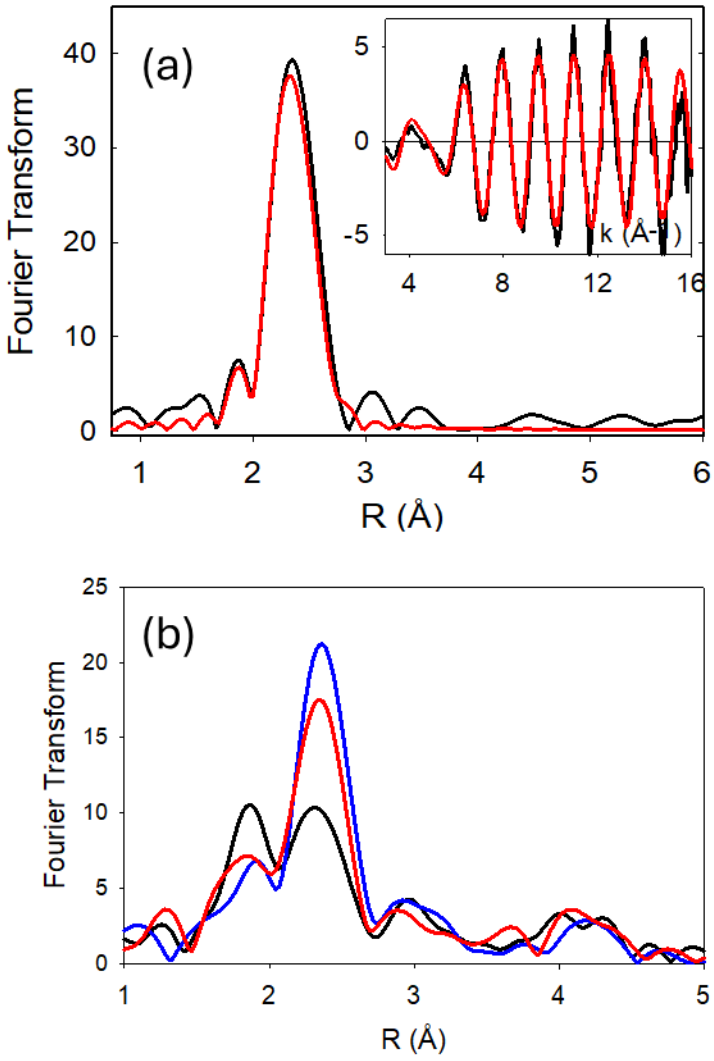

Figure 5-8 EXAFS of AAF-hSeCys peptide. *(a) Se edge Fourier transform and EXAFS (inset) for the diselenide form of the AAF-hSeCys peptide. The black trace represents experimental data, the red trace represents ((the fit simulation)). Parameters used in the fit are listed in Table 5-1. (b) Cu edge Fourier transforms for reaction of ascorbate-reduced Cu(I) PHM with different preparations of AAF-hSeCys peptide reduced with varying stoichiometries of TFA-quenched $NaBH_4$: black trace 1 equivalent of peptide reduced with 1 equivalent $NaBH_4$; red trace 2 equivalents of peptide reduced with 1 equivalent $NaBH_4$; blue trace 1 equivalent of peptide reduced with 5 equivalents $NaBH_4$.*

Table 5-1. Parameters used in the fits to EXAFS data.

Selenium edge		**Se-C**				**Se-Se**				**Se-Cu**				
	F[1] (x10^{-3})	**No[2]**	**R (Å)[3]**	**DW (Å^2)[4]**		**No**	**R (Å)**	**DW (Å^2)**		**No**	**R (Å)**	**DW (Å^2)**		**ΔE_0**
AAF-hSeCys peptide diselenide	1.08	1	1.97	0.006		1.0	2.32	0.003		-	-	-		-4.03
AAF-hSeCys reduced borohydride quenched	4.1[5]	1	1.97	0.007		0.5	2.33	0.003						-3.0
redPHM + AAF-hSeCys	0.65	1	1.96	0.007		0.1	2.31	0.003		1.8	2.39	0.008		-3.2
redPHM + AAF-SeMet	2.8	2	1.96	0.007						1	2.41	0.012		-5.7
Copper edge		**Cu-N(His)[6]**				**Cu-S**				**Cu-Se**				
	F (x10^{-3})	**No**	**R (Å)**	**DW (Å^2)**		**No**	**R (Å)**	**DW (Å^2)**		**No**	**R (Å)**	**DW (Å^2)**		**ΔE_0**
redPHM + AAF-hSeCys	0.46	2	1.93	0.020		0.5	2.21	0.011		0.85	2.38	0.008		-3.0
redPHM + AAF-SeMet	0.54	2	1.91	0.011		0.5	2.25	0.013		0.5	2.41	0.010		-0.32
oxPHM + AAF-hSeCys	0.50	2.5	1.95	0.011		0.5	2.20	0.013		0.7 0.3	2.41 2.84	0.012 0.016		-1.13

[1] F is a least-squares fitting parameter defined as $F^2 = \frac{1}{N}\sum_{i=1}^{N} k^6(Data - Model)^2$.

[2] Coordination numbers are generally considered as accurate +/- 25% unless indicated as low confidence.

[3] In any one fit, the statistical error in bond-lengths is ±0.005 Å. However, when errors due to imperfect background subtraction, phase-shift calculations, and noise in the data are compounded, the actual error is probably closer to ±0.02 Å.

[4] Debye-Waller (DW) factors are reported as $2\sigma^2$ and are defined as twice the mean square deviation of the experimental bond distance as compared to the simulated value.

[5] The larger value of F for Se arises from noisy data

[6] Imidazole rings were simulated using full multiple scattering from C2/C5 at 127^0 and C3/N4 at 163^0 from the Cu-N axis. The split shells approximate the average distortion of the imidazole plane from the Cu-N axis.

5.7.3 Reaction of the selenol form of AAF-hSeCys with fully reduced PHM

Ascorbate-reduced Cu(I)-containing PHM was reacted with borohydride-reduced TFA-quenched AAF-hSeCys and the identity of the product analyzed by XAS at both the Se and Cu edges. Data from two absorption edges have the advantage that metrical details (coordination numbers, distances and Debye Waller (DW) factors) due to Se-Cu interactions at the Se edge must exactly mirror those due to Cu-Se at the Cu edge. For a Se-bridged dicopper species, we expect each Se to "see" two Cu scatterers at the Se edge, while each Cu should "see" one Se scatterer at the Cu edge. Analysis of the Se edge data is complicated by the potential presence of residual diselenide in the sample: Se-Se interactions typically have Se-Se bond lengths of 2.31 Å while Se-Cu bond lengths are typically around 2.40 Å [102,178] which can introduce ambiguity in the accurate determination of Se-Cu occupation numbers unless the relative contributions of both species are known. To address this problem, we analyzed the Se EXAFS data in terms of a chemical model that assumes that only two distinguishable Se species are present – the Se bridged dicopper PHM complex with EXAFS contributions from 2 Se-Cu interactions and the diselenide form of the peptide with EXAFS contributions from 1 Se-Se interactions. Since the EXAFS amplitudes are normalized to the total Se in the sample, the Se-Cu shell-occupancy N_{Cu} is related to the Se-Se shell occupancy by the following equation

$$N_{Cu} = 2(1 - N_{Se}) \qquad \ldots (1)$$

Since the Se-Se distance and Debye-Waller (DW) factor for the Se-Se shell are known from simulation of the free diselenide (Figure 5-8 (a) and Table 5-1), this simple relationship allows the best estimate for the ratio of Se-Se and Se-Cu species to be determined. To test the approach, we first measured data from samples where the anticipated Se-bridged complex was not fully formed. As mentioned above, reaction of 1 equivalent of $NaBH_4$ with AAF-hSeCys followed by a TFA quench produced a mixture where the peptide was 30 percent reduced. Therefore, reacting this reagent 1:1 or 2:1 with enzyme was expected to produce N_{Cu} values of 0.6, and 1.2 respectively. (Note that the 2:1 sample was passed through two spin columns to remove excess peptide). Figure 5-8(b) shows FT data at the Cu edge for each of these samples where the Cu-Se shell intensity is seen to increase from

~30 percent to ~60%. These values were confirmed by simulation at both edges (Table 5-S1). Refinement of the 2:1 sample gave a best fit 1.2 Cu per Se with R_{Se-Cu} = 2.39 Å and DW factors $2\sigma^2$= 0.007 A^{-1} mirrored at the Cu edge but with shell occupancies that differed by half, providing validation of both the fitting approach and the chemical model.

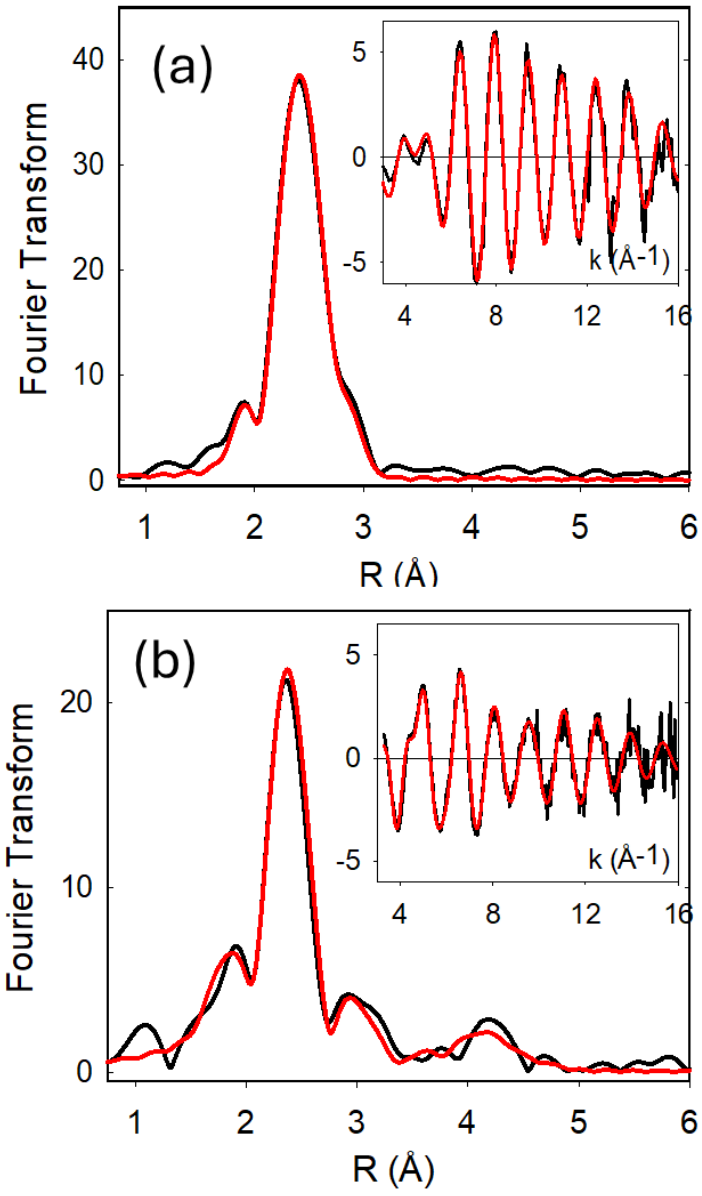

Figure 5-9 EXAFs of PHM with AAF-hSeCys. *Fourier transforms and EXAFS (insets) for (a) the Se and (b) the Cu K EXAFS of ascorbate-reduced Cu(I) PHM reacted with 1 equivalent of AAF-hSeCys. The peptide was reduced with 5 equivalents of $NaBH_4$ which was subsequently quenched with TFA as described in the text. Black traces are experimental data, red traces are simulated data. Parameters used in the fits are listed in Table 5-1.*

Our final experiments with the ascorbate-reduced PHM utilized the selenol reduced with 5-fold excess of $NaBH_4$ followed by TFA quenching. We reacted the selenol with reduced PHM at either 1:1 or 2:1 ratio followed by purification with two sequential spin desalting columns (7kDa MWCO) to remove excess unbound peptide. Analysis by ICP-OES gave a Cu:Se ratio of 2:1 showing binding of one peptide to the protein. Both procedures generated identical EXAFS spectra. The data and their simulations for the 1:1 addition are shown in Figure 5-9(a) at the Se edge and Figure 5-9(b) at the Cu edge. Simulations (Table 5-1) showed that the Se-bridged species was formed to ~85 percent in each case with Se-Cu and Cu-Se distances and DW factors again mirrored at each edge ($R_{Cu\text{-}Se}$= 2.39 Å, $DW_{Cu\text{-}Se}$= 0.008 $Å^{-1}$). The N_{Cu} value of 1.8 mirrored by half this value at the Cu edge provides unambiguous evidence for the formation of the selenolate bridge, and hence the formation of the dinuclear Cu(I) species of the closed conformer.

5.7.4 Control Reaction with AAF-SeMet

As a further test of the formation of the Se-bridged dinuclear state by the AAF-hSeCys peptide we studied the reaction with the homologous peptide containing a C-terminal selenomethionine residue (AAF-SeMet). The substitution of the strongly coordinating negatively charged selenolate donor group with the weaker neutral selenoether was expected to perturb or eliminate the open to closed transition, since the coordinating power of the SeMet ligand would be fully satisfied by binding at the CuM site. Figures 5-10 (a) and (b) show the EXAFS at the Se and Cu edges for a sample of ascorbate-reduced PHM reacted with 3 equivalents of AAF-SeMet followed by 2 spin columns to remove excess peptide. Analysis by ICP-OES gives a Cu:Se ratio of 2:1, similar to that obtained for the AAF-hSeCys showing binding of one peptide to the protein. However, the Se-Cu and Cu-Se occupation numbers at the Se and Cu edges respectively are now different, with Se “seeing” 1 Cu and Cu “seeing” 0.5 Se. Metrical details for these simulations are given in Table 5-1. This result is consistent with the AAF-SeMet peptide binding via its carboxy terminus to the R240/Y318 substrate-binding diad but forming only 1 additional linkage to a Cu atom, which we speculate is the CuM center. Thus, when the

coordinating power of the peptidyl lure is decreased it can no longer capture the H-domain and induce domain closure.

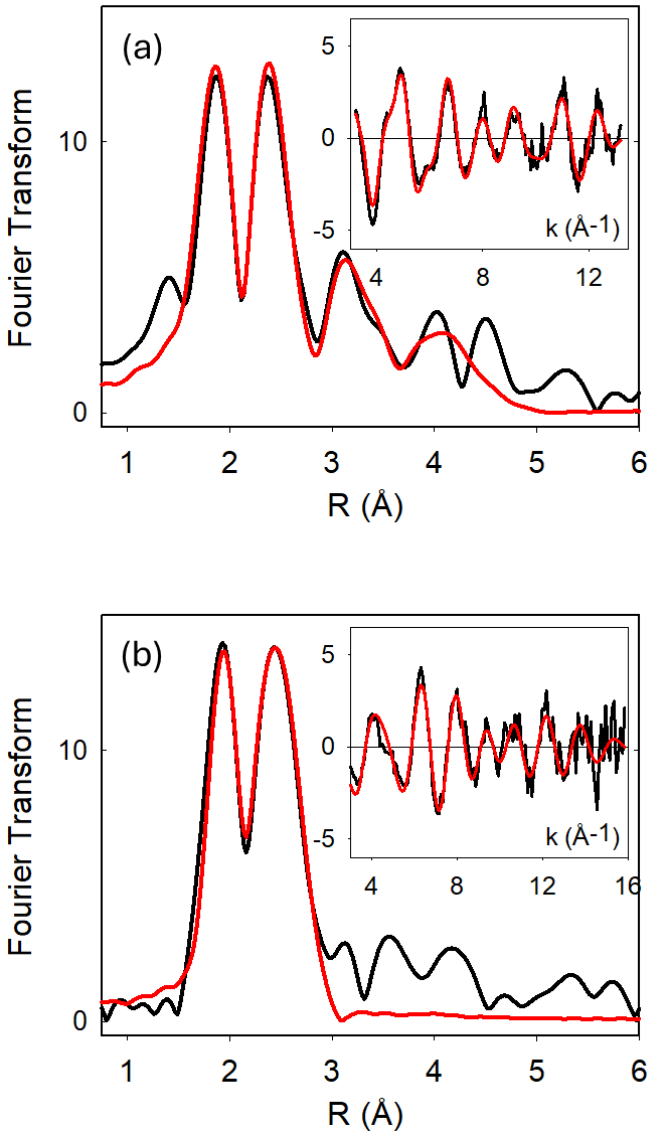

Figure 5-10 EXAFS of PHM with AAF-SeMet peptide. *Fourier transforms and EXAFS (insets) for reaction of AAF-SeMet with ascorbate-reduced Cu(I) PHM. (a) Cu edge data (b) Se edge data. Black traces are experimental data, red traces are simulated data. Parameters used in the fits are listed in Table 5-1.*

5.7.5 Reaction of the selenol peptide with oxidized PHM

In a previous communication we reported the reaction of the AAF-hCys S-containing peptide with oxidized PHM.[137] The broad NIR peak at ~925 was provisionally assigned as an intervalence charge transfer band (IVCT) by comparison with other mixed valence systems, [143,147,148,150-154,162] and from EPR analysis which showed equal concentrations of Cu(II) and Cu(I) in the purple species. It was argued that this must imply an interaction between a Cu(I) and a Cu(II) center leading to electron exchange in the excited state. Studies of the EPR characteristics of this species indicated that it was a class II IVCT system where the electron exchange was sufficiently slow that the two sites were valence localized on the time scale of the EPR absorption. This contrasted with other well-known IVCT systems such the CuA sites of cytochrome oxidase, purple Cu azurin, and N_2O reductase (λ_{max} = 460, 530, 795 nm)[143,148,150-154,159] where the electron exchange is rapid, and leads to full delocalization over both Cu nuclei. In CuA, the double cysteine bridge forms the $[(Cu)_2S_2]^{3+}$ diamond core with a short (2.4 Å) Cu-Cu distance, and a significant proportion of direct Cu-Cu bonding[152,179] which is believed to be the conduit for the electron delocalization. In the PHM case, this mode of bridging is clearly absent, yet the presence of a IVCT band would still require formation of a ligand bridge. Additionally, the Cu(I) component must be formed by reduction of either Cu_M(II) or Cu_H(II) by the thiolate of homocysteine in a "sacrificial" reductive process similar to that observed in the metalation of CuA by aqueous $CuSO_4$ where the reduced thiols of the apo protein serve as the source of the reducing electron. [180]

2 Cu(II)-Cu(II)-PHM + 2 S-Pep ⟶ *2 Cu(II)-Cu(I)-PHM + Pep-S-S-Pep* ... (2)

2 Cu(II)-Cu(I)-PHM + 2 S-Pep ⟶ *2Cu(II)-S-pep-Cu(I)-PHM (MV spectrum)* ... (3)

With an overall reaction:

Cu(II)-Cu(II)-PHM + 2 S-Pep ⟶ *Cu(II)-S-pep-Cu(I) + ½ Pep-S-S-Pep* ... (4)

This mechanism predicts that 2 equivalents of peptide are required to elicit the full mixed valence spectrum close to what is observed. Finally, in the S-peptide, EPR data suggested that even when the MV appeared to be fully formed with no further increase in UV-vis

intensity on peptide addition, only ~60 percent of the total PHM had been converted. This observation could be rationalized if the peptide disulfide could compete with peptide thiol for binding to oxidized PHM, via the carboxy-terminal peptide binding at residues R240 and Y318.

This chemistry formed the basis for exploration of the reactivity of AAF-hSeCys with oxidized PHM. Figure 5-11(a) compares the S- and Se-peptide MV spectra for equimolar (600 μM enzyme, 1.2 mM Cu) PHM samples, where the latter was generated by reaction of 2.5 equivalents of the AAF-hSeCys with the oxidized enzyme. (The S-peptide data was generated using the N-Acetyl-AAF-hCys which gave maxima at 450, 570 and 920 nm, blue shifted ~10 nm from that reported for the unmodified N-terminus). Significant differences exist between S- and Se spectra (λ_{max} (Se) = 350, 475, 560 and 1000 nm), most notable the 80 nm red-shift in the NIR band. A control reaction with the AAF-SeMet peptide (Figure 5-S4) did not lead to evolution of any bands in the 800 – 1100 nm region attributable to a mixed valence species, although some minor spectral changes in the d-d region suggested that binding of the peptide had occurred.

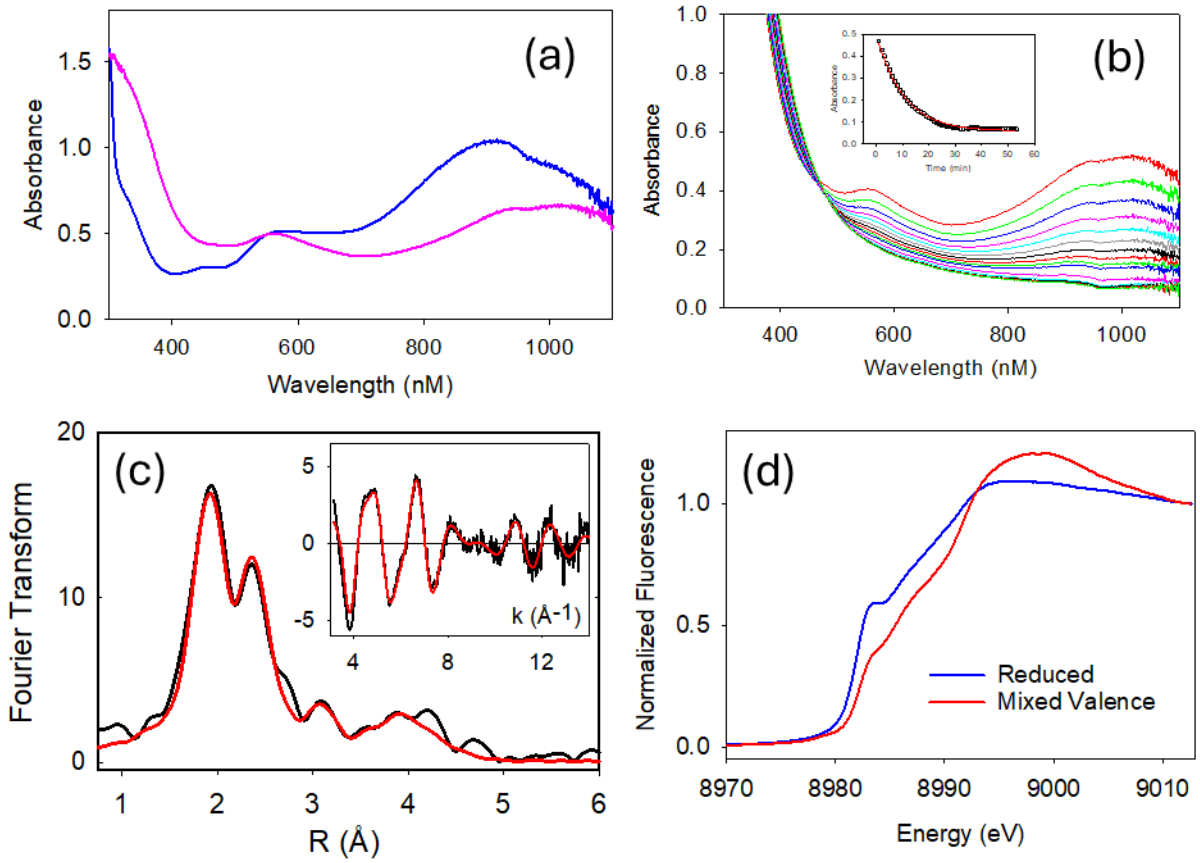

Figure 5-11 Reaction of the AAF-hSeCys peptide with oxidized Cu(II) PHM to form the mixed valence complex. *(a) Comparison of UV/vis spectra of the mixed valence complexes of PHM with AAF-hCys (pink) and AAF-hSeCys (blue) showing the intervalence charge transfer band of the selenohomocysteine MV complex red-shifted from 925 nm to 1000 nm. Extinction coefficients are calculated as described in the text and listed in Table 5-S2 (b) reduction of the MV complex formed with AAF-hSeCys with 5 mM ascorbate in a pseudo first order decay with kobs=0.1 s^{-1} (c) Fourier transform and EXAFS (inset) for the Cu edge of the seleno MV complex (parameters in Table 5-1) (d) comparison of the Cu K absorption edges of the MV (red) and reduced (blue) complexes of PHM-AAF-hSeCys complexes.*

5.7.6 EXAFS of the mixed valence species at the Cu edge

EXAFS of the AAF-hSeCys MV species was measured at the Cu edge only, since the excess Se in the sample rendered the Se edge data difficult to interpret. Cu K-EXAFS of the AAF-hSeCys complexes with oxidized PHM is shown in Figure 5-11(c) with parameters listed in Table 5-1. Best fit simulations give 2.5 Cu-N(His), 0.5 Cu-S(Met314) and 0.7 Cu-Se(hCys) with bond lengths of 1.95, 2.20, and 2.41 Å respectively. The substoichiometric occupation number for the Cu-Se shell is consistent with ~70 percent formation of the Se

bridged species, with the remaining oxidized enzyme bound by the diselenide peptide (*vide supra*). The Cu-S(Met314) interaction is notably shorter than typically found in the WT PHM possibly the result of a stronger interaction of the Se with the reduced CuH center, allowing a stronger interaction with the S(Met314) ligand. Comparison of MV and fully reduced PHM-AAF-hSeCys absorption edges (Figure 5-11(d)) shows the expected shift to lower energy for the reduced state, and a weak partially resolved 1s –> 3d quadrupole transition from the Cu(II) components in the MV complex at 8979 eV. These absorption edges are unremarkable but are shown here for completeness.

5.7.7 EPR Analysis of the AAF-hSeCys mixed-valence complex

EPR spectra for the oxidized PHM starting material and its MV complex generated from titration with the reduced selenopeptide are shown in Figure 5-12(a) and (b) respectively. For each sample, the quantity of Cu(II) represented by the EPR intensity was determined by double integration relative to a Cu(II)-EDTA standard measured under identical experimental conditions of microwave power, modulation amplitude, and temperature. The amount of EPR detectable Cu(II) is correlated with the absorbance maximum at 1000 nm in Table 5-S2. Spectra were simulated using Easyspin[155] and the simulations are shown as red traces in Figure 6 with parameters used in the simulations in Table 5-S3.

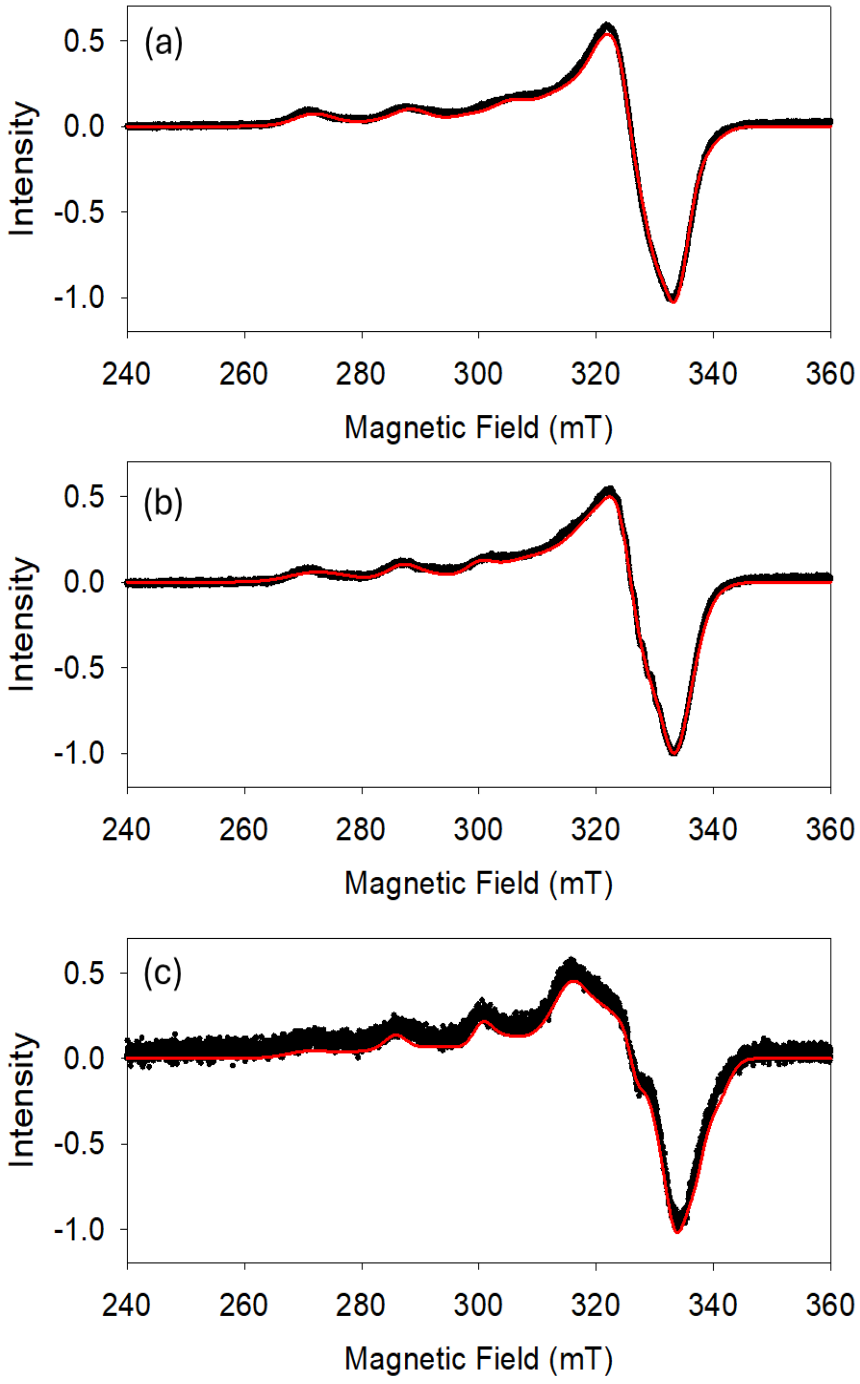

Figure 5-12 EPR spectra (black traces) of oxidized PHM and its reaction products with the AAF-hSeCys peptide. *(a) unreacted oxidized PHM (b) reacted with 2.5 equivalents of AAF-hSeCys (c) after reduction with 5 mM ascorbate. Simulated spectra (red traces) were generated using EASYSPIN (see text). Reaction conditions, concentrations and residual Cu(II) quantitation are listed in Table 5-S2. Parameters used in the fits are listed in Table 5-S3. EPR instrumental conditions were as follows: frequency 9.396 GHz, modulation amplitude 2 Gauss, microwave power 2 mW, temperature 170 K. Spectra are averages of 4 scans each.*

Oxidized PHM was found to integrate to 100 percent Cu(II) as expected. The MV complex integrated to 69 percent Cu(II) and 31 percent of an EPR indetectable form (by subtraction). If we assume that this indetectable copper is Cu(I) we may conclude that 62 percent of the total copper is present as the MV form and 38 percent as a different oxidized form. This latter form cannot be unreacted oxidized PHM since the titration proceeded to an end point where no more selenol would react. The most likely assignment for this species is a diselenide-bound state of the oxidized enzyme where the C-terminal carboxylate of a diselenide form of the peptide competes with the carboxy terminus of the reduced selenol form for the peptidyl binding site. The quantitative EPR analysis would predict that the Cu EXAFS of the titration end point should show ~0.6 Se scatterers per Cu in good agreement with the EXAFS value of 0.7.

Both visual inspection and simulation of the MV species fail to reveal evidence of a 7-line hyperfine pattern expected for a class III MV species exhibiting complete electron delocalization over both copper nuclei. Therefore, we conclude that like its S analogue, the AAF-hSeCys forms a class II localized MV entity where the rate of electron exchange between the two redox states of Cu in the Se-bridged dicopper species is slow relative to the EPR time scale at the temperature of measurement (170 K). It is possible that electron delocalization can occur at room temperature, but RT EPR measurements were of insufficient signal-to-noise to address this question. It is likely that the chemical inequivalence of the two Cu centers in PHM leads to valence localization at low temperature, as was also concluded for the AAF-hCys system.

5.7.8 Reduction of MV complexes by ascorbate

In our earlier work on the AAF-hCys PHM system we observed that the sulfur-bridged MV complex was remarkably resistant to ascorbate reduction and was reduced in a biphasic reaction

$$Abs_{925nm} = A_1 e^{-k_1 t} + A_2 e^{-k_2 t} + A_0 \quad \ldots (5)$$

with parameters $k_1 = 0.09\ min^{-1}$, and $k_2 = 0.007\ min^{-1}$ in a 1:4 ratio. [137] Like the Se system, the S-bridged complex was formed with an accompanying fully oxidized component, but because the latter was reduced much faster by ascorbate than the MV complex, it could be rendered EPR undetectable by reduction with 5 mM ascorbate allowing the EPR spectrum of the MV complex to be visualized without overlap from any additional EPR active species. Despite this, simulation of the S-bridged MV complex required contributions from two S=1/2 species in a 1:3 ratio. The structural and/or electronic differences between these two MV species were not explored but because of the slow electron exchange suggested by their class II MV character one may speculate that they could represent redox states with the unpaired electron localized or "frozen out" onto each of the CuH and CuM sites.

We carried out a similar reaction with the Se-bridged MV system with the expectation that the EPR spectrum of the MV entity could be isolated by similar differential reduction of the accompanying fully oxidized component. This experiment was only partially successful since the Se-containing MV complex appeared to be reduced much more rapidly (Figure 5-11 (b)) this time in a single exponential with $k_{obs} = 0.1 \pm 0.01\ min^{-1}$. However, comparison with the S data indicates that this rate is close to the faster rate observed in the former but is now the major/only component rather than the minor component of the reaction. Given this faster reduction the ascorbate-reduced MV species had undergone significant reduction itself before it could be frozen for EPR analysis. Figure 5-12(c) shows the EPR spectrum of this species along with its simulation, with EPR parameters listed in Table 5-S3.

The spectra shown in Figure 5-12 each required at least 2 separate S=1/2 components to obtain satisfactory residuals. For oxidized PHM and the MV complex this is expected since (i) oxidized PHM (Figure 5-12(a)) contains two chemically inequivalent copper centers, CuH and CuM and (ii) the MV complex (Figure 5-12(b)) contains a residual oxidized component and a MV component with respective Cu(II) concentrations in 4:3 proportions. A 2-component simulation for the ascorbate-reduced MV system is consistent with the result found for the S-analogue, although the single-phase reductive

kinetics are more consistent with a single species. Inspection of the EPR parameters for the MV complexes indicates that the species responsible are unremarkable with g and A values consistent with isolated S=1/2 systems in close-to-axial symmetry, typical of type II rather than type 1 Cu proteins. In particular, the covalency of the Se MV complex appears less than its S analogue where the g_3 -values of both components are in the 2.26 -2.30 region, in contrast to the S-bridged system where g_3 = 2.21 for the major component.

5.7.9 Calculation of the Extinction Coefficient for the MV complex

The extinction coefficient for the IVCT band of the mixed-valence complex was calculated as follows. For samples taken at the titration end-point before any ascorbate reduction, the difference between the total copper concentration and the Cu(II) component derived from the EPR detectable copper was presumed to be the Cu(I) component of the mixed valence complex. For the sample analyzed after ascorbate reduction, the EPR sample was thawed, the OD at 1000 nm measured, and the concentration of EPR detectable copper was now used as the concentration of MV complex, since ascorbate was deemed to have reduced all of the Cu(II) not contained in the MV. These calculations led to 3 independent measurements of the MV extinction coefficient (per protein) as shown in Table 5-S2 which average to 516 ± 16 $M^{-1}cm^{-1}$.

5.8 Discussion

Understanding the mechanism of copper monooxygenase such as PHM and DBM has been a topic of intense interest in the field of copper biochemistry, and more broadly in the biomedical community since these enzymes catalyze pharmacologically important processes. Based on an accumulation of evidence, we and others have advanced the idea that the mechanism proceeds via an "open-to-closed" conformational gate that allows the resting mononuclear copper state (Cu-Cu= 10 – 14 Å) to transition to a binuclear copper state (Cu-Cu = 4- 5 Å) induced by some structural or chemical event along the reaction coordinate. In a previous report, we suggested that the open to closed transition might be induced by binding of the anionic substrate to the protonated R240 residue coupled to reduction of the two Cu(II) centers to Cu(I), a process that reduces the net charge in the active site pocket from +5 to +2, and thereby significantly diminishes the electrostatic repulsion between the H and M subdomains. The existence of structures of closed conformers of both PHM and DBM, albeit of only partial copper occupancy, together with supporting evidence from QM/MM calculations that the open-to-closed mechanism is energetically feasible, and indeed that subdomain closure costs a mere 2 kcals mol^{-1}, has spurred efforts to develop approaches to the isolation and characterization of binuclear states that retain their full complement of copper and that can be studied spectroscopically.

Recently we reported the discovery of a binuclear state of PHM in complex with the peptidyl inhibitor AAF-hCys where we proposed that the inhibitor binds in a bifunctional fashion, with the C-terminal carboxylate occupying the usual peptidyl binding site at R240 and Y318, and the thiol from homocysteine coordinating copper, and bridging between the CuM and CuH sites. The evidence for bridging was derived from the Cu K-EXAFS of the ascorbate-reduced forms which required a Cu-S shell occupancy of 1.5 in the native enzyme which dropped to 1S per Cu in the M314H variant where the M-site coordinating methionine was absent. An additional feature of the AAF-hCys-bound system was the formation of an unusual and extremely stable mixed-valence species when the inhibitor reacted with the fully oxidized enzyme. Since a MV intermediate had been proposed as the

initiator of hydrogen atom abstraction (HAT) chemistry in Wang's QM/MM study, observation of a stable MV entity carried additional significance.

In the present study we extended these studies to provide unambiguous evidence for the binuclear state. Substitution of the thiol of homocysteine with selenol provided an additional spectroscopic window via the ability to probe the Se-Cu interactions at both the Cu and the Se X-ray absorption edges. After solving the challenging issue of diselenide reduction, we were successful in forming the AAF-hSeCys-PHM complex in both the fully reduced and mixed-valence states. The fully reduced derivative gave conclusive evidence for the Se bridge between the two coppers where the Se EXAFS data gave a Se-Cu shell occupancy of 1.8, twice that of the Cu-Se shell occupancy (0.85) measured at the Cu edge. Of particular importance, the metrical parameters and DW factors were exactly mirrored at each absorption edge, as required for validation of the chemical model. Our results showed that stoichiometric addition of peptide led to ~90% formation of the bridged species.

The AAF-hSeCys peptide was also able to form the mixed valence species, giving rise to a UV-vis absorption spectrum with a red-shifted NIR band, but similar higher energy features. Red shifted Se-Cu(II) CT bands have been observed in a SeCys analogue of azurin [181,182] suggesting that the more reducing Cu(II)-Se interaction lowers the energy of the half-filled LUMO, and/or stabilizes the transient Cu(I) species in the excited state. Studies on selenium and sulfur Cu(I) biomimetic complexes[183,184] have also demonstrated a strong decrease in redox potential (increased reducing power) and strong stabilization of Cu(I) by the selenium ligand. However, any analysis of the UV-vis data for this apparent MV complex must make assumptions as to which of the two Cu centers (H or M) is reduced and which remains oxidized. In the absence of bound substrate, the M-site redox potential is more negative by 285 mV, although the two potentials equalize at +83 mV when the substrate Ac-YVG is bound.[109] This may suggest that the M-center is more favorable for Cu(II) binding, and when coordinated by a chalcogenide ligand would exhibit a "cupredoxin-like" His_2-Met-S/Se(Cys) ligand set, which has been described in terms of the coupled distortion model.[185,186].

Cupredoxins such as plastocyanin and azurin have distorted tetrahedral symmetry with the Cu(II) center coordinated by 2 His and one Cys residue in roughly trigonal arrangement and a long weak axial interaction with the thioether of a methionine residue. These classic "blue" or type I copper proteins exhibit intense low energy (~600 nm) S(p_π) to Cu(II) charge transfer absorption bands and short Cu-S distances (2.07 – 2.15 Å) associated with the strong covalency of their $d_{x^2-y^2}$ to S-p π-bond. A weaker band assigned as a S(p_σ) to Cu(II) CT is observed around 400 nm[187,188]. As the protein structures across the cupredoxin family are perturbed the coordination geometry of the copper center distorts such that the overlap between the Cu(II) d(x^2-y^2) and the S(p_σ) increases while that with the Sp($_\pi$) weakens and loses intensity. The distortion causes the interaction with the axial ligand to increase, and In the limit of a strong axial interaction a 5-coordinate distorted square pyramidal site is formed of the type found in the "red" copper proteins nitrosocyanin[189,190] and Sco [145]. The latter exhibit normal Cu-S distances around 2.25 Å and dominant higher energy LMCT bands between 350 and 400 nm due to ligand-σ to Cu(II) charge transfer[145,191]. Green copper proteins such as nitrite reductase have intermediate LMCT behavior where weakened Sp($_\pi$) together with lower energy ligand-σ interactions result in two bands of almost equal intensity between 460 and 500 nm[186]. However, while the coupled distortion model is an excellent basis for discussing cupric thiolate and selenolate electronic spectra, significant diversity exists within the family, a notable example being the "green" center of AcoP from *Acidithiobacillus ferrooxidans* where a long Cu-S(cys) bond of 2.23 Å is not compensated by a shortened axial Cu-S(Met) bond [192].

The electronic absorption spectra of the sulfur-containing AAF-hCys complexes of PHM shows very similar properties to that of AcoP while EXAFS gives a long Cu-S distance (2.25 Å) accompanied by uncompensated long Cu-S(Met) distances. [137] The Se complex, on the other hand, while showing a normal Cu-Se bond (2.39 Å), appears to have a compensatory short Cu-S(Met) bond (2.20 Å). This could be due to different degrees of ligand set distortion arising from the thiolate versus the selenolate coordination, perhaps as the result of varying interaction of the chalcogenide with the Cu(I) component of the

ligand bridge. This interpretation is reasonable in light of the anticipated stronger Cu(I) selenolate interaction.

While not yet validated experimentally, the binuclear formulation explains experimental data that are poorly accounted for in the mononuclear mechanism. First, contrary to expectation from model studies in organic solvents at low-temperature,[70,164,167-174] O_2 appears unreactive towards *water soluble* mononuclear M-site protein analogues engineered into the small metallochaperone scaffold CusF.[102] Both Cu(II) and Cu(I) derivatives could be formed by simple reconstitution with either aqueous Cu(II) or Cu(I)-acetonitrile, and these faithfully reproduced the spectroscopy of the WT, CO- and azide-complexes of the PHM M-site. To test the oxygen reactivity we exposed the Cu(I) complex to air in the presence of sodium azide and monitored the appearance of any Cu(II)-azido species at 390 nm but observed no reaction over a period of 24 h. If O_2 reacted with the mononuclear Cu(I)His_2Met ligand set to form a Cu(II)-superoxo, azide should displace the $O_2^{-\bullet}$ which would then rapidly disproportionate in aqueous solution to O_2 and H_2O_2 leading to full formation of the Cu(II)-azido complex.

A second compelling line of evidence in favor of a binuclear intermediate stems from peroxide shunt chemistry.[66] In earlier work we reported that product could be formed catalytically from oxidized PHM and hydrogen peroxide, but when $H_2{}^{18}O_2$ was used as the source of O in the product the hydroxylated isomer contained 60 percent ^{16}O due to exchange with ambient molecular oxygen. Solvent was eliminated as the origin of the ^{16}O by testing the reaction of $H_2{}^{16}O_2$ in D_2O where no exchange was observed. Under strictly anaerobic conditions, product formation and peroxide consumption were tightly coupled, and the rate of product formation was identical to that measured under aerobic conditions. The result required the reaction to cycle through an intermediate where a Cu(II)-peroxide or hydroperoxide is in equilibrium with a Cu(I) dioxygen species. The simplest explanation for this chemistry would be a species similar to that of the well characterized binuclear copper centers of hemocyanin and tyrosinase, [193,194] but at the time we were reluctant to propose such an entity in PHM since there was no evidence for any closed conformations. Instead we proposed that peroxide first reduced CuH

generating Cu(I)H and superoxide, and the latter then channeled across the 11 Å solvent-filled cleft where it bound as the Cu(II)M superoxo species which was theoretically in equilibrium with Cu(I)-dioxygen. In retrospect, this mechanism has serious flaws; (i) it requires peroxide to act as both a reductant and oxidant under the same conditions, (ii) crystallography has shown that peroxide binds only at CuM[101] and (iii) superoxide should leak from the site leading to uncoupling of peroxide consumption from product formation. Therefore, access to a binuclear state via a closed conformation seems a more plausible explanation.

A third observation not readily accommodated by the canonical mechanism derives from kinetic isotope studies on the H172A variant. Removal of a CuH ligand might be expected to reduce ET rates from H to M and indeed the mutation lowered rates of electron transfer 400 - 2000 fold. However, a much larger effect was observed for the H atom abstraction (HAA) step where the rate was reduced by a factor of 12000 relative to WT. This implies that H172A has a large influence on the energy and/or dynamics required to form the transition state within which HAA chemistry can proceed. While this might involve solvent-induced reorganization of H-bonding pathways or global conformational effects that perturb the structure of the ES complex, the magnitude of the effect suggests direct structural involvement of this ligand in the transition state.

Other data underscore the requirement for substrate triggering of catalysis via induction of an active state such as the closed conformer. Substrate binding is always completely coupled to product hydroxylation even with slow substrates and/or slow variants establishing that substrate activation is required to generate the catalytically active species.[40,82,103] Furthermore, structural evidence for substrate-induced perturbation of CuM electronic and/or geometric structure is well-documented from CO reactivity where the CO stretching frequency for CuM-CO complex is red shifted by 30 cm^{-1} in the presence of the substrate Ac-YVG. It has been suggested that this shift may be due to formation of a bridging or semi-bridging mode previously attributed to homo- or hetero-bimetallic systems[42,50,52,114].

The stability of the MV complexes is remarkable where both S- and Se- complexes are stable for hours at room temperature. In the presence of reducing agents (5 mM ascorbate) both complexes undergo slow bleaching due to reduction of the Cu(II) component. As mentioned above, the recent QM/MM study invoking the open-to-closed mechanism has predicted a MV complex with a bridging peroxo ligand as an energetically feasible intermediate for H atom abstraction from the substrate C-alpha. The inherent stability of the PHM active site in a MV form adds experimental validation to this premise, since active sites built to accommodate MV species are rare, unless they are mechanistically relevant. We may speculate that in the absence of an exogenous bifunctional reagent such as AAF-hCys, a viable path to a *catalytic* MV intermediate would be an imidazole bridge formed by sharing of a His residue between both Cu centers. H-site ligand H172 is a good candidate for this role, since *vide supra*, this His must play an essential role in the structural organization of the chemical intermediate.[41] Other candidates include hitherto unidentified protein side groups or hydroxide from solvent. Further studies using C-terminal histidine- and threonine containing tetrapeptides are underway to test these possibilities.

5.9 Materials and Methods

5.9.1. Materials

All materials were of reagent grade and were purchased from Sigma-Aldrich unless stated otherwise. Peptidylglycine monooxygenase catalytic core (residues 42 – 356) was produced from recombinant chinese hamster ovary cells (CHO) in a Accusyst MiniMax hollow fiber bioreactor (Cell Culture Co., Minneapolis) using methodologies previously described [82,106]. Enzyme purification, copper reconstitution, and copper to protein analysis were performed as previously described [82,106,195]. Protein concentration was determined from the OD_{280} (1%) = 0.985, and copper and selenium concentrations were determined by inductively coupled plasma optical emission (ICPOES) spectrometry on a Perkin Elmer Optima 2000 ICPOES instrument. Enzyme samples used in this work were >95% pure by SDS gel electrophoresis and routinely contained 2.0 ± 0.1 Cu atoms per monomer of 35 kDaltons.

5.9.2 Solid-phase synthesis, purification, and mass spectrometry characterization of the AAF-hSeCys peptide

The AAF-hSeCys and AAF-SeMet peptides were synthesized on a Chorus peptide synthesizer (Protein Technologies Inc.). The synthesis followed standard Fmoc procedures provided by the manufacturer and was carried out on a 0.10 mmol scale. All natural Fmoc-amino acids were purchased from Protein Technologies Inc. Fmoc-hSeCys(pMOB)-OH and Fmoc-L-Selenomethionine were purchased from ChemPep (#350313 and #351303). For the syntheses, 300 mg of 2-chlorotrityl chloride resin 100-200 mesh (ChemPep) was loaded with 0.10 mmol of Fmoc-hSeCys(pMOB)-OH or Fmoc-L-Selenomethionine. The resin was washed three times with 5 mL N,N-dimethylformamide (DMF) and three times with 5 mL dichloromethane (DCM). Each respective Fmoc amino acid (AA) was dissolved in 1 mL of 1:1 DCM with 0.15 mmol diisopropylethylamine (DIPEA). This solution was added to the resin and gently shaken for 1 hour. The Fmoc-AA/DIPEA solution was then drained from the resin, and the resin was washed three times with 5 mL of DCM. The uncapped sites on the resin were capped by washing with 20 mL of 17:2:1 DCM:methanol. The resin

was then washed three times with 5 mL of DCM and three times with 5 mL of DMF. The resin was then transferred to the reaction vessel.

All Fmoc-amino acids (0.60 mmol, 6 equivalents) were coupled by in situ activation with (1-[bis(dimethylamino)methylene]-1H-1,2,3-triazolo[4,5-b]pyridinium 3-oxide hexafluorophosphate (HATU) (0.60 mmol, 6 equivalents; ChemPep) in 0.6 M N-methylmorpholine. The AAF-hSeCys peptide was deprotected and cleaved from the resin in a solution containing 96% (v/v) trifluoroacetic acid (TFA), 2% (v/v) water (H_2O), and 2% (v/v) triisopropylsilane (TIS). 5mL of the cleavage buffer was added to the resin and the slurry was stirred at 50 °C for 4 hours. The cleavage reaction was filtered into 30 mL of ice-cold diethyl ether to precipitate the peptide. The solution was centrifuged at 11,000 x g for 3 minutes and the supernatant was decanted. The remaining residue was re-suspended in 30 mL of ice-cold diethyl ether and centrifuged again at 11,000 x g for 3 minutes. The supernatant was decanted once more, and the remaining residue was placed under a slow-flow nitrogen line for 10 minutes to evaporate any residual diethyl ether. The remaining peptide residue was re-suspended in 20 mL of water, flash frozen in liquid nitrogen, and lyophilized. The AAF-SeMet peptide underwent the same process but was cleaved for 2 h at RT instead.

The peptides were purified using high-performance liquid chromatography (HPLC) with a Phenomenex Jupiter C18 preparative column (21.2 mm x 250 mm, 5 µm particle size, 300Å pore size) with buffer A as 0.1% trifluoroacetic acid (TFA, HPLC grade) in nanopure water and buffer B as 0.1% TFA (HPLC grade) in acetonitrile (ACN, HPLC grade). The separation used a flow rate of 5 mL/min with a linear gradient of buffer A from 88% to 55% over 70 minutes. The deprotected diselenide peptide eluted at 49 minutes under these conditions and the AAF-SeMet peptide eluted at 44 minutes. Fractions were analyzed by LC-MS using a HPLC-HRMS setup (Vanquish UHPLC with a diode array detector connected to a Q-Exactive) fitted with a Hypersil GOLD C18 column (2.1 mm x 150 mm, 1.9 µm particle size) for separations at 0.2 mL/min. The LC-MS program for peptide fraction identification was set up as follows: buffer A was LC-MS Optima water (Fisher)/0.1% (v/v) LC-MS Optima TFA (Fisher) and buffer B was LC-MS Optima ACN

(Fisher)/0.1% (v/v) LC-MS Optima TFA (Fisher). The 15-minute separation consisted of washing the column with 100% A for 3 minutes, followed by a linear gradient to 100% B from 3 to 6 minutes, followed by washing the column with 100% B from 6 to 9 minutes, a decreased gradient from 100% B to 0% B over 9 to 12 minutes, and finally re-equilibration in 100% A from 12 to 15 minutes. The MS detectors operated in positive ion mode, and the FT analyzer settings were as follows: 70,000 resolution, 1 microscan, and 200 ms maximum injection time. MS data analysis used Xcalibur software (Thermo Fisher). Mass spectra of the peptide products are reported in Figure 5-S6.

5.9.3 Inhibitory effects of reductants on PHM activity

To determine if DTT and borohydride interfered with enzyme activity an oxygen consumption experiment was performed using a Rank Brother oxygen electrode as previously described.[119] Similar procedures were used to test the inhibitory effect of DTT and $NaBH_4$. For $NaBH_4$ three separate reactions were performed, each in 2 ml of buffered solution (50 mM MES pH 5.5, 30 mg/ml catalase, 25 µM $CuSO_4$, 100 µM acetyl-YVG substrate) with 1 µM PHM. Reactions were initiated by adding 10 µl of 2 M ascorbate. In the first reaction, normal enzyme activity was assessed with no additional additives, resulting in complete deoxygenation of the buffer over the course of approximately 5 minutes. In the second experiment, after approximately half the oxygen was consumed a small volume of concentrated $NaBH_4$ in DMSO was added to a final concentration of 50 µM. The reaction was instantly arrested, accompanied by the formation of hydrogen gas. In the final reaction, after approximately half the oxygen was consumed a small volume of concentrated borohydride in DMSO quenched with 1 molar equivalent of TFA was added to a final concentration of 50 uM, resulting in no decrease in catalytic rate.

5.8.4 Generation of TFA quenched, borohydride reduced, AAF-hSeCys peptide.

50 µl of 50 mM AAF-hSeCys peptide in anhydrous anaerobic DMSO was thawed in a Vacuum Atmospheres anaerobic chamber (oxygen < 1 PPM). Peptide was reduced by adding 1 M $NaBH_4$ in DMSO to a final concentration of 250 mM (5 molar equivalents), which resulted in rapid evolution of hydrogen gas. The solution was allowed to react for 30

minutes after which the remaining excess borohydride was quenched via the addition of 250 mM TFA (1 molar equivalent per initial borohydride concentration), again resulting in rapid evolution of gas. After 5 minutes another 0.2 molar equivalents of TFA was added resulting in no further effervescence. The solution of TFA quenched AAF-hSeCys peptide was then transferred to a septum-sealed vial for use in further experiments.

5.9.5 XAS sample preparation of AAF-hSeCys peptide with borohydride

50 µl of 50 mM AAF-hSeCys peptide in anhydrous anaerobic DMSO was thawed in the anaerobic chamber as above and used to make a 2 mM stock solution in 50 mM sodium phosphate buffer pH 7.5 with 20% ethylene glycol as a cryoprotectant. Samples reduced with 1 molar equivalent (2 mM) borohydride, 5 molar equivalents (10 mM), and 5 molar equivalents followed by a TFA quench were prepared as above and transferred to EXAFS cuvettes. The samples were frozen by rapid immersion in liquid nitrogen and stored under liquid N_2 before loading into cassettes at the beam line.

5.9.6 XAS sample preparation of reduced PHM with AAF-hSeCys peptide

900 uM PHM (1.8 mM in Cu) in 50 mM sodium phosphate buffer pH 7.5 was brought into the anaerobic chamber and allowed to degas exhaustively overnight. Once degassed the PHM solution was reduced via the addition of 5 mM sodium ascorbate, resulting in an immediate color change from blue to clear. Parallel to this, TFA-quenched AAF-hSeCys peptide was prepared using the protocol described above. Two 100 µl samples of 900 µM PHM with either 1 or 2 molar equivalents per protein of AAF-hSeCys peptide were prepared in 50 mM sodium phosphate pH 7.5 with 20% ethylene glycol. For the 1:2 sample any excess peptide was then removed using spin-desalting columns pre-equilibrated with 50 mM sodium phosphate pH 7.5, 5 mM ascorbate and 20% ethylene glycol. All samples were loaded into XAS cuvettes, flash frozen in liquid nitrogen, and stored under liquid nitrogen until data collection.

5.9.7 Titration of oxidized PHM with TFA-quenched AAF-hSeCys peptide

UV-vis spectra were collected on a Varian Cary 50 UV-vis spectrophotometer between 300 and 1100 nm. A 1 ml solution of 600 µM oxidized PHM (1.2 mM Cu) in 100 mM sodium phosphate buffer pH 7.5 was transferred to a quartz cuvette. Aliquots of 0.5 molar equivalents of anaerobic TFA-quenched reduced AAF-hSeCys were added via syringe and mixed by inverting the cuvette. During the titration the solution turned from blue to deep purple. In some experiments, precipitation was observed, and these samples were spun at 10000 x g for 2 minutes to clarify the solution. Spectra were measured immediately after mixing and again after 5 minutes at a scan rate of 1200 nm/min. Aliquots of peptide were added until no further increase at 1000 nm was observed.

5.9.8 Reduction of the mixed valence complex by ascorbate

Reduction kinetics of the purple MV species were assessed after the titration had reached a maximum absorbance. 2 M stock sodium ascorbate was added to a final concentration of 5 mM and mixed by gentle inversion of the cuvette. Spectra were collected every 5 minutes for 2 hours, then every hour for the next 24 hours.

5.9.9 EPR of oxidized PHM, mixed valence, and ascorbate-reduced mixed valence species

300 µl of oxidized PHM (600 uM, 1.2 mM in Cu) was frozen in a quartz EPR tube. Further EPR samples were derived from the UV-vis titration to ensure comparability. After the final addition of AAF-hSeCys peptide, 300 µl of this solution was transferred to an EPR tube. Immediately after the addition of 5 mM ascorbate another 300 µl was removed and placed in a EPR tube and frozen as quickly as possible (approximately 3 minutes) to minimize reduction of the MV species. A final 300 µl was removed after 24 hours of reduction and placed in a EPR tube. EPR data were collected on a Bruker E500 X-Band EPR spectrometer with a liquid nitrogen cryostat. Spectra are averages of 4 scans and collected at a frequency of 9.396 GHz, 170K temperature, 2 mW microwave power, and 2 gauss modulation amplitude. Spectra at higher powers and different modulation amplitudes were also measured to check for power saturation and/or modulation broadening (not observed). Experimental data were simulated using EasySpin. [155]

5.9.10 Titration of oxidized PHM with AAF-SeMet and reduction with ascorbate

UV-vis spectra were collected similarly as above. 1 ml of 600 uM oxidized PHM (1.2 mM Cu) in 100 mM sodium phosphate buffer pH 7.5 was transferred to a quartz cuvette. Aliquots of AAF-SeMet peptide in 50% methanol, 50% 100 mM sodium phosphate buffer were added, then mixed by inversion of the cuvette. Slight cloudiness was observed and removed by spinning at 10000 x g for 2 minutes. Spectra were taken immediately and after 5 minutes at a scan rate of 1200 nm/min. Aliquots were added up to 5 molar equivalents which elicited only minor perturbation of the oxidized PHM spectrum. The spectra are shown in Figure 5-S9.

After the titration to 5 molar equivalents, 600 μM sodium ascorbate was added to assess if the addition of one molar equivalent per copper of a reducing agent could induce the formation of a mixed valence complex. This reaction resulted in decrease in the 650 nm Cu(II) d-d band but did not elicit any bands in the MV region.

5.10 Acknowledgements

Use of the Stanford Synchrotron Radiation Lightsource, SLAC National Accelerator Laboratory, is supported by the U.S. Department of Energy (DOE), Office of Science, Office of Basic Energy Sciences under Contract No. DE-AC02-76SF00515. The SSRL Structural Molecular Biology Program is supported by the DOE Office of Biological and Environmental Research, and by the National Institutes of Health, National Institute of General Medical Sciences (P30GM133894). The authors would like to thank Tamar Conner for assistance with cell growth and protein purification.

Chapter Six: Summary and Future Directions

6.1 Chapter Summaries

These studies sought to evaluate the binuclear, open to closed, mechanism of PHM via kinetic, spectroscopic, and structural methodologies to determine if this hypothesis performs better than the mononuclear canonical mechanism. Here we summarize each chapter's contribution to this hypothesis and compare how well it supports an open-closed mechanism over the canonical mechanism.

6.1.1 Summary of Chapter Three

Chapter three explored the roles of oxygen and ascorbate as initiators and drivers of reaction. The first observation was the relative indifference of reduced diCu(I) PHM to oxidation by dioxygen. This is perhaps not surprising in the context of PHM's firm stoichiometry where unproductive oxygen consumption is not observed. At the same time, it is a mark against the canonical mechanism that predicts oxygen binding as a key reaction initiator. This observation suggests that there is some other step or series of steps on which oxygen binding is predicated.

The next observation was the discovery that fully reduced, ascorbate free, PHM does not react to completion. Or, put another way, only a minority population of PHM undergoes turnover without exogenous ascorbate. Increasing concentrations of ascorbate bias the population increasingly towards a reactive state, pushing stoichiometry closer to 100%. Simultaneously, FTIR experiments provide a spectroscopic signal for this reactive state. Without excess ascorbate the bulk of enzyme is in a configuration that yields a 2093 cm^{-1} band, typical for CO bound to a single copper site with a His_2Met ligand set. Increasing concentrations of ascorbate bias that population towards a species that produces a 2063 cm^{-1} IR band. This demonstrates that substrate and ascorbate work together combinatorially to induce a reactive conformation of the enzyme and correlate that reactivity to the 2063 cm^{-1} state of the enzyme, although it does not define what that reactive conformer is.

These observations together suggest a regime where the enzyme is in equilibrium between a reactive and unreactive state and that ascorbate, substrate, and oxygen combinatorially induce the enzyme to a reactive state. These observations are directly in support of the open-closed hypothesis and are difficult to reconcile with the canonical mechanism. Wang's QM/MM mechanism hypothesizes that hydrogen atom abstraction from ascorbate is energetically favorable, and that this hydrogen atom abstraction is a key initiator of the enzyme closing. The requirement for exogenous ascorbate for reactivity lends support to this idea. However, other mechanisms for ascorbate activation, such as binding in the active site pocket to generate a closed conformer are also possible. Furthermore, the presence of a closed conformer provides a very good explanation for the 2063 cm^{-1} IR band – a bridged or semibridged species where the copper sites are coupled.

6.1.2 Summary of Chapter Four

Chapter four explores the possibility of crystallizing and characterizing alternate conformers of PHM. Our goal was to find crystallization conditions or mutations that could produce the structure of a closed conformer, ideally complexed with substrate. In this goal we were ultimately unsuccessful. Attempts to crystallize in the presence of ascorbate, substrate, and carbon monoxide (modeling the conditions that partition the enzyme towards 2063 cm^{-1}) resulted in crystals that despite their size were extremely poor diffractors (result unpublished). We can only speculate why this condition was unsuccessful, but given the hypothesis that substrate, ascorbate, and oxygen induce a conformational change it is perhaps not surprising that those conditions failed to produce a well-ordered crystal.

Serendipitously, we were successful in crystallizing an alternate conformation anyway. PHM crystallized in a microaerobic environment was found in a previously unseen configuration with a Cu-Cu distance of 14 Å. The existence of a WT PHM structure with an altered Cu-Cu distance is important evidence for the open-closed hypothesis. A key requirement for this hypothesis is a low energy barrier (calculated to be 2kcal / mol) between conformational states.

A similar configuration was also crystallized in two mutants, Q272A and Q272E. Why these mutants preferentially adopt the fully open 14 Å configuration is not entirely clear. In the case of Q272E it is speculated that changes to hydrogen bonding stabilize the closed conformer relative to the open one. Why the Q272A (which lacks that hydrogen bond) crystallizes in the fully open conformer is almost entirely enigmatic, and in truth likely has more to do with crystallization conditions than the mutation itself.

Nonetheless, these structures, particularly the WT "fully open" structure, provide irrefutable evidence that the Cu-Cu distance is not immutable. Reorganization around the hinge domain is possible and a wide range of Cu-Cu distances are possible. These experiments also demonstrate one general challenge to interpretation that must be considered when PHM crystal structures are discussed. Crystallization provides a snapshot of an enzyme's structure, and while that snapshot is potentially very useful, it does not preclude the existence of other structures. Or, put another way, a crystal structure at one Cu-Cu distance does not refute other distances.

6.1.3 Summary of Chapter Five

Chapter five provides the strongest evidence of a coupled binuclear reaction so far collected. The goal of these experiments was to find a substrate analogue or inhibitor that held the enzyme in a closed conformer. Prior experiments indicated that n-terminal homocysteine peptides were potent inhibitors of PHM[142]. The mechanism of this inhibition was not conclusively known, but it was suspected that the thiol group of the C-terminal homocysteine bound tightly to the CuM, resulting in inhibition.

Given the putative mechanism and the previous experiments suggesting that a closed conformer might be important to reactivity, it was logical that the thiol might form a bridged species between the two copper centers. In truth our expectation was that a bridged thiol was an unlikely but potentially very interesting outcome. This outcome was realized, as the addition of AAF-hCys resulted in the immediate formation of an intense 925 nm^{-1} UV-Vis band. This characteristic spectroscopic feature was indicative of an IVCT

band, which we suspected was due to a mixed valence interaction between the two copper centers.

To test that suspicion we performed EPR and XAS on PHM bound with AAF-hCys peptide. In both cases we found conclusive evidence of a binuclear form of the enzyme. EPR found clear evidence of a binuclear mixed valence which persisted after reduction by ascorbate. XAS also found evidence of a bridged species in the fully reduced form, although with initial ambiguity. XAS indicated that there were 1.5 sulfurs per copper, which was hypothesized to be one bridged sulfur seen by both copper centers, and the M314 sulfur seen by the CuM site alone (therefore contributing .5 sulfurs per copper). To remove any ambiguity the XAS was also performed with an M314H mutant (lacking that extra sulfur), which gave precisely 1.0 copper to sulfur ratio. These spectroscopic observations provide extremely powerful evidence of a binuclear, closed form of the enzyme.

As confirmation of the veracity of this binuclear state, a final set of experiments were performed. One particularly powerful use of XAS is correlating one absorption edge associated with the enzyme to another absorption edge associated with the substrate. By having two different absorbing atoms the different “perspectives” of the absorbing atoms can be compared, which gives additional information and surety. To that end, we employed a selenium containing peptide, AAF-homoselenocysteine (AAF-hSeCys).

Using AAF-hSeCys peptide opens another spectroscopic window into the conformational dynamics of PHM. This peptide recapitulated the IVCT mixed valence UV-Vis band, with appropriate shifting due to the incorporation of a selenium ligand. From there we conducted XAS on the complex with reduced PHM, which gave .85 selenium per copper and 1.8 copper per selenium, each with precisely the same parameters. This correlation from two different metal centers is irrefutable evidence that this peptide bridges the two copper sites.

This study gives the strongest evidence to date of an open-closed mechanism. First, the existence and remarkable stability of a mixed valence IVCT band. The mechanism

proposed computationally by the Wang lab is predicated on the formation of a mixed valence species, so the detection of a mixed valence, particularly one so stable, is significant. Second is the unambiguous detection of a bridged binuclear form of the enzyme. This demonstrates that WT PHM can undergo a conformational change to a closed conformer in solution.

6.2 Future Directions

Structural confirmation of a closed conformer remains the most elusive evidence for a binuclear intermediate. The canonical mechanism was itself founded on crystal structures, especially the dioxygen bound "precatalytic" structure. Refutation of the closed conformer is equally based on its apparent absence in structural studies. Crystallographic studies have so far been insufficient, ultimately suggesting that the closed conformer may not be crystallizable.

Cryo-electron microscopy (Cryo-EM) is an alternate structural approach with many advantages over crystallographic approaches. The much-touted advantage is the increased resolution with difficult to crystallize proteins. A high-resolution structure would certainly be valuable and potentially informative, but the real value of Cryo-EM for this study is something different. Crystallography fundamentally strips information about protein dynamics away, forcing the protein into a single repeated structure. Cryo-EM can be conducted at near native conditions where the entire gamut of conformational states is available, although separating and classifying those conformational states is nontrivial[196].

Unfortunately, PHM is only a 36 kDa protein and traditional lower limits for Cryo-EM are around 80 to 100 kDa depending on protein specifics. Therefore, we have turned our attention back to the bifunctional enzyme PAM and its sister enzyme DBM. PAM is a ~70 kDa protein, although various isoforms have different masses which is near the limit for Cryo-EM[7]. DBM is a 65 kDa molecule, but it is found natively as a dimer or tetramer which puts it well above the Cryo-EM size limit. (130 kDa or 260 kDa respectively)[31]. Thus, synthesis and purification of high quality DBM and PAM are the current focuses of the lab.

The production of DBM protein enables parallel experiments to be performed to corroborate our current model. DBM offers several advantages and challenges compared to PHM for such experiments. Firstly, it has been found natively in a closed conformer, including as an open-closed heterodimer, removing ambiguities of the physiological relevance of such a closed conformer. At the same time, these heterodimers could make the assignation of spectroscopic signals very challenging and add challenges to experimental design. Secondly, unlike PHM which is the catalytic core of a subdomain of a larger protein, DBM is essentially a native protein. This increases its relevance and assuages concerns that its reactivity is an artifact of the protein construct, but at the same time increases the overall complexity of the system.

Spectroscopic experiments on PAM are also potentially informative. One hypothesis is that DBM heterodimers employ a coupled conformational change where movement at one monomer influences the other. Under this hypothesis it's entirely possible that a similar mechanism is at play in PAM, where reactivity and conformational movement at the PHM domain is influenced by the PAL domain. FTIR experiments with PAM might be particularly fruitful, where the presence of the PAL domain may change the populations of 2063 cm^{-1} and 2093 cm^{-1} bands.

There are also several interesting synthetic peptide experiments that could be conducted. Thus far we have employed alpha-substituted substituted synthetic peptides and generated informative spectroscopic data, but the generation of beta-substituted peptides is also possible. Because PHM and by extension PAM transfer an electron to the alpha-carbon it is possible that by moving the functional group to the beta carbon it will allow the enzyme to perform some parts of its reactivity. This could result in the formation, and potentially trapping, of a radical species which would then be detectable by EPR.

A relatively simple but potentially very informative experiment is cleaving the PHM into its separate CuM and CuH domains and testing reactivity in solution. Under the canonical mechanism this approach would be expected to result in reactivity, albeit perhaps at a reduced rate, as the CuH site would still be present to provide electrons and

the CuM site. Under our proposed mechanism, which is contingent on an orchestrated conformational change, the reactivity would likely be entirely abrogated.

One final approach, although not part of our lab's core competency, would be to use a computational approach to search for energetically accessible conformers. This workflow combines DFT, ideally with a more modern functional, solvation model, etc with a conformational search algorithm. This includes algorithms such as CREST[197] (Conformer-Rotamer Ensemble Sampling Tool) which examines the conformational space of a molecule of interest to find energetically available conformers. These conformers then run back through the DFT workflow to make chemical predictions.

6.3 Conclusion

To conclude, this series of spectroscopic, kinetic, and structural studies demonstrate powerful evidence for a binuclear, open-to closed hypothesis in copper monooxygenases. They represent a large step forward in our understanding of these important and enigmatic enzymes and will hopefully help other researchers design cogent experiments, synthetic complexes, and targeted therapeutics.

References

1 Eipper, B. A., Stoffers, D. A. & Mains, R. E. The Biosynthesis of Neuropeptides: Peptide alpha-Amidation. *Annual Review of Neuroscience* **15**, 57-85 (1992). https://doi.org/10.1146/annurev.ne.15.030192.000421

2 Merkler, D. J. C-Terminal amidated peptides: Production by the in vitro enzymatic amidation of glycine-extended peptides and the importance of the amide to bioactivity. *Enzyme and Microbial Technology* **16**, 450-456 (1994). https://doi.org/10.1016/0141-0229(94)90014-0

3 Suchanek, G. & Kreil, G. Translation of melittin messenger RNA in vitro yields a product terminating with glutaminylglycine rather than with glutaminamide. *Proc Natl Acad Sci U S A* **74**, 975-978 (1977).

4 Eipper, B. A., Milgram, S. L., Husten, E. J., Yun, H. Y. & Mains, R. E. Peptidylglycine alpha-amidating monooxygenase: a multifunctional protein with catalytic, processing, and routing domains. *Protein Sci* **2**, 489-497 (1993).

5 Bradbury, A. F., Finnie, M. D. A. & Smyth, D. G. Mechanism of C-terminal amide formation by pituitary enzymes. *Nature* **298**, 686-688 (1982). https://doi.org/10.1038/298686a0

6 Eipper, B. A., Mains, R. E. & Glembotski, C. C. Identification in pituitary tissue of a peptide alpha-amidation activity that acts on glycine-extended peptides and requires molecular oxygen, copper, and ascorbic acid. *Proc Natl Acad Sci U S A* **80**, 5144-5148 (1983).

7 Eipper, B. A. *et al.* Structure of the Precursor to an Enzyme Mediating COOH-Terminal Amidation in Peptide Biosynthesis. *Molecular Endocrinology* **1**, 777-790 (1987). https://doi.org/10.1210/mend-1-11-777

8 Eipper, B. A. *et al.* Peptidyl-alpha-hydroxyglycine alpha-amidating lyase. Purification, characterization, and expression. *Journal of Biological Chemistry* **266**, 7827-7833 (1991). https://doi.org/10.1016/S0021-9258(20)89524-6

9 Attenborough, R. M. F., Hayward, D. C., Kitahara, M. V., Miller, D. J. & Ball, E. E. A "Neural" Enzyme in Nonbilaterian Animals and Algae: Preneural Origins for Peptidylglycine α-Amidating Monooxygenase. *Molecular Biology and Evolution* **29**, 3095-3109 (2012). https://doi.org/10.1093/molbev/mss114

10 Jiang, N. *et al.* PHM Is Required for Normal Developmental Transitions and for Biosynthesis of Secretory Peptides in Drosophila. *Developmental Biology* **226**, 118-136 (2000). https://doi.org/10.1006/dbio.2000.9832

11 Fan, X., Spijker, S., Akalal, D.-B. G. & Nagle, G. T. Neuropeptide amidation: cloning of a bifunctional α-amidating enzyme from Aplysia. *Molecular Brain Research* **82**, 25-34 (2000). https://doi.org/10.1016/S0169-328X(00)00173-X

12 Mair, G. R. *et al.* A functionally atypical amidating enzyme from the human parasite Schistosoma mansoni. *The FASEB Journal* **18**, 114-121 (2004). https://doi.org/10.1096/fj.03-0429com

13 Kolhekar, A. S. *et al.* Neuropeptide Amidation in Drosophila: Separate Genes Encode the Two Enzymes Catalyzing Amidation. *J. Neurosci.* **17**, 1363-1376 (1997). https://doi.org/10.1523/JNEUROSCI.17-04-01363.1997

14 Czyzyk, T. A. *et al.* Deletion of peptide amidation enzymatic activity leads to edema and embryonic lethality in the mouse. *Developmental Biology* **287**, 301-313 (2005). https://doi.org/10.1016/j.ydbio.2005.09.001

15 Gaier, E. D., Eipper, B. A. & Mains, R. E. Pam heterozygous mice reveal essential role for Cu in amygdalar behavioral and synaptic function. *Ann N Y Acad Sci* **1314**, 15-23 (2014). https://doi.org/10.1111/nyas.12378

16 Braas, K. M., Stoffers, D. A., Eipper, B. A. & May, V. Tissue Specific Expression of Rat Peptidylglycine α-Amidating Monooxygenase Activity and mRNA. *Molecular Endocrinology* **3**, 1387-1398 (1989). https://doi.org/10.1210/mend-3-9-1387

17 Eipper, B. A. *et al.* Alternative splicing and endoproteolytic processing generate tissue-specific forms of pituitary peptidylglycine alpha-amidating monooxygenase (PAM). *Journal of Biological Chemistry* **267**, 4008-4015 (1992). https://doi.org/10.1016/S0021-9258(19)50625-1

18 Wand, G. S., Ney, R. L., Mains, R. E. & Eipper, B. A. Characterization of peptide alpha-amidation activity in human cerebrospinal fluid and central nervous system tissue. *Neuroendocrinology* **41**, 482-489 (1985). https://doi.org/10.1159/000124223

19 Prigge, S. T., Kolhekar, A. S., Eipper, B. A., Mains, R. E. & Amzel, L. M. Amidation of Bioactive Peptides: The Structure of Peptidylglycine α-Hydroxylating Monooxygenase. *Science* **278**, 1300-1305 (1997). https://doi.org/10.1126/science.278.5341.1300

20 Eipper, B. A., Quon, A. S. W., Mains, R. E., Boswell, J. S. & Blackburn, N. J. The Catalytic Core of Peptidylglycine .alpha.-Hydroxylating Monooxygenase: Investigation by Site-Directed Mutagenesis, Cu X-ray Absorption Spectroscopy, and Electron Paramagnetic Resonance. *Biochemistry* **34**, 2857-2865 (1995). https://doi.org/10.1021/bi00009a016

21 Boswell, J. S., Reedy, B. J., Kulathila, R., Merkler, D. & Blackburn, N. J. Structural Investigations on the Coordination Environment of the Active-Site Copper Centers of Recombinant Bifunctional Peptidylglycine α-Amidating Enzyme. *Biochemistry* **35**, 12241-12250 (1996). https://doi.org/10.1021/bi960742y

22 Yang, T.-Y., Dudev, T. & Lim, C. Mononuclear versus Binuclear Metal-Binding Sites: Metal-Binding Affinity and Selectivity from PDB Survey and DFT/CDM Calculations. *J. Am. Chem. Soc.* **130**, 3844-3852 (2008). https://doi.org/10.1021/ja076277h

23 Brewster, J. T., II *et al.* Synthesis and Characterization of a Binuclear Copper(II) Naphthoisoamethyrin Complex Displaying Weak Antiferromagnetic Coupling. *Inorg. Chem.* **56**, 12665-12669 (2017). https://doi.org/10.1021/acs.inorgchem.7b01669

24 Amini, M., Sheykhi, A., Khandar, A. A. & Janczak, J. Binuclear copper complex as a new dual-use catalyst for cycloaddition and coupling reactions: Synthesis, characterization, and application. *Applied Organometallic Chemistry* **38**, e7472 (2024). https://doi.org/10.1002/aoc.7472

25 Sánchez-Ferrer, Á., Neptuno Rodríguez-López, J., García-Cánovas, F. & García-Carmona, F. Tyrosinase: a comprehensive review of its mechanism. *Biochimica et Biophysica Acta (BBA) - Protein Structure and Molecular Enzymology* **1247**, 1-11 (1995). https://doi.org/10.1016/0167-4838(94)00204-T

26 Maheshwari, S. *et al.* Effects of copper occupancy on the conformational landscape of peptidylglycine α-hydroxylating monooxygenase. *Commun Biol* **1**, 1-11 (2018). https://doi.org/10.1038/s42003-018-0082-y

27 Prigge, S. T., Eipper, B. A., Mains, R. E. & Amzel, L. M. Dioxygen Binds End-on to Mononuclear Copper in a Precatalytic Enzyme Complex. *Science* **304**, 864-867 (2004).

28 Jaron, S. & Blackburn, N. J. Characterization of a Half-Apo Derivative of Peptidylglycine Monooxygenase. Insight into the Reactivity of Each Active Site Copper. *Biochemistry* **40**, 6867-6875 (2001). https://doi.org/10.1021/bi002849y

29 Prigge, S. T., Kolhekar, A. S., Eipper, B. A., Mains, R. E. & Amzel, L. M. Substrate-mediated electron transfer in peptidylglycine α-hydroxylating monooxygenase. *Nat Struct Mol Biol* **6**, 976-983 (1999). https://doi.org/10.1038/13351

30 Jaron, S., Mains, R. E., Eipper, B. A. & Blackburn, N. J. The Catalytic Role of the Copper Ligand H172 of Peptidylglycine α-Hydroxylating Monooxygenase (PHM): A Spectroscopic

Study of the H172A Mutant. *Biochemistry* **41**, 13274-13282 (2002). https://doi.org/10.1021/bi020404z
31 Vendelboe, T. V. *et al.* The crystal structure of human dopamine β-hydroxylase at 2.9 Å resolution. *Sci Adv* **2**, e1500980 (2016). https://doi.org/10.1126/sciadv.1500980
32 Aravind, L. DOMON: an ancient extracellular domain in dopamine β-monooxygenase and other proteins. *Trends in Biochemical Sciences* **26**, 524-526 (2001). https://doi.org/10.1016/S0968-0004(01)01924-7
33 Merkler, D. J., Hawley, A. J., Eipper, B. A. & Mains, R. E. Peptidylglycine α-amidating monooxygenase as a therapeutic target or biomarker for human diseases. *British Journal of Pharmacology* **179**, 3306-3324 (2022). https://doi.org/10.1111/bph.15815
34 Bolkenius, F. N., Ganzhorn, A. J., Chanal, M.-C. & Danzin, C. Selective mechanism-based inactivation of peptidylglycine α-hydroxylating monooxygenase in serum and heart atrium vs. brain. *Biochemical Pharmacology* **53**, 1695-1702 (1997). https://doi.org/10.1016/S0006-2952(97)00051-8
35 Abou-Mohamed, G. A. *et al.* Vascular and Endothelial Actions of Inhibitors of Substance P Amidation. *Journal of Cardiovascular Pharmacology* **35**, 871 (2000).
36 Cao, F. & Easton, C. J. Production and Regulation of Levels of Amidated Peptide Hormones*. *Aust. J. Chem.* **66**, 297-307 (2013). https://doi.org/10.1071/CH12546
37 Jiménez, N. *et al.* Androgen-independent expression of adrenomedullin and peptidylglycine α-amidating monooxygenase in human prostatic carcinoma. *Molecular Carcinogenesis* **38**, 14-24 (2003). https://doi.org/10.1002/mc.10134
38 Thouënnon, E. *et al.* Identification of Potential Gene Markers and Insights into the Pathophysiology of Pheochromocytoma Malignancy. *The Journal of Clinical Endocrinology & Metabolism* **92**, 4865-4872 (2007). https://doi.org/10.1210/jc.2007-1253
39 Horton, T. M. *et al.* PAM staining intensity of primary neuroendocrine neoplasms is a potential prognostic biomarker. *Sci Rep* **10**, 10943 (2020). https://doi.org/10.1038/s41598-020-68071-6
40 Evans, J. P., Ahn, K. & Klinman, J. P. Evidence that dioxygen and substrate activation are tightly coupled in dopamine β -monooxygenase: Implications for oxygen activation. *J. Biol. Chem.* **278**, 49691-49698 (2003).
41 Evans, J. P., Blackburn, N. J. & Klinman, J. P. The Catalytic Role of the Copper Ligand H172 of Peptidylglycine α-Hydroxylating Monooxygenase: A Kinetic Study of the H172A Mutant. *Biochemistry* **45**, 15419-15429 (2006). https://doi.org/10.1021/bi061734c
42 Jaron, S. & Blackburn, N. J. Does Superoxide Channel between the Copper Centers in Peptidylglycine Monooxygenase? A New Mechanism Based on Carbon Monoxide Reactivity. *Biochemistry* **38**, 15086-15096 (1999). https://doi.org/10.1021/bi991341w
43 Blackburn, N. J., Rhames, F. C., Ralle, M. & Jaron, S. Major changes in copper coordination accompany reduction of peptidylglycine monooxygenase: implications for electron transfer and the catalytic mechanism. *JBIC* **5**, 341-353 (2000). https://doi.org/10.1007/PL00010663
44 Francisco, W. A., Merkler, D. J., Blackburn, N. J. & Klinman, J. P. Kinetic Mechanism and Intrinsic Isotope Effects for the Peptidylglycine α-Amidating Enzyme Reaction. *Biochemistry* **37**, 8244-8252 (1998). https://doi.org/10.1021/bi973004y
45 Chen, P. & Solomon, E. I. Oxygen Activation by the Noncoupled Binuclear Copper Site in Peptidylglycine α-Hydroxylating Monooxygenase. Reaction Mechanism and Role of the Noncoupled Nature of the Active Site. *J. Am. Chem. Soc.* **126**, 4991-5000 (2004). https://doi.org/10.1021/ja031564g
46 Cowley, R. E., Tian, L. & Solomon, E. I. Mechanism of O2 activation and substrate hydroxylation in noncoupled binuclear copper monooxygenases. *Proceedings of the*

National Academy of Sciences **113**, 12035-12040 (2016). https://doi.org/10.1073/pnas.1614807113

47 Klinman, J. P. The Copper-Enzyme Family of Dopamine β-Monooxygenase and Peptidylglycine α-Hydroxylating Monooxygenase: Resolving the Chemical Pathway for Substrate Hydroxylation*. *Journal of Biological Chemistry* **281**, 3013-3016 (2006). https://doi.org/10.1074/jbc.R500011200

48 Kolhekar, A. S., Mains, R. E. & Eipper, B. A. in *Methods in Enzymology* Vol. 279 *Vitamins and Coenzymes Part I* 35-43 (Academic Press, 1997).

49 Reedy, B. J. & Blackburn, N. J. Preparation and Characterization of Half-Apo Dopamine-.beta.-hydroxylase by Selective Removal of CuA. Identification of a Sulfur Ligand at the Dioxygen Binding Site by EXAFS and FTIR Spectroscopy. *J. Am. Chem. Soc.* **116**, 1924-1931 (1994). https://doi.org/10.1021/ja00084a037

50 Kline, C. D. & Blackburn, N. J. Substrate-Induced Carbon Monoxide Reactivity Suggests Multiple Enzyme Conformations at the Catalytic Copper M-Center of Peptidylglycine Monooxygenase. *Biochemistry* **55**, 6652-6661 (2016). https://doi.org/10.1021/acs.biochem.6b00845

51 Fager, L. Y. & Alben, J. O. Structure of the carbon monoxide binding site of hemocyanins studied by Fourier transform infrared spectroscopy. *Biochemistry* **11**, 4786-4792 (1972). https://doi.org/10.1021/bi00775a023

52 Welch, E. F., Rush, K. W., Arias, R. J. & Blackburn, N. J. Copper monooxygenase reactivity: Do consensus mechanisms accurately reflect experimental observations? *Journal of Inorganic Biochemistry* **231**, 111780 (2022). https://doi.org/10.1016/j.jinorgbio.2022.111780

53 Blackburn, N. J., Pettingill, T. M., Seagraves, K. S. & Shigeta, R. T. Characterization of a carbon monoxide complex of reduced dopamine-ß-hydroxylase: evidence for inequivalence of the Cu(I) centers. *J. Biol. Chem.* **265**, 15383-15386 (1990).

54 Alwan, K. B., Welch, E. F. & Blackburn, N. J. Catalytic M Center of Copper Monooxygenases Probed by Rational Design. Effects of Selenomethionine and Histidine Substitution on Structure and Reactivity. *Biochemistry* **58**, 4436-4446 (2019). https://doi.org/10.1021/acs.biochem.9b00823

55 Einarsdottir, O., Killough, P. M., Fee, J. A. & Woodruff, W. H. An infrared study of the binding and photodissociation of carbon monoxide in cytochrome ba3 from Thermus thermophilus. *J. Biol. Chem* **264**, 2405-2408 (1989).

56 Himes, R. A., Park, G. Y., Siluvai, G. S., Blackburn, N. J. & Karlin, K. D. Structural studies of copper(I) complexes of amyloid-beta peptide fragments: formation of two-coordinate bis(histidine) complexes. *Angew. Chem. Int. Ed. Engl.* **47**, 9084-9087 (2008).

57 Himes, R. A., Park, Y. G., Barry, A. N., Blackburn, N. J. & Karlin, K. D. Synthesis and X-ray absorption spectroscopy structural studies of Cu(I) complexes of histidylhistidine peptides: The predominance of linear 2-coordinate geometry. *J. Am. Chem. Soc.* **129**, 5352-5353 (2007).

58 Park, G. Y. *et al.* Copper-peptide complex structure and reactivity when found in conserved His-X(aa)-His sequences. *J Am Chem Soc* **136**, 12532-12535 (2014). https://doi.org/10.1021/ja505098v

59 Sanyal, I., Karlin, K. D., Strange, R. W. & Blackburn, N. J. Chemistry and structural studies on the dioxygen-binding copper-1,2-dimethylimidazole system. *J. Am. Chem. Soc.* **115**, 11259-11270 (1993). https://doi.org/10.1021/ja00077a027

60 Kealy, S., White, A. J. P., Gee, A. D. & Long, N. J. Evaluation of [^{12}C/^{11}C] carbon monoxide binding to Cu(I) *tris*-(pyrazolyl)borate complexes. *Eur. J. Inorg. Chem.*, 1896-1905 (2014).

61 Lee, Y. *et al.* Copper(I)/O2 chemistry with imidazole containing tripodal tetradentate ligands leading to mu-1,2-peroxo-dicopper(II) species. *Inorg Chem* **48**, 11297-11309 (2009). https://doi.org/10.1021/ic9017695

62 Lee, D. H. *et al.* Copper(I) complex O_2-reactivity with a N_3S thioether ligand: a copper-dioxygen adduct including sulfur ligation, ligand oxygenation, and comparisons with all nitrogen ligand analogues. *Inorg. Chem.* **46**, 6056-6068 (2007).

63 Bailey, L. J. & Fox, B. G. Crystallographic and catalytic studies of the peroxide-shunt reaction in a diiron hydroxylase. *Biochemistry* **48**, 8932-8939 (2009). https://doi.org/10.1021/bi901150a

64 Corder, A. L. *et al.* Peroxide-Shunt Substrate-Specificity for the Salmonella typhimurium O2-Dependent tRNA Modifying Monooxygenase (MiaE). *Biochemistry* **52**, 6182-6196 (2013). https://doi.org/10.1021/bi4000832

65 Mukherjee, M. & Dey, A. A heterogeneous bio-inspired peroxide shunt for catalytic oxidation of organic molecules. *Chem. Commun.* **56**, 11593-11596 (2020). https://doi.org/10.1039/D0CC03468A

66 Bauman, A. T., Yukl, E. T., Alkevich, K., McCormack, A. L. & Blackburn, N. J. The Hydrogen Peroxide Reactivity of Peptidylglycine Monooxygenase Supports a Cu(II)-Superoxo Catalytic Intermediate*. *Journal of Biological Chemistry* **281**, 4190-4198 (2006). https://doi.org/10.1074/jbc.M511199200

67 Bauman, A. T., Broers, B. A., Kline, C. D. & Blackburn, N. J. A Copper–Methionine Interaction Controls the pH-Dependent Activation of Peptidylglycine Monooxygenase. *Biochemistry* **50**, 10819-10828 (2011). https://doi.org/10.1021/bi201193j

68 Bursch, M., Mewes, J.-M., Hansen, A. & Grimme, S. Best-Practice DFT Protocols for Basic Molecular Computational Chemistry. *Angewandte Chemie* **134**, e202205735 (2022). https://doi.org/10.1002/ange.202205735

69 Chen, P. & Solomon, E. I. O2 activation by binuclear Cu sites: Noncoupled versus exchange coupled reaction mechanisms. *Proceedings of the National Academy of Sciences* **101**, 13105-13110 (2004). https://doi.org/10.1073/pnas.0402114101

70 Kunishita, A. *et al.* Active Site Models for the CuA Site of Peptidylglycine α-Hydroxylating Monooxygenase and Dopamine β-Monooxygenase. *Inorg. Chem.* **51**, 9465-9480 (2012). https://doi.org/10.1021/ic301272h

71 Wang, B., Walton, P. H. & Rovira, C. Molecular Mechanisms of Oxygen Activation and Hydrogen Peroxide Formation in Lytic Polysaccharide Monooxygenases. *ACS Catal* **9**, 4958-4969 (2019). https://doi.org/10.1021/acscatal.9b00778

72 Wu, P. *et al.* Theory Demonstrated a "Coupled" Mechanism for O2 Activation and Substrate Hydroxylation by Binuclear Copper Monooxygenases. *J. Am. Chem. Soc.* **141**, 19776-19789 (2019). https://doi.org/10.1021/jacs.9b09172

73 Chauhan, S. *Kinetic and spectroscopic study of peptidylglycine monooxygenase*, Oregon Health and Science University, (2016).

74 Burke, K. & Wagner, L. O. DFT in a nutshell. *International Journal of Quantum Chemistry* **113**, 96-101 (2013). https://doi.org/https://doi.org/10.1002/qua.24259

75 Kohn, W. & Sham, L. J. Self-Consistent Equations Including Exchange and Correlation Effects. *Physical Review* **140**, A1133-A1138 (1965). https://doi.org/10.1103/PhysRev.140.A1133

76 Tishchenko, O., Zheng, J. & Truhlar, D. G. Multireference Model Chemistries for Thermochemical Kinetics. *Journal of Chemical Theory and Computation* **4**, 1208-1219 (2008). https://doi.org/10.1021/ct800077r

77 Neese, F. A critical evaluation of DFT, including time-dependent DFT, applied to bioinorganic chemistry. *JBIC Journal of Biological Inorganic Chemistry* **11**, 702-711 (2006). https://doi.org/10.1007/s00775-006-0138-1

78 Mardirossian, N. & and Head-Gordon, M. Thirty years of density functional theory in computational chemistry: an overview and extensive assessment of 200 density functionals. *Molecular Physics* **115**, 2315-2372 (2017). https://doi.org/10.1080/00268976.2017.1333644

79 Paier, J., Marsman, M. & Kresse, G. Why does the B3LYP hybrid functional fail for metals? *The Journal of Chemical Physics* **127** (2007). https://doi.org/10.1063/1.2747249

80 Tirado-Rives, J. & Jorgensen, W. L. Performance of B3LYP Density Functional Methods for a Large Set of Organic Molecules. *Journal of Chemical Theory and Computation* **4**, 297-306 (2008). https://doi.org/10.1021/ct700248k

81 Chéron, N., Jacquemin, D. & Fleurat-Lessard, P. A qualitative failure of B3LYP for textbook organic reactions. *Phys. Chem. Chem. Phys.* **14**, 7170-7175 (2012). https://doi.org/10.1039/C2CP40438A

82 Welch, E. F., Rush, K. W., Arias, R. J. & Blackburn, N. J. Pre-Steady-State Reactivity of Peptidylglycine Monooxygenase Implicates Ascorbate in Substrate Triggering of the Active Conformer. *Biochemistry* **61**, 665-677 (2022). https://doi.org/10.1021/acs.biochem.2c00080

83 Klinman, J. P. The copper-enzyme family of dopamine β -monooxygenase and peptidylglycine α -hydroxylating monooxygenase: Resolving the chemical pathway for substrate hydroxylation. *J. Biol. Chem.* **281**, 3013-3016 (2006).

84 Hess, C. R., Klinman, J. P. & Blackburn, N. J. The copper centers of tyramine beta-monooxygenase and its catalytic-site methionine variants: an X-ray absorption study. *J. Biol. Inorg. Chem.* **15**, 1195-1207 (2010).

85 Prigge, S. T., Mains, R. E., Eipper, B. A. & Amzel, L. M. New insights into copper monooxygenases and peptide amidation: structure, mechanism and function. *Cell. Mol. Life Sci.* **57**, 1236-1259 (2000).

86 Kumar, D., Mains, R. E. & Eipper, E. 60 YEARS OF POMC: From POMC and alphaMSH to PAM, molecular oxygen, copper and vitamin C. *Journal of molecular endocrinology* **56** T63-76 (2016). https://doi.org/10.1530/JME-15-0266

87 Ipsen, J. O., Hallas-Moller, M., Brander, S., Lo Leggio, L. & Johansen, K. S. Lytic polysaccharide monooxygenases and other histidine-brace copper proteins: structure, oxygen activation and biotechnological applications. *Biochem. Soc. Trans.* **49**, 531-540 (2021). https://doi.org/10.1042/BST20201031

88 Ross, M. O. *et al.* Particulate methane monooxygenase contains only mononuclear copper centers. *Science* **364**, 566-570 (2019). https://doi.org/10.1126/science.aav2572

89 Jodts, R. J. *et al.* Coordination of the copper centers in particulate methane monooxygenase: comparison between methanotrophs and characterization of the CuC Site by EPR and ENDOR spectroscopies. *J Am Chem Soc* **143**, 15358-15368 (2021). https://doi.org/10.1021/jacs.1c07018

90 Chufan, E. E. *et al.* Differential reactivity between two copper sites in peptidylglycine alpha-hydroxylating monooxygenase. *J. Am. Chem. Soc.* **132**, 15565-15572 (2010).

91 Prigge, S. T., Eipper, B. A., Mains, R. E. & Amzel, M. Dioxygen binds end-on to mononuclear copper in a precatalytic enzyme complex. *Science* **304**, 864-867 (2004).

92 Prigge, S. T., Kolhekar, A. S., Eipper, B. A., Mains, R. E. & Amzel, L. M. Substrate-mediated electron transfer in peptidylglycine α-hydroxylating monooxygenase. *Nature Struct. Biol.* **6**, 976-983 (1999).

93 Boswell, J. S., Reedy, B. J., Kulathila, R., Merkler, D. J. & Blackburn, N. J. Structural investigations on the coordination environment of the active-site copper centers of recombinant bifunctional peptidylglycine α-amidating enzyme. *Biochemistry* **35**, 12241-12250 (1996).

94 Chen, P., Bell, J., Eipper, B. A. & Solomon, E. I. Oxygen activation by the noncoupled binuclear copper site in peptidylglycine α-hydroxylating monooxygenase. Spectroscopic definition of the resting sites and the putative $CuII_M$-OOH intermediate. *Biochemistry* **43**, 5735-5747 (2004).

95 Martin-Diaconescu, V. *et al*. Kβ Valence to core X-ray emission studies of Cu(I) binding proteins with mixed methionine - histidine coordination. Relevance to the reactivity of the M- and H-sites of peptidylglycine monooxygenase. *Inorg Chem* **55**, 3431-3439 (2016). https://doi.org/10.1021/acs.inorgchem.5b02842

96 Francisco, W. A., Blackburn, N. J. & Klinman, J. P. Oxygen and hydrogen isotope effects in an active site tyrosine to phenylalanine mutant of peptidylglycine α -hydroxylating monooxygenase: mechanistic implications. *Biochemistry* **42**, 1813 - 1819 (2003).

97 Francisco, W. A., Knapp, M. J., Blackburn, N. J. & Klinman, J. P. Hydrogen tunneling in peptidylglycine α-hydroxylating monooxygenase. *J. Am. Chem. Soc.* **124**, 8194 - 8195 (2002).

98 Osborne, R. L., Zhu, H., Iavarone, A. T., Blackburn, N. J. & Klinman, J. P. Interdomain long-range electron transfer becomes rate-limiting in the Y216A variant of tyramine β-monooxygenase. *Biochemistry* **52**, 1179-1191 (2013). https://doi.org/10.1021/bi3013609

99 Zhu, H., Sommerhalter, M., Nguy, A. K. & Klinman, J. P. Solvent and temperature probes of the long-range electron-transfer step in tyramine β-monooxygenase: demonstration of a long-range proton-coupled electron-transfer mechanism. *J Am Chem Soc* **137**, 5720-5729 (2015). https://doi.org/10.1021/ja512388n

100 Chen, P. & Solomon, E. I. Oxygen activation by the noncoupled binuclear copper site in peptidylglycine α-hydroxylating monooxygenase. Reaction mechanism and role of the noncoupled nature of the active site. *J. Am. Chem. Soc.* **126**, 4991-5000 (2004).

101 Rudzka, K. *et al*. Coordination of peroxide to the Cu(M) center of peptidylglycine α-hydroxylating monooxygenase (PHM): structural and computational study. *J. Biol. Inorg. Chem.* **18**, 223-232 (2013). https://doi.org/10.1007/s00775-012-0967-z

102 Alwan, K. B., Welch, E. F., Arias, R. J., Gambill, B. F. & Blackburn, N. J. Rational Design of a Histidine–Methionine Site Modeling the M-Center of Copper Monooxygenases in a Small Metallochaperone Scaffold. *Biochemistry* **58**, 3097-3108 (2019). https://doi.org/10.1021/acs.biochem.9b00312

103 Kline, C. D., Mayfield, M. & Blackburn, N. J. HHM motif at the CuH-site of peptidylglycine monooxygenase is a pH-dependent conformational switch. *Biochemistry* **52**, 2586-2596 (2013). https://doi.org/10.1021/bi4002248

104 Bauman, A. T., Jaron, S., Yukl, E. T., Burchfiel, J. R. & Blackburn, N. pH dependence of peptidylglycine monooxygenase. Mechanistic implications for Cu-methionine binding dynamics. *Biochemistry* **45**, 11140-11150 (2006).

105 Cardenas, D. J., Cuerva, J. M., Alias, M., Bunuel, E. & Campana, A. G. Water-based hydrogen-atom wires as mediators in long-range proton-coupled electron transfer in enzymes: a new twist on water reactivity. *Chemistry* **17**, 8318-8323 (2011). https://doi.org/10.1002/chem.201100964

106 Bauman, A. T., Ralle, M. & Blackburn, N. Large scale production of the copper enzyme peptidylglycine monooxygenase using an automated bioreactor. *Protein Expression and Purification* **51**, 34-38 (2007).
107 Evans, J. P., Blackburn, N. J. & Klinman, J. P. The catalytic role of the copper ligand H172 of peptidylglycine α–hydroxylating monooxygenase: a kinetic study of the H172A mutant. *Biochemistry* **45**, 15419-15429 (2006).
108 McIntyre, N. R. *et al*. Evidence for substrate preorganization in the peptidylglycine alpha-amidating monooxygenase reaction describing the contribution of ground state structure to hydrogen tunneling. *J. Am. Chem. Soc.* **132**, 16393-16402 (2010). https://doi.org/10.1021/ja1019194
109 Chauhan, S., Hosseinzadeh, P., Lu, Y. & Blackburn, N. J. Stopped-flow studies of the reduction of the copper centers suggest a bifurcated electron transfer pathway in peptidylglycine monooxygenase. *Biochemistry* **55**, 2008-2021 (2016). https://doi.org/10.1021/acs.biochem.6b00061
110 Brander, S. *et al*. Biochemical evidence of both copper chelation and oxygenase activity at the histidine brace. *Sci Rep* **10**, 16369 (2020). https://doi.org/10.1038/s41598-020-73266-y
111 Lucas, H. R. & Karlin, K. D. Copper-carbon bonds in mechanistic and structural probing of proteins as well as in situations where copper is a catalytic or receptor site. *Met Ions Life Sci* **6**, 295-361 (2009). https://doi.org/10.1039/BK9781847559159-00295
112 Pettingill, T. M., Strange, R. W. & Blackburn, N. J. Carbonmonoxy dopamine-β-hydroxylase: structural characterization by FTIR, fluorescence and XAS spectroscopy. *J. Biol. Chem.* **266**, 16996-17003 (1991).
113 Ray, G. B., Li, X.-Y., Ibers, J. A., Sessler, J. L. & Spiro, T. G. How far can proteins bend the FeCO unit? Distal polar and steric effects in heme proteins and models. *J. Am. Chem. Soc.* **116**, 162-176 (1994).
114 Dyer, R. B., Einarsdottir, O., Killough, P. M., Lopez, G. J. J. & Woodruff, W. H. Transient binding of photodissociated carbon monoxide to CuB+ of eukaryotic cytochrome oxidase at ambient temperature. Direct evidence from time-resolved infrared spectroscopy. *J. Am. Chem. Soc.* **111**, 7657-7659 (1989).
115 Ishigami, I. *et al*. Crystal structure of CO-bound cytochrome c oxidase determined by serial femtosecond X-ray crystallography at room temperature. *Proc Natl Acad Sci U S A* **114**, 8011-8016 (2017). https://doi.org/10.1073/pnas.1705628114
116 Diliberto, E. J., Jr. & Allen, P. L. Mechanism of dopamine β–hydroxylation. Semidehydroascorbate as the enzyme oxidation product of ascorbate. *J. Biol. Chem.* **256**, 3385-3393 (1981).
117 Merkler, D. J., Kulathila, R., Tamburini, P. P. & Young, S. D. Selective inactivation of the hydroxylase activity of bifunctional rat peptidylglycine α-amidating enzyme. *Arch. Biochem. Biophys.* **294**, 594-602 (1992).
118 Dhariwal, K. R., Washko, P., Hartzell, W. O. & Levine, M. Ascorbic acid within chromaffin granules. In situ kinetics of norepinephrine biosynthesis. *J. Biol. Chem.* **264**, 15404-15409 (1989).
119 Arias, R. J., Welch, E. F. & Blackburn, N. J. New structures reveal flexible dynamics between the subdomains of peptidylglycine monooxygenase. Implications for an open to closed mechanism. *Protein Science* **32**, e4615 (2023). https://doi.org/10.1002/pro.4615
120 Hess, C. R., Klinman, J. P. & Blackburn, N. J. The copper centers of tyramine β-monooxygenase and its catalytic-site methionine variants: an X-ray absorption study. *JBIC Journal of Biological Inorganic Chemistry* **15**, 1195–1207 (2010).

121 Merkler, D. J., Hawley, A. J., Eipper, B. A. & Mains, R. E. Peptidylglycine alpha-amidating monooxygenase as a therapeutic target or biomarker for human diseases. *Br J Pharmacol* (2022). https://doi.org/10.1111/bph.15815
122 Klinman, J. P. Mechanisms whereby mononuclear copper proteins functionalize organic substrates. *Chem. Rev.* **1996**, 2541-2561 (1996).
123 Bell, J., El Meskini, R., D'Amato, D., Mains, R. E. & Eipper, B. A. Mechanistic investigation of peptidylglycine α-hydroxylating monooxygenase via intrinsic tryptophan fluorescence and mutagenesis. *Biochemistry* **42**, 7133-7142 (2003).
124 Siebert, X. *et al.* The catalytic copper of peptidylglycine alpha-hydroxylating monooxygenase also plays a critical structural role. *Biophys. J.* **89**, 3312-3319 (2005).
125 Horton, R. M., Cai, Z. L., Ho, S. N. & Pease, L. R. Gene splicing by overlap extension: tailor-made genes using the polymerase chain reaction. *BioTechniques* **8**, 528-535 (1990).
126 Kolhekar, A. S., Keutman, H. T., Mains, R. E., Quon, A. S. W. & Eipper, B. A. Peptidylglycine α-hydroxylating monooxygenase: active site residues, disulfide linkages, and a two-domain model of the catalytuc core. *Biochemistry* **36**, 10901-10909 (1997).
127 Kabsch, W. Integration, scaling, space-group assignment and post-refinement. *Acta Crystallogr D Biol Crystallogr* **66**, 133-144 (2010). https://doi.org/10.1107/S0907444909047374
128 Leslie, A. G. The integration of macromolecular diffraction data. *Acta Crystallogr D Biol Crystallogr* **62**, 48-57 (2006). https://doi.org/10.1107/S0907444905039107
129 Winn, M. D. *et al.* Overview of the CCP4 suite and current developments. *Acta Crystallogr D Biol Crystallogr* **67**, 235-242 (2011). https://doi.org/10.1107/S0907444910045749
130 Emsley, P., Lohkamp, B., Scott, W. G. & Cowtan, K. Features and development of Coot. *Acta Crystallogr D Biol Crystallogr* **66**, 486-501 (2010). https://doi.org/10.1107/S0907444910007493
131 *The PyMOL Molecular Graphics System*. 2.0 edn.
132 EXAFSPAK (Stanford Synchrotron Radiation Laboratory, Menlo Park, CA, 1990).
133 EXAFSPAK (Stanford Synchrotron Radiation Laboratory, Menlo Park, CA, 1995).
134 EXCURVE v. 9.2 (Daresbury Laboratory, Warrington, England, 1998).
135 Gurman, S. J., Binsted, N. & Ross, I. A rapid, exact, curved-wave theory for EXAFS calculations. *J. Phys. C* **17**, 143-151 (1984).
136 Gurman, S. J., Binsted, N. & Ross, I. A rapid, exact, curved-wave theory for EXAFS calculations. II. The multiple-scattering contributions. *J. Phys. C* **19**, 1845-1861 (1986).
137 Rush, K. W., Eastman, K. A. S., Welch, E. F., Bandarian, V. & Blackburn, N. J. Capturing the Binuclear Copper State of Peptidylglycine Monooxygenase Using a Peptidyl-Homocysteine Lure. *J Am Chem Soc* **146**, 5074-5080 (2024). https://doi.org/10.1021/jacs.3c14705
138 Welch, E. F., Rush, K. W., Eastman, K. A. S., Bandarian, V. & Blackburn, N. J. The binuclear copper state of peptidylglycine monooxygenase visualized through a selenium-substituted peptidyl-homocysteine complex. *Dalton Trans* (2025). https://doi.org/10.1039/d5dt00082c
139 Koo, C. W. & Rosenzweig, A. C. Biochemistry of aerobic biological methane oxidation. *Chem Soc Rev* **50**, 3424-3436 (2021). https://doi.org/10.1039/d0cs01291b
140 Schroder, G. C., O'Dell, W. B., Webb, S. P., Agarwal, P. K. & Meilleur, F. Capture of activated dioxygen intermediates at the copper-active site of a lytic polysaccharide monooxygenase. *Chem Sci* **13**, 13303-13320 (2022). https://doi.org/10.1039/d2sc05031e
141 Crespo, A., Marti, M. A., Roitberg, A. E., Amzel, L. M. & Estrin, D. A. The catalytic mechanism of peptidylglycine α-hydroxylating monooxygenase investigated by computer simulation. *J. Am. Chem. Soc.* **128**, 12817-12828 (2006). https://doi.org/10.1021/ja062876x

142 Erion, M. D., Tan, J., Wong, M. & Jeng, A. Y. Inhibition of peptidylglycine alpha-amidating monooxygenase by N-substituted homocysteine analogs. *J. Med. Chem.* **37**, 4430-4437 (1994). https://doi.org/10.1021/jm00052a002
143 Blackburn, N. J. *et al.* X-ray Absorption studies on the mixed-valence and fully reduced forms of the soluble Cu_A domains of *Thermus thermophilus* and *Bacillus subtilis* cytochrome *c* oxidase: Structural evidence for minimal electron transfer reorganizational energy. *J. Am. Chem. Soc.* **119**, 6135-6143 (1997).
144 Siluvai, G. S., Nakano, M., Mayfield, M. & Blackburn, N. J. The essential role of the Cu(II) state of Sco in the maturation of the Cu(A) center of cytochrome oxidase: evidence from H135Met and H135SeM variants of the Bacillus subtilis Sco. *J. Biol. Inorg. Chem.* **16**, 285-287 (2011).
145 Siluvai, G. S., Mayfield, M., Nilges, M. J., DeBeer George, S. & Blackburn, N. J. Anatomy of a red copper center: Spectroscopic identification and reactivity of the copper centers of *Bacillus subtilis* Sco and Its Cys-to-Ala variants. *J. Am. Chem. Soc.* **132**, 5215-5226 (2010).
146 Clark, K. M., Yu, Y., van der Donk, W. A., Blackburn, N. & Lu, Y. Modulating the Copper-Sulfur Interaction in Type 1 Blue Copper Azurin by Replacing Cys112 with Nonproteinogenic Homocysteine. *Inorganic chemistry frontiers* **1**, 153-158 (2014). https://doi.org/10.1039/C3QI00096F
147 Westmoreland, T. D., Wilcox, D. E., Baldwin, M. J., Mims, W. B. & Solomon, E. I. Detailed spectroscopic analysis of half-met hemocyanins: mixed-valent contributions to electronic properties and structure. *J . Am. Chem. Soc.* **111**, 6106-6123 (1989).
148 Blackburn, N. J., Barr, M. E., Woodruff, W. H., van der Oost, J. & de Vries, S. Metal-metal bonding in biology: EXAFS evidence for a 2.5 Å copper-copper bond in the Cu_A center of cytochrome oxidase. *Biochemistry* **33**, 10401-10407 (1994).
149 Blackburn, N. J. *et al.* X-ray Absorption Studies on the Mixed-Valence and Fully Reduced Forms of the Soluble CuA Domains of Cytochrome c Oxidase. *J. Am. Chem. Soc.* **119**, 6135-6143 (1997). https://doi.org/10.1021/ja970513e
150 Farrar, J. A. *et al.* The electronic structure of Cu_A: A novel mixed-valence dinuclear copper electron transfer center. *J. Am. Chem. Soc.* **118**, 11501-11514 (1996).
151 Kroneck, P. M. H. Walking the seven lines: binuclear copper A in cytochrome c oxidase and nitrous oxide reductase. *Journal of biological inorganic chemistry : JBIC : a publication of the Society of Biological Inorganic Chemistry* **23**, 27-39 (2018). https://doi.org/10.1007/s00775-017-1510-z
152 Gamelin, D. R. *et al.* Spectroscopy of mixed-valence Cu_A centers: ligand field control of ground state properties related to electron transfer. *J. Am. Chem. Soc.* **120**, 5246-5263 (1998).
153 Williams, K. R. *et al.* The influence of copper-sulfur covalency and copper-copper bonding on valence delocalization and electron transfer in the Cu_A site of cytochrome *c* oxidase. *J. Am. Chem. Soc.* **119**, 613-614 (1997).
154 Houser, R. P., Young, V. G. J. & Tolman, W. B. A thiolate-bridged fully delocalized mixed-valence dicopper (I,II) complex that models the Cu_A biological electron-transfer site. *J. Am. Chem. Soc.* **118**, 2101-2102 (1996).
155 Stoll, S. & Schweiger, A. EasySpin, a comprehensive software package for spectral simulation and analysis in EPR. *J. Magn. Reson.* **178**, 42-55 (2006).
156 Kaim, W., Klein, A. & Glockle, M. Exploration of mixed-valence chemistry: inventing new analogues of the Creutz-Taube ion. *Acc Chem Res* **33**, 755-763 (2000). https://doi.org/10.1021/ar960067k

157 Williams, P. A. *et al.* The Cu_A domain of *Thermus thermophilus* ba_3- type cytochrome *c* oxidase at 1.6 Å resolution. *Nat. Str. Biol.* **6**, 509-516 (1999).
158 Haltia, T. *et al.* Crystal structure of nitrous oxide reductase from Paracoccus denitrificans at 1.6 A resolution. *Biochem J* **369**, 77-88 (2003). https://doi.org/10.1042/BJ20020782
159 Hay, M. T. *et al.* Spectroscopic characterization of an engineered purple Cu_A center in azurin. *Inorg. Chem.* **37**, 191-198 (1998).
160 Robinson, H. *et al.* Structural basis of electron transfer modulation in the purple Cu_A center. *Biochemistry* **38**, 5677-5683 (1999).
161 Ross, M. O. *et al.* Formation and Electronic Structure of an Atypical CuA Site. *J Am Chem Soc* **141**, 4678-4686 (2019). https://doi.org/10.1021/jacs.8b13610
162 Gagne, R. R., Koval, C. A., Smith, T. J. & Cimolino, M. C. Binuclear complexes of macrocyclic ligands. Electrochemical and spectral properties of homobinuclear Cu(II)Cu(II), Cu(II)Cu(I), and Cu(I)Cu(I) species including an estimated intramolecular electron transfer rate. *J. Am. Chem. Soc.* **101**, 4571-4580 (1979).
163 Xie, X. *et al.* Perturbations to the geometric and electronic structure of the CuA site: factors that influence delocalization and their contributions to electron transfer. *J Am Chem Soc* **130**, 5194-5205 (2008). https://doi.org/10.1021/ja7102668
164 Chen, P., Root, D. E., Campochiaro, C., Fujisawa, K. & Solomon, E. I. Spectroscopic and electronic structure studies of the diamagnetic side-on CuII-superoxo complex $Cu(O_2)[HB(3\text{-}R\text{-}5\text{-}iPrpz)_3]$: antiferromagnetic coupling versus covalent delocalization. *J. Am. Chem. Soc.* **125**, 466-474 (2003).
165 Lanci, M. P. *et al.* Isotopic probing of molecular oxygen activation at copper(I) sites. *J Am Chem Soc* **129**, 14697-14709 (2007). https://doi.org/10.1021/ja074620c
166 Maiti, D. *et al.* A 1:1 copper-dioxygen adduct is an end-on bound superoxo copper(II) complex which undergoes oxygenation reactions with phenols. *J Am Chem Soc* **129**, 264-265 (2007). https://doi.org/10.1021/ja067411l
167 Woertink, J. S. *et al.* Spectroscopic and computational studies of an end-on bound superoxo-Cu(II) complex: geometric and electronic factors that determine the ground state. *Inorg Chem* **49**, 9450-9459 (2010). https://doi.org/10.1021/ic101138u
168 Peterson, R. L. *et al.* Cupric superoxo-mediated intermolecular C-H activation chemistry. *J Am Chem Soc* **133**, 1702-1705 (2011). https://doi.org/10.1021/ja110466q
169 Ginsbach, J. W., Peterson, R. L., Cowley, R. E., Karlin, K. D. & Solomon, E. I. Correlation of the Electronic and Geometric Structures in Mononuclear Copper(II) Superoxide Complexes. *Inorg Chem* **52**, 12872-12874 (2013). https://doi.org/10.1021/ic402357u
170 Peterson, R. L. *et al.* Stepwise Protonation and Electron-Transfer Reduction of a Primary Copper-Dioxygen Adduct. *J. Am. Chem. Soc.* **135**, 16454-16467 (2013). https://doi.org/10.1021/ja4065377
171 Tano, T. *et al.* Redox properties of a mononuclear copper(II)-superoxide complex. *Inorg. Chem.* **52**, 10431-10437 (2013). https://doi.org/10.1021/ic401261z
172 Kunishita, A. *et al.* Mononuclear Copper(II)-Superoxo Complexes that Mimic the Structure and Reactivity of the Active Centers of PHM and DbetaM. *J. Am. Chem. Soc.* **131**, 2788-2789 (2009).
173 Kim, S. *et al.* A N3S(thioether)-Ligated Cu(II)-Superoxo with Enhanced Reactivity. *J Am Chem Soc* **137**, 2796-2799 (2015). https://doi.org/10.1021/ja511504n
174 Sanchez-Eguia, B. N., Flores-Alamo, M., Orio, M. & Castillo, I. Side-on cupric-superoxo triplet complexes as competent agents for H-abstraction relevant to the active site of PHM. *Chem Commun (Camb)* **51**, 11134-11137 (2015). https://doi.org/10.1039/c5cc02332g

175 Strange, R. W., Blackburn, N. J., Knowles, P. F. & Hasnain, S. S. X-ray absorption spectroscopy of metal-histidine coordination in metalloproteins. Exact simulation of the EXAFS of tetrabis(imidazole)copper(II) nitrate and other copper-imidazole complexes by the use of a multiple-scattering treatment. *J. Am. Chem. Soc.* **109**, 7157-7162 (1987). https://doi.org/10.1021/ja00257a042
176 Hess, C. R., McGuirl, M. M. & Klinman, J. P. Mechanism of the insect enzyme, tyramine beta-monooxygenase, reveals differences from the mammalian enzyme, dopamine beta-monooxygenase. *J. Biol. Chem.* **283**, 3042-3049 (2008).
177 Mydy, L. S. *et al.* An intramolecular macrocyclase in plant ribosomal peptide biosynthesis. *Nat Chem Biol* **20**, 530-540 (2024). https://doi.org/10.1038/s41589-024-01552-1
178 Barry, A. N. & Blackburn, N. J. A selenocysteine variant of the human copper chaperone for superoxide dismutase. A Se-XAS probe of cluster composition at the domain 3-domain 3 dimer interface. *Biochemistry* **49**, 4916-4928 (2008).
179 DeBeer George, S. *et al.* A quantitative description of the ground-state wave function of Cu(A) by X-ray absorption spectroscopy: comparison to plastocyanin and relevance to electron transfer. *J Am Chem Soc* **123**, 5757-5767 (2001).
180 Chacon, K. N. & Blackburn, N. J. Stable Cu(II) and Cu(I) Mononuclear Intermediates in the Assembly of the CuA Center of Thermus thermophilus Cytochrome Oxidase. *J Am Chem Soc* **134**, 16401-16412 (2012). https://doi.org/10.1021/ja307276z
181 Berry, S. M., Gieslelman, M. D., Nilges, M. J., van der Donk, W. A. & Lu, Y. An engineered azurin variant containing a selenocysteine copper ligand. *J. Am. Chem. Soc.* **124**, 2084-2085 (2002).
182 Ralle, M. *et al.* The selenocysteine-substituted blue copper center: spectroscopic investigations of Cys112SeCys *Pseudomonas aeruginosa* azurin. *J. Am. Chem. Soc.* **126**, 7244-7256 (2004).
183 Kimani, M. M., Brumaghim, J. L. & VanDerveer, D. Probing the antioxidant action of selenium and sulfur using Cu(I)-chalcogenone tris(pyrazolyl)methane and -borate complexes. *Inorg Chem* **49**, 9200-9211 (2010). https://doi.org/10.1021/ic100668b
184 Sánchez-Eguía, B. N. *et al.* Hemilabile Thio– and Selenoethers in Bis(benzimidazolyl)Amine Copper Complexes Relevant to the Active Sites of Copper-Dependent Monooxygenases. *ChemCatChem* **17**, e202401330 (2025). https://doi.org/https://doi.org/10.1002/cctc.202401330
185 Solomon, E. I. Spectroscopic methods in bioinorganic chemistry: blue to green to red copper sites. *Inorg. Chem.* **45**, 8012-8025 (2006).
186 LaCroix, L. B. *et al.* Electronic structure of the perturbed blue copper site in nitrite reductase: spectroscopic properties, bonding and implications for the entatic/rack state. *J. Am. Chem. Soc.* **118**, 7755-7768 (1996).
187 Solomon, E. I., Baldwin, M. J. & Lowery, M. L. Electronic structures of active sites in copper proteins: contributions to reactivity. *Chem. Rev.*, 521-542 (1992).
188 Shadle, S. E. *et al.* X-ray absorption spectroscopic studies of the blue copper site: metal and ligand K-edge studies to probe the origin of the EPR splitting in plastocyanin. *J. Am. Chem. Soc.* **115**, 767-776 (1993).
189 Arciero, D. M., Pierce, B. S., Hendrich, M. P. & Hooper, A. B. Nitrosocyanin, a red cupredoxin-like protein from *Nitrosomonas europaea*. *Biochemistry* **41**, 1703-1709 (2002).
190 Lieberman, R. L., Arciero, D. M., Hooper, A. B. & Rosenzweig, A. C. Crystal structure of a novel red copper protein from *Nitrosomonas europaea*. *Biochemistry* **40**, 5674-5681 (2001).

191 Andruzzi, L., Nakano, M., Nilges, M. J. & Blackburn, N. J. Spectroscopic studies of metal binding and metal selectivity in *Bacillus subtilis* BSco, a homologue of the yeast mitochondrial protein Sco1p. *J. Am. Chem. Soc* **127**, 16548-16558 (2005).
192 Roger, M. *et al.* Beyond the coupled distortion model: structural analysis of the single domain cupredoxin AcoP, a green mononuclear copper centre with original features. *Dalton Trans* **53**, 1794-1808 (2024). https://doi.org/10.1039/d3dt03372d
193 Kitajima, N., Katayama, T., Fujisawa, K., Iwata, Y. & Morooka, Y. Synthesis, molecular structure, and reactivity of (alkylperoxo)copper(II) complex. *J. Am. Chem. Soc.* **115**, 7872-7873 (1993). https://doi.org/10.1021/ja00070a041
194 Christiansen, M. A. H., Peña-Torres, A., Jónsson, E. Ö. & Jónsson, H. Single-Atom Substituents in Copper Surfaces May Adsorb Multiple CO Molecules. *The Journal of Physical Chemistry Letters* **15**, 5654-5658 (2024). https://doi.org/10.1021/acs.jpclett.4c00899
195 Rush, K. W., Alwan, K. B., Conner, A. T., Welch, E. F. & Blackburn, N. J. Mechanisms of Copper Selectivity and Release by the Metallochaperone CusF: Insights from CO-Binding, Rapid-Freeze-Quench EXAFS, and Unnatural Amino Acid Substitution. *Inorg. Chem.* **63**, 21519-21530 (2024). https://doi.org/10.1021/acs.inorgchem.4c03578
196 Murata, K. & Wolf, M. Cryo-electron microscopy for structural analysis of dynamic biological macromolecules. *Biochimica et Biophysica Acta (BBA) - General Subjects* **1862**, 324-334 (2018). https://doi.org/https://doi.org/10.1016/j.bbagen.2017.07.020
197 Grimme, S. Exploration of Chemical Compound, Conformer, and Reaction Space with Meta-Dynamics Simulations Based on Tight-Binding Quantum Chemical Calculations. *Journal of Chemical Theory and Computation* **15**, 2847-2862 (2019). https://doi.org/10.1021/acs.jctc.9b00143
198 Kuzmic, P. Program DYNAFIT for the analysis of enzyme kinetic data: application to HIV proteinase. *Anal. Biochem.* **237**, 260-273 (1996).

Appendix

Supplementary Information for Chapter Three

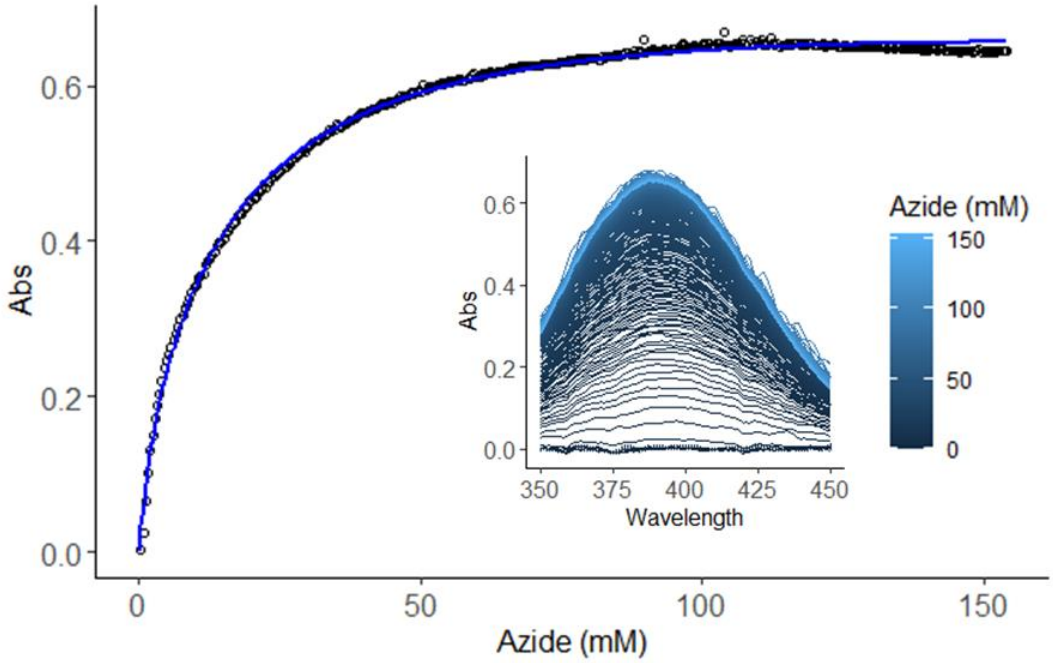

Figure 3-S1 Titration of oxidized Cu(II) PHM with azide. *1 mL of 1 mM oxidized PHM (2.0 mM in Cu(II)) in pH 8.0 20 mM sodium phosphate was titrated with a 2 M stock solution of sodium azide using a syringe pump. An azido adduct was formed with a broad maximum at 390 nm. The baseline corrected absorbance at 390 was plotted versus azide concentration to give the isotherm shown in the insert. The experimental data was simulated in DynaFit4[198] and fit to a equilibrium binding scheme shown below*:

```
P + Az <==> P.Az        :       KD1     dissociation
P.Az + Az <==> P.Az.Az  :       KD2     dissociation
```

The model supposes that each protein molecule (P) initially binds one azide molecule equivalent to azide binding to one of the two Cu centers, followed by the weaker binding of a second azide molecule. Note that the data provide no information on which copper binds azide, nor whether the second azide binds to the unligated copper, or forms a bis-azido adduct at the first binding site. Dissociation constants are K_D1 = 980 μM and K_D2 = 1.8 mM, with molar extinction coefficients 160 $M^{-1}cm^{-1}$ for the single azido species and 736 $M^{-1}cm^{-1}$ for the double binding site.

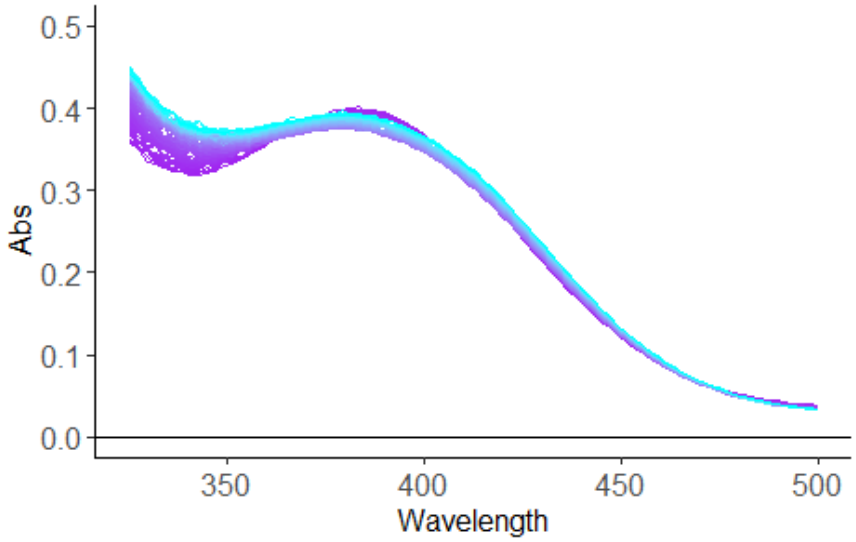

Figure 3-S2 Rate of Cu(II)-Azido formation by Stopped Flow. *A 500 μM solution of oxidized PHM (1 mM in Cu(II)) in 20 mM sodium phosphate buffer, pH 7.5 was shot against a 20 mM solution of sodium azide using an Applied Photophysics SX20 stopped flow module and photodiode array detector. Spectra were collected every 5 ms from 2 – 500 ms and plotted in the figure. The data indicate that the PHM-Cu(II) azido adduct forms within the mixing time of the instrument. Therefore the Cu(II)-azido signal formation is not rate limiting and can be used as a reporter for enzyme oxidation in the presence of azide.*

Table 3-S1. Copper to protein ratios determined by ICP-OES *after initial reconstitution and removal of excess Cu(II) (samples A and B) and after ascorbate reduction and removal of excess ascorbate (C and D).*

	[Protein] nM	[Copper] nM	Copper to Protein
After reconstitution A	300	580	1.9
After reconstitution B	300	594	2.0
After reduction and ascorbate removal C	300	502	1.7
After reduction and ascorbate removal D	300	566	1.9

Table 3-S2 Quantitation of pre-steady state reactions of fully reduced PHM using rapid freeze quench EPR. *Rapidly frozen EPR samples were prepared using a Quench Flow-3 (KinTek) apparatus configured for RFQ by the manufacturer. Reduced, 200 μM ascorbate-free protein samples (400 μM in Cu(I)) in anaerobic buffer and 200 uM acetyl-YVG substrate in fully oxygenated buffer ([O2] ≈ 1.1 mM before 1:1 dilution on mixing) were loaded onto the instrument and rapidly mixed at the desired time point. A universal buffer was used comprised of equal volumes of 50 mM MES, HEPES and CHES adjusted to pH 7.5. Mixtures were quenched in liquid ethane at -170°C. The resulting snow was then packed into 707-SQ-250M EPR tubes (Wilmad LabGlass). Oxidation was monitored in a Bruker E500 X-Band EPR spectrometer equipped with a superX microwave bridge and a dual-mode cavity with a helium flow cryostat (ESR900, Oxford Instrument, Inc). The table lists peak to peak intensity at g⊥ at each time point calibrated versus the concentration of a 250 μM solution of Cu(II)-EDTA prepared by RFQ but shot against buffer. The final concentration of Cu(II) for each time point is determined from the peak-to-peak height of the g⊥ resonance relative to that of a 250 μM solution of Cu(II)-EDTA taken through an identical cycle of mixing, freezing and packing. Errors in concentrations determined from the peak heights are estimated from triplicate measurements of a Cu(II)-EDTA standard to be ≅15 percent and are mainly due to differences in packing density of the samples.*

Sample- Time point	Relative Peak Intensity	[EPR detectable Cu(II)] (μM)
13 ms	7.92	1.6
25 ms	7.53	1.5
100 ms	15.0	3.0
300 ms	14.3	2.9
250 μM Cu(II)-EDTA standard	1250	250.0

Table 3-S3 CO stretching frequencies of Cu(I)-carbonyl complexes of selected copper proteins and model complexes

Sample	Ligand Set (excluding CO)	Coord. No (including CO)	Frequency (cm^{-1})	Reference
PHM	$2N_{(His)}$ $1S_{(Met)}$	4	2093	[42]
DBM	$2N_{(His)}$ $1S_{(Met)}$	4	2089	[53]
PHM + AcYVG	$2N_{(His)}$ $1S_{(Met)}$	4	2093, 2063	[42]
PHM + Benzoylglycine	$2N_{(His)}$ $1S_{(Met)}$	4	2093, 2075	[42]
PHM M314H	$3N_{(His)}$	4	2075	[50]
PHM M314H + AcYVG	$3N_{(His)}$	4	2051	[50]
CusF W44AM49H (M-site model)	$2N_{(His)}S_{(Met)}$	4	2089	[102]
SeM CusF W44AM49H (M-site model)	$2N_{(His)}Se_{(Met)}$	4	2087	[54]
Hc (mollusk)	$3N_{(His)}$ + Cu-Cu	4	2062	[51]
Hc (limulus)	$3N_{(His)}$ + Cu-Cu	4	2053	[51]
Hc (arthropod)	$3N_{(His)}$ + Cu-Cu	4	2043	[51]
aa_3-cytochrome oxidase	$3N_{(His)}$ + Cu-Fe	4	2066, 2054, 2039	[55]
ba_3-cytochrome oxidase	$3N_{(His)}$ + Cu-Fe	4	2054	[55]
Aβ(10-14) YEVHH	$2N_{(His)}$	3	2110	[56]
Histidylhistidine (Nδ coordinated)	$2N_{(His)}$	3	2110-2105 weak	[57]
Histidylhistidine + N-methylimidazole	$2N_{(His)}N_{(imid)}$	4	2075 strong	[57]
HisXHis (X=Gly) (Nε coordinated)	$2N_{(His)}$	3	2092 strong	[58]
bis-dimethylimidazole ($[Cu\text{-}(Me_2imid)_2]^+$)	$2N_{(imid)}$		No reaction	[59]
tris-dimethylimidazole ($[Cu\text{-}(Me_2imid)_3]^+$)	$3N_{(imid)}$	4	2069	[59]
tris-(3,5-pyrazolyl)borate	$3N_{(pyrazole)}$	4	2083	[60]
tris-(3,5-dimethylpyrazolyl)borate	$3N_{(pyrazole)}$	4	2066	[60]
tris-(3,5-diisopropylpyrazolyl)borate	$3N_{(pyrazole)}$	4	2056	[60]
tris-(3-trifluoromethyl,5-H-pyrazolyl)borate	$3N_{(pyrazole)}$	4	2100	[60]
tris-(2-methylpyridyl)amine (TMPA)	$3N_{(py)}$ and $4N_{(py)}$	4 and 5	2094, 2075	[61]
1*H*-imidazol-4-yl)-*N,N*-bis((pyridin-2-yl)methyl)ethanamine	$2N_{(py)}N_{(imid)}$	Probably 4	2082	[61]
2-Ethylthio-N,N-bis(pyridin-2-yl)methylethanamine	$2N_{(py)}S_{thioether}$ or $3N_{(py)}$	4	2094	[62]

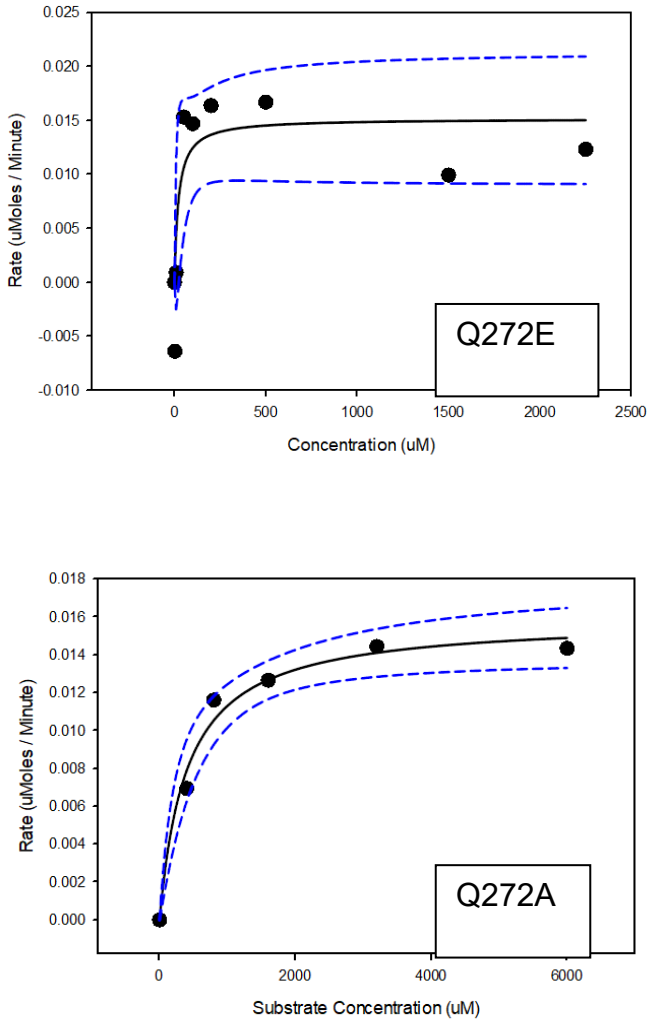

Figure 4-S1. Steady state kinetic parameters for the Q272E and Q272A variants of peptidylglycine monooxgenase derived from oxygen consumption measurements using an oxygen electrode. *The figure shows plots of rate of O_2 consumption versus peptidyl substrate concentration fitted to the Michaelis-Menton equation $V = V_{max}[S]/(K_m+[S])$. Solid lines are the best fit generated by non-linear regression, with dashed lines representing 95% (2σ) confidence levels.*

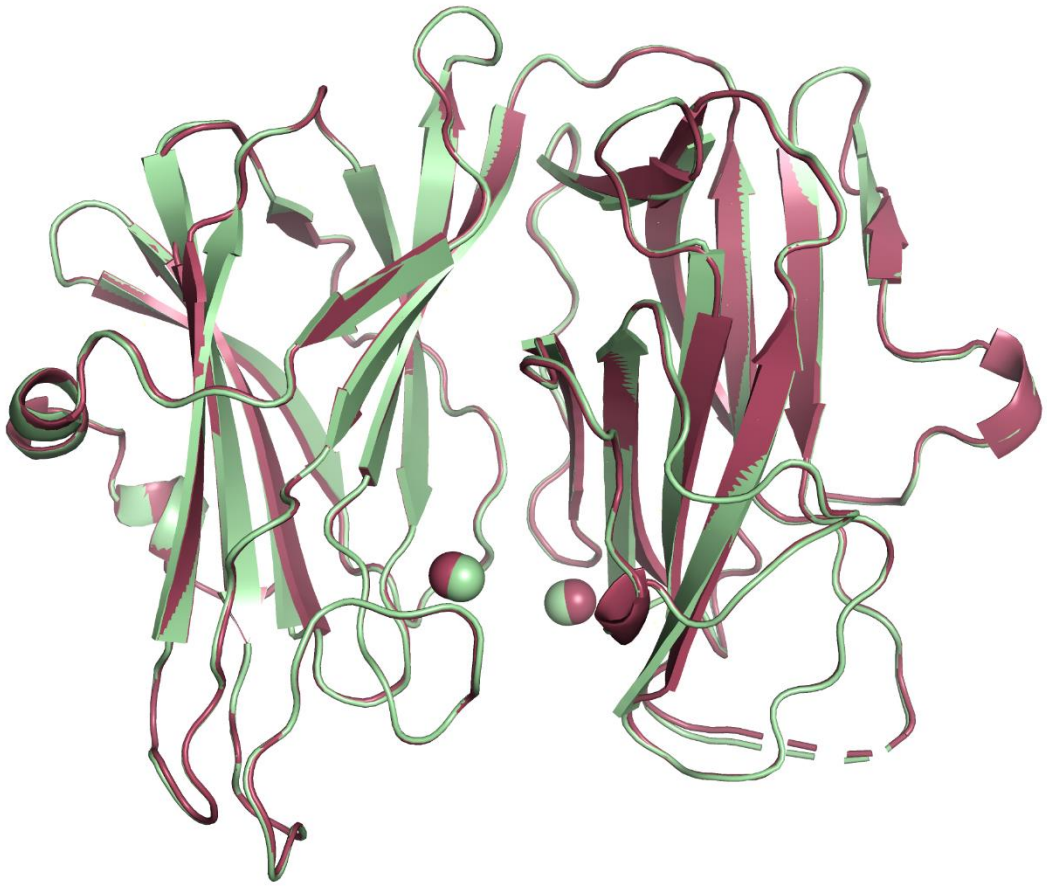

Figure 4-S2 WT PHM under new crystallization conditions. *Overlay of WT oxidized PHM crystallized using new crystallization conditions (pale green) with the published WT PHM structure (1PHM) (raspberry red). The Cu-Cu distances are 11.0 and 11.3 Å respectively, and the RMSD for the alignment is 0.164 Å².*

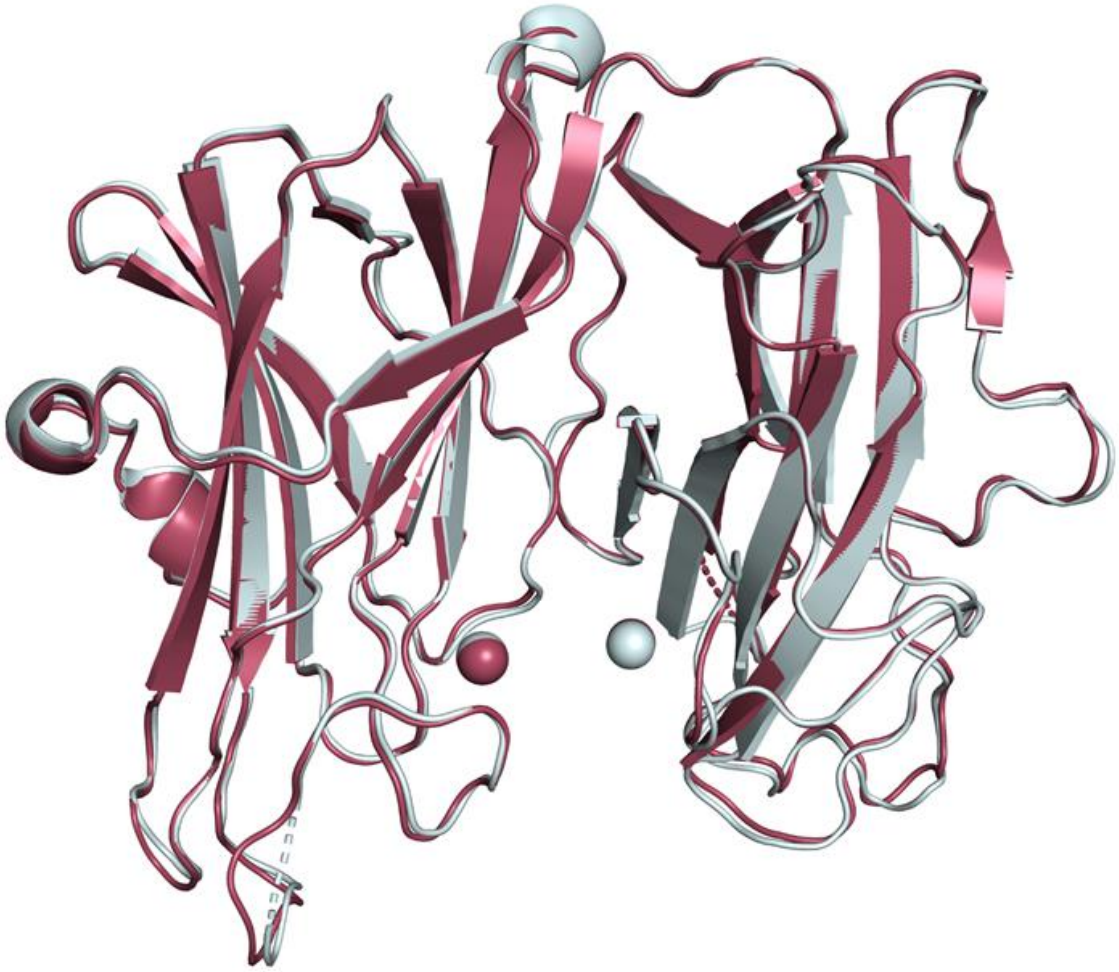

Figure 4-S3 Comparison of Q272E and WT PHM. *Overlay of the structures of Q272E (raspberry red) and WT PHM crystallized under anaerobic conditions (grey-green). The copper to copper distance in both structures is ~ 14 Å. Structures were aligned and rendered in PYMOL 2.3.3. Metrical and other details are listed in Table 4-2.*

Table 4-S1. Statistics for data collection and processing, structure solution and refinement of the crystal structures PHM WT anaerobic, Q272E, and Q272A.

Crystal		PHM WT Anaerobic	PHM Q272E	PHM Q272A	PHM WT
PDB accession code		8DSJ	8DSL	8DSN	N/A
Data collection and processing					
Space group		P 1	P 1	P 1	P 212121
Cell dimensions	a, b, c (Å)	38.14, 53.263, 86.424	39.17, 53.53, 86.14	38.55, 53.42, 86.16	68.96, 69.05, 82.01
	α, β, γ (°)	84.845, 89.962, 78.504	85.03, 89.79, 77.63	84.82, 89.84, 78.20	90.00, 90.00, 90.00
Resolution range (Å)		37.37-1.80 (1.84-1.80)	38.28-1.43 (1.45-1.43)	37.74-2.00 (2.05-2.00)	35.26-2.60 (2.60-2.50)
No. of unique reflections		57073 (2118)	78626 (143)	42250 (2842)	92758 (10510)
Completeness (%)		92.8 (57.5)	98.9 (2.2)	93.3 (83.8)	99.8 (99.9)
Multiplicity		7.9 (4.8)	8.4 (1.3)	7.6 (4.9)	6.6 (6.8)
Mean I/σ(I)		3.6 (0.3)	8.8 (0.0)	4.2 (1.6)	11.9 (1.7)
Wilson B factor ($Å^2$)		34.575	27.527	40.612	67.754
R-merge		0.594 (200.735)	0.101 (0.046)	0.814 (7.475)	0.081 (0.926)
R-meas		0.694(0.182)	.115(0.052)	1.401(0.218)	0.096 (1.087)
CC1/2		0.855(0.982)	0.999(0.998)	0.207(0.990)	0.999 (0.745)
Structure solution and refinement					
Refined resolution (Å)		2.80	2.05	2.80	2.50
Resolution range (Å)		37.37-2.95 (2.80-2.87)	38.25-2.05 (2.05-2.11)	38.02-2.95 (2.95-2.80)	35.26-2.60 (2.60-2.50)
No. of unique reflections		142480 (20489)	372589 (27742)	284075(40784)	92758 (10510)
Completeness (%)		100.0 (100.00)	98.1 (96.8)	99.4(99.3)	99.8 (99.9)
Multiplicity		8.7 (8.5)	8.9 (8.7)	17.2(16.9)	6.6 (6.8)
Mean I/σ(I)		7.4 (4.4)	15.9 (3.5)	9.9(6.4)	11.9 (1.7)
R-merge		0.193 (0.356)	0.071 (0.539)	0.311(0.942)	0.081 (0.926)
R-meas		0.220(0.407)	0.076(0.579)	0.328(0.973)	0.096 (1.087)
CC1/2		0.984(0.962)	0.999(0.950)	0.897(0.379)	0.999 (0.745)
R-work (%)		0.198	0.195	0.198	0.213
R-free (%)		0.274	0.239	0.296	0.258

R.m.s.d.	bonds (Å)	0.006	0.010	0.008	0.0078
	angles (°)	1.472	1.701	1.610	1.550
Average B factor (Å^2)		36.841	43.64	43.221	60.667
Clashscore		6	7	9	4.43
Ramachandran (%)	favored	93	94	92	285
	allowed	6	5	7	N/A
	outliers	1	1	1	2

Table 4-S2. Fits obtained to the oxidized and ascorbate-reduced Cu K-EXAFS of the PHM Q272E and Q272A variants by curve-fitting using the program EXCURVE 9.2.

	F[a]	No[b]	R (Å)[c]	DW (Å²)	No[b]	R (Å)[c]	DW[d] (Å²)	No[b]	R (Å)[c]	DW (Å²)	E_0
Sample		Cu-N(His)[e]			Cu-N/0			Cu-S			
Cu(II)-Q272E	0.75	2.5	1.95	0.012	1.5	1.95	0.012				-2.6
Cu(I)-Q272E	0.41	2	1.91	0.011				0.5	2.22	0.018	-1.0
Cu(II)-Q272A	0.48	2.5	1.96	0.012	1.5	1.96	0.012				-4.0
Cu(I)-Q272A	0.55	2	1.91	0.009				0.5	2.15	0.015	-1.9

[a] F is a least-squares fitting parameter defined as $F^2 = \frac{1}{N}\sum_{i=1}^{N} k^6 (Data - Model)^2$

[b] Coordination numbers are generally considered accurate to ± 25%

[c] In any one fit, the statistical error in bond-lengths is ±0.005 Å. However, when errors due to imperfect background subtraction, phase-shift calculations, and noise in the data are compounded, the actual error is probably closer to ±0.02 Å.

[d] Debye Waller terms are reported as $2\sigma^2$

[e] Fits included both single and multiple scattering contributions from the imidazole ring. Outer shell C and N atoms were located at appropriate distances and are omitted for clarity.

Crystallography data collection and analysis: Additional Details

Offset and normal data (data without the horizontal detector offset at the beamline) were merged in Aimless, and statistics were deposited into the PDB without any truncation. All post-processing was performed on the original map generated from this initial merge. Data was trimmed to the final resolution in REFMAC5. Data collection statistics (pre-truncation) as well as processing statistics (post-truncation at the final resolution) are in included in Table 4-S1. The deposited data in the PDB will be untruncated.

Structures with R-work – R-free differences above 5%

We attempted to mitigate the spread between R-work and R-free for the new structures in three different ways.

An all alanine-model was generated using the CCP4-embedded program Chainsaw, and this was used for the molecular replacement instead of the unmodified 1PHM model. Molecular replacement (Molrep) was performed with the all-alanine model, followed by a short series of refinements (less than 10 cycles) in Refmac5. Following the refinements, each residue was manually fit back into the model using Coot and real-space refinement. The resulting coordinates were used in Refmac5 for several more refinements. The resulting R-factor and R-work remained at 8%.

Another method to minimize the spread between R-factors was to use the original mtz file generated from Aimless in all refinements. Rather than iteratively using the refined maps throughout refinement, only the refined coordinates were used against the original mtz. After a few rounds of refinement using Refmac5, the spread remained at approximately 8%.

Lastly, we attempted to delete flexible loop regions from the coordinate files (those with unsatisfactory electron densities). These coordinate files were then used for refinements, but again, the spread between R-factors remained at 8%.

All validation reports generated from wwPDB Deposition are provided in the supplementary information, which provided Ramachandran and Clashscore statistics. No pseudosymmetry or twinning was observed (the twinning fractions from the L-test were 0.03-0.05).

The WT structure

The WT structure was not deposited into the PDB, as structures using these conditions have already been published by others. Molprobity was used to generate Clashscore and Ramachandran statistics (documents provided in the supplemental information). Molprobity did not generate the “Allowed Ramachandran” metric, so is not provided in the final crystal table.

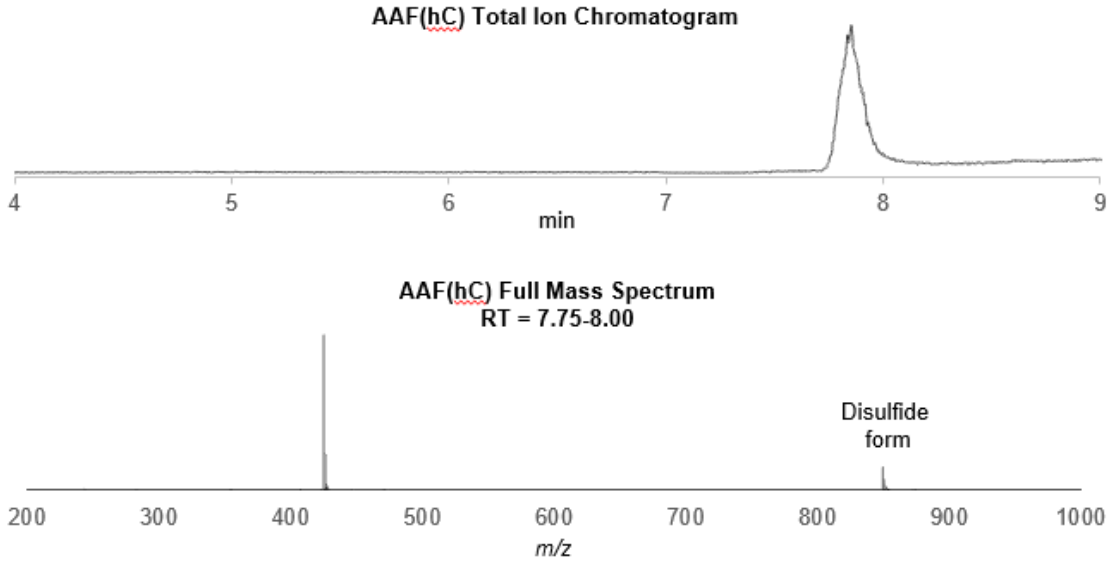

Variant	Expected monoisotopic mass	Observed monoisotopic mass	ppm error
AAF-hCys	425.1853 *z* = 1	425.1867 *z* = 1	3.29

Figure 5-S1. Total ion chromatogram and mass spectrum for the AAF-hCys tetrapeptide used in this work. *The homocysteine-containing peptide is seen via MS in monomer and disulfide forms.*

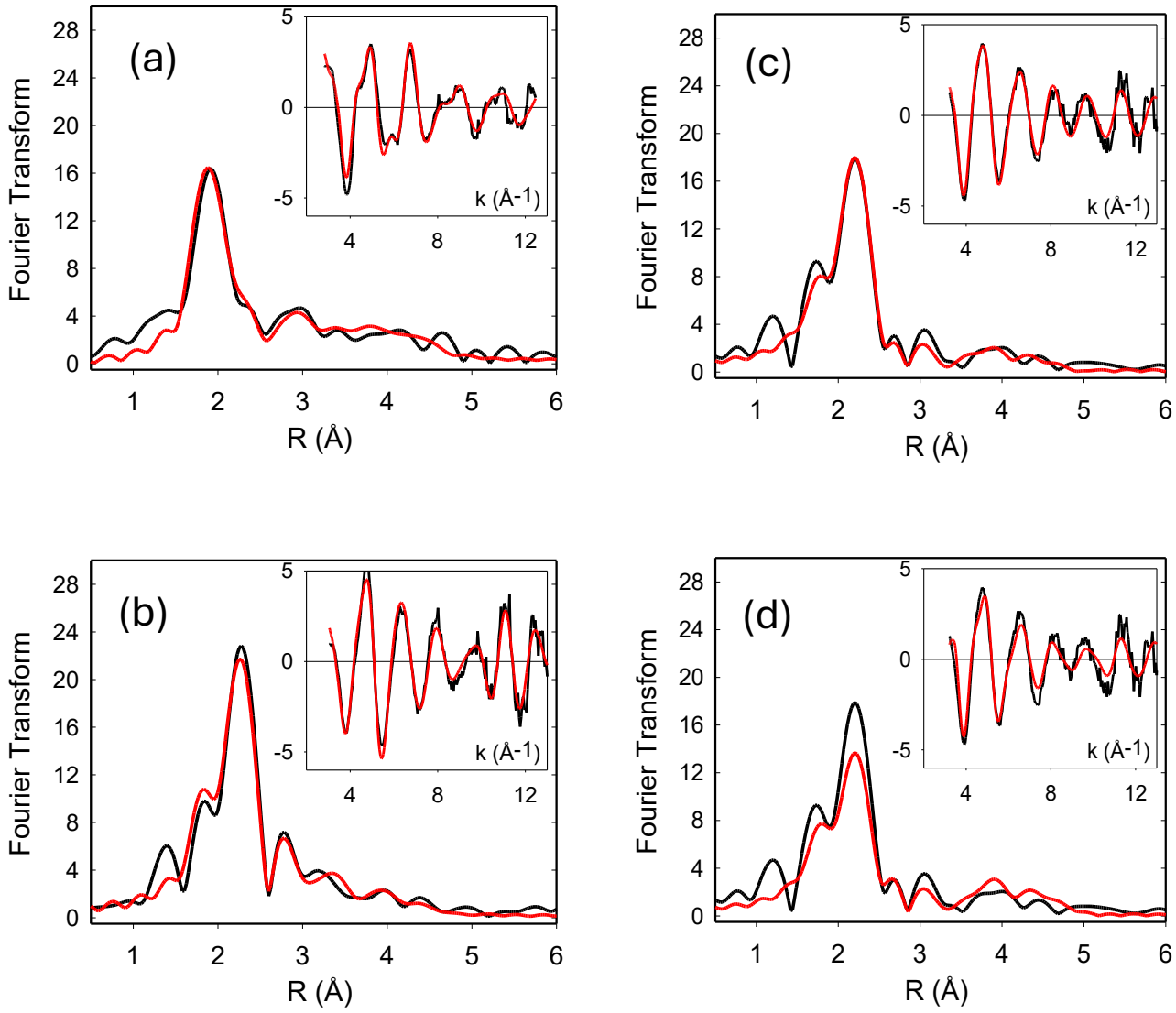

Figure 5-S2 Comparison of EXAFS and Fourier Transform fits. *Comparison of fits to the EXAFS and Fourier transforms of (a) WT PHM with 0.5 S(met) and no thiolate; (b) WT PHM + AAF-hCys with 1S(thiolate) + 0.5 S (met) expected for a thiolate-bridge; (c) M314H - AAF-hCys complex with 1 S per Cu expected for a thiolate bridge and (d) M314H - AAF-hCys complex with 0.5 S per Cu expected for a mononuclear thiolate complex. Parameters for all fits are listed in Table 5-S4.*

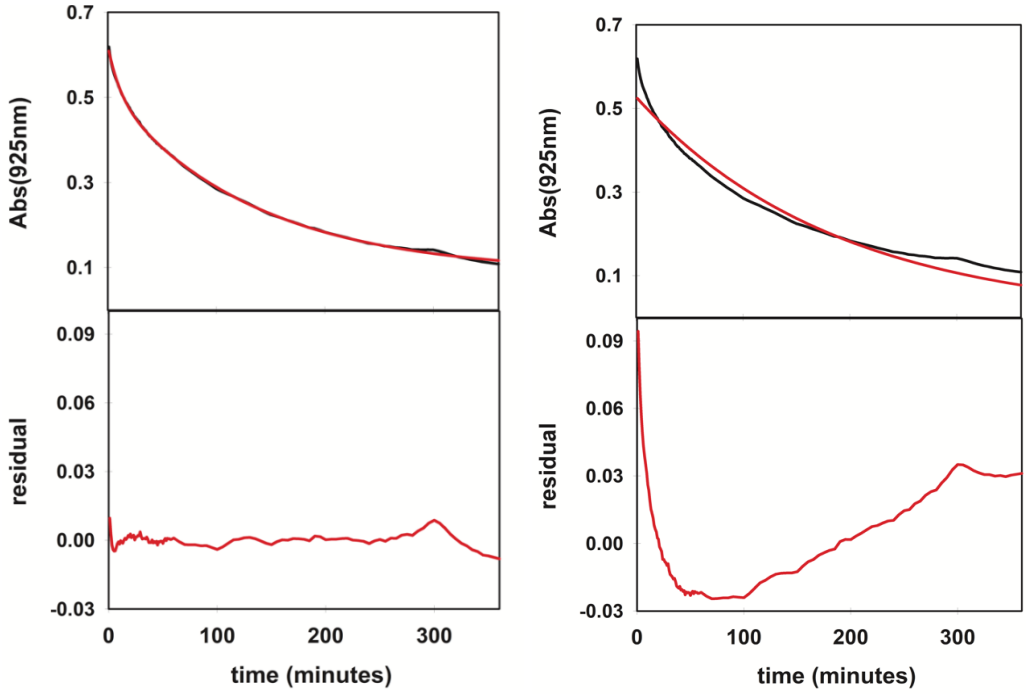

Figure 5-S3. Kinetics of reduction of the wtPHM:AAF-hCys complex by sodium ascorbate.

Reduction was monitored by disappearance of the UV-visible absorbance feature at 925 nm characteristic of the purple mixed-valence species. Kinetic parameters were extracted by least-squares fitting to a double exponential model (left panel) in the program SigmaPlot represented by the following equation:

$$Abs_{925nm} = A_1 e^{-k_1 t} + A_2 e^{-k_2 t} + A_0$$

Parameters for the double exponential fit to the data are as follows with the calculated value in parenthesis: A_1 (0.11), k_1 (0.088 min^{-1}), A_2 (0.43), k_2 (0.007 min^{-1}), A_0 (0.09).

A single exponential model is also shown for comparison in the right panel, though this represents a significantly worse fit to the data. The single exponential fit used the following equation and yielded metrical values of A_1 (0.45), k_1 (0.010 min^{-1}), A_0 (0.12):

$$Abs_{925nm} = A_1 e^{-k_1 t} + A_0$$

Residuals are shown in separate panels below each fit.

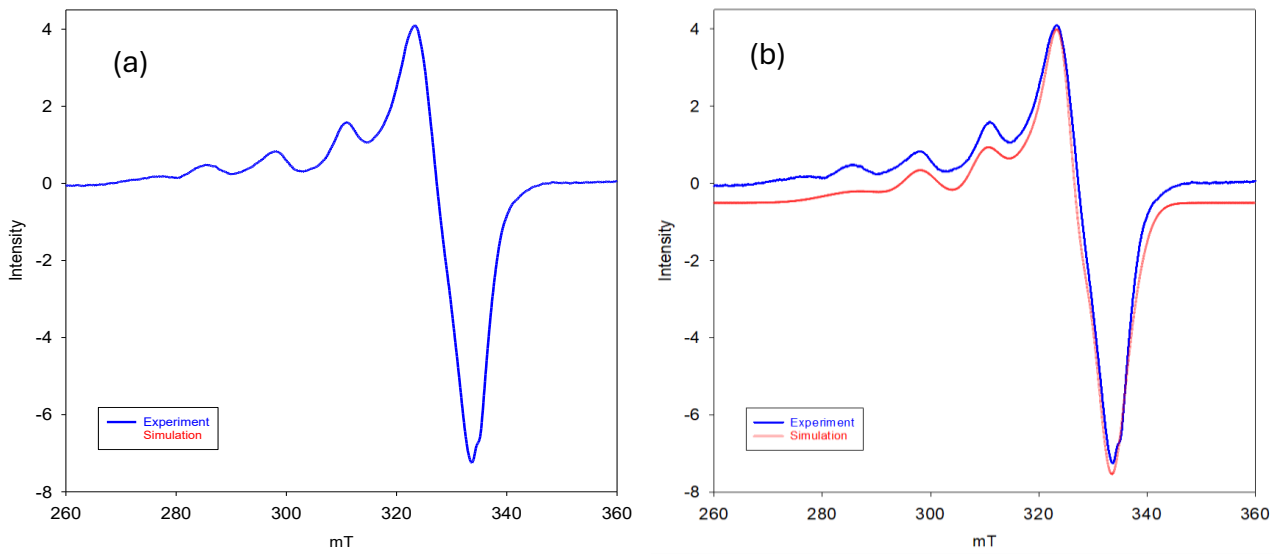

Figure 5-S4. Alternative EPR simulations for the mixed-valence species prepared by 3 minute ascorbate reduction of the PHM-AAF-hCys complex. *The mixed-valence PHM-AAF-hCys complex prepared by 3 min ascorbate reduction of the fully formed complex (see Figure 3 of the main text) was simulated using EASYSPIN. Panel (a) is a simulation that corresponds to a 2-component spectrum with a hyperfine interaction between the unpaired electron and both Cu nuclei of the MV species (A2,3) and parameters as listed in Fit 2 Table 5-S4. Panel (b) is the simulation with parameters listed in Fit 3 (Table 5-S4) and corresponds to a 1-component S=1/2 system with hyperfine coupling to a single Cu nuclei (A3). EPR conditions were as follows: Microwave frequency 9.398 GHz, microwave power 2 mW, modulation frequency 100 KHz, modulation amplitude 10 G, temperature 100 K, sweep width 1000G, sweep time 40 s. EPR fitting parameters are listed in Table 5-S$.*

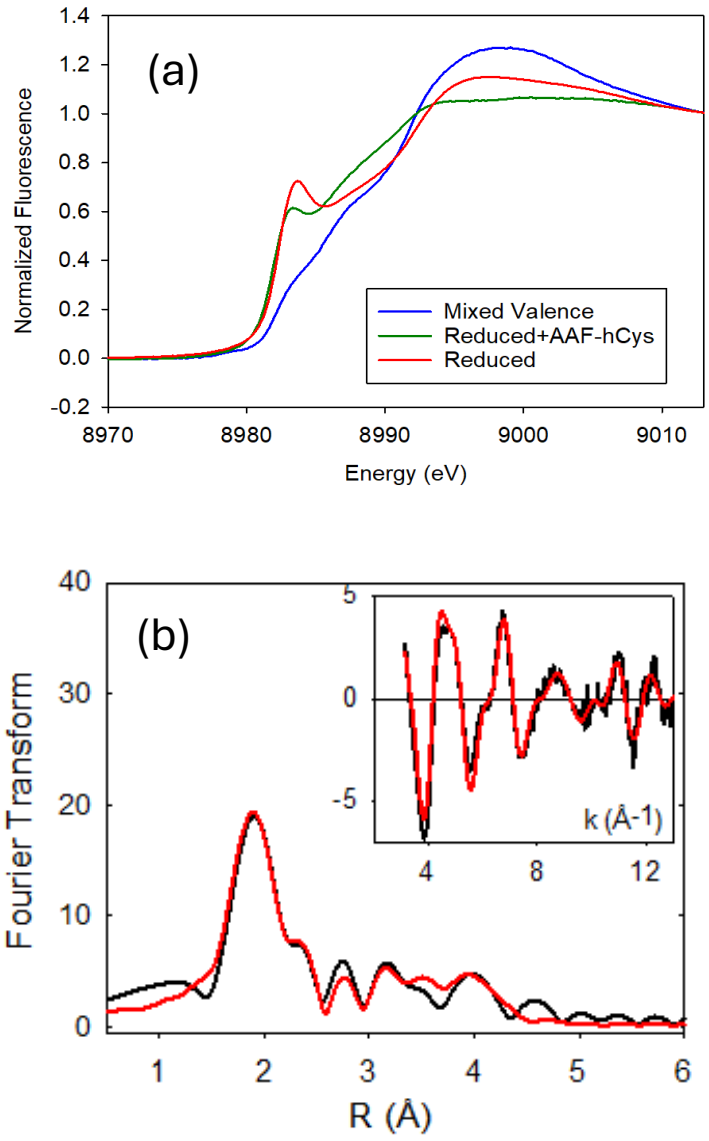

Figure 5-S5 EXAFS of AAF-hCys PHM MV complexes. *(a) Comparison of Cu K-edge absorption edges of the AAF-hCys wtPHM complexes in mixed valence and fully reduced forms. The unligated fully reduced edge is included for comparison. A weak 1s to 3d transition is apparent in the MV complex at 8979 eV due to the Cu(II) component of the MV complex together with the signal from the residual fully oxidized enzyme (see main text). Spectra are normalized at 9013 eV. (b) EXAFS of the oxidized (mixed valence) AAF-hCys wtPHM complex in 20 mM sodium phosphate pH 7.5. Experimental data are in black and simulations are in red. Full simulation parameters can be found in Table 5-S5.*

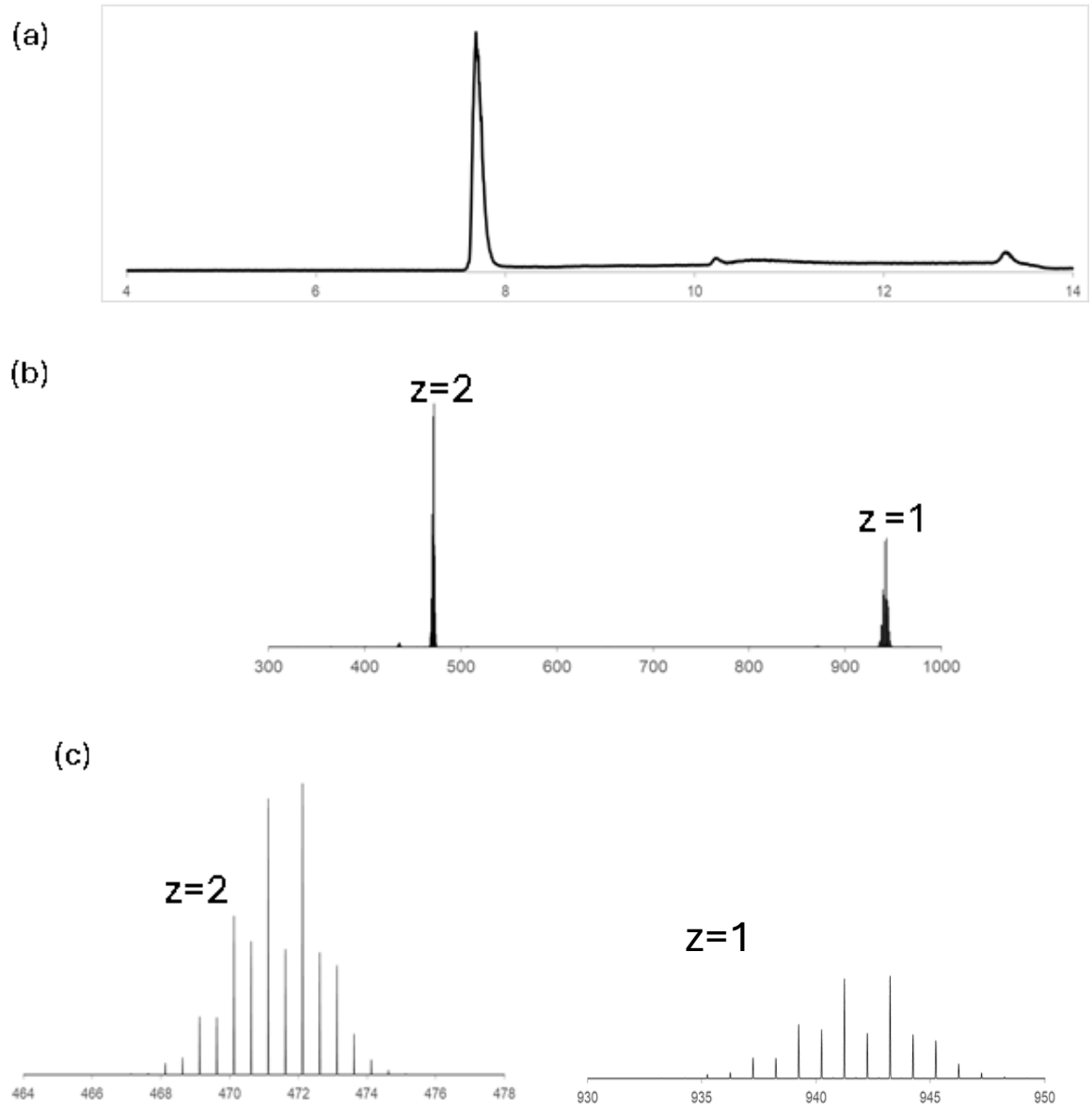

Figure 5-S6. Purification and characterization of the selenium-containing peptide Ala-Ala-Phe-homoselenocysteine (AAF-hSeCys). *(a) HPLC chromatograph (b) mass spectrum showing z=1 and z=2 ions and (c) an expanded view of the z= 1 and z=2 isotope distribution.*

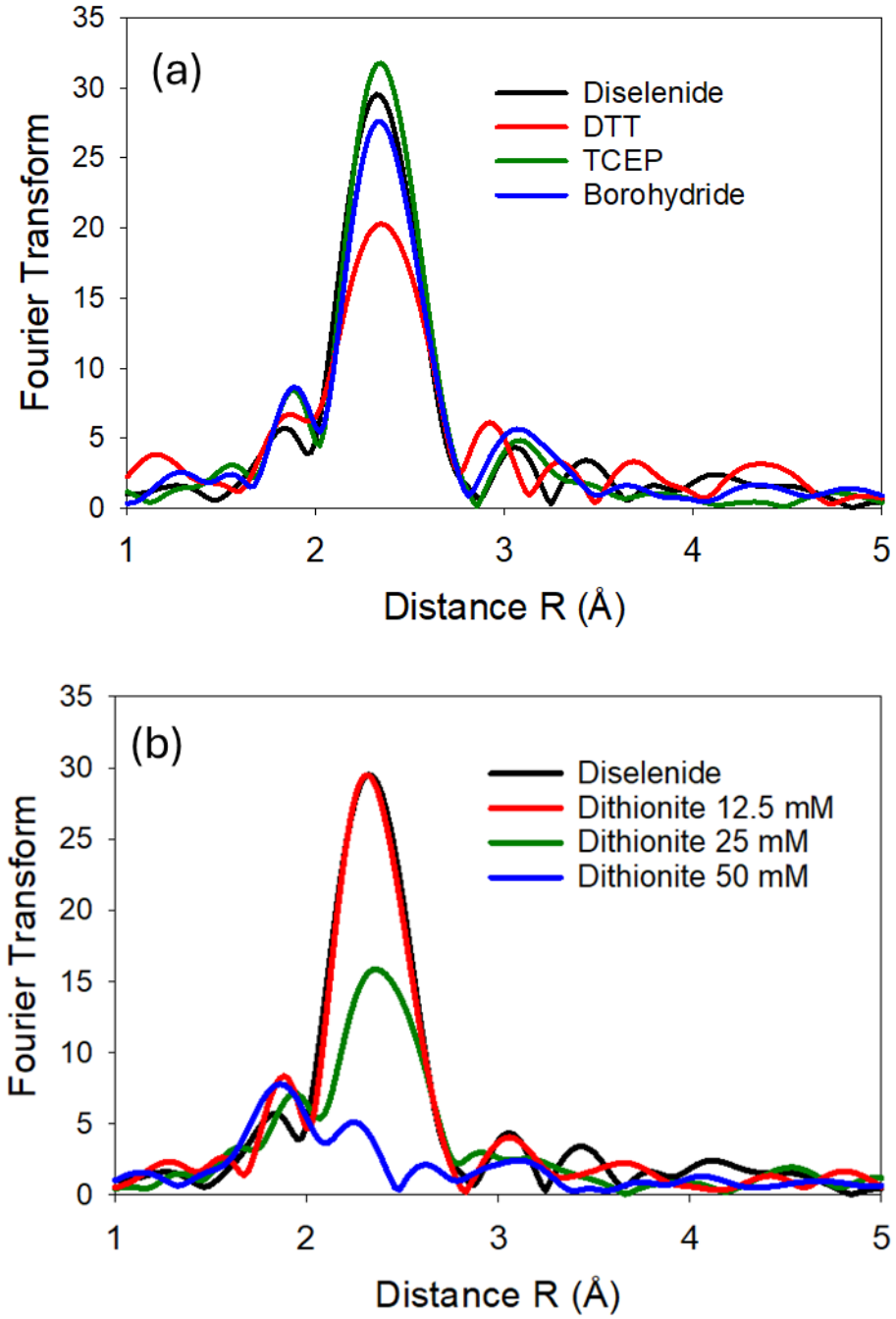

Figure 5-S7. Exploration of the ability of various reductants to reduce the diselenide of AAF-hSeCys using X-ray absorption spectroscopy. *The intensity of the Se-Se shell in the Fourier transform was compared for dithiothreitol (DTT), tricarboxyethylphosphine (TCEP), sodium borohydride, and sodium dithionite. The extent of reduction is indicated by the decrease in the intensity of this Se-Se interaction. (a) 1 mM AAF-hSeCys in 20 mM phosphate buffer pH 7.5 was treated with 10 mM each of DTT, TCEP and $NaBH_4$ (b) 1 mM AAF-hSeCys was treated with increasing concentrations of sodium dithionite.*

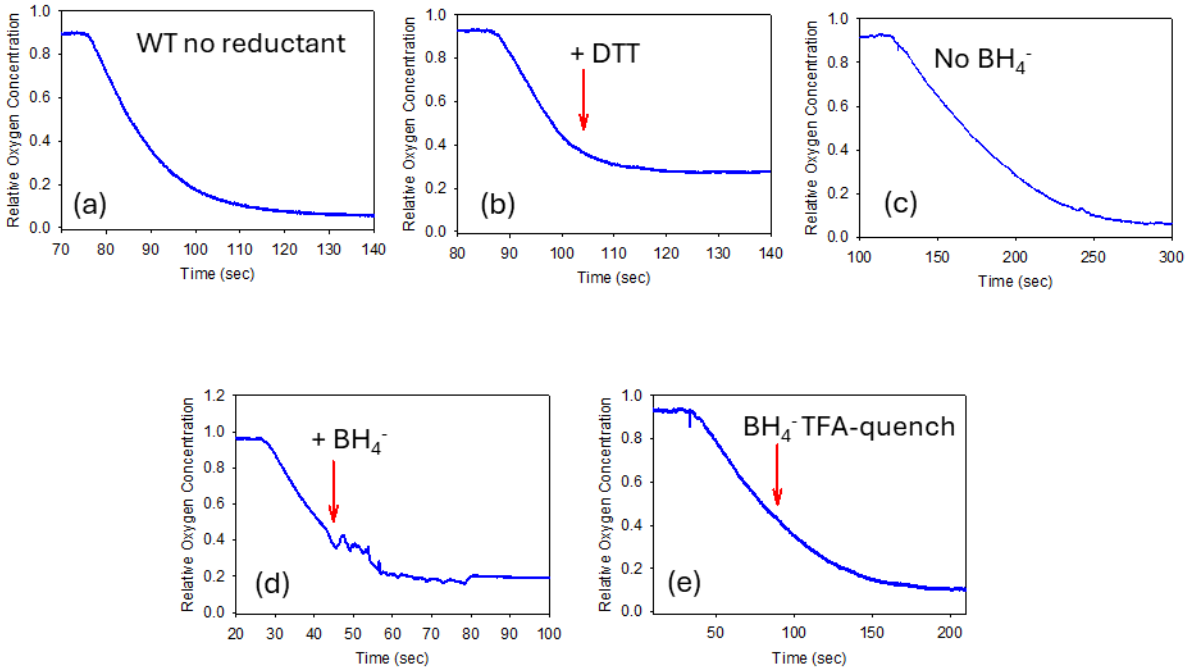

Figure 5-S8 Effect of various added reductants on the enzyme activity of peptidylglycine monooxygenase (PHM). *Reactions were performed, in 2 ml of buffered solution (50 mM MES pH 5.5, 30 mg / ml catalase, 25 uM CuSO4, 100 uM acetyl-YVG substrate) with 1 µM PHM. Reactions were initiated by adding 10 ul of 2 M ascorbate. The reagent to be tested was added after the oxygen had decreased to ~50 percent. Panels represent conditions as follows (a) no added reagent (b) 5 mM DTT. Panels (c) – (e) tested the effect of borohydride and its removal by quenching with TFA. Three separate reactions were performed. In the first reaction, normal enzyme activity was assessed with no additional additives, resulting in complete deoxygenation of the buffer over the course of approximately 5 minutes. In the second experiment, after approximately half the oxygen was consumed a small volume of concentrated borohydride in DMSO was added to a final concentration of 50 µM. The reaction was instantly arrested, accompanied by the formation of hydrogen gas. In the final reaction, after approximately half the oxygen was consumed a small volume of concentrated borohydride in DMSO quenched with 1 molar equivalent of TFA was added to a final concentration of 50 uM, resulting in no reaction.*

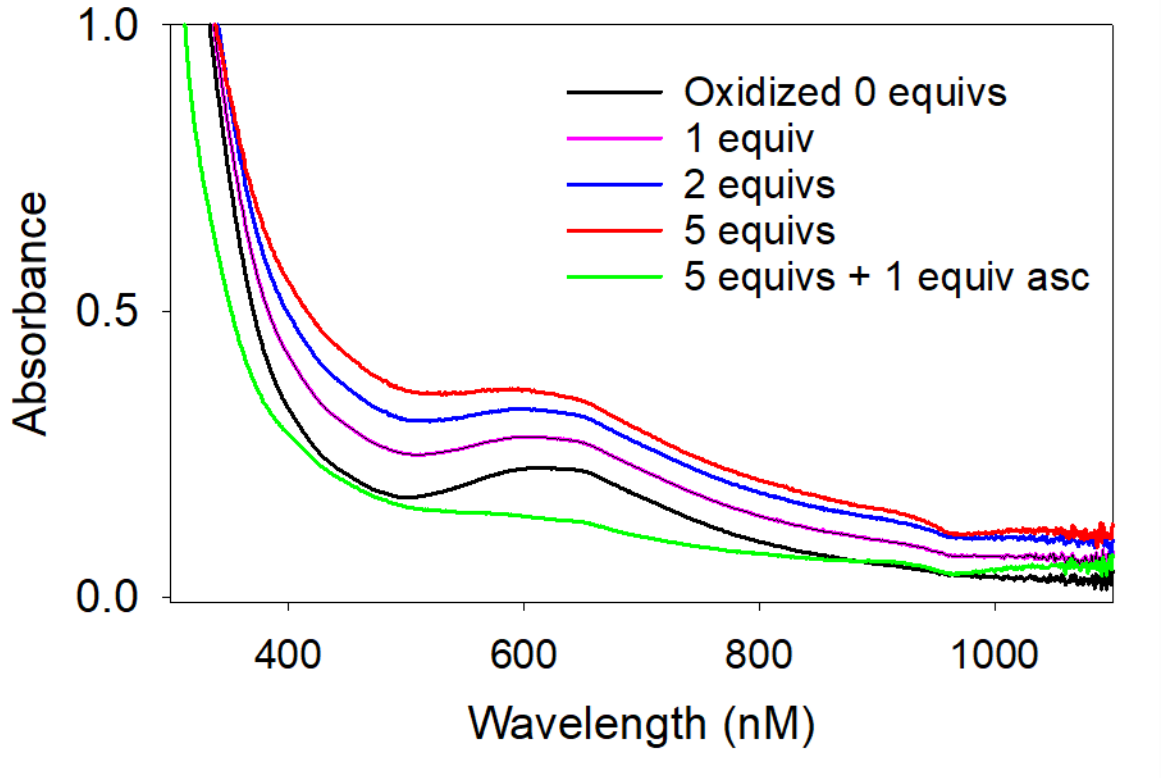

Figure 5-S9. Reaction of oxidized PHM with AAF-SeM.

Table 5-S1. Parameters used in the fits to EXAFS data of PHM reacted with 1 and 2 equivalents of AAF-hSeCys prepared by reduction with equimolar sodium borohydride followed by quenching with TFA.

Selenium edge		Se-C			Se-Se			Se-Cu			
	F ($x10^{-3}$)	No	R (Å)	DW ($Å^2$)	No	R (Å)	DW ($Å^2$)	No	R (Å)	DW ($Å^2$)	ΔE_0
2 equivalents		1	1.95	0.002	0.4	2.31	0.005	1.2	2.39	0.006	-2.4

Copper edge		Cu-N(His)			Cu-S			Cu-Se			
	F ($x10^{-3}$)	No	R (Å)	DW ($Å^2$)	No	R (Å)	DW ($Å^2$)	No	R (Å)	DW ($Å^2$)	ΔE_0
1 equivalent	0.58	2	1.91	0.011	0.5	2.20	0.005	0.3	2.40	0.007	2.3
2 equivalents	0.57	2	1.92	0.017	0.5	2.20	0.004	0.6	2.40	0.007	3.5

Table 5-S2. Titration of oxidized PHM with selenopeptide. *Four different titrations were carried out. Sample 1 was saved and used for EXAFS studies. Samples 2 – 4 were used for EPR quantitation and analysis as described in the text. Data for sample 4 is reported in Figure 6 with simulation parameters in Table 5-S3. Extinction coefficients for the mixed-valence complex were calculated as follows. For samples taken at the titration end point before any ascorbate reduction, the difference between the total copper concentration and the Cu(II) component derived from the EPR detectable copper was presumed to be the Cu(I) component of the mixed valence complex. For the sample analyzed after ascorbate reduction, the EPR sample was thawed, the OD at 1000 nm measured, and the concentration of EPR detectable copper was now used as the concetration of MV complex, since ascorbate was deemed to have reduced all of the Cu(II) not contained in the MV. These calculations led to 3 independent measurements of the MV extinction coefficient as shown in the Table which average to 516 ± 16 M-1 cm-1.*

Sample	$[Cu_{total}]$ (μM)	Equivalents selenopeptide at λ_{max}=1000 nm	Max Abs at 1000 nm	[Cu(II)] (μM) from EPR	[MV] (μM)	Extinction coeff MV ($M^{-1}cm-1$)	Percent EPR detectable
1	1000	3.0	0.60	N/A	N/A		N/A
2	580	4.0	0.51	305	275	539	53
3	1200	3.0	0.65	391	N/A		32
4	659	2.5	0.81	455	408	504	69
+ 5 mM Asc	572		0.49	124	248	506	21

Table 5-S3. EPR parameters used in the fits to the unreacted oxidized PHM, mixed valence species, and mixed-valence species treated with 5 mM ascorbate and frozen immediately. *Data correspond to sample 4 in Table 5-S2. Spectra are averages of 4 scans and collected at a frequency of 9.396 GHz, 170K temperature, 2 mW microwave power, and amplitudes of 2, 6, and 10 Gauss depending on particular experimental conditions, as well as to assess the possibility of spectra broadening. Experimental data was simulated using EasySpin as described in the text. The spectrum of the mixed-valence species showing the position of the g3 hyperfine peaks of both components is shown below the Table.*

Sample	Component 1				Component 2				Ratio	rmsd
	g-value	**A-value**	**Line Width**	**Strain**	**g-value**	**A-value**	**Line width**	**Strain**		
PHM oxidized	g_1 2.071 g_2 2.043 g_3 2.262	A_1 30 A_2 10 A_3 521	3.7	g_3 0.04 A_3 5	g_1 2.085 g_2 2.015 g_3 2.295	A_1 30 A_2 40 A_3 412	8.0	g_3 0.04 A_3 74	1: 1	0.0231
Mixed-Valence	g_1 2.070 g_2 2.058 g_3 2.258	A_1 15 A_2 25 A_3 531	10.0	g 0.03 A_3 0	g_1 2.067 g_2 2.017 g_3 2.288	A_1 10 A_2 5 A_3 409	3.9	g_3 0.002 A_3 227	1: 0.8	0.0180
Mixed-Valence + ascorbate	g_1 2.060 g_2 2.015 g_3 2.290	A_1 20 A_2 10 A_3 465	3.2	g_3 0.004 A_3 167	g_1 2.104 g_2 2.000 g_3 2.253	A_1 45 A_2 55 A_3 343	4.60	g 0.05 A_3 50	1: 0.8	0.0114

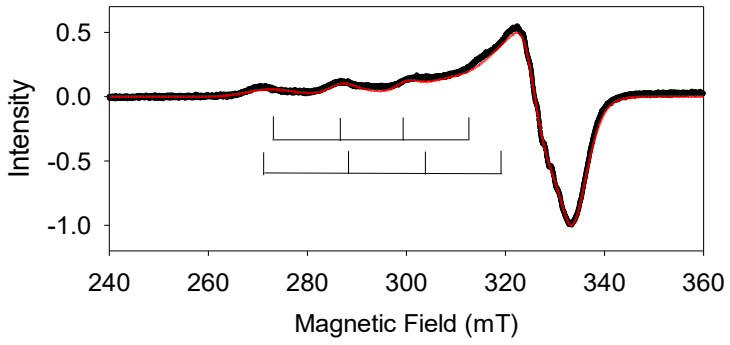

Table 5-S4. EPR simulation parameters of the oxidized wtPHM:AAF-hCys complex. *The mixed-valence AAF-hCys wtPHM complex prepared by 3 min ascorbate reduction of the fully formed complex (see Figure 3 of the main text) was simulated using EASYSPIN. Fit 1 is the simulation shown in Figure 5-3 top panel of the main text and corresponds to a 2-component S=1/2 system with hyperfine coupling to a single Cu nuclear spin (A3,1,) in the parallel region of the spectrum. Fit 2 is the simulation shown in Figure 5-S2(a) and corresponds to a 2-component S=1/2 system with hyperfine coupling to two Cu nuclear spins (A3,1, A3,2). Fit 3 is the simulation shown in Figure 5-S2(b) and corresponds to a 1-component S=1/2 system with hyperfine coupling to a single Cu nuclei (A3). EPR conditions were as follows: Microwave frequency 9.398 GHz, microwave power 2 mW, modulation frequency 100 KHz, modulation amplitude 10 G, temperature 100 K, sweep width 1000G, sweep time 40 s. A values are reported in MHz.*

Sample	Component 1				Component 2				Ratio	rmsd
	g-value	**A-value (MHz)**	**Line Width (mT)**	**Strain (g, A (mT))**	**g-value**	**A-value (MHz)**	**Line width (mT)**	**Strain (g, A (mT))**		
Fit 1	g_1 2.069 g_2 2.018 g_3 2.213	A_1 10 A_2 10 A_3 389	4.6	g 0.005 A_3 272	g_1 2.057 g_2 2.015 g_3 2.297	A_1 10 A_2 10 A_3 393	3.0	g_3 0.026 A_3 60	1: 0.35	0.00679
Fit 2	g_1 2.070 g_2 2.018 g_3 2.212	A_1 10 A_2 10 $A_{3,1}$ 391 $A_{3,2}$ 33	4.5	g_3 0.006 A_3 262	g_1 2.058 g_2 2.015 g_3 2.298	A_1 10 A_2 10 $A_{3,1}$ 392 $A_{3,2}$ 6	6.0	g_3 0.023 A_3 60	1: 0.35	0.00666
Fit 3	g_1 2.066 g_2 2.017 g_3 2.208	A_1 10 A_2 10 A_3 365	4.8	g 0.005 A_3 208					1: 0.00	0.01495

Table 5-S5. Alternative fits to the EXAFS of wtPHM and its M314H variant treated with 3 equivalents of the AAF-hCys peptide inhibitor. *For all fully reduced samples, the first shell interactions arise from histidine residues and include multiple scattering interactions from imidazole ligands as described in detail in SI reference 11, but these are omitted for clarity in the table. For the MV complex (fit 11) imidazole MS interactions are included for the N shell.*

Fit #	Sample	Fit Index[1]	1st shell Cu-N(His)/O			2nd shell Cu-S (hCys /Met)			Weak Scatterer Cu-N/O/S/Cu				
		F (x10^{-3})	No[2]	R (Å)[3]	DW (Å^2)[4]	No	R (Å)	DW (Å^2)	Atom	No	R (Å)	DW (Å^2)	ΔE_0
1	Red PHM	0.46	2	1.92	0.0077	0.5 (Met)	2.24	0.0120					-0.55
2	Red PHM + AAF-hCys	0.45	2	1.96	0.0123	1.5 hCys+Met	2.27	0.0060					-2.7
3	Red PHM + AAF-hCys	0.45	2	1.96	0.0123	1.0 hCys	2.27	0.0040					-2.8
						0.5 Met	2.25	0.0120					
4[5]	Red PHM + AAF-hCys	0.30	2	1.96	0.0123	1.0 hCys	2.27	0.0017					-3.0
						0.5 Met	2.82	0.0023					
5	Red PHM + AAF-hCys	0.43	2	1.96	0.0123	1.0 hCys+Met	2.27	0.0016					-2.8
6	Red PHM + AAF-hCys	0.45	2	1.96	0.0123	1.5	2.27	0.0062	N/C	1	2.69	0.0050	-2.7
7	Red PHM + AAF-hCys	0.52	2	1.96	0.0123	1.5	2.27	0.0060	O	1	2.66	0.0084	-2.8
8	Red PHM + AAF-hCys	0.39	2	1.96	0.0123	1.5	2.27	0.0058	Cu	1	2.70	0.0235	-2.8
9	Red M314H+ AAF-hCys	0.50	2.5	1.94	0.0248	1.0	2.22	0.0062					0.30
10	Red M314H+ AAF-hCys	0.83	2.5	1.94	0.0248	0.5	2.22	0.0032					0.30
11	MV PHM + ascorbate	0.50	2.4 N	1.90	0.0073	0.4	2.28	0.0057					-1.5
	(3 min)		1.2 O	1.99	0.0030								

[2] Coordination numbers are generally considered as accurate +/- 25% unless indicated as low confidence.
[3] In any one fit, the statistical error in bond-lengths is ±0.005 Å. However, when errors due to imperfect background subtraction, phase-shift calculations, and noise in the data are compounded, the actual error is probably closer to ±0.02 Å.
[4] Debye-Waller (DW) factors are reported as $2\sigma^2$ and are defined as twice the mean square deviation of the experimental bond distance as compared to the simulated value.

[5] Although this fit gives the lowest least squares residual, the DW factors are chemically unreasonable. The fit suggests that the Met ligand is bound at 2.8 Å, but the simulated DW of 0.002 $Å^2$ is much lower than is reasonable for a weakly bound thioether at this distance, especially since the Met ligand is known to coordinate only weakly to Cu(I) in the unreacted reduced protein (Fit 1